ANISOTROPY AND THE STRUCTURAL EVOLUTION OF THE OCEANIC UPPER MANTLE

by

DONALD WILLIAM FORSYTH

B.A. Grinnell College
(1969)

SUBMITTED IN PARTIAL FULFILLMENT OF THE
REQUIREMENTS FOR THE DEGREE OF
DOCTOR OF PHILOSOPHY

at the

MASSACHUSETTS INSTITUTE OF TECHNOLOGY

and the

WOODS HOLE OCEANOGRAPHIC INSTITUTION

September, 1973
i.e. February, 1974

Signature of Author..... Donald W. Forsyth .....
Joint Program in Oceanography, Massachusetts Institute of Technology - Woods Hole Oceanographic Institution, and Department of Earth and Planetary Sciences, and Department of Meteorology, Massachusetts Institute of Technology, September 1973

Certified by..... Frank Press .....
Thesis Supervisor

Accepted by..... S. M. Stinard .....
Chairman, Joint Oceanography Committee in the Earth Sciences, Massachusetts Institute of Technology - Woods Hole Oceanographic Institution

Lindgren

ANISOTROPY AND THE STRUCTURAL EVOLUTION OF THE OCEANIC UPPER MANTLE

by

Donald William Forsyth

Submitted to the Department of Earth and Planetary Sciences on September 26, 1973 in partial fulfillment of the requirements for the degree of Doctor of Philosophy.

ABSTRACT

The dispersion of Love and Rayleigh waves in the period range 17-167 sec. is used to detect the change in the structure of the upper mantle as the age of the sea-floor increases away from the mid-ocean ridge. Using the single station method, the group and phase velocities of Rayleigh waves were measured for 78 paths in the east Pacific. The focal mechanisms of the source events were determined from P-wave first motion data and the azimuthal variation in Rayleigh wave amplitudes. In order to describe the observed Rayleigh wave dispersion, both a systematic increase in velocities with the age of the sea-floor and anisotropy of propagation are required. The maximum change in velocity with age is about 5%, with the contrast between age zones

decreasing with increasing period. The greatest change occurs in the first few million years, due to the rapid cooling and solidification of the upper part of the lithosphere. In the 0-5 m.y. age zone, the average thickness of the lithosphere can be no greater than 30 km, including the water and crustal layers. Within 10 m.y. after formation, the lithosphere reaches a thickness of about 60 km. As the mantle continues to cool, the shear velocity within the lithosphere increases. Within the area of this study, no change occurs in the upper mantle deeper than about 80 km.

Rayleigh waves travel fastest in the direction of spreading. The degree of anisotropy in Rayleigh wave propagation is frequency-dependent, reaching a maximum of 2.0 ± 0.2 percent at a period of about 70 sec. Several models are constructed which can reproduce this frequency-dependent anisotropy.

The regional phase velocities of the fundamental and first higher Love modes have been simultaneously measured using a new technique. The squares of the difference between the observed phase and the predicted phase are summed over 45 paths for a set of trial phase velocities. The trial velocities which give the minimum sum correspond to the average phase velocities of the fundamental and first higher modes. The Love wave data is inconsistent with the Rayleigh

wave data unless SH velocity is higher than SV velocity within the uppermost 125 km of the mantle. Anisotropy deeper than 250 km is suggested, but not required, by the data.

Thesis Supervisor:

Frank Press
Professor of Geophysics

Acknowledgements

I would first like to thank my wife, Doris, whose patience and impatience at the proper times, along with loving care, enabled me to finish this thesis. I am particularly grateful for the opportunity to work with Dr. Frank Press, whose creative guidance and inspiration served me well throughout my graduate career. His example, both as a scientist and as a man, will always mean a great deal to me.

Interactions with the faculty and students at Woods Hole and MIT have been of great help. Dr. Joe Phillips kindled my first interests in geophysics. Dr. Sean Solomon and Dr. Keiiti Aki contributed advice on both practical and theoretical matters. Dr. Frank Press suggested the original research topic. Al Smith helped me with inversion theory and Ken Anderson helped with computer programming expertise. Dr. Don Weidner guided me in the early stages of research. It is a special pleasure to acknowledge stimulating discussions about nearly everything with Ray Brown, Ed Chapman, Paul Kasameyer and Frank Richter.

This research was sponsored by the Office of Naval Research under contract N00014-67-0204-0048.

Table of Contents

1. Introduction

1.1 Outline of Study

Hot mantle material rises under mid-ocean ridges to form the new oceanic lithosphere. As the lithospheric plates spread away from the ridges, the mantle cools, causing a number of temperature-dependent changes in physical properties of the lithosphere and asthenosphere. Geophysical studies of these changing properties have contributed much to the understanding of the thermal regime of the mid-ocean ridges and their role in the convective overturn of the mantle. However, most of the observations to date measure only the near-surface effects of the elevated mantle temperatures, such as high heat flow (Lee and Uyeda, 1965; Sclater and Francheteau, 1970) or unusually low P_n and S_n velocities (Talwani, et al., 1965; Keen and Tramontini, 1970; Hart and Press, 1972). Other techniques measure a total effect averaged over a vertical section of the upper mantle. Gravity anomalies (Talwani et al., 1965), the elevation of the ridges (Sclater et al., 1971), and the attenuation or delay of seismic body waves (Molnar and Oliver, 1969; Solomon, 1973; Long and Mitchell, 1970), all measure in different ways the total changes in density or elastic properties summed over the upper 100 to 200 km of the oceanic mantle.

The dispersion of surface waves is also controlled

by the average properties of the mantle over a large depth interval. However, by sampling the dispersion of different modes over a wide frequency range, the distribution of shear velocity with depth can be measured. The advantage of multiple measurements is illustrated in figure 1 by the varying sensitivity of the phase and group velocities of surface waves to shear velocity structure of the mantle (to a lesser extent, Rayleigh waves depend on the density and compressional velocity, and Love waves depend somewhat on the density). At 40 sec, the phase and group velocity of Rayleigh waves are most sensitive to the shear velocity at a depth of about 50 to 60 km. The depth of the peak sensitivity increases with period, roughly in proportion to the increase in wavelength. Thus, measurements at different frequencies give averages over different depth ranges. The group velocity, which is related to the derivative of the phase velocity with respect to frequency, is more sensitive to the structure than the phase velocity. Unless the phase velocity is perfectly known over the entire range of frequencies sampled, an independent measurement of the group velocity can add important information. Phase velocity measurements are needed because it is possible to have two structures with similar group velocities but different phase velocities. The dispersion of Love waves yields additional information. In particular, the phase velocity

of the first higher Love mode is most sensitive to the structure within the low velocity zone of the mantle and if it can be measured with sufficient accuracy, it will give unique data on the deeper structure beneath the mid-ocean ridges. The higher mode Rayleigh waves are not considered because they are not sufficiently excited by moderate-sized earthquakes to be a significant contribution to the typical sesimic record. Due to the existence of different modes of propagation and a readily observable range of frequencies, surface waves can be used to directly detect the depth distribution of the thermal anomalies associated with the mid-ocean ridges.

The purpose of this study is to measure the dispersion of Rayleigh and Love waves as a function of the age of the sea-floor, in order to determine the structure of the upper mantle beneath a mid-ocean ridge and the changes that occur in an oceanic plate as it moves away from the ridge. The most rapid changes are expected within the first few million years (Forsyth and Press, 1971) after formation of the oceanic crust. This study therefore concentrates on the surface wave dispersion within the east Pacific. Here the separation rates between the Nazca and Pacific plates are the highest in the world (Herron, 1972), allowing the most detailed examination of the early evolution of the lithosphere. In addition to changes with age of the sea floor, the possibility that surface wave

velocities depend on the direction of propagation is considered. Raitt et al. (1969) and Morris et al. (1969) have shown that the Pacific mantle immediately beneath the Moho is anisotropic. If this anisotropy continues to an appreciable depth, it should affect the surface wave velocities, creating the possibility of mistakenly attributing directional variations to regional changes. There have been several previous, regional, surface-wave studies in the Pacific (Kuo et al., 1962; Santo and Sato, 1963; Savage and White, 1969; Knopoff et al., 1970; Kausel, 1972; Leeds, 1973; and others): none has considered the possibility of anisotropy or simultaneously measured regional phase and group velocities or measured the phase velocity of the first higher Love mode. The results of these previous investigations are compared with the results of this study later in the text.

The two-station method of measuring phase velocity (Brune et al., 1960) is inadequate for the purposes of this study. There are very few island stations, so the number of possible two-station paths within the ocean is very limited. In addition, the technique I employ for measuring the phase velocity of the first higher Love mode is possible only using the single station method, in which the phase velocity is computed for a path between the source earthquake and a single station.

Figure 1. Partial derivatives of surface wave velocities at 40 seconds period with respect to shear wave velocity $\beta(z)$. Steps in the curves are due to discontinuities in the model of the upper mantle. Curve labelled R_u is the derivative of the fundamental mode Rayleigh wave group velocity; R_c, fundamental mode, Rayleigh wave phase velocity; L_o, fundamental mode, Love wave phase velocity; L_1, first higher mode, Love wave phase velocity.

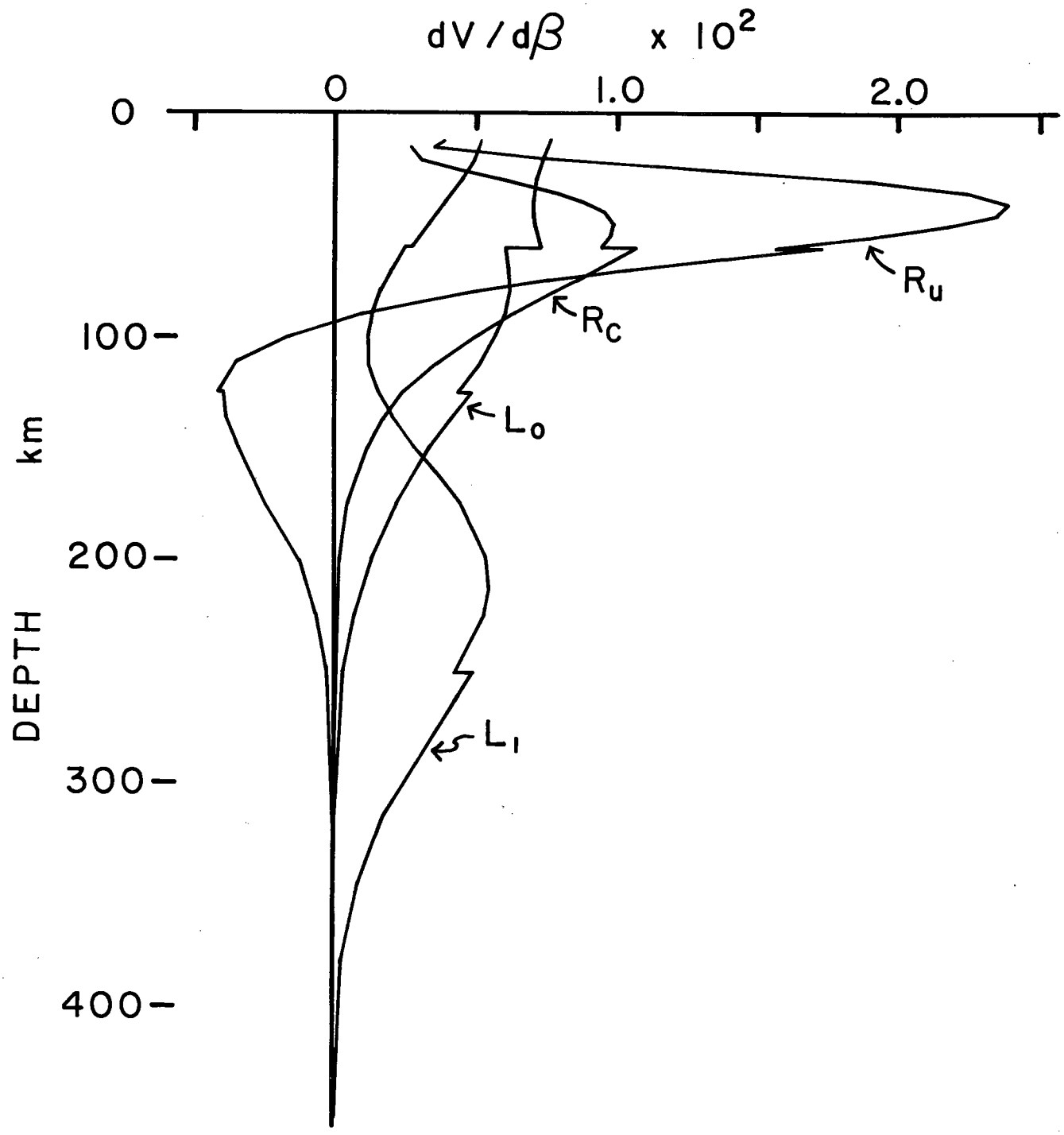
dV / dβ x 10²
0
1.0
2.0
0
100
200
300
400
km
DEPTH
Ru
Rc
Lo
L1

1.2 The single station method

The technique for measuring phase velocities using only one station was originally developed by Brune et al. (1960). Early studies using this method (Kuo et al., 1962) were hampered by the necessity of choosing an arbitrary initial phase which was independent of period. Subsequent developments in the theory of the excitation of surface waves (Haskell, 1964; Ben-Menahem and Harkrider, 1964; Saito, 1967) have made it possible to compute the initial phase as a function of frequency for an arbitrarily oriented point source in realistic earth models. Recently, Knopoff and others have extensively employed this method in regional studies of the earth (for review, see Knopoff, 1972; also Kausel, 1972; Weidner, 1972).

The phase velocity between the earthquake and the station is given by

$$c(\omega) = \frac{\omega \, DIST}{\phi_{obs}(\omega) + \omega t_1 - \phi_{inst}(\omega) - \phi_f(\omega) \pm n} \qquad (1)$$

where DIST is the distance between source and receiver, ω is the frequency, and t_1 is the time to the beginning of the record. For convenience, throughout this paper the observed phase ϕ_{obs}, the phase delay due to instrument response ϕ_{inst}, and the initial phase at the source ϕ_f will be given in fractions of a circle rather than in radians. n is an integer which allows for the inherent ambiguity of n circles in determining the total phase

shift. This ambiguity is removed by placing limits on the acceptable value of c at long periods. ϕ_{obs} is obtained from the Fourier integral of the digitized record f(t),

$$A(\omega)\, e^{2\pi i \phi_{obs}(\omega)} = \int_{t_1}^{t_2} f(t)\, e^{i\omega t}\, dt \qquad (2)$$

Because the initial phase depends on the depth and the orientation of the source, the first requirement for a study based on the single station method is a set of reliable focal mechanism solutions. The determination of the source geometries and the steps used in signal processing are described in the following sections.

2. Source events: Focal mechanisms and depths

Seventeen earthquakes were used as sources for the single-station study of phase and group velocities. The focal mechanisms of fourteen of these events were based on both P-wave first motions and the azimuthal variation in surface wave amplitudes. The source parameters for the three events determined from body wave observations alone (events 13, 14 and 16 in Table 1) were given by Anderson and Sclater (1972). A list of the earthquakes and source characteristics are given in Table 1. As shown in figure 2, two of the events are intra-plate earthquakes characterized by thrust-faulting, one event associated with the Galapagos Rift Zone is characterized by normal faulting, the rest, which show predominantly strike slip motion, are associated with transform faults of the active ridge system of the East Pacific. The remote location and small size of these earthquakes make it difficult to obtain sufficient observations to allow a satisfactory determination of the focal mechanism from body waves alone. However, by combining the first motion observations of P-waves with the fitting of theoretical radiation patterns to the observed distribution of Rayleigh wave amplitudes, it is possible to accurately describe the geometry of the source. The steps involved in the focal mechanism determination for events 1-12 and 15 are described in the following paragraphs.

(1) Measurement of observed Rayleigh wave radiation patterns.

The long period vertical component of seismograph records of WWSSN stations are digitized at regular time intervals of 1.0 to 2.0 sec. Records from 20 to 25 stations were Fourier-analyzed for each event, except for the March 7, 1963 earthquake for which only 13 records were available. Using the amplitude equalization method (Aki, 1966), the amplitude spectral densities observed at each station are corrected for geometrical spreading on the spherical earth and for attenuation. Hagiwara's formula (Hagiwara, 1958) is employed to correct for instrument response. These corrected amplitudes, plotted as a function of azimuth from the source to the station, form a radiation pattern which is dependent on the strike and dip of the fault plane, the direction of the slip on the fault, the source depth, and the medium in which the earthquake occurs. For Rayleigh waves at long periods, a shallow, strike-slip source yields a four lobed pattern, with the nodes in the direction of the strikes of the fault and auxiliary planes. A dip-slip event gives a two-lobed radiation pattern. Because long period data is less sensitive to the focal depth and effects of the finiteness of the source, the focal mechanism solutions are primarily based on the 67 second period radiation patterns. In addition, the lateral heterogeneities of the earth affect the long period data to a lesser degree than at very short periods. At periods

much greater than 67 sec., long period noise reduces the reliability of the observed amplitudes. For events 3 and 9, the 50 sec. period data gave slightly better results, but for all other events, the scatter in the 67 sec. period amplitudes was less than or equal to the scatter in the shorter period data. In correcting for the attenuation, I assume a Q value of 125 (Ben-Menahem, 1965) and a group velocity of 4.0 km/sec for 50 and 67 sec. periods. The solutions were found to be insensitive to reasonable variations in Q. The focal depths are based primarily on the 20 sec. period Rayleigh wave amplitudes for which Q is assumed to be 500 (Tsai and Aki, 1969). The seismic moments computed from the 67 and 20 sec. data were found to agree within 10% for these assumed Q values, suggesting that at least the relative values of Q are accurate.

(2) Generation of theoretical radiation patterns.

A number of authors have treated the problem of the excitation of surface waves by an earthquake. I use the results of Saito (1967) as discussed by Tsai and Aki (1970). The fault plane geometry and coordinate system used throughout this paper are defined in Appendix 1. Also given are the equations describing the excitation of Love and Rayleigh waves by a double couple, point force in a layered medium. These equations are used in computing the initial phase of the source as well as the theoretical amplitude radiation patterns.

Using the oceanic earth model by Harkrider and Anderson (1966) with a 3 km water layer, I generate a standard set

of radiation patterns for a wide variety of source geometries. 3 km is the approximate depth to the ridge axis, where the source events occur. The shape of each pattern depends only on the depth, and the dip and slip angles. The seismic moment is a scalar factor which is adjusted for each trial pattern to best fit the observed amplitudes. A change in strike corresponds to a rotation of the pattern, so it is not necessary to generate a new pattern for each trial value of the strike of fault plane. The least squares fit of each theoretical pattern to the observed data is computed, then a statistical test is used to define the family of acceptable models. Most of the earthquakes used as sources occur near the ridge axis. In a later section, I show that the Harkrider-Anderson average ocean model is not a good description of the mantle in the source region. However, neither the shape of the Rayleigh wave amplitude patterns nor the initial phase is very sensitive to the details of the structure (Tsai and Aki, 1970, Mendiguren, 1971; Weidner, 1972) and no significant error is introduced by using the standard ocean model.

(3) Defining the family of acceptable source geometries.

It is possible using the Rayleigh wave amplitudes to accurately define the source mechanism even for some small events for which there are very few reliable observations of first motion polarities.

For example, the smallest event studied, Sept. 9, 1969, can be shown to be predominantly strike-slip with an uncertainty

in the strike of only ± 9 degrees, despite the fact that there are only 6 reliable first motion observations (figure 3). The process of defining the limits on the fault parameters is illustrated in figure 4. The least squares fit of three radiation patterns is plotted versus assumed strike of the fault plane. After the best model is found, an F-test is performed comparing the fit of all other models with the best model. With 26 data, in this case, and the one scalar variable, the seismic moment, a ratio of 1.95 between the sum of the squares of the errors for a trial model and the best fitting model means there is only a 5% chance that the difference in fit is due to random fluctuations in the data. In other words, the best pattern is a significantly better model of the source at the 95% confidence level. In figure 4, the best model has dip, 80°, slip, -165° and strike, 100°, but a pure strike-slip source cannot be rejected. A dip of 60° and slip of -150° is unacceptable. In this way, a range of possible models is defined, with limits set at the boundaries of the 95% confidence region in the three-dimensional space of the fault parameters, strike, slip, and dip. As in this example, the strike of a predominantly strike-slip source is usually well-determined, while the dip and slip are somewhat more uncertain. The data used for each of the earthquakes is given in Appendix 2. For purposes of determining the region of acceptable models, a depth of 5 km below sea bottom (base

of the crust) was assigned to each event, following the results of Weidner and Aki (1973) and Tsai (1969). Although variation of a few kilometers in depth affects the quality of the fit, the best fitting source mechanism to the long period data is usually not significantly altered. Further tests (paragraph 5) justify the assigned depth.

(4) Compatibility with first motion observations.

The fitting of radiation patterns within the three dimensional space of fault parameters is a non-linear problem leading to regions of local minima in the error. Some first motion observations or other independent information are required in choosing the correct local minima. For example, a pure thrust event will yield the same two-lobed pattern characteristic of pure normal faulting. Generally it requires only a few P-wave observations to resolve this ambiguity. The last step, then, is to choose a model consistent with the first motions which is as close as possible to the center of the region of possible models. In every case, a solution was found which was consistent with the body wave data and within the range of possible models defined by the Rayleigh wave amplitudes. A further check on the solutions is provided by the observations of Love and Rayleigh phase velocities. If, due to an error in the source mechanism, the azimuth from the epicenter to the station is assigned to the wrong quadrant, an error of π will result in the initial phase. Such an error

is easily detected at long periods, yet no such mistake was found.

(5) Determination of focal depth.

The shape of the radiation pattern from pure strike-slip motion on a vertical fault is independent of depth; the shape from pure dip-slip motion on a fault dipping at 45° varies only slowly with depth. In these two cases, measuring depth with surface waves is possible only by observing the changes in amplitude with period, requiring a precise knowledge of the effects of attenuation and the transfer function for the continent to ocean transition (or by measuring the π phase shift that occurs when the hypocenter is deeper than the change from retrograde to prograde particle motion). For shallow events, amplitudes for periods of 10-20 sec. are required, yet for oceanic paths, there is a great deal of scatter in the amplitudes for periods less than 20 seconds (personal observations and Weidner, 1972). For these reasons, I believe the most precise depth determinations can be made only for earthquakes with components of both dip and strike-slip motion. The radiation pattern at periods of 20 sec. or less for this type of event varies rapidly with depth and the gross changes in shape can easily be detected despite scatter in the data and uncertainty in the attenuation correction (Mendiguren, 1971).

The event in this study which most clearly shows both

dip and strike-slip motion is event 4, Nov. 6, 1965. Using only the 20 sec. period data, the depth of the earthquake is restricted to less than 11 km. This limit is established at the 95% confidence level. As shown in figure 5, the best fitting model is the 5 km source depth, which is consistent with the results of Weidner and Aki (1973) for the mid-Atlantic ridge and those of Thatcher and Brune (1970) in the Gulf of California. The seismic moment for the best fitting model, 9.2×10^{24} dyne-cm, is very close to the seismic moment estimated from the 67 sec. data (Table 1), indicating that the choice of Q is approximately correct. For purposes of computing initial phase, all events were assigned a focal depth of 5 km, except event 17, which was shown by Mendiguren to be 9 km beneath the ocean bottom. The initial phase of a pure strike-slip event is independent of depth, so that no error is introduced by misassignment of the focal depth for such an event. The initial phase, like the amplitude radiation pattern, is most sensitive to depth if the earthquake is characterized by components of both dip and strike-slip motion. However, as discussed above, the sensitivity of the radiation pattern for these events provides good control on the source depth. The effect of the uncertainties in focal depth and mechanism on the initial phase are discussed later in the section on error analysis.

Table 1. Earthquake source characteristics

	Origin time		Location	
No.	Date	h: m: s	Lat.	Long.
1	26 June 1969	02:30:58.4	2.01	-90.48
2	20 Sept. 1969	15:26:41.5	1.78	-101.03
3	9 Sept. 1969	15:23:10.8	-4.43	-105.93
4	6 Nov. 1965	09:21:48.6	-22.13	-113.76
5	3 Nov. 1965	18:21:08.6	-22.34	-113.98
6	7 Mar. 1963	05:21:59.6	-26.87	-113.58
7	18 Nov. 1970	20:10:58.2	-28.72	-112.74
8	12 Oct. 1964	21:55:34.0	-31.4	-110.8
9	29 Dec. 1966	11:56:23.1	-32.81	-111.76
10	6 Oct. 1964	07:17:56.7	-36.2	-100.9
11	19 April 1964	05:13:00.5	-41.7	-84.0
12	21 Jan. 1967	02:54:00.4	-49.71	-114.9
13	1 April 1967	10:41:00.2	-4.59	-105.81
14	2 Sept. 1966	07:59:05.2	-4.5	-106.1
15	9 May 1971	08:25:01.7	-39.78	-104.84
16	20 July 1966	13:22:53.6	-13.33	-111.47
17	25 Nov. 1965	10:50:40.2	-17.1	-100.2

Table 1. Earthquake source characteristics (cont.)

	Fault parameters			Magnitude	Seismic moment
No.	strike	dip	slip	m_b	10^{25} dyne-cm.
1	175	80	-160	5.0	0.60
2	204	60	-75	5.5	2.73
3	100	80	-165	5.2	0.48
4	52	60	166	6.2	0.96
5	65	85	165	5.8	1.94
6	110	82	-8		7.64
7	119	80	-6	5.6	1.37
8	249	87	167	6.0	2.40
9	50	60	-160	5.4	2.16
10	268	58	-12	5.5	2.93
11	271	62	-11	5.5	0.94
12	108	90	172	5.4	3.96
13	103	90	180	5.0	
14	104	90	180	5.1	
15	196	60	90	6.2	8.96
16	103	90	180	4.8	
17	202	46	68	5.7	

Figure 2. Focal mechanisms of earthquakes in the east Pacific used as sources for Love or Rayleigh waves. In the projections of the lower focal hemisphere, shaded quadrants represent compressional first motions. Double lines are spreading centers, single lines are transform faults.

Figure 3. Focal mechanism of the Sept. 9, 1969 earthquake. In the left hand figure, dots indicate observed amplitudes of 50-sec. Rayleigh waves as function of azimuth. The amplitude is proportional to the distance from the center of the figure. Smooth, continuous line is the theoretical radiation pattern. Figure on the right is a Schmidt net projection of the lower focal hemisphere showing the distribution of P-wave polarities. Solid circles represent compressional arrivals, open circles are dilatational. Smaller symbols indicate less reliable observations.

Figure 4. Sum of the squares of the residuals in amplitude for three trial values of dip and slip. A dip of 80°, slip of -165°, and strike of 100° gives the best fit to the observed amplitudes of the Sept. 9, 1969 event. Scale for sum of squares

is arbitrary. Dotted line gives 95% confidence limit discussed in text.

Figure 5. Sum of squares of residuals in amplitude given as a function of model source depth. Best fit to observed 20 sec. period amplitudes is at about 5 km. with strike, dip and slip held at 52°, 60°, and 166°, respectively. The 95% confidence limit on the depth of the Nov. 6, 1965 event is 10.5 km. Vertical scale is arbitrary.

Figure 6. Vertical component of Rayleigh wave observed at Tucson from March 7, 1963 event. Motion toward top of figure is upward. Horizontal scale gives group arrival time in km/sec. Time between tick marks is 1 minute. Note apparent long period undulation superimposed on shorter period oscillations between 3.8 and 3.6 km/sec.

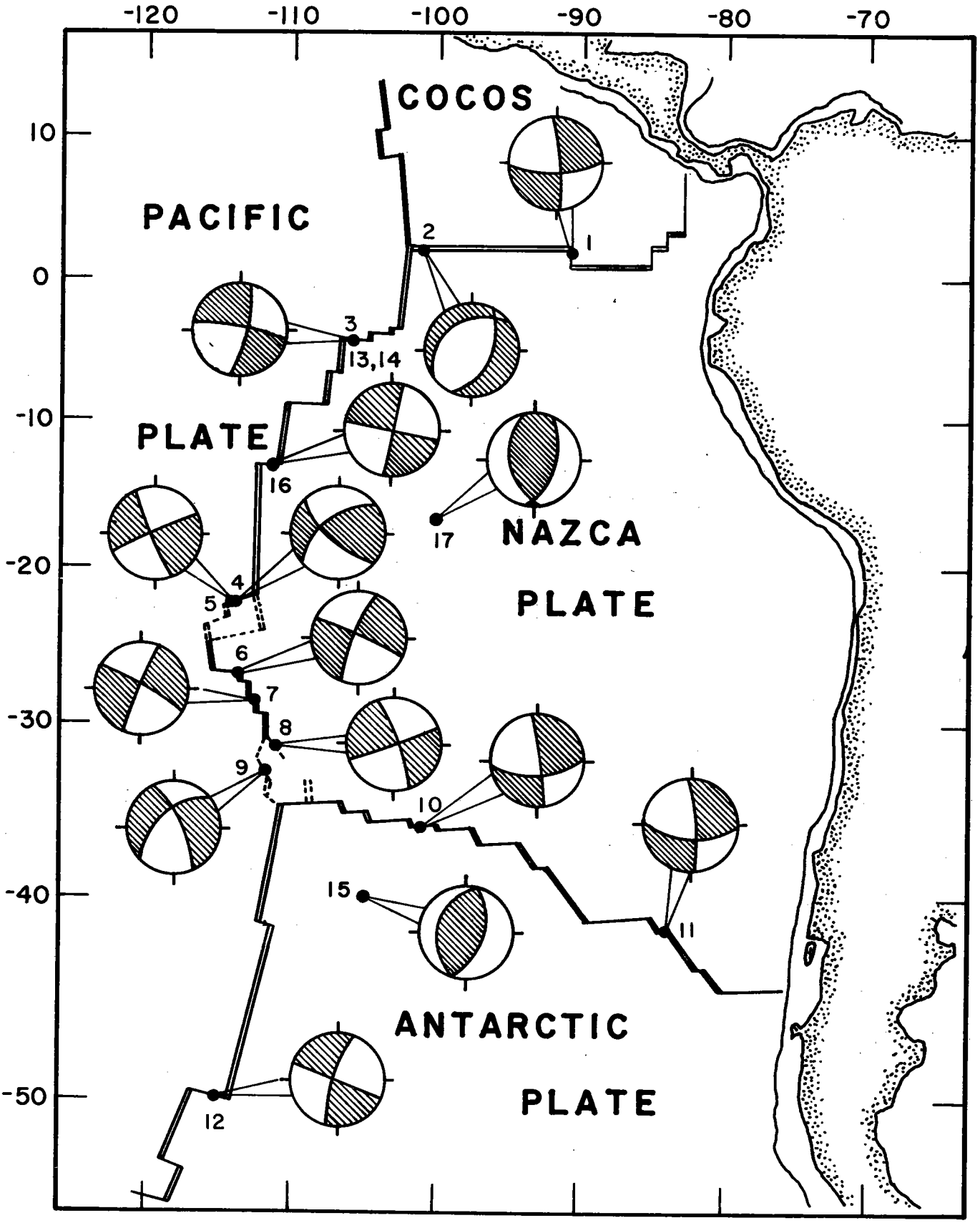
-120
-110
-100
-90
-80
-70
10
0
-10
-20
-30
-40
-50
COCOS
PACIFIC
PLATE
NAZCA
PLATE
ANTARCTIC
PLATE
1
2
3
13,14
16
17
4
5
6
7
8
9
10
11
15
12

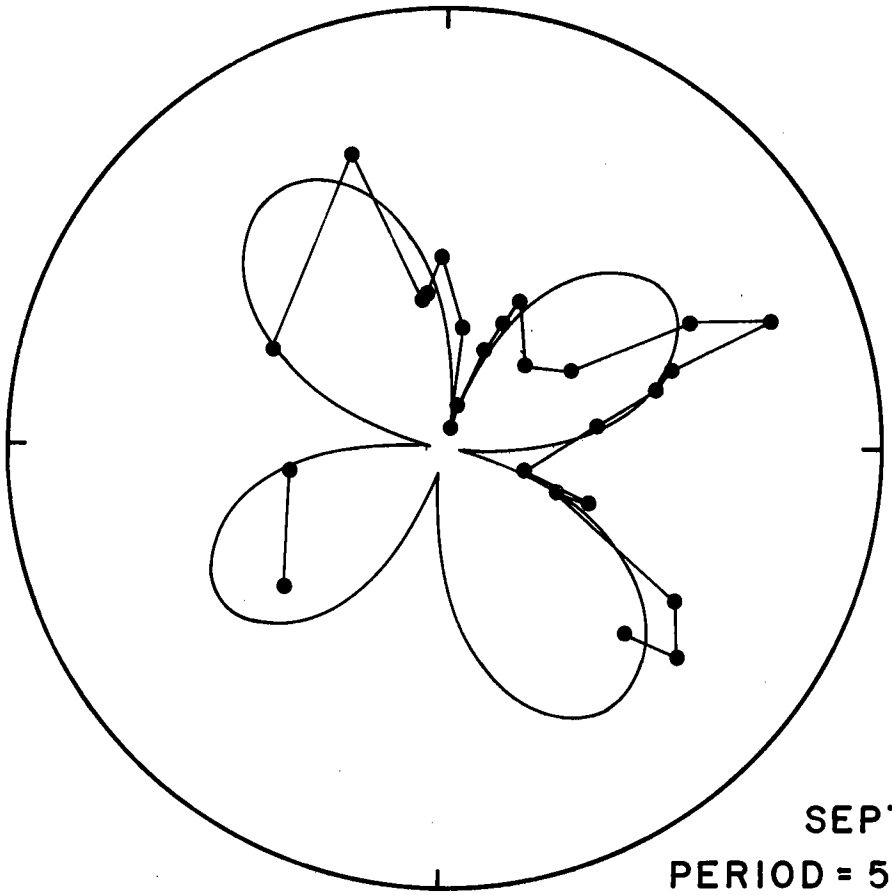

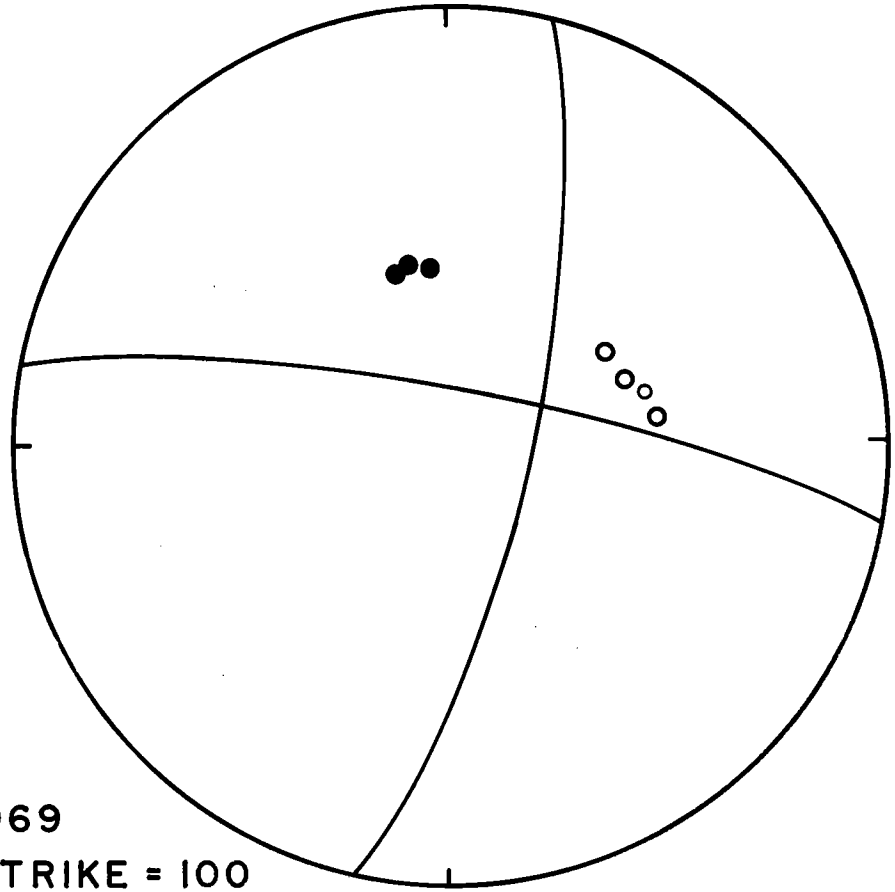

SEPT 9, 1969

PERIOD = 50	STRIKE = 100
Q = 125	DIP = 80
DEPTH = 5	SLIP = -165

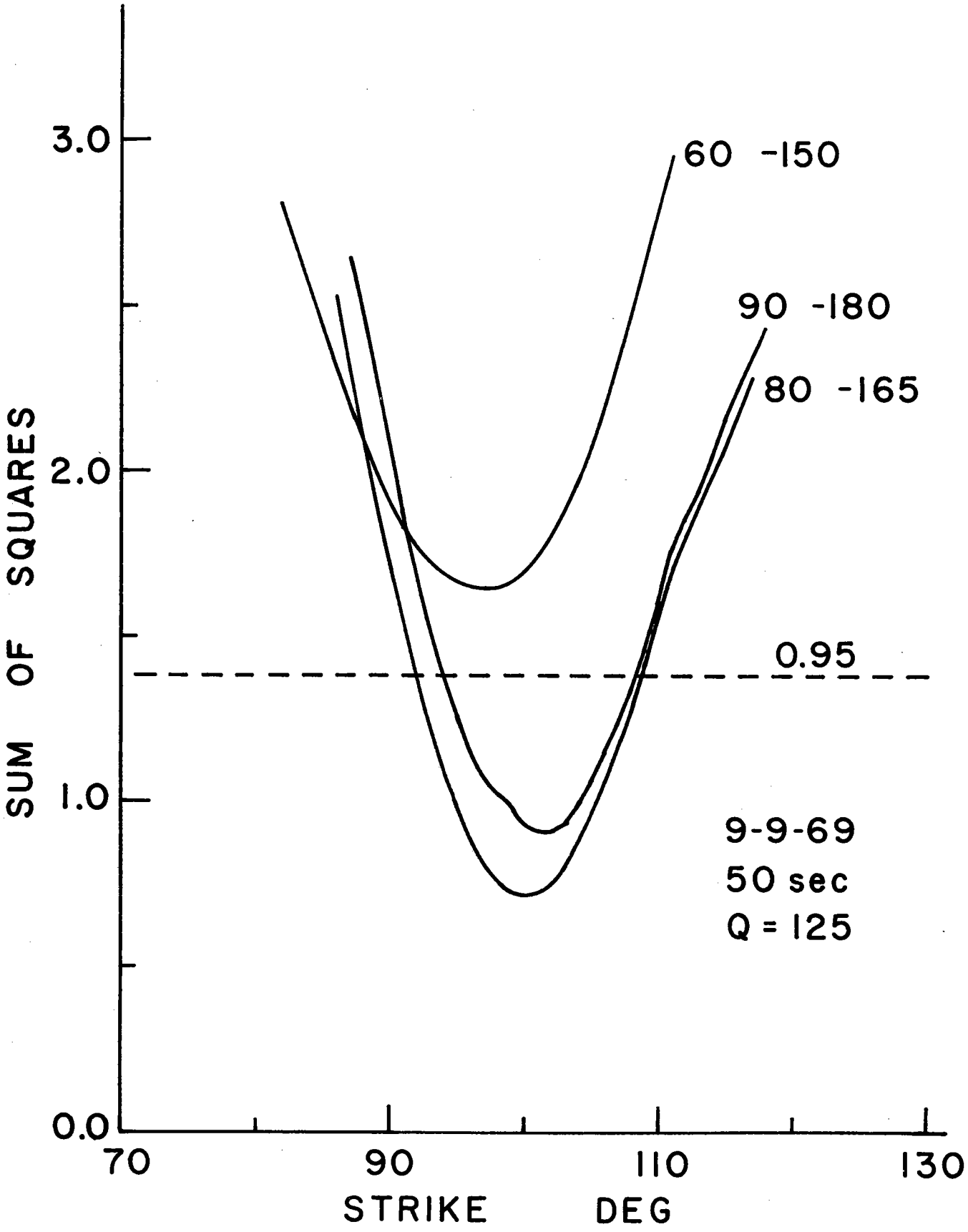
3.0
2.0
1.0
0.0
SUM OF SQUARES
60 -150
90 -180
80 -165
0.95
9-9-69
50 sec
Q = 125
70
90
110
130
STRIKE DEG

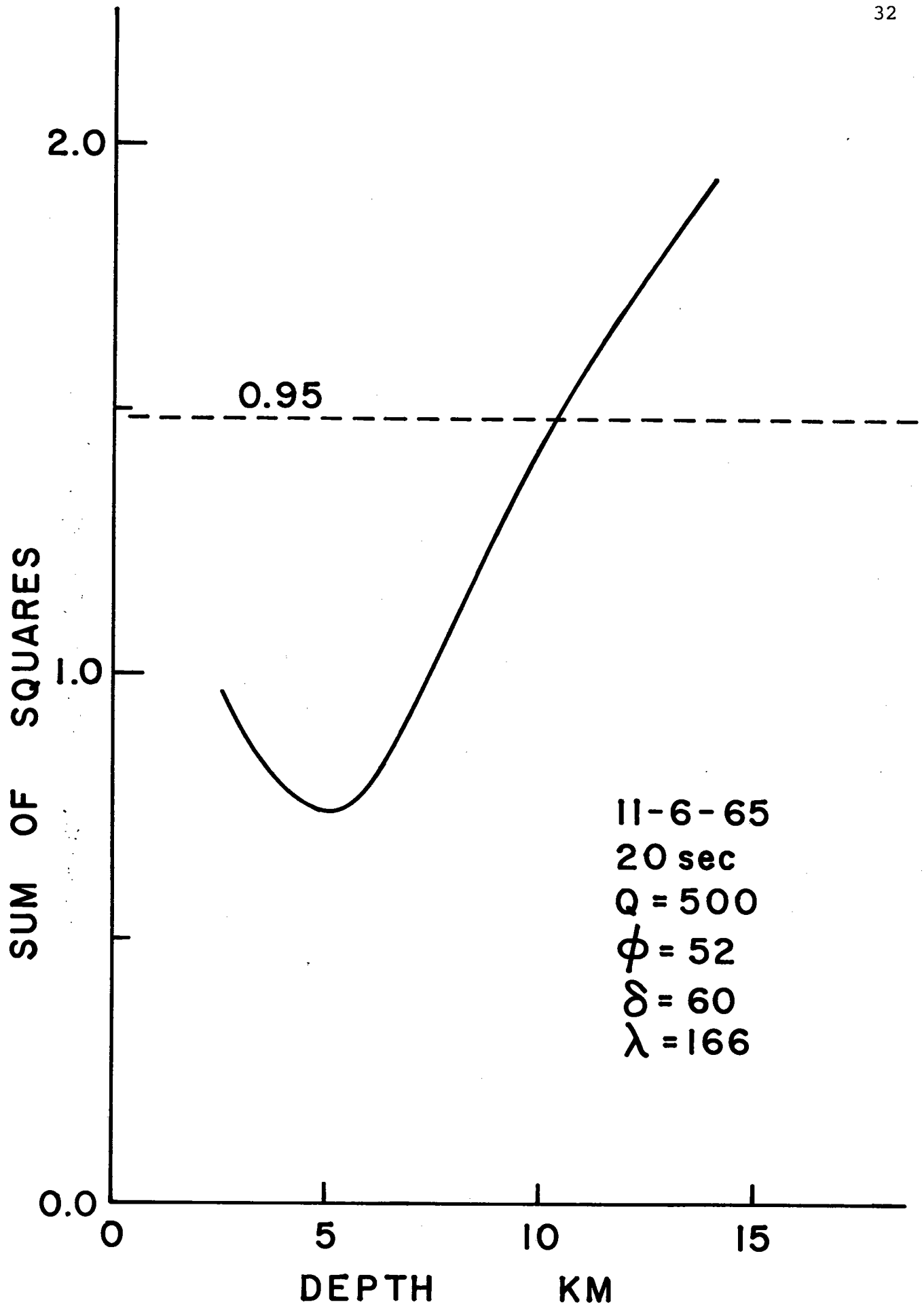
2.0
0.95
1.0
SUM OF SQUARES
0.0
0
5
10
15
DEPTH KM
11-6-65
20 sec
Q = 500
φ = 52
δ = 60
λ = 166

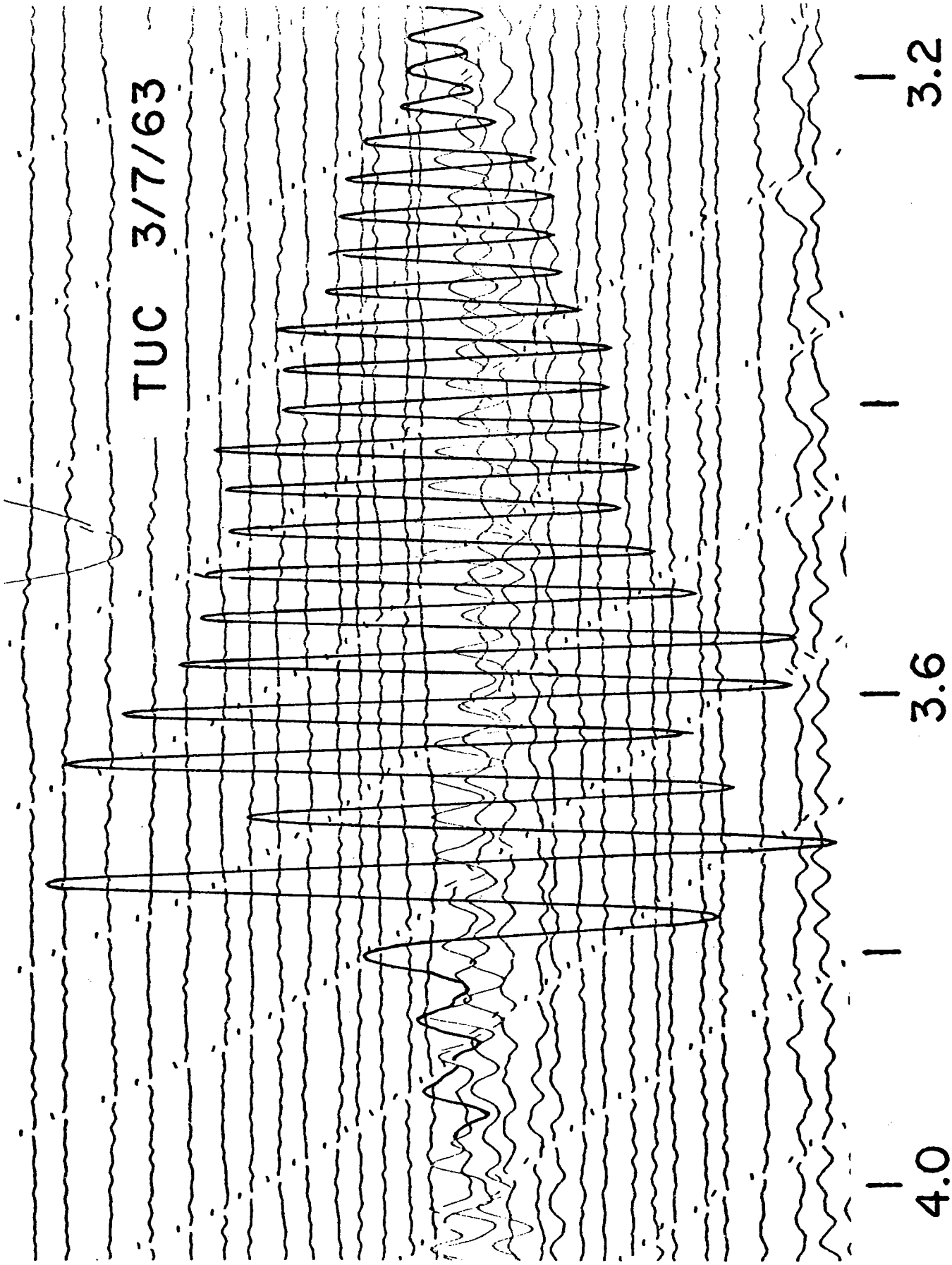
TUC 3/7/63
3.2
3.6
4.0

3. Rayleigh wave data

3.1 Signal processing and data selection

The digitized records used in the focal mechanism study form the primary data base for the measurement of the phase and group velocities. The length of the digitized record depends on the dispersive character and length of each path, but most often is 8 to 10 minutes long. I started one to two minutes before the onset of the Rayleigh wave, which is usually very clear, and continued past the arrival time of 15 sec. period waves. For example, for the record shown in figure 6, I digitized from the left to the right hand side of the figure, for a total record length of about 8 minutes. Many of the stations are not considered in this portion of the study, because only relatively simple paths with a high percentage of ocean were desired. Stations that met this requirement for some or all of the sources were ALQ, TUC, BKS, and GSC in North America, BHP and LPS in Central America, GIE in the Galapagos Islands, and BOG, QUI, NNA, ARE, LPB, ANT, and PEL on the west coast of South America (figure 12). The diagram in figure 7 outlines the steps employed in selecting and processing the data after the digitized signal is obtained. Only the first 3 boxes apply to the treatment of Love wave data, which will be discussed later. The steps are best illustrated by following an example, such as the path from event 8 on Oct. 12, 1964 to the station at Alburquerque (ALQ).

The first selection test is obvious; this is primarily

a study of the ocean floor, so any path which is not predominantly oceanic is of little value. The paths accepted in this study are on the average 89.5% oceanic. 82.5% of path 8-ALQ is within the ocean (table 2) which is acceptable. The next test allows for uncertainty in the focal mechanism of the source. The initial phase of the surface wave changes rapidly with azimuth in the vicinity of a node in the amplitudes. A small error in the assignment of the strike of the fault plane can then lead to a large error in the assumed initial phase. To eliminate this possibility, we reject all paths within 10° in azimuth of a node. For a strike-slip event, this eliminates nearly 25% of the possible data. 8-ALQ is approximately 25° clockwise from the nearest node, passing the test. Following the screening of the paths, the records are Fourier-analyzed (this step is already complete for events 1-12 and 15).

Moving window analysis (Landisman, et al., 1969) is performed on each record. This yields contours of energy levels on a velocity (travel time) versus log period plot. When corrected for instrument delay, the time of arrival of the peak energy level of a wave packet for a given frequency gives the group velocity at that frequency. All records in this study were analyzed with a cosine-squared window shape and a window length of 4.0 times the period of analysis. I find that normalizing the energy contours relative to the peak amplitude separately

for each period produces a more easily interpretable plot. The results are shown in figure 8 for 8-ALQ. The broken line represents the arrarent group velocity, not corrected for instrument response.

Normally, record 8-ALQ would be rejected at this point on the basis of the holes in the amplitude spectrum and the oscillations in the observed phase (thin lines in figures 9 and 10). These phenomena are characteristics of records showing beating or the interference of two simultaneously arriving signals. However, in this case the moving window analysis shows there are two clearly separated arrivals of energy in the period range 20 to 50 sec. When interference is caused by a distinctly separate signal, the interference can often be removed by time-variable filtering. A frequency-domain time-variable filter (Landisman et al.) based on the moving window analysis is used to extract the desired signal.

With this filter, energy of a particular frequency is allowed to pass only within a specified time window. In the example shown in figure 8, the 40 sec. period signal arriving with an apparent group velocity of 3.4 km/sec would not be passed, but the signal arriving with a group velocity of 3.7 km/sec would be accepted. The window is centered at the group velocity of the desired signal. The filtering is achieved by first transforming the original time series into

a series of sine and cosine coefficients using the fast Fourier transform algorithm. The filtered seismogram is then constructed from the linear superposition of these harmonic signals (from the Fourier analysis) of period T after they are windowed by the operator.

$$W(t) = \begin{cases} 0 & t < t_a \\ \cos\left\{ \dfrac{\pi \left[t - DIST/U(T) \right]}{t_b - t_a} \right\} & t_a \le t \le t_b \\ 0 & t > t_b \end{cases} \qquad (3)$$

$$t_a = DIST/U(T) - T\left\{ \alpha + \beta \left| \frac{d\,U(t)}{d\,T} \right| \right\}$$

$$t_b = DIST/U(T) + T\left\{ \alpha + \beta \left| \frac{d\,U(t)}{d\,T} \right| \right\}$$

where T is the period and U(T) is the velocity of the desired signal determined from the moving window analysis. In this study, $\alpha = 3.5$ and $\beta = (\text{DIST} \times \sec^2)/(100\ \text{km}^2)$ were found to give satisfactory results.

The unfiltered and filtered seismograms for 8-ALQ are shown in figure 11. Periods shorter than about 20 sec. have been eliminated due to the complexity of the energy versus velocity plot at these high frequencies. The relatively high amplitude, long period component is readily apparent in both the filtered and unfiltered seismograms, and it is also clearly seen in the seismogram for the similar path 6-TUC, shown in figure 6. The minimum in the amplitude spectrum at about 40 sec. (figure 9) is typical of all paths traveling along a substantial portion of the ridge axis, but is not found for paths outside this zone. The apparently high amplitude of the long-period signal is actually primarily due to the greater attenuation of the shorter periods, although in this particular case, focusing or defocusing of the signal may also be important (see later discussion of horizontal refraction). The details of the character of the observed amplitude spectra will be the subject of a subsequent study. The phase spectrum of the filtered seismogram shows no unusual phase shifts (solid line, figure 10) and is therefore passed for further study. The group velocity diagram of 8-ALQ shows a sharp change at periods greater than about 160 seconds,

which I attribute to long period noise, so the final, selected range of acceptable data for 8-ALQ is 20-167 sec. With my initial selection of the portion of the record to be digitized, time-variable filtering was found to be necessary or useful only when a clearly separable, interfering signal or noise was observed. Thus, the phase and group velocities were normally derived from unfiltered seismograms. If the interfering signal was not sufficiently separated in time, the record or portions of it were rejected.

The phase velocity is computed according to (1), the instrumental phase correction is computed by Hagiwara's (1958) formula as corrected by Brune (1962), and the initial phase for each path follows from the source mechanism and the relations given in Appendix 1. Rayleigh wave phase and group velocities were measured for the 78 paths in the East Pacific area shown in figure 12. The path identification, path length corrected for the ellipticity of the earth, and other descriptive characteristics of the paths are given in Table 2. Group and phase velocities for each path are given in Tables 3 and 4 respectively. Two of the paths, GI-PEL and GI-ANT are two-station paths. These are processed in the same way as the single station data, except the original, digitized signal is the windowed cross-correlogram of the Rayleigh waves observed at each station. The errors which

may produce scatter in the individual observations of velocity are discussed in the following section.

Table 2. Path characteristics; Rayleigh waves

PATHID	TOTAL LENGTH	AGE ZONES M.Y. 0-5	5-10	10-20	GT 20	BATHYMETRIC ZONES KM. LT 3.5	3.5-4.0	GT 4.0	AZIMUTHAL CS	SN	CONTINENTAL S.A.	N.A.
1-BHP	1433.7	36.3	326.6	660.3	77.3	1100.5	0.0	0.0	0.428	-0.637	333.1	0.0
1-PEL	4412.5	336.5	165.7	0.0	3701.0	765.0	1160.1	2278.1	0.508	-0.523	209.3	0.0
2-BOG	3013.3	1525.9	564.4	0.0	506.2	2596.5	0.0	0.0	0.858	-0.079	416.9	0.0
2-ARE	3822.8	278.2	340.1	755.0	1646.8	724.8	942.3	1353.0	-0.329	-0.713	802.6	0.0
2-PEL	5010.1	333.1	407.2	687.0	3393.4	467.6	1711.3	2641.8	0.237	-0.929	189.5	0.0
3-TUC	4098.7	500.0	2000.2	778.8	0.0	721.4	2295.3	262.3	0.765	-0.184	0.0	819.7
3-BOG	3682.9	1495.1	671.7	543.2	489.5	2633.2	566.3	0.0	0.047	0.083	483.5	0.0
3-QUI	3086.6	725.0	669.3	864.0	518.4	2032.5	744.2	0.0	-0.273	0.159	309.9	0.0
3-ARE	3990.0	309.6	309.7	887.3	2001.0	315.7	957.6	2234.3	-0.681	-0.548	482.4	0.0
3-PEL	4844.8	332.1	332.1	1630.7	2366.1	228.4	2134.7	2297.8	-0.120	-0.952	183.8	0.0
3-BHP	3280.7	1396.0	598.3	859.0	90.7	2723.2	220.8	0.0	0.228	-0.036	336.7	0.0
4-TUC	6032.8	1458.7	894.1	2654.4	0.0	1972.8	2258.2	776.1	0.809	-0.137	0.0	1025.6
4-ALQ	6363.4	2071.3	887.7	2163.6	0.0	2049.0	2602.3	471.3	0.780	-0.034	0.0	1240.9
4-BKS	6701.1	1067.2	574.6	1641.8	3049.0	981.6	1868.1	3482.9	0.574	-0.674	0.0	368.6
4-GSC	6364.4	1161.5	429.6	3118.6	954.7	1076.2	2532.0	2056.2	0.772	-0.429	0.0	700.1
4-QUI	4527.4	633.8	498.0	1442.5	1553.0	648.0	1679.8	1799.5	-0.277	0.865	400.1	0.0
4-ARE	4472.9	521.1	409.4	1501.5	1839.9	239.2	320.4	3712.2	-0.900	0.314	200.9	0.0
4-LPB	4821.0	520.4	408.9	1510.2	1885.1	246.5	324.3	3753.8	-0.859	0.255	496.4	0.0
4-ANT	4433.0	516.1	405.5	1456.5	2001.9	258.4	2041.1	2080.5	-0.987	-0.036	53.0	0.0
4-PEL	4389.6	566.8	482.9	1484.4	1696.5	389.2	2953.0	888.4	-0.838	-0.474	159.0	0.0
5-TUC	6057.3	1464.6	897.7	2665.2	0.0	1970.8	2161.8	894.9	0.809	-0.135	0.0	1029.7
5-ALQ	6389.3	2079.7	891.3	2172.4	0.0	1995.6	2659.1	488.6	0.780	-0.036	0.0	1245.9
5-GSC	6386.5	1165.5	431.1	3129.4	958.0	1080.0	2495.3	2108.8	0.774	-0.426	0.0	702.5
5-GIE	3506.3	764.7	651.5	2090.1	0.0	743.3	1542.8	1220.2	0.144	0.907	0.0	0.0
5-ARE	4495.8	535.5	420.7	1495.1	1817.3	264.7	354.3	3649.7	-0.893	0.317	227.2	0.0
5-BHP	5107.9	1270.3	1172.6	2163.4	183.8	2026.2	1590.3	1173.6	0.112	0.388	317.8	0.0
6-TUC	6556.2	1925.5	992.0	2589.7	0.0	2621.4	2158.8	726.9	0.815	-0.157	0.0	1049.0
6-ALQ	6882.4	2563.0	1098.4	1961.5	0.0	2631.5	2620.3	371.1	0.799	0.012	0.0	1259.5
7-TUC	6755.7	2296.3	1182.9	2229.4	0.0	2968.5	2163.6	576.6	0.812	-0.171	0.0	1047.1
7-ALQ	7075.3	2702.6	1103.9	1981.1	0.0	2951.7	2529.2	306.7	0.800	0.022	0.0	1287.7
7-BKS	7436.4	1784.7	594.9	1636.0	3048.9	1752.0	1886.2	3426.3	0.592	-0.671	0.0	371.8
7-BHP	5483.8	1421.5	834.8	2179.3	781.7	1966.9	1513.0	1737.4	0.192	0.453	266.5	0.0
7-NNA	4156.1	442.9	443.0	1569.7	1563.8	824.0	884.3	2311.1	-0.518	0.815	136.8	0.0
7-ARE	4427.6	416.6	416.6	1410.4	2005.4	1126.0	743.6	2379.4	-0.760	0.586	178.5	0.0
7-LPB	4752.9	413.9	414.0	1417.5	2042.9	1179.3	857.7	2251.4	-0.752	0.498	464.6	0.0
7-ANT	4244.2	405.3	405.4	1347.2	2020.7	819.0	3359.6	0.0	-0.945	0.278	65.6	0.0
8-BKS	7760.1	2141.8	535.4	1668.4	3026.4	2145.3	1909.3	3317.4	0.588	-0.676	0.0	388.0
8-TUC	7051.6	2513.9	1540.8	1939.2	0.0	2409.5	3200.7	383.6	0.814	-0.204	0.0	1057.7
8-ALQ	7357.8	4105.7	309.0	1655.5	0.0	2124.6	3605.7	339.9	0.797	-0.039	0.0	1287.6

PATHID	TOTAL LENGTH	AGE ZONES M.Y. 0-5	5-10	10-20	GT 20	BATHYMETRIC ZONES KM. LT 3.5	3.5-4.0	GT 4.0	AZIMUTHAL CS	SN	CONTINENTAL S.A.	N.A.
8-GIE	4025.2	404.3	750.9	2870.0	C.0	998.2	1618.1	1408.8	0.548	0.761	0.0	0.0
8-BHP	5573.2	1196.7	765.1	1972.9	1337.6	2251.3	1534.2	1486.8	0.288	0.671	301.0	0.0
8-QUI	4851.2	348.7	481.6	1868.1	1631.0	822.6	1450.3	2056.5	0.090	0.887	521.9	0.0
8-ANT	4059.3	372.C	372.0	1238.0	2017.7	540.0	3459.7	0.0	-0.897	0.406	59.5	0.0
8-PEL	3765.1	393.2	393.2	1780.7	1049.0	795.5	2386.6	433.9	-0.955	-0.093	148.9	0.0
9-BKS	7900.6	2218.5	625.7	1619.6	3065.4	2243.7	1739.2	3546.2	0.603	-0.669	0.0	371.3
9-GSC	7558.2	2620.8	137.9	3174.4	907.0	2318.8	2626.6	1894.7	0.778	-0.452	0.0	718.0
9-TUC	7208.7	2876.3	1232.7	2054.5	C.0	3402.3	2225.0	536.2	0.822	-0.194	0.0	1045.3
9-ALQ	7520.3	3943.7	342.9	1917.7	0.0	2736.1	3133.2	335.0	0.803	-0.030	0.0	1316.1
9-NNA	4239.0	405.0	373.8	1551.7	1765.7	737.3	1146.9	2211.9	-0.331	0.907	142.7	0.0
9-ARE	4426.4	413.5	413.5	1392.2	2028.8	666.9	1669.5	1911.6	-0.622	0.731	178.5	0.0
9-LPB	4732.1	423.1	423.2	1251.6	2169.3	682.8	2261.6	1322.8	-0.642	0.633	464.9	0.0
9-PEL	3814.7	547.1	547.1	1530.7	1028.3	1015.6	2181.0	456.6	-0.958	-0.002	161.4	0.0
10-GIE	4077.1	113.1	229.6	3060.8	673.6	448.5	1961.1	1667.5	0.850	-0.406	0.0	0.0
10-QUI	4610.3	106.4	106.4	1566.3	2098.3	135.7	1298.9	2442.8	0.417	0.730	732.9	0.0
10-BOG	5314.9	109.3	109.4	1472.1	2063.3	142.7	1321.4	2290.0	0.303	0.638	1560.8	0.0
10-NNA	3609.5	130.6	130.6	1110.2	2083.8	145.1	1478.8	1831.2	0.079	0.953	154.4	0.0
10-ARE	3637.0	157.5	157.5	891.4	2252.3	179.9	2040.6	1238.2	-0.326	0.893	178.3	0.0
10-LPB	3903.3	154.7	154.7	833.0	2296.8	223.5	2283.6	932.0	-0.410	0.780	464.1	0.0
10-ANT	3235.6	214.1	214.1	713.7	2016.3	284.2	2874.0	0.0	-0.676	0.704	77.3	0.0
11-QUI	4625.8	106.2	0.0	595.9	2802.6	59.6	1184.6	2260.5	0.701	0.288	1121.0	0.0
11-NNA	3362.0	112.1	0.0	507.2	2548.1	57.0	1111.8	1998.6	0.787	0.518	194.6	0.0
11-ARE	3040.0	124.2	0.0	366.7	2348.1	51.1	871.6	1916.3	0.489	0.796	201.1	0.0
11-ANT	2357.8	142.2	0.0	290.3	1765.4	46.2	764.9	1386.9	0.208	0.909	160.0	0.0
11-PEL	1508.4	233.4	0.0	173.6	814.1	61.1	0.0	1160.0	-0.338	0.736	287.3	0.0
12-TUC	9094.0	4161.9	976.2	2910.1	C.0	4080.4	3179.0	788.7	0.848	-0.201	0.0	1045.8
12-GSC	9418.6	2196.4	1947.8	3089.3	1507.0	2569.7	3889.5	2281.3	0.819	-0.432	0.0	678.1
13-TUC	4117.6	502.3	2009.4	782.3	0.0	774.1	2256.4	263.5	0.765	-0.185	0.0	823.5
15-ARE	4131.6	165.2	165.3	1322.1	2313.7	245.9	2609.8	1110.5	-0.246	0.928	165.3	0.0
15-LPB	4384.7	153.4	153.4	1315.4	2302.0	306.1	2833.3	784.8	-0.335	0.830	460.4	0.0
15-GIE	4569.1	143.3	290.8	3655.3	479.8	685.4	2627.3	1256.5	0.843	0.490	0.0	0.0
16-ALQ	5368.6	996.7	1123.9	1959.5	C.0	1228.1	2529.7	322.3	0.738	0.054	0.0	1288.5
16-TUC	5051.0	500.0	1166.8	2323.5	C.0	1276.9	2202.6	510.8	0.768	-0.132	0.0	1060.7
16-GSC	5411.7	719.7	308.5	3598.8	C.0	485.8	3035.3	1105.9	0.722	-0.433	0.0	784.7
17-ANT	3187.2	0.0	0.0	1070.9	2062.1	0.0	282.0	2851.0	-0.842	-0.505	54.2	0.0
17-LPB	3418.5	C.C	0.0	977.7	1880.2	0.0	120.0	2737.8	-0.833	-0.044	560.6	0.0
17-ARE	3058.8	0.0	0.0	978.8	1820.0	0.0	148.3	2650.4	-0.913	-0.020	260.0	0.0
GI-PEL	4132.8	C.0	132.2	132.2	3599.7	347.8	1255.8	2260.4	0.598	-0.719	268.6	0.0
GI-ANT	3326.8	C.0	186.3	0.0	3060.7	487.0	357.2	2402.8	0.322	-0.919	79.8	0.0

Table 3. Individual Rayleigh wave group velocities

PERIOD	1-BHP	1-PEL	2-BOG	2-ARE	2-PEL	3-TUC	3-BOG	3-QUI	3-ARE	3-PEL	3-BHP
16.4	3.33	3.70	0.0	3.67	3.78	3.54	0.0	3.69	0.0	3.68	3.59
18.7	3.39	3.72	0.0	3.70	3.81	3.57	0.0	3.72	3.81	3.76	3.64
21.5	3.43	3.75	0.0	3.73	3.83	3.63	0.0	3.76	3.83	3.83	3.66
23.9	3.48	3.81	3.62	3.75	3.85	3.72	3.73	3.80	3.85	3.87	3.70
27.1	3.52	3.87	3.69	3.78	3.88	3.77	3.73	3.85	3.88	3.90	3.72
30.8	3.57	3.90	3.71	3.82	3.89	3.79	3.70	3.85	3.90	3.93	3.72
34.8	3.60	3.91	3.73	3.84	3.91	3.79	3.68	3.85	3.89	3.92	3.70
39.4	3.61	3.90	3.77	3.85	3.90	3.78	3.67	3.83	3.89	3.90	3.71
44.6	3.58	3.90	3.78	3.84	3.89	3.76	3.67	3.83	3.87	3.89	3.72
50.8	3.55	3.90	3.75	3.82	3.85	3.73	3.70	3.83	3.85	3.85	3.72
57.5	3.49	3.84	3.72	3.82	3.83	3.69	3.70	0.0	3.84	3.83	3.73
64.9	3.47	3.75	3.72	3.80	3.81	3.66	3.67	0.0	3.81	3.81	3.72
73.5	3.44	3.70	3.74	3.79	3.78	3.65	3.64	0.0	3.75	3.78	3.72
83.3	0.0	3.65	0.0	3.77	3.76	3.66	3.61	0.0	3.72	3.75	3.73
94.3	0.0	0.0	0.0	3.76	3.75	0.0	3.53	0.0	0.0	3.74	3.75
107.5	0.0	0.0	0.0	3.69	3.69	0.0	0.0	0.0	0.0	3.67	3.78
122.0	0.0	0.0	0.0	3.49	3.62	0.0	0.0	0.0	0.0	3.59	0.0
137.0	0.0	0.0	0.0	0.0	3.54	0.0	0.0	0.0	0.0	3.56	0.0
156.2	0.0	0.0	0.0	0.0	0.0	0.0	0.0	0.0	0.0	0.0	0.0

PERIOD	4-TUC	4-ALQ	4-BKS	4-GSC	4-QUI	4-ARE	4-LPB	4-ANT	4-PEL	5-TUC	5-GSC
16.4	3.59	3.50	3.68	0.0	0.0	3.72	3.70	3.77	3.58	3.60	0.0
18.7	3.64	3.54	3.76	3.75	3.82	3.77	3.72	3.81	3.81	3.70	3.79
21.5	3.69	3.58	3.82	3.80	3.84	3.83	3.74	3.86	3.85	3.72	3.81
23.9	3.73	3.64	3.87	3.82	3.87	3.87	3.76	3.90	3.89	3.74	3.83
27.1	3.76	3.68	3.89	3.84	3.89	3.91	3.78	3.93	3.91	3.76	3.84
30.8	3.78	3.70	3.90	3.84	3.91	3.93	3.81	3.95	3.92	3.79	3.85
34.8	3.79	3.72	3.89	3.84	3.91	3.94	3.82	3.96	3.91	3.81	3.85
39.4	3.78	3.72	3.86	3.82	3.87	3.93	3.81	3.95	3.90	3.80	3.84
44.6	3.76	3.73	3.85	3.81	3.86	3.93	3.83	3.94	3.88	3.77	3.82
50.8	3.73	3.71	3.83	3.79	3.83	3.90	3.83	3.90	3.83	3.74	3.79
57.5	3.71	3.68	3.80	3.75	3.80	3.87	3.84	3.87	3.80	3.73	3.77
64.9	3.70	3.66	3.78	3.72	3.76	3.85	3.83	3.85	3.76	3.71	3.73
73.5	3.68	3.64	3.75	3.70	3.71	3.82	3.80	3.80	3.71	3.69	3.70
83.3	3.66	3.62	3.72	3.68	3.70	3.80	3.77	3.71	3.64	3.68	3.69
94.3	3.63	3.61	3.69	3.66	0.0	3.75	3.71	3.67	3.58	3.65	3.66
107.5	0.0	3.59	3.65	3.64	0.0	0.0	3.68	3.63	0.0	3.63	3.64
122.0	0.0	3.56	3.64	3.64	0.0	0.0	3.65	0.0	0.0	3.60	3.61
137.0	0.0	0.0	0.0	3.60	0.0	0.0	3.66	0.0	0.0	3.59	3.58
156.2	0.0	0.0	0.0	0.0	0.0	0.0	0.0	0.0	0.0	0.0	0.0

PERIOD	5-ALQ	5-GIF	5-ARE	5-BHP	6-TUC	6-ALQ	7-TUC	7-ALQ	7-BKS	7-BHP	7-NNA
16.4	3.51	3.73	0.0	3.69	3.60	3.55	3.59	3.54	3.70	3.73	3.80
18.7	3.55	3.77	3.79	3.71	3.63	3.58	3.61	3.57	3.75	3.77	3.84
21.5	3.59	3.84	3.84	3.74	3.69	3.61	3.67	3.60	3.83	3.79	3.87
23.9	3.65	3.89	3.87	3.80	3.74	3.66	3.71	3.63	3.85	3.81	3.89
27.1	3.68	3.92	3.90	3.86	3.77	3.69	3.73	3.66	3.86	3.83	3.91
30.8	3.72	3.94	3.93	3.88	3.78	3.71	3.75	3.69	3.87	3.85	3.91
34.8	3.73	3.91	3.94	3.87	3.78	3.73	3.77	3.72	3.88	3.86	3.90
39.4	3.74	3.89	3.94	3.83	3.78	3.73	3.77	3.73	3.87	3.85	3.91
44.6	3.73	3.86	3.93	3.81	3.76	3.72	3.74	3.71	3.84	3.84	3.89
50.8	3.71	3.81	3.88	3.78	3.74	3.70	3.72	3.69	3.79	3.81	3.88
57.5	3.70	0.0	3.83	3.76	3.72	3.68	3.69	3.68	3.74	3.77	3.83
64.9	3.67	0.0	3.80	3.74	3.68	3.68	3.69	3.67	3.73	3.71	3.80
73.5	3.65	0.0	3.78	3.70	3.65	3.66	3.66	3.64	3.72	3.65	3.78
83.3	3.64	0.0	3.79	3.65	3.62	3.64	3.65	3.62	3.72	0.0	3.78
94.3	3.65	0.0	0.0	0.0	3.62	3.62	3.64	3.63	0.0	0.0	3.78
107.5	3.66	0.0	0.0	0.0	3.62	3.59	3.62	3.63	0.0	0.0	3.79
122.0	3.67	0.0	0.0	0.0	3.62	3.57	0.0	3.63	0.0	0.0	0.0
137.0	3.67	0.0	0.0	0.0	3.61	3.56	0.0	3.63	0.0	0.0	0.0
156.2	3.66	0.0	0.0	0.0	3.59	0.0	0.0	0.0	0.0	0.0	0.0

PERIOD	7-ARE	7-LPB	7-ANT	8-BKS	8-TUC	8-ALQ	8-GIE	8-BHP	8-QUI	8-ANT	8-PEL
16.4	3.71	0.0	3.77	3.70	3.64	0.0	3.74	3.79	0.0	3.82	3.77
18.7	3.75	3.72	3.79	3.78	3.68	3.65	3.80	3.82	0.0	3.85	3.84
21.5	3.80	3.76	3.81	3.81	3.72	3.66	3.83	3.85	0.0	3.89	3.88
23.9	3.83	3.77	3.85	3.83	3.74	3.68	3.86	3.86	0.0	3.91	3.90
27.1	3.87	3.78	3.87	3.85	3.76	3.70	3.87	3.86	0.0	3.93	3.94
30.8	3.91	3.78	3.90	3.86	3.78	3.72	3.88	3.85	3.85	3.95	3.95
34.8	3.91	3.79	3.90	3.87	3.77	3.73	3.86	3.83	3.85	3.93	3.94
39.4	3.90	3.80	3.89	3.85	3.75	3.73	3.83	3.80	3.86	3.91	3.94
44.6	3.89	3.81	3.87	3.81	3.73	3.71	3.81	3.76	3.86	3.90	3.92
50.8	3.85	3.80	3.85	3.78	3.71	3.69	3.77	3.75	3.84	3.88	3.88
57.5	3.81	3.81	3.84	3.75	3.69	3.67	3.75	3.73	3.78	3.85	3.83
64.9	3.79	3.79	3.83	3.71	3.68	3.64	3.72	3.71	3.75	3.83	3.80
73.5	3.78	3.76	3.82	3.68	3.68	3.64	3.70	3.67	3.73	3.80	3.79
83.3	3.77	3.75	3.80	3.68	3.66	3.62	3.67	3.65	3.74	3.79	3.77
94.3	0.0	3.76	0.0	3.68	3.65	3.60	3.66	3.62	3.74	0.0	3.77
107.5	0.0	0.0	0.0	3.68	3.66	3.59	3.62	3.60	3.71	0.0	0.0
122.0	0.0	0.0	0.0	0.0	3.67	3.59	3.56	0.0	3.68	0.0	0.0
137.0	0.0	0.0	0.0	0.0	3.70	3.59	3.48	0.0	3.66	0.0	0.0
156.2	0.0	0.0	0.0	0.0	0.0	3.61	3.46	0.0	3.62	0.0	0.0

PERIOD	9-BKS	9-GSC	9-TUC	9-ALQ	9-NNA	9-ARE	9-LPB	9-PEL	10-GIE	10-QUI	10-BOG
16.4	3.70	3.63	0.0	0.0	3.78	3.77	0.0	3.61	3.72	3.70	0.0
18.7	3.78	3.75	3.67	3.66	3.81	3.81	3.75	3.72	3.81	3.71	0.0
21.5	3.81	3.77	3.69	3.67	3.87	3.85	3.78	3.86	3.86	3.73	3.62
23.9	3.83	3.79	3.71	3.68	3.90	3.89	3.80	3.90	3.88	3.78	3.64
27.1	3.85	3.80	3.73	3.69	3.93	3.91	3.81	3.93	3.90	3.84	3.67
30.8	3.85	3.81	3.75	3.70	3.96	3.94	3.81	3.93	3.90	3.86	3.69
34.8	3.85	3.81	3.76	3.71	3.95	3.94	3.82	3.92	3.89	3.88	3.71
39.4	3.85	3.81	3.75	3.72	3.94	3.92	3.82	3.91	3.87	3.85	3.73
44.6	3.83	3.79	3.74	3.71	3.91	3.91	3.83	3.90	3.83	3.83	3.75
50.8	3.80	3.76	3.72	3.70	3.90	3.90	3.83	3.86	3.80	3.82	3.75
57.5	3.76	3.74	3.70	3.68	0.0	3.88	3.83	3.82	3.77	3.80	3.76
64.9	3.73	3.72	3.69	3.66	0.0	3.85	3.81	3.77	3.74	3.78	3.75
73.5	3.71	3.71	3.66	3.65	0.0	3.82	3.79	3.74	3.71	3.77	3.75
83.3	3.68	3.69	3.65	3.62	0.0	3.79	3.79	0.0	3.66	3.76	3.73
94.3	3.65	3.67	3.65	3.60	0.0	3.78	0.0	0.0	3.62	3.75	3.72
107.5	3.64	3.64	3.66	3.59	0.0	0.0	0.0	0.0	3.60	3.71	3.71
122.0	3.68	3.66	0.0	3.57	0.0	0.0	0.0	0.0	3.60	3.67	3.71
137.0	0.0	3.68	0.0	3.55	0.0	0.0	0.0	0.0	0.0	3.62	3.71
156.2	0.0	3.65	0.0	3.53	0.0	0.0	0.0	0.0	0.0	3.57	0.0

PERIOD	10-NNA	10-ARE	10-LPB	10-ANT	11-QUI	11-NNA	11-ARE	11-ANT	11-PEL	12-TUC	12-GSC
16.4	3.63	0.0	0.0	3.77	0.0	3.67	3.65	0.0	3.55	0.0	3.69
18.7	3.69	3.81	3.73	3.81	3.61	3.84	3.80	3.82	3.63	3.63	3.78
21.5	3.80	3.86	3.76	3.87	3.69	3.91	3.84	3.86	3.70	3.78	3.82
23.9	3.86	3.90	3.80	3.91	3.72	3.94	3.89	3.90	3.77	3.79	3.85
27.1	3.90	3.93	3.81	3.94	3.75	3.98	3.93	3.94	3.84	3.80	3.87
30.8	3.90	3.94	3.83	3.95	3.77	3.99	3.96	3.97	3.86	3.81	3.87
34.8	3.89	3.94	3.83	3.96	3.79	4.00	3.96	3.98	3.87	3.81	3.87
39.4	3.88	3.94	3.81	3.95	3.81	3.99	3.95	3.97	3.86	3.80	3.84
44.6	3.85	3.93	3.82	3.92	3.82	3.95	3.92	3.92	3.84	3.77	3.81
50.8	3.84	3.90	3.82	3.89	3.82	3.92	3.89	3.87	3.83	3.72	3.80
57.5	3.80	3.86	3.81	3.86	3.82	3.87	3.85	3.82	3.81	3.69	3.76
64.9	3.78	3.81	3.80	3.83	3.78	3.84	3.81	3.78	3.80	3.67	3.72
73.5	3.75	3.77	3.77	3.82	3.75	3.81	3.77	3.77	3.77	3.66	3.68
83.3	3.71	3.72	3.73	3.80	3.72	3.78	3.72	3.76	3.74	3.65	3.66
94.3	3.69	3.69	3.70	3.80	3.70	3.76	3.66	3.76	3.71	3.64	3.67
107.5	3.66	3.65	3.68	3.76	3.69	3.70	0.0	0.0	3.66	3.61	3.65
122.0	3.63	3.61	3.66	3.66	3.63	3.63	0.0	0.0	3.60	3.57	3.59
137.0	3.61	3.60	3.65	3.58	0.0	3.56	0.0	0.0	3.53	3.54	3.55
156.2	3.60	0.0	3.66	3.54	0.0	3.51	0.0	0.0	3.44	0.0	0.0

PERIOD	13-TUC	15-ARE	15-LPB	15-GIE	16-ALQ	16-TUC	16-GSC	17-ANT	17-LPB	17-ARE	GI-PEL
16.4	3.51	0.0	0.0	3.57	3.47	3.51	0.0	0.0	0.0	0.0	3.76
18.7	3.61	3.85	0.0	3.77	3.50	3.59	3.75	0.0	0.0	0.0	3.80
21.5	3.61	3.90	3.78	3.85	3.53	3.65	3.78	3.91	3.70	3.83	3.84
23.9	3.72	3.92	3.82	3.89	3.59	3.71	3.80	3.95	3.72	3.88	3.87
27.1	3.72	3.94	3.83	3.91	3.65	3.75	3.83	3.97	3.74	3.91	3.90
30.8	3.72	3.94	3.84	3.91	3.69	3.77	3.85	3.98	3.77	3.93	3.92
34.8	3.73	3.94	3.85	3.89	3.71	3.78	3.85	4.00	3.77	3.95	3.93
39.4	3.73	3.93	3.85	3.87	3.71	3.76	3.84	4.00	3.78	3.95	3.93
44.6	3.73	3.91	3.83	3.83	3.72	3.74	3.81	3.98	3.80	3.93	3.94
50.8	3.73	3.89	3.81	3.78	3.71	3.72	3.79	3.94	3.83	3.89	3.92
57.5	3.69	3.85	3.80	3.75	3.69	3.71	3.77	3.88	3.84	3.86	3.90
64.9	3.66	3.81	3.78	3.71	3.66	3.70	3.73	3.82	3.85	3.84	3.88
73.5	3.65	3.77	3.77	3.69	3.64	3.68	3.70	3.82	3.85	3.81	3.86
83.3	3.64	3.73	3.76	3.66	3.62	3.68	3.65	3.83	3.83	3.78	3.84
94.3	3.62	3.69	3.73	3.63	3.61	0.0	3.63	0.0	3.81	0.0	0.0
107.5	3.63	3.67	3.71	3.60	3.59	0.0	3.61	0.0	3.78	0.0	0.0
122.0	3.61	3.72	3.68	3.63	3.55	0.0	3.64	0.0	0.0	0.0	0.0
137.0	3.60	0.0	3.65	3.65	0.0	0.0	0.0	0.0	0.0	0.0	0.0
156.2	0.0	0.0	0.0	0.0	0.0	0.0	0.0	0.0	0.0	0.0	0.0

PERIOD	GI-ANT
16.4	3.75
18.7	3.79
21.5	3.82
23.9	3.86
27.1	3.90
30.8	3.94
34.8	3.96
39.4	3.93
44.6	3.89
50.8	3.86
57.5	3.84
64.9	3.82
73.5	3.80
83.3	3.78
94.3	3.77
107.5	0.0
122.0	0.0
137.0	0.0
156.2	0.0

Table 4. Individual Rayleigh wave phase velocities

PERIOD	1-BHP	1-PEL	2-BOG	2-ARE	2-PEL	3-TUC	3-BOG	3-QUI	3-ARE	3-PEL	3-BHP
16.7	3.605	3.852	0.0	3.833	3.875	3.758	0.0	3.829	3.882	3.881	3.742
20.0	3.645	3.895	0.0	3.856	3.906	3.794	0.0	3.867	3.919	3.909	3.768
25.0	3.679	3.920	3.743	3.886	3.918	3.811	3.777	3.878	3.936	3.919	3.783
33.3	3.719	3.917	3.808	3.914	3.919	3.814	3.793	3.879	3.942	3.911	3.802
40.0	3.719	3.927	3.807	3.919	3.920	3.813	3.831	3.888	3.943	3.906	3.819
50.0	3.760	3.915	3.836	3.934	3.925	3.817	3.861	3.914	3.972	3.912	3.840
58.8	3.812	3.934	3.881	3.948	3.939	3.849	3.881	0.0	3.970	3.927	3.857
66.7	3.837	3.953	3.921	3.969	3.955	3.874	3.934	0.0	3.992	3.923	3.878
76.9	3.903	3.996	0.0	4.010	3.985	3.910	3.968	0.0	4.050	3.976	3.899
90.9	0.0	0.0	0.0	4.024	4.021	0.0	4.036	0.0	0.0	3.983	3.944
100.0	0.0	0.0	0.0	4.052	4.054	0.0	0.0	0.0	0.0	4.008	3.972
111.1	0.0	0.0	0.0	4.115	4.090	0.0	0.0	0.0	0.0	4.061	0.0
125.0	0.0	0.0	0.0	0.0	4.150	0.0	0.0	0.0	0.0	4.153	0.0
142.9	0.0	0.0	0.0	0.0	0.0	0.0	0.0	0.0	0.0	4.275	0.0
166.7	0.0	0.0	0.0	0.0	0.0	0.0	0.0	0.0	0.0	0.0	0.0

PERIOD	4-TUC	4-ALQ	4-BKS	4-GSC	4-QUI	4-ARE	4-LPB	4-ANT	4-PEL	5-TUC	5-ALQ
16.7	3.755	3.700	3.855	0.0	3.846	3.904	0.0	3.915	3.954	3.767	3.711
20.0	3.783	3.737	3.878	3.840	3.911	3.946	3.866	3.946	3.979	3.798	3.749
25.0	3.803	3.766	3.882	3.848	3.930	3.961	3.896	3.959	3.985	3.819	3.776
33.3	3.813	3.786	3.872	3.847	3.913	3.966	3.916	3.955	3.981	3.830	3.797
40.0	3.813	3.795	3.870	3.848	3.917	3.968	3.932	3.950	3.980	3.829	3.807
50.0	3.828	3.813	3.878	3.850	3.925	3.970	3.960	3.949	3.983	3.845	3.826
58.8	3.850	3.838	3.885	3.868	3.929	3.986	3.973	3.959	3.999	3.859	3.845
66.7	3.865	3.862	3.899	3.888	3.950	4.007	3.985	3.964	4.024	3.881	3.869
76.9	3.911	3.905	3.925	3.915	4.009	4.021	4.013	3.993	4.067	3.914	3.911
90.9	3.962	3.957	3.958	3.958	0.0	4.057	4.059	4.078	4.115	3.956	3.968
100.0	0.0	3.998	3.998	3.994	0.0	4.132	4.104	4.077	0.0	3.993	3.998
111.1	0.0	4.029	4.035	4.052	0.0	0.0	4.149	0.0	0.0	4.032	4.030
125.0	0.0	4.064	4.064	4.079	0.0	0.0	4.202	0.0	0.0	4.107	4.084
142.9	0.0	0.0	0.0	4.191	0.0	0.0	0.0	0.0	0.0	0.0	4.148
166.7	0.0	0.0	0.0	0.0	0.0	0.0	0.0	0.0	0.0	0.0	4.243

PERIOD	5-GSC	5-GIE	5-ARE	5-BHP	6-TLC	6-ALQ	7-TUC	7-ALQ	7-BKS	7-BHP	7-NNA
16.7	3.832	3.887	3.902	3.838	3.754	3.700	3.751	3.700	3.839	3.824	3.904
20.0	3.853	3.904	3.942	3.859	3.782	3.732	3.779	3.731	3.863	3.849	3.931
25.0	3.857	3.910	3.957	3.878	3.795	3.758	3.796	3.760	3.865	3.862	3.936
33.3	3.857	3.898	3.968	3.862	3.801	3.776	3.806	3.780	3.861	3.864	3.937
40.0	3.856	3.893	3.968	3.866	3.806	3.784	3.810	3.787	3.858	3.864	3.939
50.0	3.866	3.910	3.967	3.876	3.816	3.803	3.828	3.813	3.863	3.873	3.945
58.8	3.876	0.0	3.985	3.904	3.833	3.825	3.850	3.831	3.888	3.887	3.967
66.7	3.899	0.0	4.013	3.930	3.852	3.845	3.874	3.855	3.908	3.886	3.983
76.9	3.920	0.0	4.056	3.946	3.891	3.872	3.906	3.891	3.945	0.0	4.013
90.9	3.970	0.0	0.0	0.0	3.943	3.920	3.963	3.947	3.985	0.0	4.088
100.0	4.001	0.0	0.0	0.0	3.977	3.960	3.975	3.984	0.0	0.0	4.105
111.1	4.041	0.0	0.0	0.0	4.014	3.998	4.024	4.027	0.0	0.0	4.130
125.0	4.098	0.0	0.0	0.0	4.067	4.058	0.0	4.075	0.0	0.0	0.0
142.9	0.0	0.0	0.0	0.0	4.150	4.114	0.0	4.147	0.0	0.0	0.0
166.7	0.0	0.0	0.0	0.0	4.273	0.0	0.0	0.0	0.0	0.0	0.0

PERIOD	7-ARE	7-LPB	7-ANT	8-BKS	8-TLC	8-ALQ	8-GIE	8-BHP	8-QUI	8-ANT	8-PEL
16.7	0.0	0.0	3.876	3.825	3.758	0.0	3.850	0.0	3.858	3.917	3.903
20.0	3.905	3.854	3.901	3.849	3.786	3.742	3.865	3.864	3.893	3.936	3.930
25.0	3.923	3.861	3.915	3.855	3.792	3.765	3.864	3.864	3.878	3.937	3.940
33.3	3.924	3.886	3.917	3.848	3.796	3.781	3.853	3.864	3.890	3.936	3.933
40.0	3.924	3.907	3.915	3.845	3.803	3.789	3.851	3.861	3.901	3.933	3.925
50.0	3.928	3.921	3.927	3.850	3.818	3.803	3.853	3.872	3.906	3.949	3.920
58.8	3.945	3.938	3.938	3.868	3.842	3.827	3.866	3.890	3.914	3.959	3.934
66.7	3.963	3.958	3.952	3.893	3.862	3.852	3.890	3.916	3.937	3.969	3.959
76.9	4.002	4.005	3.981	3.916	3.890	3.885	3.923	3.957	3.991	4.012	3.979
90.9	4.020	4.064	0.0	3.976	3.934	3.936	3.969	3.978	4.020	0.0	4.028
100.0	0.0	0.0	0.0	3.999	3.966	3.975	3.997	4.001	4.049	0.0	0.0
111.1	0.0	0.0	0.0	4.042	4.004	4.023	4.033	0.0	4.102	0.0	0.0
125.0	0.0	0.0	0.0	0.0	4.053	4.083	4.094	0.0	4.160	0.0	0.0
142.9	0.0	0.0	0.0	0.0	4.109	4.165	4.203	0.0	4.238	0.0	0.0
166.7	0.0	0.0	0.0	0.0	0.0	4.285	4.405	0.0	4.398	0.0	0.0

PERIOD	9-BKS	9-GSC	9-TUC	9-ALQ	9-NNA	9-ARE	9-LPB	9-PEL	10-GIE	10-QUI	10-BOG
16.7	3.825	3.803	3.740	0.0	3.933	3.908	0.0	3.902	3.875	0.0	0.0
20.0	3.850	3.823	3.769	3.746	3.955	3.940	0.0	3.934	3.894	3.870	3.804
25.0	3.857	3.832	3.788	3.765	3.962	3.955	3.886	3.935	3.891	3.902	3.815
33.3	3.856	3.836	3.799	3.786	3.955	3.952	3.903	3.925	3.881	3.905	3.865
40.0	3.855	3.838	3.807	3.798	3.950	3.957	3.918	3.929	3.879	3.914	3.890
50.0	3.862	3.855	3.824	3.816	3.949	3.969	3.933	3.930	3.876	3.928	3.921
58.8	3.875	3.870	3.845	3.841	0.0	3.962	3.951	3.935	3.908	3.946	3.951
66.7	3.901	3.891	3.868	3.865	0.0	3.987	3.963	3.960	3.919	3.971	3.974
76.9	3.927	3.928	3.899	3.899	0.0	4.013	4.003	0.0	3.951	4.001	4.009
90.9	3.975	3.960	3.950	3.956	0.0	4.043	4.051	0.0	3.991	4.045	4.062
100.0	4.017	4.004	3.991	3.998	0.0	4.073	0.0	0.0	4.081	4.077	4.094
111.1	4.070	4.057	4.027	4.051	0.0	0.0	0.0	0.0	4.108	4.119	4.146
125.0	4.132	4.099	0.0	4.113	0.0	0.0	0.0	0.0	4.176	4.177	4.193
142.9	0.0	4.171	0.0	4.208	0.0	0.0	0.0	0.0	0.0	4.269	4.289
166.7	0.0	0.0	0.0	4.366	0.0	0.0	0.0	0.0	0.0	4.421	0.0

PERIOD	10-NNA	10-ARE	10-LPB	10-ANT	11-QUI	11-NNA	11-ARE	11-ANT	11-PEL	12-TUC	12-GSC
16.7	3.865	3.857	0.0	3.921	3.762	3.929	3.890	3.909	3.826	3.788	3.832
20.0	3.905	3.935	3.855	3.959	3.815	3.968	3.936	3.940	3.877	3.812	3.854
25.0	3.919	3.945	3.884	3.972	3.850	3.974	3.949	3.965	3.907	3.815	3.857
33.3	3.912	3.938	3.890	3.966	3.881	3.962	3.938	3.952	3.905	3.817	3.846
40.0	3.910	3.929	3.903	3.954	3.889	3.951	3.935	3.938	3.911	3.813	3.843
50.0	3.913	3.922	3.919	3.960	3.914	3.949	3.925	3.935	3.924	3.826	3.847
58.8	3.931	3.927	3.933	3.970	3.914	3.961	3.934	3.947	3.930	3.849	3.857
66.7	3.949	3.941	3.949	3.974	3.934	3.958	3.948	3.968	3.953	3.878	3.881
76.9	3.980	3.969	3.971	4.011	3.964	3.989	3.975	4.011	3.969	3.919	3.914
90.9	4.023	4.001	4.022	4.026	4.016	4.032	4.021	4.052	4.001	3.953	3.971
100.0	4.060	4.056	4.060	4.039	4.040	4.047	4.060	4.073	4.040	3.999	3.993
111.1	4.103	4.102	4.106	4.080	4.071	4.112	0.0	0.0	4.076	4.030	4.039
125.0	4.174	4.145	4.165	4.148	4.133	4.156	0.0	0.0	4.117	4.109	4.094
142.9	4.277	4.268	4.247	4.265	0.0	4.253	0.0	0.0	4.288	4.233	4.195
166.7	4.380	0.0	4.363	0.0	0.0	0.0	0.0	0.0	0.0	0.0	0.0

PERIOD	13-TUC	15-ARE	15-LPB	15-GIE	16-ALQ	16-TUC	16-GSC	17-ANT	17-LPB	17-ARE	GI-PEL
16.7	3.757	C.C	0.0	0.0	3.689	3.749	3.816	0.0	0.0	3.879	3.854
20.0	3.792	3.944	3.862	0.0	3.727	3.782	3.838	3.984	3.834	3.939	3.908
25.C	3.806	3.951	3.888	3.897	3.760	3.797	3.847	3.988	3.866	3.964	3.932
33.3	3.811	3.938	3.904	3.880	3.784	3.806	3.847	3.995	3.899	3.973	3.936
40.0	3.815	3.936	3.910	3.872	3.798	3.810	3.839	3.987	3.932	3.968	3.932
50.0	3.823	3.936	3.928	3.877	3.811	3.837	3.851	3.988	3.957	3.965	3.936
58.8	3.844	3.945	3.949	3.903	3.842	3.857	3.863	3.997	3.976	3.994	3.948
66.7	3.865	3.965	3.970	3.929	3.862	3.867	3.874	4.023	3.987	4.017	3.956
76.9	3.900	3.988	4.001	3.947	3.896	3.892	3.898	4.067	4.017	4.042	3.975
90.9	3.956	4.041	4.045	4.025	3.947	0.C	3.963	4.116	4.049	0.0	4.003
100.0	3.991	4.096	4.079	4.063	3.969	0.0	3.981	0.0	4.071	0.0	4.017
111.1	4.032	4.152	4.126	4.125	4.CC8	0.C	4.045	0.0	4.109	0.0	0.0
125.0	4.083	4.201	4.180	4.208	4.102	0.0	4.147	0.0	0.0	0.0	0.0
142.9	4.160	0.C	4.261	4.283	0.0	0.0	0.0	0.0	0.0	0.0	0.0
166.7	0.0	0.0	0.0	0.0	0.0	0.0	0.0	0.0	0.0	0.0	0.0

PERIOD	GI-ANT
16.7	C.0
20.0	3.921
25.C	3.954
33.3	3.950
40.0	3.949
50.0	3.971
58.8	3.985
66.7	3.993
76.9	4.023
90.9	0.0
100.0	0.0
111.1	0.0
125.0	0.0
142.9	C.0
166.7	C.0

Figure 7. Steps used in processing and selecting Rayleigh wave data.

Figure 8. Energy versus group arrival time as a function of period for Rayleigh wave observed at Albuquerque. Source event occurred on Oct. 12, 1964. Energy contours are in db reduced from peak energy at each frequency. Dotted line gives apparent group velocity, not corrected for instrument response.

Figure 9. Amplitude spectral density of Rayleigh wave signal observed for path 8-ALQ. Amplitudes are corrected for instrument response. Thin line represents amplitude spectra of original signal; heavy line represents filtered signal with cutoff at 0.05 Hz.

Figure 10. Phase spectral density of Rayleigh wave signal observed for path 8-ALQ in radians. Phases are corrected for instrument response, but expressed relative to an arbitrary origin time for clarity. Thin line, original signal, heavy line, filtered signal.

Figure 11. Original and filtered seismograms of the vertical component of the Rayleigh wave for path 8-ALQ. The top of the figure is up. Filtering was done with the time-variable-filter described in the text. All periods shorter than 20 sec. were eliminated.

Figure 12. Great circle paths of the Rayleigh waves considered in this study. Station locations indicated by triangles include all stations used as receivers for either Love or Rayleigh waves.

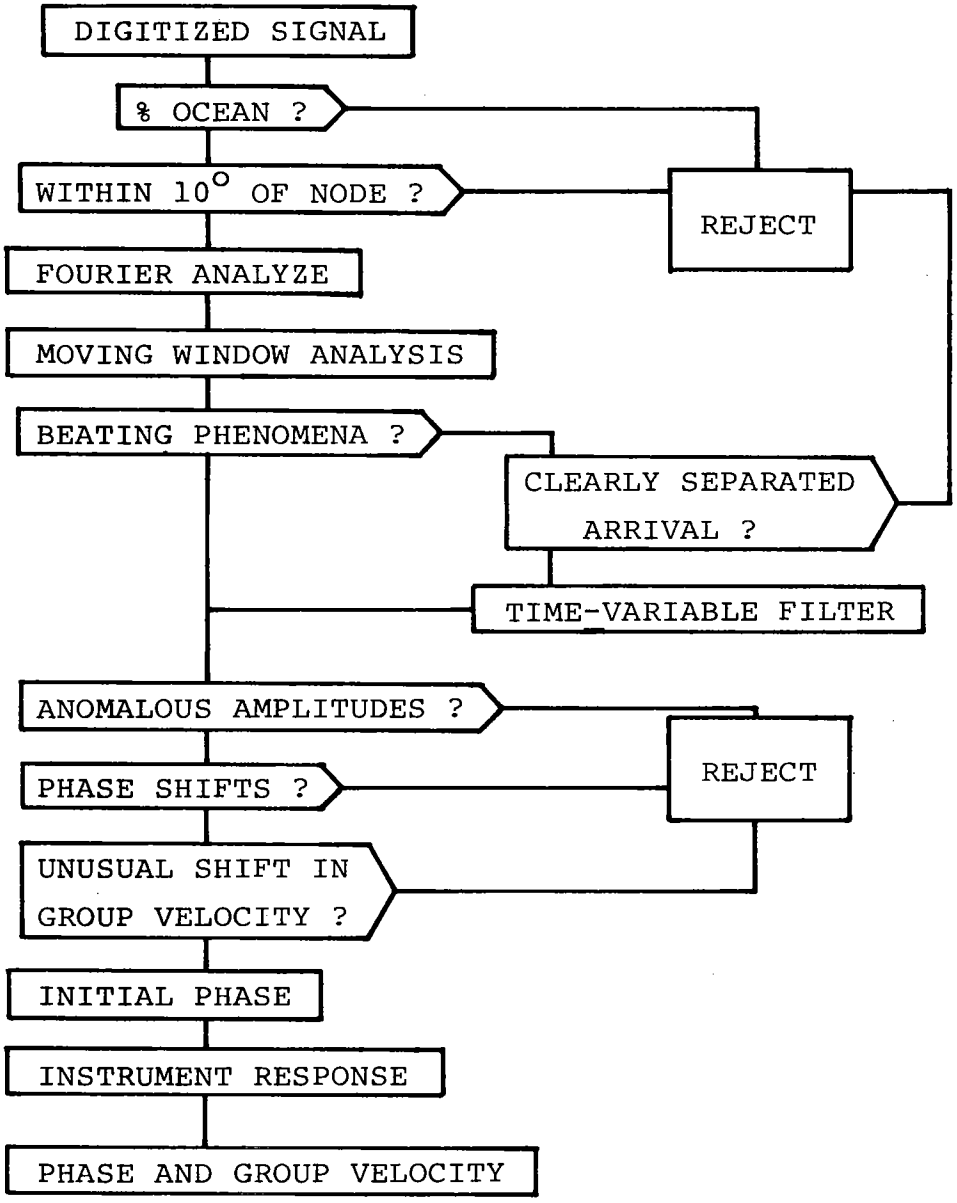
DIGITIZED SIGNAL
% OCEAN ?
WITHIN 10° OF NODE ?
REJECT
FOURIER ANALYZE
MOVING WINDOW ANALYSIS
BEATING PHENOMENA ?
CLEARLY SEPARATED ARRIVAL ?
TIME-VARIABLE FILTER
ANOMALOUS AMPLITUDES ?
PHASE SHIFTS ?
REJECT
UNUSUAL SHIFT IN GROUP VELOCITY ?
INITIAL PHASE
INSTRUMENT RESPONSE
PHASE AND GROUP VELOCITY

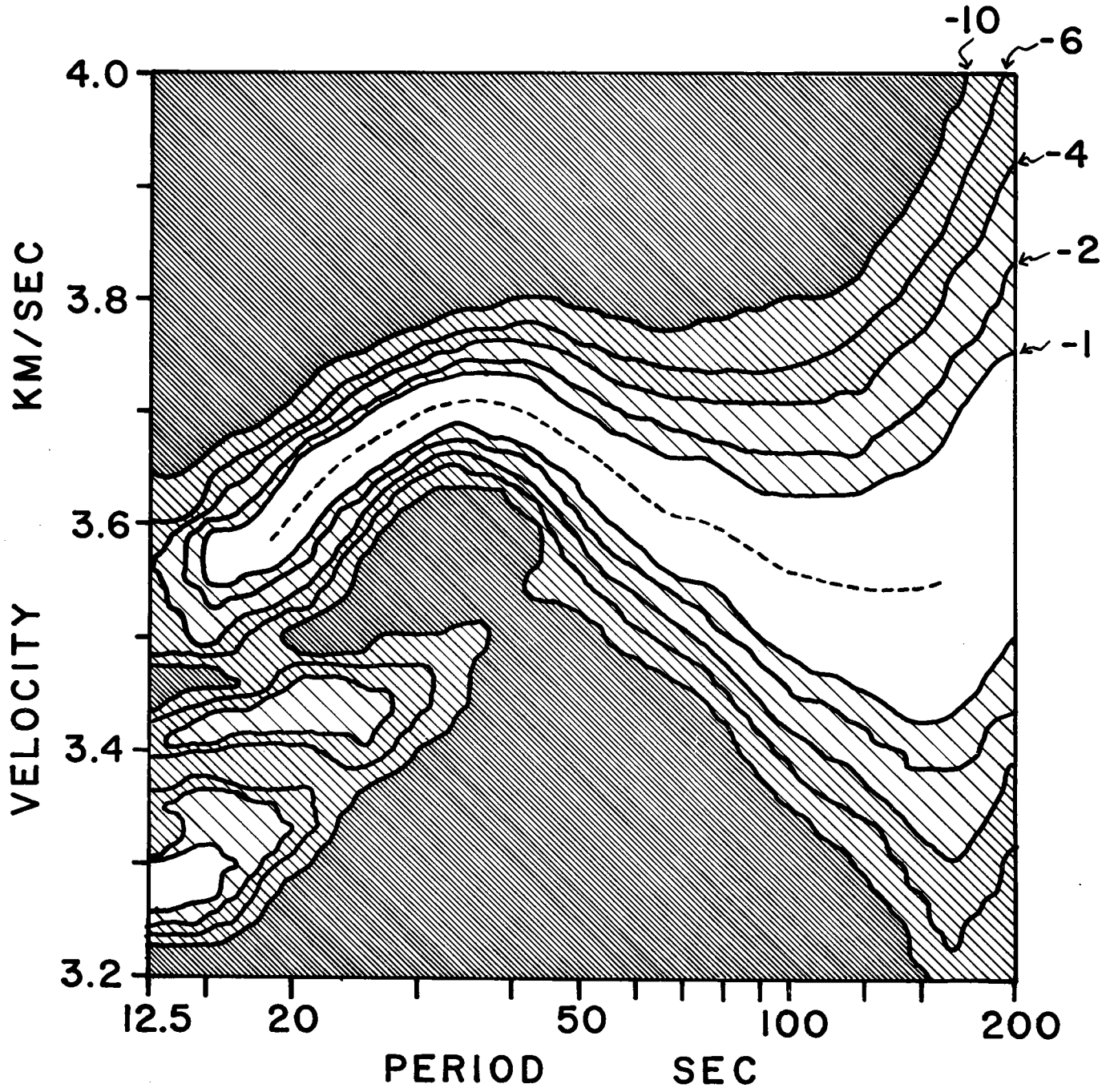
-10
-6
-4
-2
-1
4.0
3.8
3.6
3.4
3.2
KM/SEC
VELOCITY
12.5
20
50
100
200
PERIOD
SEC

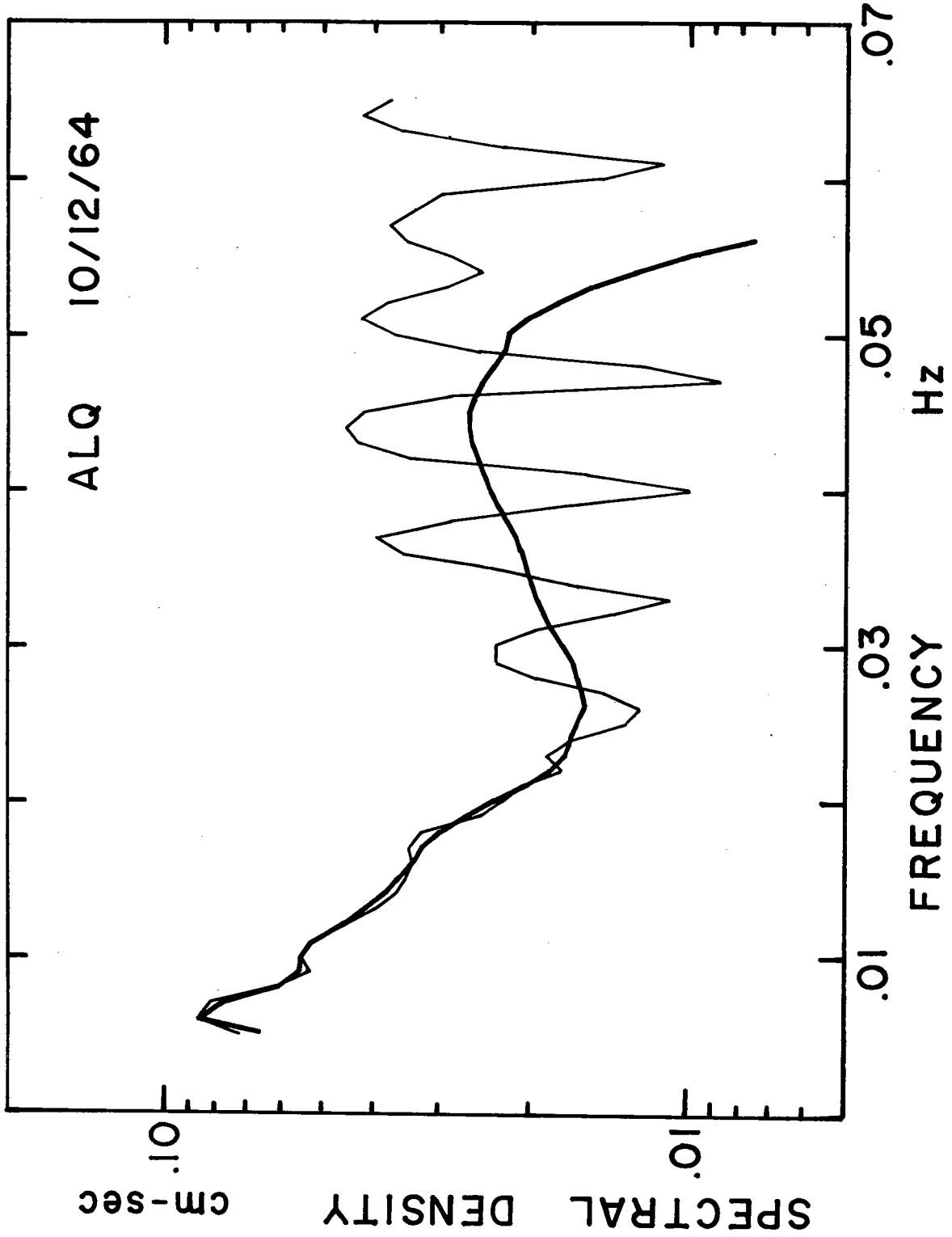
ALQ 10/12/64
SPECTRAL DENSITY
cm-sec
1.0
0.1
FREQUENCY
Hz
.01
.03
.05
.07

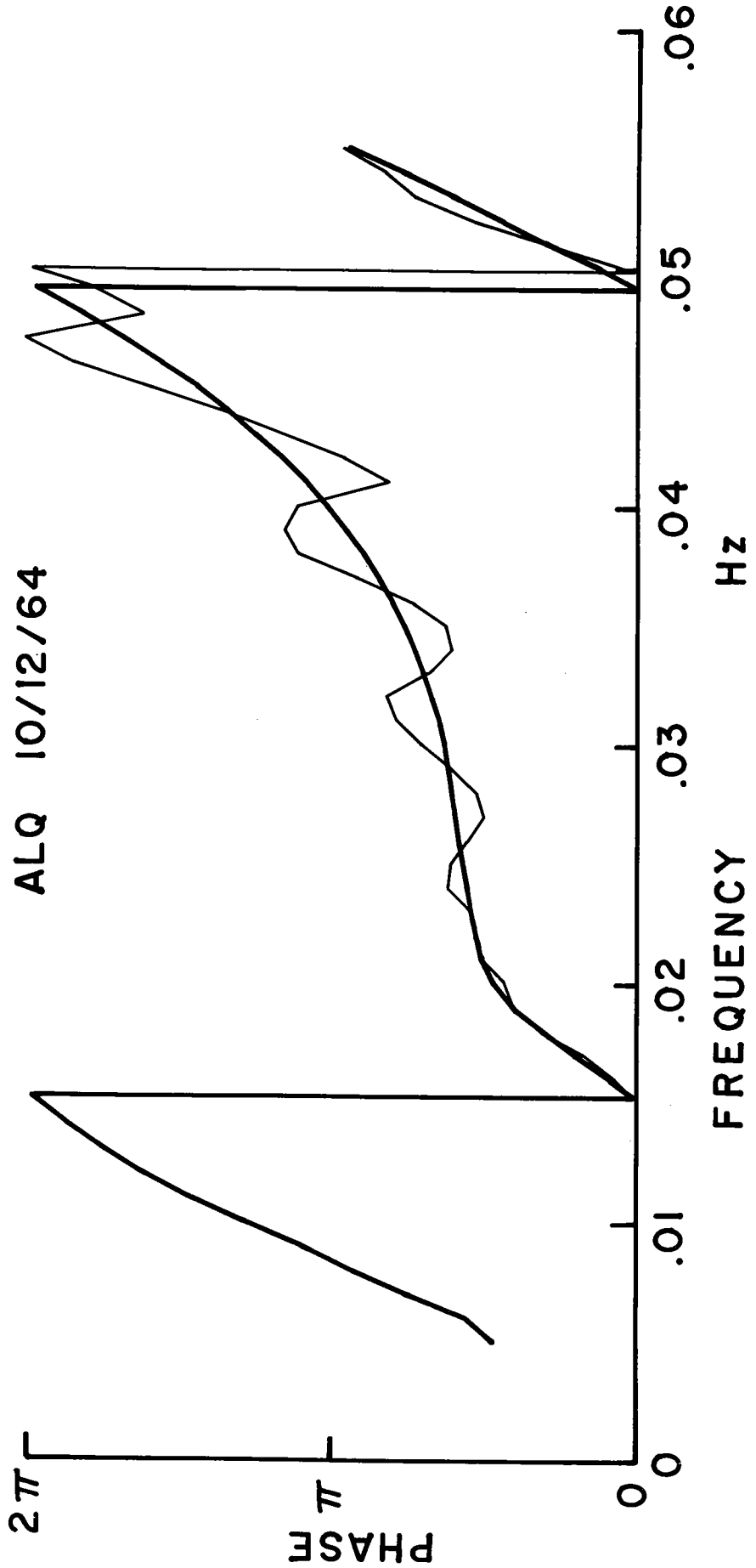
ALQ 10/12/64
PHASE
2π
π
0
0
.01
.02
.03
.04
.05
.06
FREQUENCY
Hz

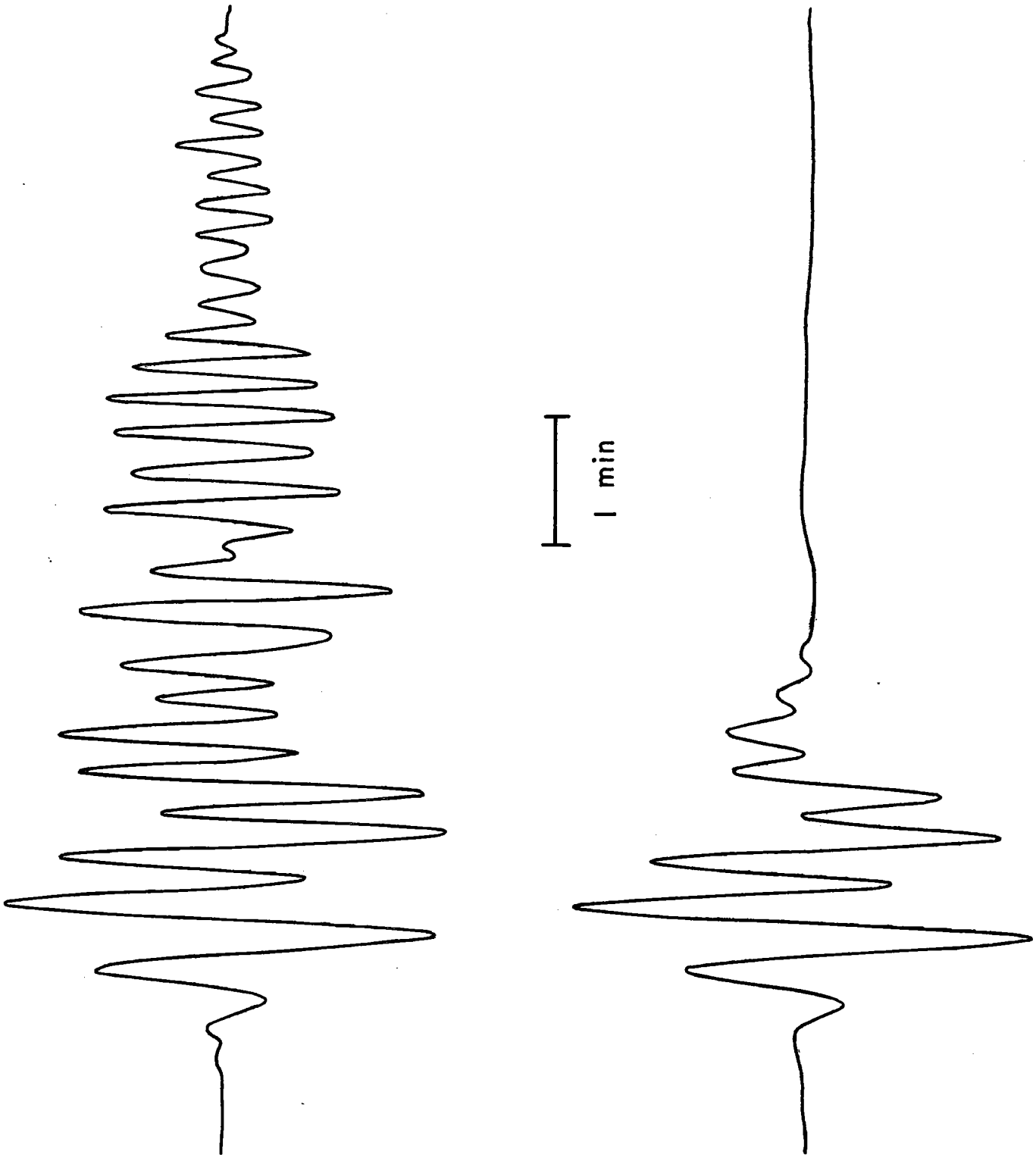
1 min

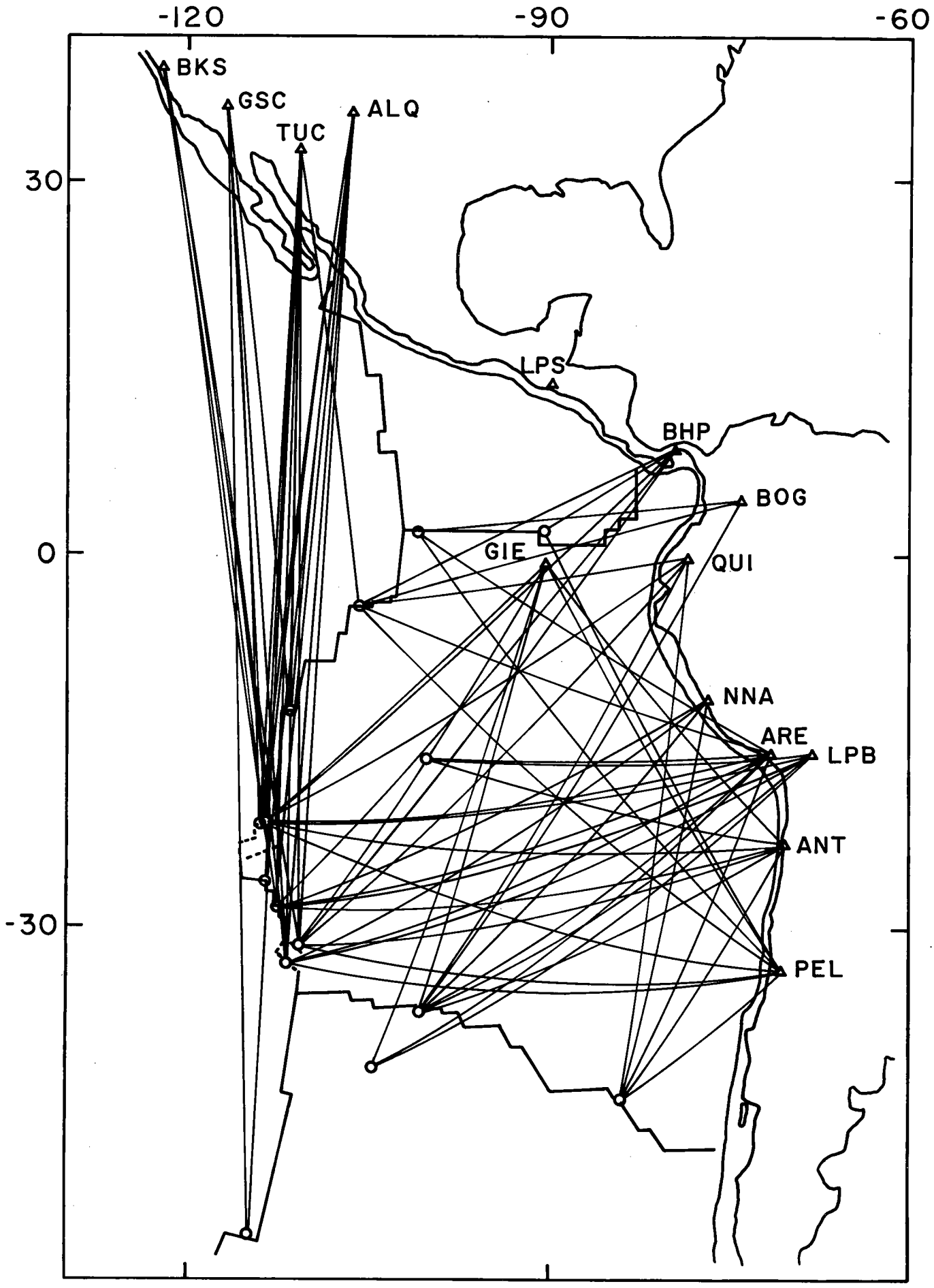
-120
-90
-60
30
0
-30
BKS
GSC
TUC
ALQ
LPS
BHP
BOG
GIE
QUI
NNA
ARE
LPB
ANT
PEL

3.2 Error analysis

Several possible sources of error will contribute to uncertainty in the measured phase and group velocities. Two types of errors can be anticipated: systematic errors which will bias the determination of the characteristic regional velocities; and random errors which will merely contribute to scatter in the data. Possible systematic errors are explored in the section following the discussion of the regionalized velocities. The finiteness of the source, uncertainty in the origin time, errors in digitizing, uncertainty in the focal mechanism, mislocation of the epicenter, and ambient noise are expected to contribute to scatter in the data. For convenience, all errors, E_i, will be discussed in terms of seconds. This can be converted to an equivalent phase error E_i/T for each period T, or to approximate velocity error $E_i V^2/DIST$. For the average path length of about 4800 km and a phase velocity of 4.0 km/sec., a 5 second error corresponds to about 0.016 km/sec or a 0.4% error.

Digitizing errors. Errors due to the mechanical translation of the analog data into digital form were estimated by repeated digitization of several of the seismograms. From comparisons of the phase spectra of the duplicated records, I estimate the root-mean square (RMS) digitizing error, E_d, to be less than 2.0 sec. All data was digitized by the same person (the author). As an independent check, a student was asked to

digitize a portion of the data. After some practice, his precision was comparable, and the phases were consistent with mine.

Source mechanism. Figures 13a and 13b illustrate the variation of initial phase with azimuth for several source geometries. Inaccuracy in the assumed focal mechanism or depth produces a longer phase error at the shorter periods than at long periods, but the equivalent error in seconds is about the same. Except in the zone of rapid change of phase with azimuth, the initial phase of a strike-slip event will be close to either 3/8 or 7/8 circle, and relatively little error will be introduced by changes in the assigned dip or slip. The possibility of misassignment of phase in the steep portions of the curves has been eliminated by throwing out all records within 10° in azimuth of a mode in the amplitude radiation pattern. The azimuth of the most rapid phase change is also the direction of minimum excitation. Although the strike of the fault plane may not be known within 10° due to tradeoffs between strike and dip or slip (Forsyth, 1973), the azimuths of the nodes are known to that accuracy. Thus the error is unlikely to exceed 3 sec., but the average error should be much less. I assign the error due to uncertainty in the focal mechanism, E_s, an RMS value of 2.0 sec. Initial phases were computed for the Harkrider-Anderson standard oceanic earth model even though the source events occurred on a mid-ocean

ridge. For these shallow events, the uncertainty in mantle structure has a negligible effect on the initial phase.

Origin time, finiteness, and mislocation. These errors may include a systematic component in addition to the random variation, and therefore are considered in another section. Following the conclusions of that discussion, the RMS magnitude of the random errors are given as finiteness E_f = 1.75 sec., origin time E_t = 1.5 sec., and mislocation E_m = 3.5 sec.

The total expected RMS error E can be easily be estimated if we assume the errors are normally distributed. The error arising from several sources is given by $E = \sqrt{E_d^2+E_s^2+E_f^2+E_t^2+E_m^2}$ = 5.05 sec. I believe the magnitude of each of the constituent errors has been generously estimated; therefore, if the medium is properly described, it should be possible to predict the observed phases with an RMS error or standard deviation of about five seconds. However, in one out of every twenty measurements the error is expected to exceed ten seconds, amounting to 0.06 km/sec. for a path as short as 2500 km. Thus, care must be taken in attaching significance to small details of any one measurement of phase velocity. In particular, it is dangerous to assume that the lowest measured value of phase velocity represents the true phase velocity in a region (Kausel, 1972; Weidner, 1972), even if that region is expected to be characterized by low phase velocities.

All the errors discussed above except E_d will be nearly

independent of frequency for any one path, resulting in a shift of the entire phase velocity curve. Therefore, the shape of the curve is more reliably determined than its absolute level. This should be reflected in the precision attainable for the group velocity observations, which measure the derivatives of the phase velocity curve. If only the level of the phase velocity curves changed, group velocity measurements would have about the same degree of scatter. In addition to E_d, the errors due to small-scale, lateral inhomogeneities and ambient noise are frequency dependent. The process of data selection insures that there will be a large signal-to-noise level at short periods, but the ambient noise and long period drift of the instruments are increasingly more important at the longer periods, where the instrument response decays. The short periods (25 sec. or less) are very sensitive to variations in crustal thickness or water depth. These horizontal variations may occur on a scale too small to be included in any regional analysis of dispersion, so that the apparent scatter at short periods will be increased. The least scatter in the radiation patterns occurred in the 50-70 sec. range; 50-70 sec. should also be the range of least scatter in the phase and group velocities.

Figure 13a,b. Theoretical initial phase of the source for four different fault geometries. The apparent source phase of Rayleigh waves is given for a), 67 sec. period, and b), 20 sec. period. The phase shift which would introduce a 3 sec. error is indicated by the vertical bar. Model 1 has dip 80°, slip -150°, and depth 5 km: model 2; dip 80°, slip -170°, depth 5 km: model 3; dip 60°, slip -150°, depth 5 km: and model 4; dip 80°, slip -150°, depth 11.5 km. Azimuth is in degrees counterclockwise from the strike of the fault.

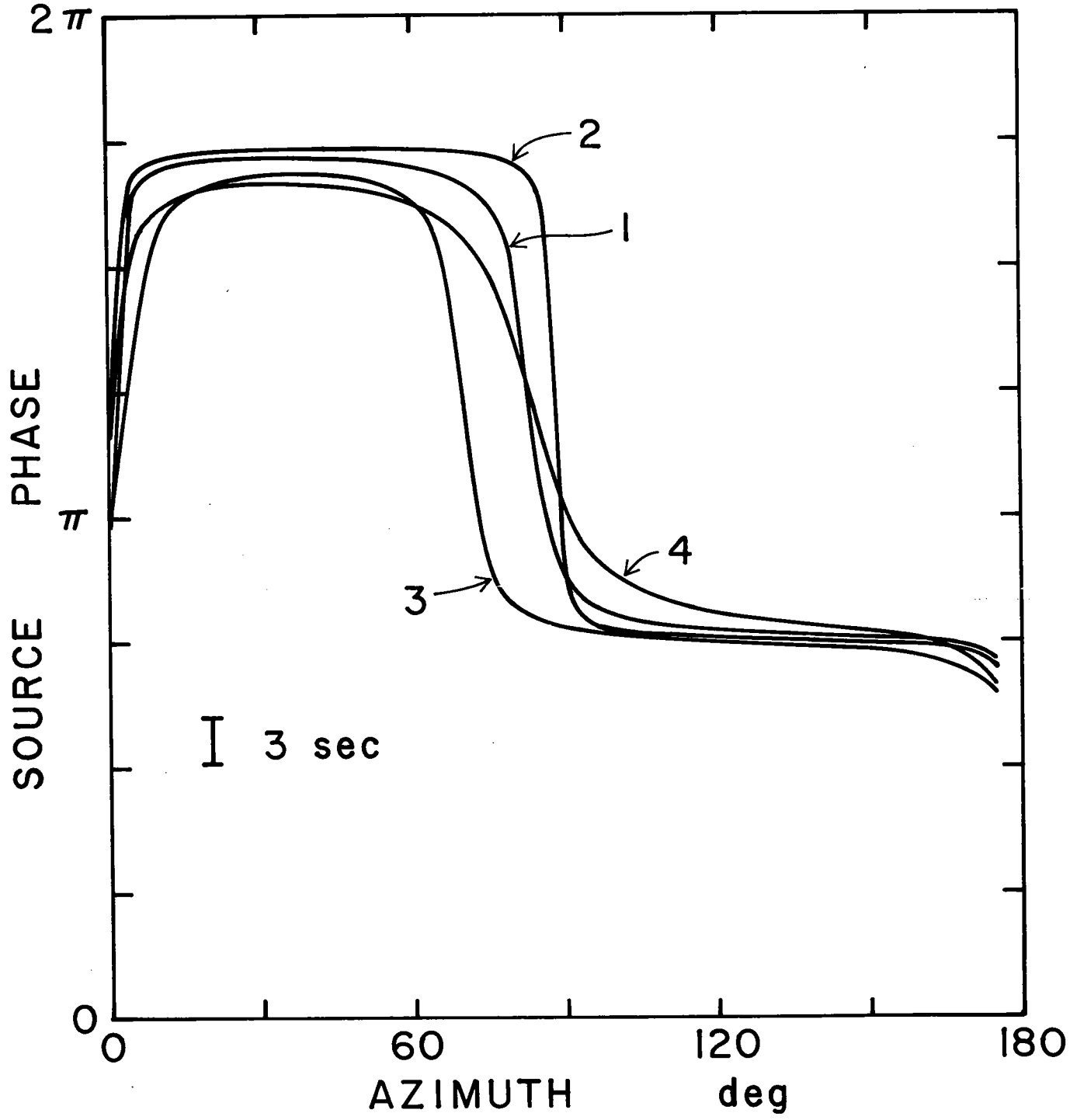
2π
π
0
SOURCE PHASE
2
1
4
3
I 3 sec
0
60
120
180
AZIMUTH deg

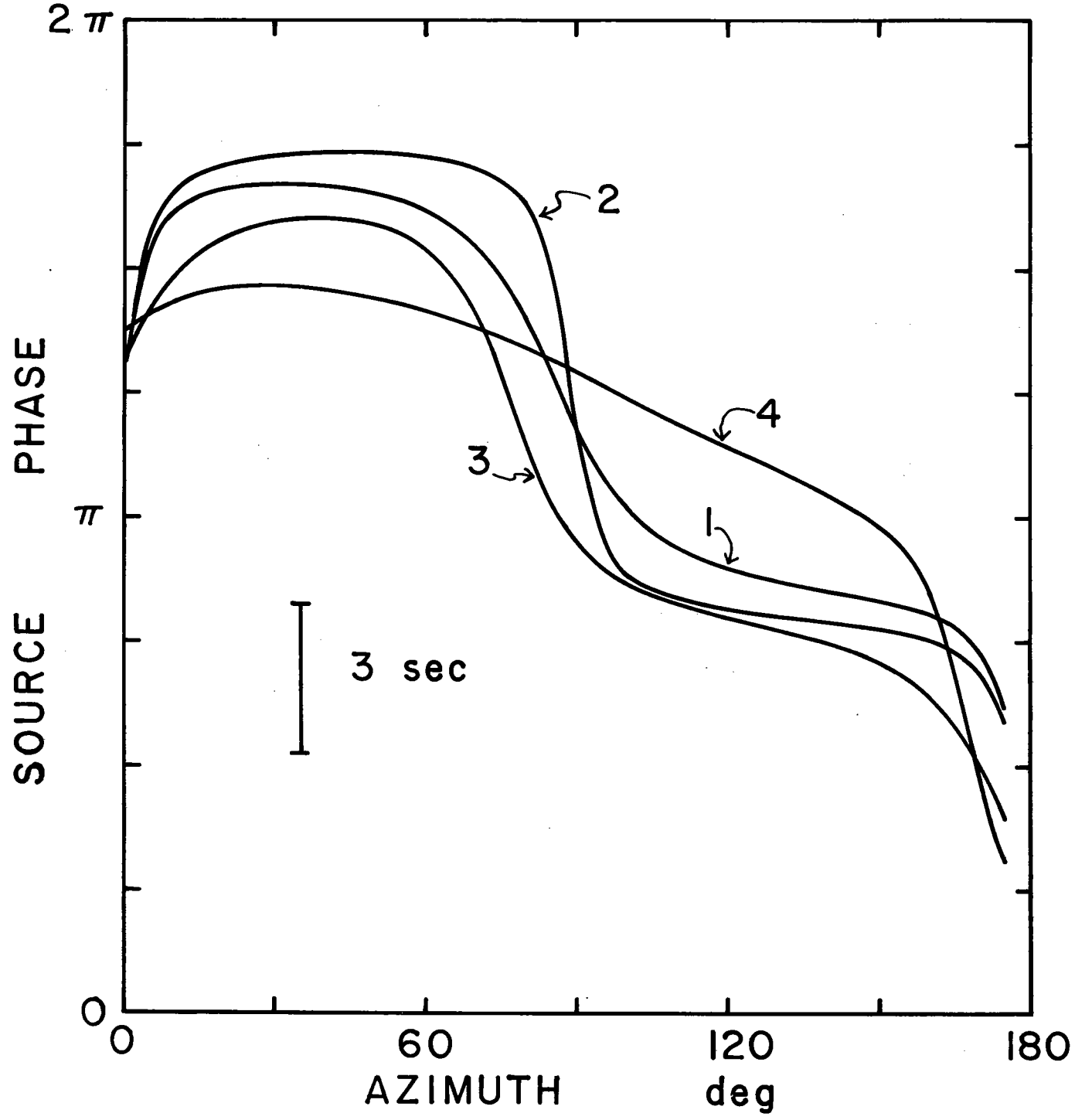
2 π
π
0
SOURCE PHASE
0
60
120
180
AZIMUTH
deg
1
2
3
4
3 sec

3.3 Regionalization

A progressive increase in phase velocity with distance from the mid-ocean ridge can readily be deduced from an examination of the dispersion over a few representative paths. In figure 14, path 8-TUC travels up the East Pacific rise to North America; 10-NNA begins outside the ridge crest area on the Chile fracture zone and crosses the Nazca plate to South America; and although 11-NNA starts on the Chile ridge, it primarily travels within the oldest part of the plate, far from the East Pacific rise. These three paths, and other similar sets, show successively higher velocities, with the lowest velocities being associated with the mid-ocean ridges. Yet the phase velocity over path 4-ARE crossing the entire Nazca plate from the ridge crest to South America seems to be faster than that observed in the oldest section of the plate over path 11-NNA. Because it crosses each of the regions covered by the other three curves in the figure, it would be expected to be roughly an average of the three curves. The regional variation is very clear, but it also appears that Rayleigh waves traveling from west to east are faster than those traveling from south to north. To be of use in future modeling of the evolving physical and chemical properties of the lithosphere, the regional changes must be related to an accurate time scale and a system of tying the directional dependence to a physically meaningful coordinate system must be employed.

In order to correlate surface wave velocities with the age of the sea floor, I divided the eastern Pacific area into a number of zones whose boundaries are lines of constant age, and then found the characteristic pure-path dispersion for each region. Two methods were used to delineate the age boundaries. The first method is based on the identification of linear magnetic anomalies formed at the mid-ocean ridge crests in the process of sea-floor spreading. Anomalies 3, 5, 6, 13 and 21 are often easy to identify and form convenient dividing points at ages of about 5, 9.5, 20, 38 and 53 million years, respectively, on the Heirtzler et al. (1968) and Talwani et al. (1971) time scales. The zones in figure 15, with approximate ages of 0-5 m.y., 5-10 m.y., 10-20 m.y., and older than 20 m.y., were formed by extrapolating between the anomalies interpreted chiefly by Herron (1971, 1972), and others identified by Pitman et al. (1968), Morgan et al. (1969), Herron and Hayes (1969), Herron and Heirtzler (1967), Grim (1970), Larson and Chase (1970), Hey et al. (1972), and Atwater and Menard (1970). The 38 m.y. isochron is also shown in the figure, but it was not used to define another zone because the area within this study older than 38 m.y. is relatively small. Some complications are introduced by the complex history of spreading in this area. The Galapagos rise, a north-south trending topographic feature within the Nazca plate centered at about 95°W, is apparently the fossil crest of a formerly active spreading-

center. At some point in the past, spreading ceased on the Galapagos rise and shifted to the west to form the current spreading-center, the East Pacific rise. Herron (1972) dates the cessation of spreading on the Galapagos rise at about 9 m.y.b.p., although both ridge axes were active simultaneously for several million years before the old ridge died out. Thus, starting at the crest of the East Pacific rise, the age of the sea floor increases to the east until the point is reached where the crust was generated at the old Galapagos rise spreading center. From there, the age decreases eastward to the crest of the fossil ridge, then the age of the seafloor starts increasing again until it is consumed in the Peru-Chile trench. The progression of ages and the fossil ridge axis are illustrated in figure 15. A similar shift also occurred north of the equator, where the axis jumped from the Mathematician ridge eastward to the East Pacific rise. Unfortunately, a controversy exists over the precise time of the shift.

In much of the equatorial region, the magnetic anomalies are not well-developed and are difficult to identify. Sclater and colleagues have developed another technique for dating the seafloor. After establishing an empirical depth versus age curve in areas which are well-dated, they can determine the approximate age of the ocean floor in other areas by comparing the bathymetry to the standard curve. Applying this technique in the east Pacific yields an age of about 5 m.y. for cessation

of spreading on the old centers (Sclater et al., 1971; Anderson and Sclater, 1972). I cannot resolve this discrepancy; therefore, I have also regionalized the area on the basis of bathymetry (figure 16). Three zones were constructed; less than 3500 m in depth; 3500 to 4000 m; and greater than 4000 m. The 3500 and 4000 m dividing points correspond roughly to 8 m.y. and 20 m.y. on the depth-versus-age scale. To be done rigorously, a subsidence scale should be used rather than a depth scale (Sclater, personal communication), but that would be impractical for the purposes of this study. The youngest zone in both regionalizations is quite similar, but there are significant disagreements in the central portion of the Nazca plate.

The directional dependence of surface wave velocities is quantitatively related to the sea floor spreading process by describing the azimuth of propagation in a coordinate system centered on the pole of relative motion between two plates. For example, path 4-ARE crosses the Nazca plate, whose crust was formed at the Nazca-Pacific boundary. The propagation direction at each point along the path is described by an angle θ, which is the angle between the azimuth to the pole of relative motion of the Nazca and Pacific plates and the azimuth to the station. Angles are positive clockwise and the azimuths are computed from the point in question. For propagation perpendicular to the direction of spreading and roughly parallel to the ridge axis, θ is zero or π. The poles

of relative motion used in this study are: 60°N, 90°W for crust within the Nazca plate, except; 0°N, 130°W for crust formed at the Galapagos Rift Zone on the Nazca-Cocos boundary; 70°S, 118°E for crust formed at the Pacific-Antarctic Ridge; 40°N, 110°W for crust formed on the Cocos-Pacific boundary; and 79°N, 111°E for the crust of the Pacific plate older than about 10 million years formed on the old Pacific-Farallon plate boundary (Morgan, 1968). These poles are consistent with those found in the literature cited previously. No a priori coordinate system is known for the continents, so the possibility of continental anisotropy was not considered. For general anisotropy, the velocity will depend only on the sine or cosine of even multiples of θ (Smith and Dahlen, 1973). Listed in Table 2 is the average value of sin 2θ and cos 2θ for the oceanic portion of each path, multiplied by the fraction of the path which is oceanic. Also given in Table 2 is the length of each path within the regions described here.

Figure 14. Rayleigh wave phase velocities over four individual paths.

Figure 15. Boundaries of age zones used in regionalization. Approximate ages of the crust are in millions of years. Continental regions are considered to extend to the shelf break, indicated by the light line on the oceanic side of the heavy continental outlines. Continuous, double lines are actively spreading ridges. The dashed, double lines indicate the approximate location of fossil ridge crests. The arrows are in the direction of increasing age.

Figure 16. Bathymetry of the east Pacific. Contours are based on the International Tectonic World Map (USSR). The water depth in the gray area is less than 3500 m. The stipled area is 3500 to 4000 m, and the diagonally lined region is greater than 4000 m in depth. The unshaded areas within the ocean are aseismic ridges. For purposes of regionalization of surface wave propagation, the aseismic ridges are assigned to the depth range of the surrounding area. The trenches are included within the closest neighboring zone.

Figure 17. Pure-path Rayleigh phase velocities for three oceanic age divisions. Triangles 0-10 m.y.;

crosses, 10-20 m.y.; and circles, older than 20 m.y. Solid lines are one standard deviation away from the observed velocities. Values given are from model 7, table 5.

Figure 18. Pure-path Rayleigh group velocities for three oceanic age divisions. Triangles, 0-10 m.y.; crosses, 10-20 m.y.; and circles, older than 20 m.y. Solid lines are one standard deviation away from the observed velocities. Values given are from model 7, table 5.

Figure 19. Cos 2θ coefficient of anisotropy for Rayleigh waves. Bands of values given are within one standard deviation of the coefficients derived for model 7, table 5.

Figure 20. Sin 2θ coefficient of anisotropy for Rayleigh waves. Bands of values given are within one standard deviation of the coefficients derived for model 7, table 5.

Figure 21. Pure-path Rayleigh phase velocities corrected to standard water depth. Values are from model 10, table 5.

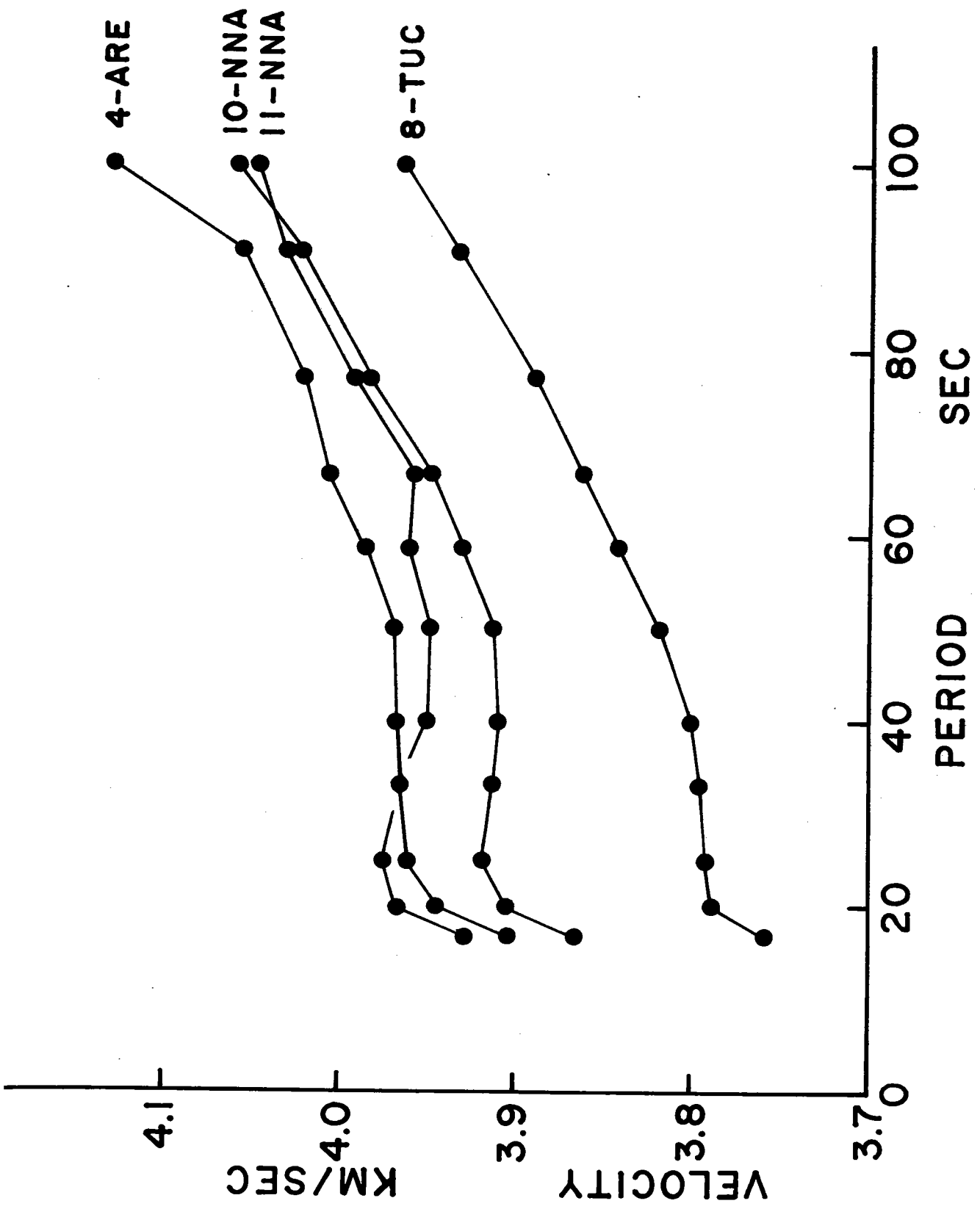
4-ARE
10-NNA
11-NNA
8-TUC
VELOCITY
KM/SEC
4.1
4.0
3.9
3.8
3.7
0
20
40
60
80
100
PERIOD
SEC

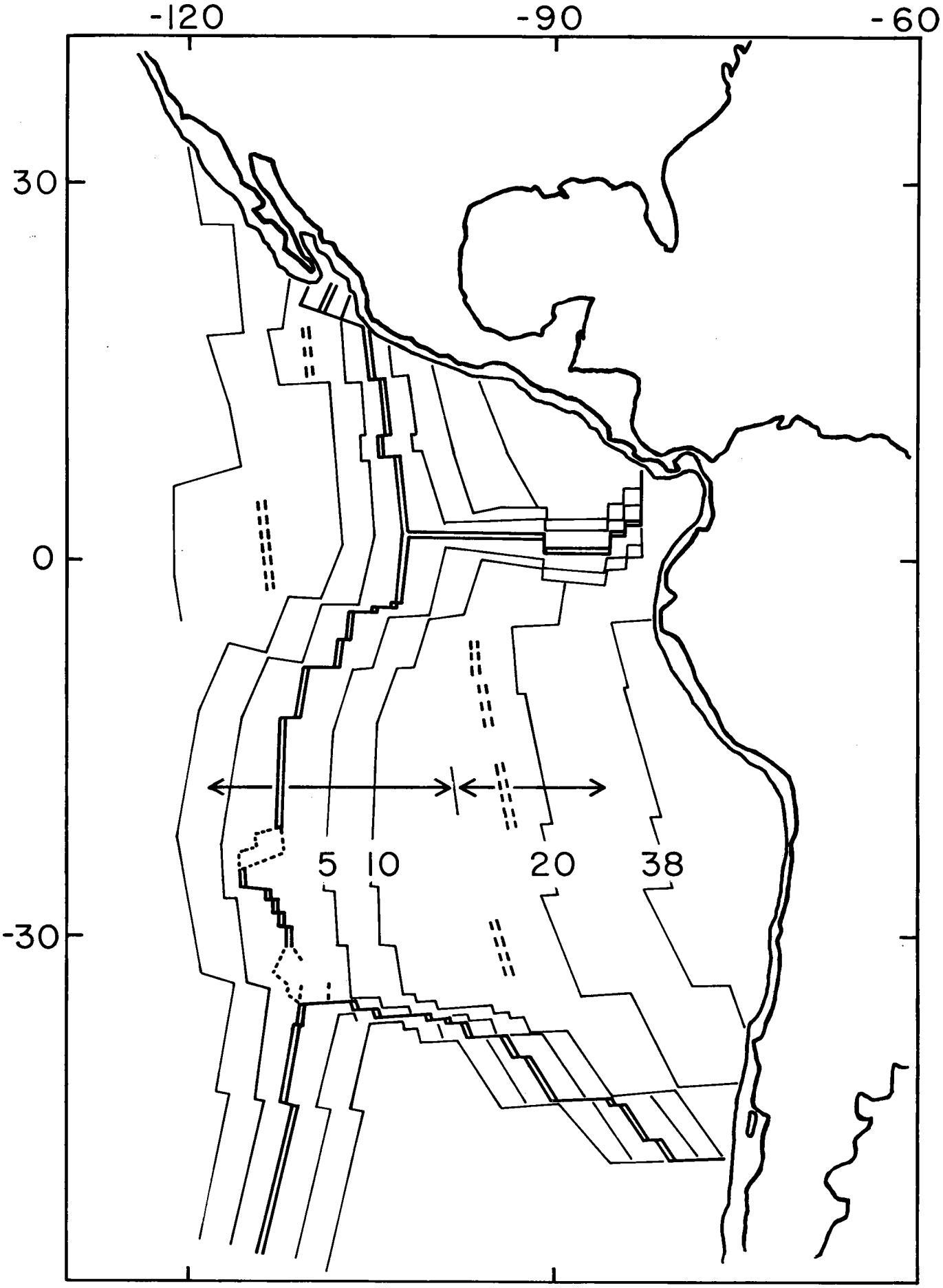
-120
-90
-60
30
0
-30
5
10
20
38

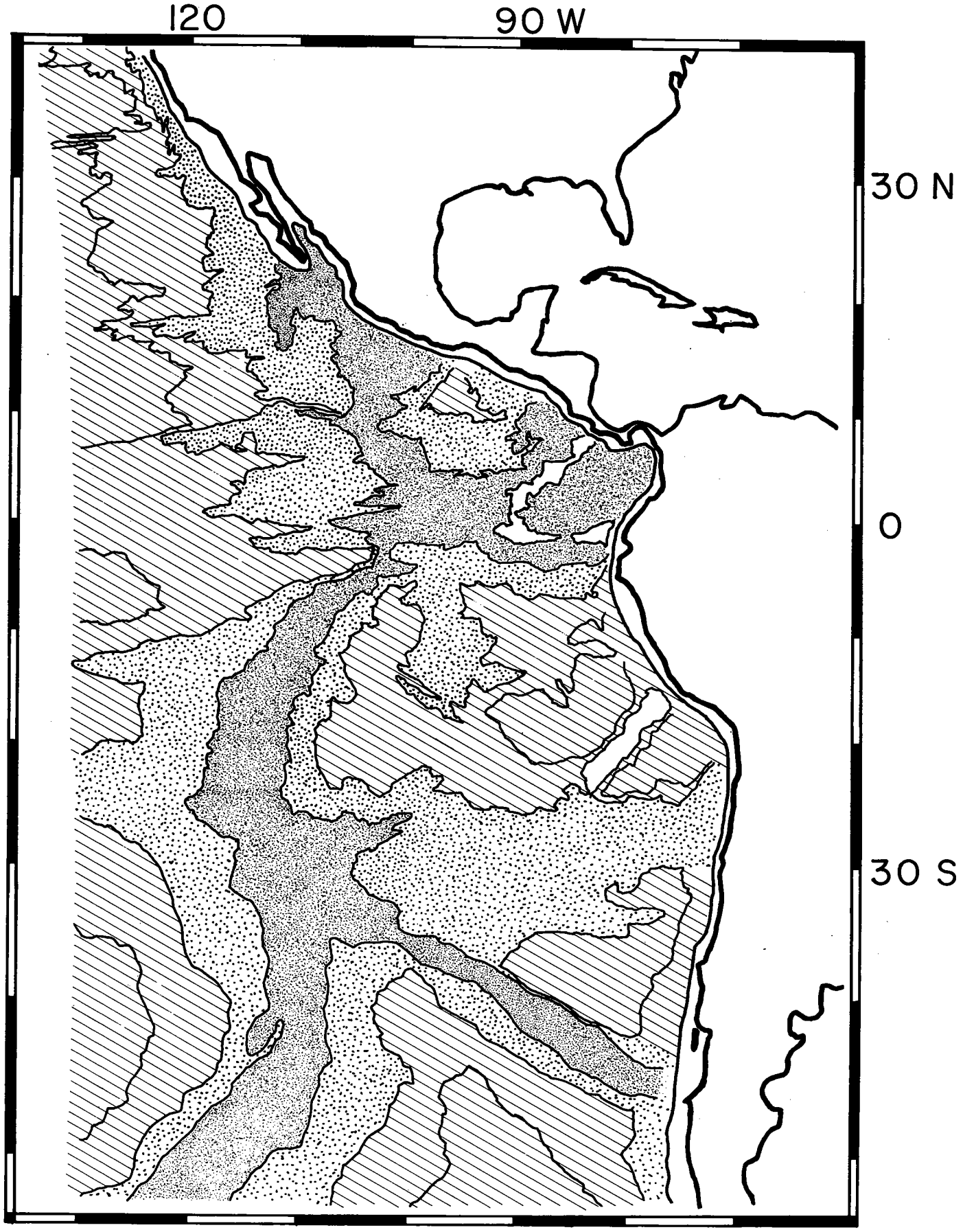
120
90 W
30 N
0
30 S

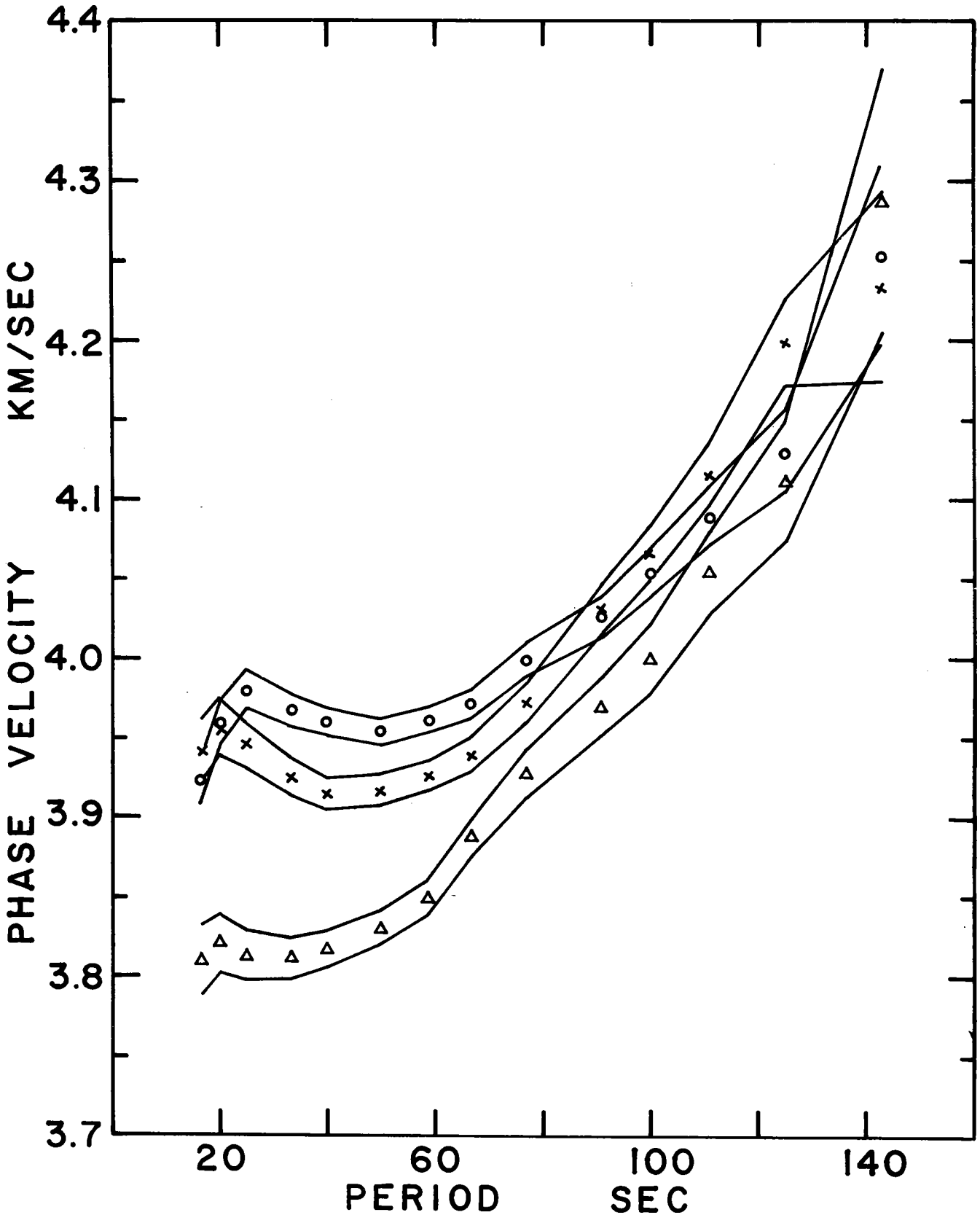
4.4
4.3
4.2
4.1
4.0
3.9
3.8
3.7
PHASE VELOCITY KM/SEC
20
60
100
140
PERIOD SEC

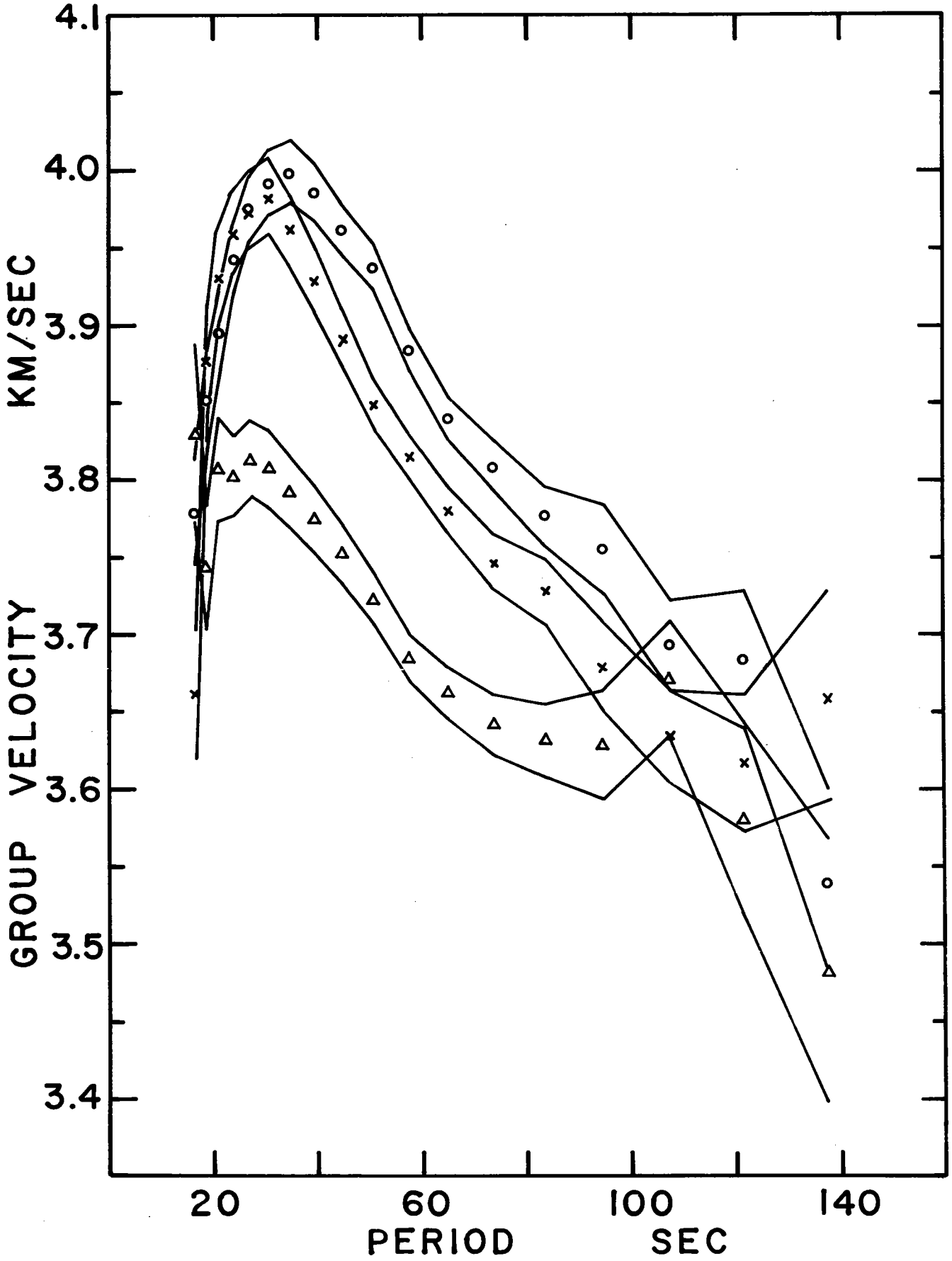
4.1
4.0
3.9
3.8
3.7
3.6
3.5
3.4
KM/SEC
GROUP VELOCITY
20
60
100
140
PERIOD
SEC

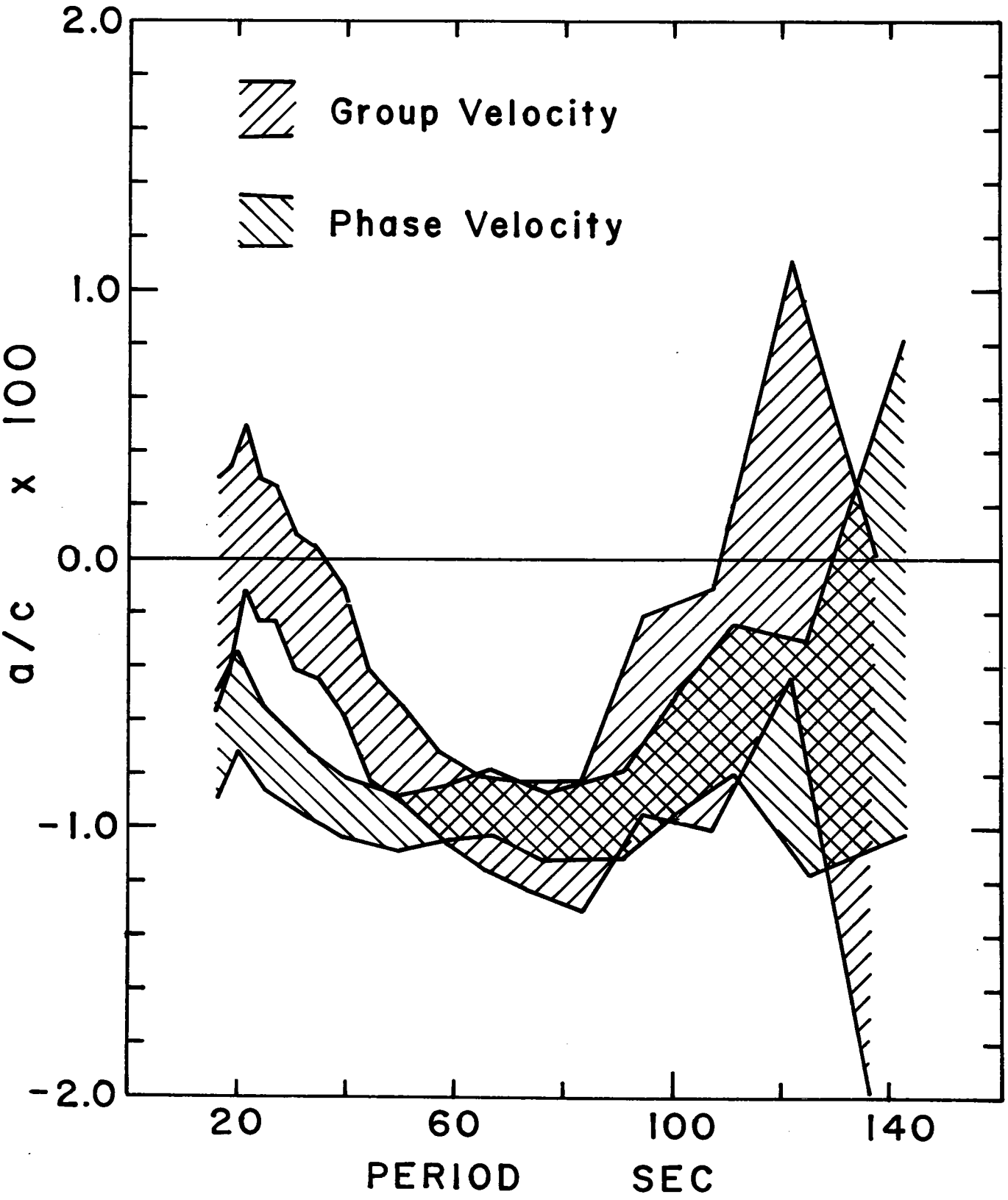
2.0
1.0
0.0
-1.0
-2.0
a/c x 100
Group Velocity
Phase Velocity
20
60
100
140
PERIOD SEC

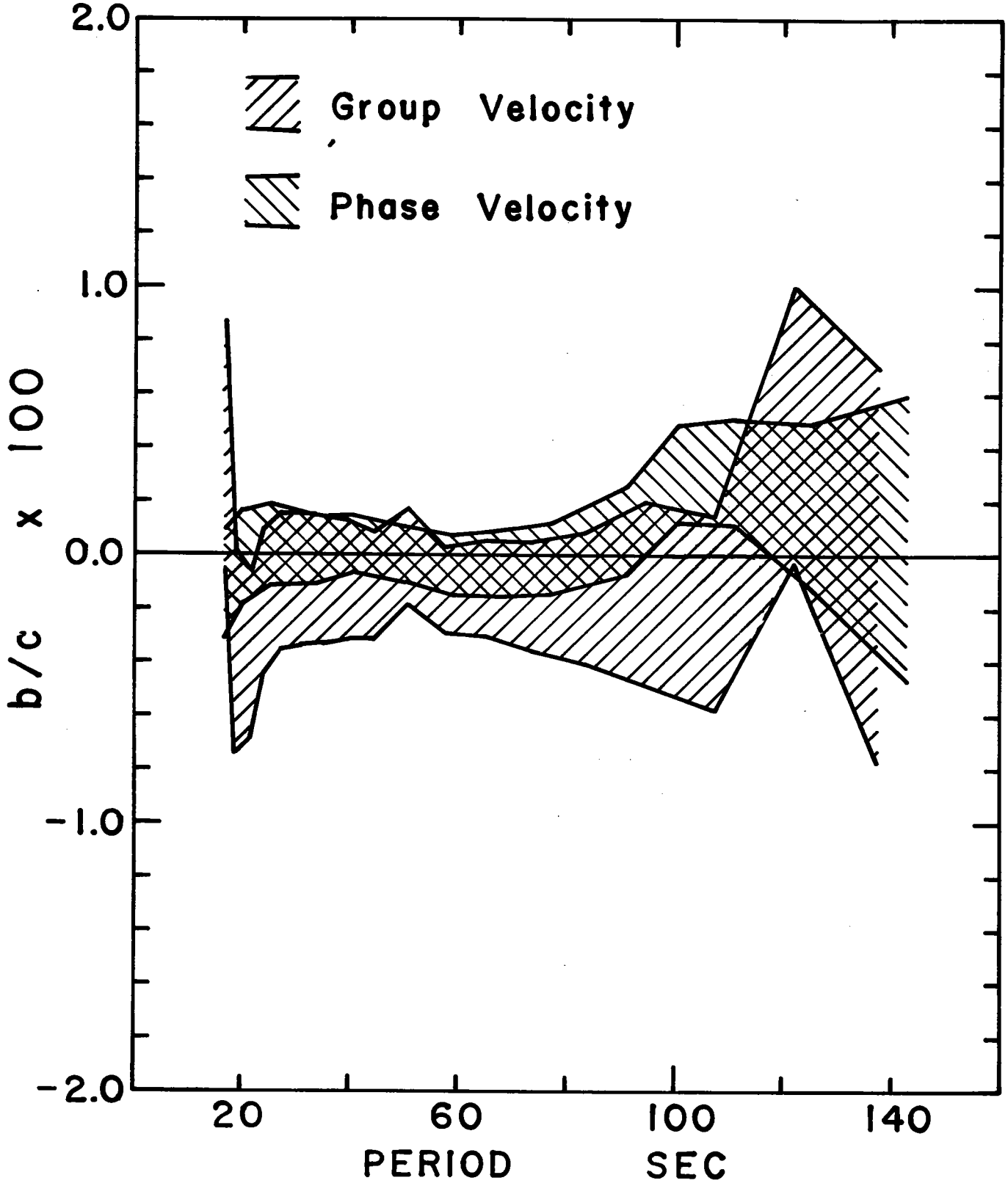
Group Velocity
Phase Velocity
2.0
1.0
0.0
-1.0
-2.0
b/c x 100
20
60
100
140
PERIOD SEC

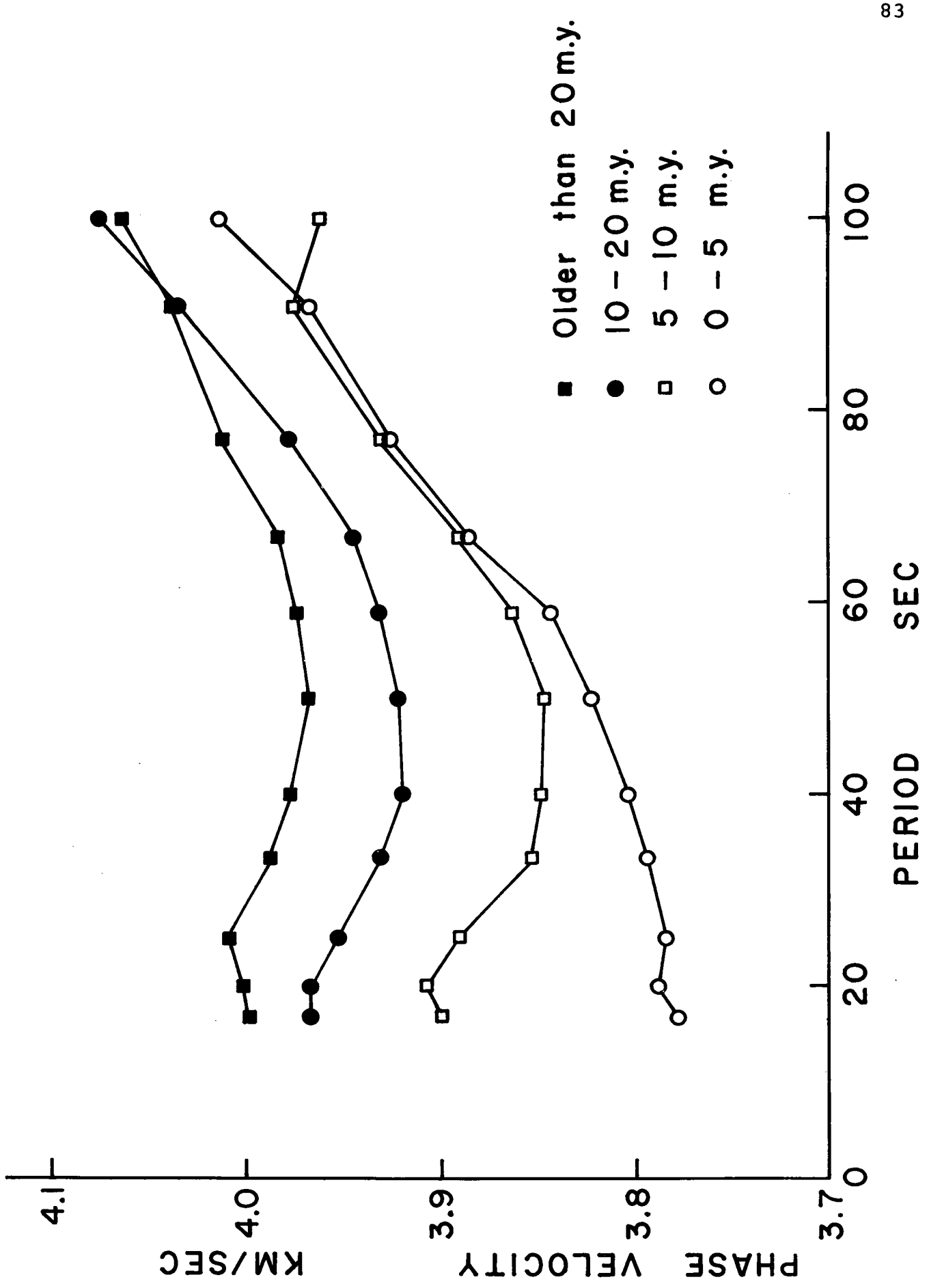
Older than 20 m.y.
10 – 20 m.y.
5 – 10 m.y.
0 – 5 m.y.
PHASE VELOCITY KM/SEC
4.1
4.0
3.9
3.8
3.7
0
20
40
60
80
100
PERIOD SEC

3.4 Pure-path method

Many measurements of phase and group velocity are presented for paths containing varying amounts of different tectonic provinces, such as continent, mid-ocean ridge, and ocean. In order to describe each region individually, we must deduce from this data the velocities which would describe the propagation of a wave which travels entirely within a single province (hence the name "pure-path" velocities). The technique applied in deriving the pure-path velocities is based on the fact that in an inhomogeneous, dispersive medium, the total phase shift due to propagation along the entire path is the sum of the phase shifts in each subpart of the path and the total group delay or group travel time is equal to the sum of the group delays within each subpart of the path (Knopoff, 1969). For convenience, I define an "effective travel time" for phase velocity by multiplying the total phase shift in circles by the period of the wave. The theoretical effective travel time T_j for a path$_j$ traveling across n provinces is

$$T_j(\omega) = \sum_{i=1}^{n} \frac{L_{ji}}{V_i(\omega)} \qquad (4)$$

where V_i is the pure path phase or group velocity of, and L_{ji} is the length of path within each zone i. The V_i are

determined by a least squares method, which minimizes the sum over the m paths of the squares of the differences between the actual travel time and the theoretical travel time. In practice,

$$\sum_{j=1}^{m}\left(\sum_{i=1}^{n}\frac{L_{ji}}{V_i(\omega)} - \frac{L_j}{V_{aj}(\omega)}\right)^2$$

is minimized with respect to the slownesses, $(1/V_i)$. L_j is the total length of each path, as given in Table 2, and V_{aj} is the average phase or group velocity for the path from Table 3 or 4. The uncertainty in each velocity is computed from the product of the diagonal elements of the covariance matrix of the variables and the experimental variance σ_ϵ^2 estimated from the error of fit. In this case,

$$\sigma_\epsilon^2 = |\epsilon|^2/(m-n) \qquad (5)$$

where $|\epsilon|^2$ is the sum of the squares of the errors.

In addition to regional changes in velocity, there may be an azimuthal variation due to the anisotropy of the medium. Smith and Dahlen (1973) have shown that the general form of the azimuthal dependence of the phase and group velocities of Rayleigh waves is

$$V(\omega,\theta) = A_1(\omega) + A_2(\omega)\cos 2\theta + A_3(\omega)\sin 2\theta + A_4(\omega)\cos 4\theta + A_5(\omega)\sin 4\theta \qquad (6)$$

where θ is the direction of propagation in a laterally homogeneous, slightly anisotropic medium. Because I simply do not have enough observations to consider variations as sensitive to azimuth as those implied by the 4θ terms, only the first three terms are retained. Smith and Dahlen point out that this may be justified for Rayleigh waves, because the 4θ terms are likely to be an order of magnitude smaller than the 2θ terms. Allowing for anisotropy, the theoretical travel time becomes

$$T_j(\omega) = \sum_i \frac{L_{ji}}{(c_i + a_i CS_{ji} + b_i SN_{ji})} \qquad (7)$$

where c_i, a_i, and b_i correspond to A_1, A_2, and A_3 respectively. On a sphere, the values of cos 2θ and sin 2θ with respect to any fixed coordinate system vary along the length of the great circle path. CS_{ji} and SN_{ji} are the average values of cos 2θ and sin 2θ along the portion of the path within each zone. Using (7) as the expression for the theoretical travel time leads to a non-linear least squares problem. However, for small anisotropy, $a_i << c_i$ and $b_i << c_i$. Therefore, to a first approximation,

$$T_j(\omega) = \sum_i \frac{L_{ji}}{c_i}\left\{ 1 - \left[\frac{a}{c}\right]_i CS_{ji} - \left[\frac{b}{c}\right]_i SN_{ji} \right\} \qquad (8)$$

which leads to an entirely linear problem in the slowness $1/c_i$ and the azimuthal components $(a/c^2)_i$ and $(b/c^2)_i$.

If the degree of anisotropy is assumed to be independent of region (the ratios a/c and b/c are constant), then further simplification results. Defining the terms

$$CS_{ji} = CS_j + \delta_i \ ,$$

where $$CS_j = \frac{1}{L_j} \sum_i CS_{ji} \ L_{ji} \ ,$$

and $$1/C_i = \frac{1}{V_{aj}} (1 + \Delta_i)$$

Then the cosine term with constant a/c is given by

$$-\sum_i \frac{L_{ji}}{c_i} \left(\frac{a}{c}\right)_i CS_{ji} = -\frac{a}{c} \sum_i \frac{L_{ji} CS_{ji}}{c_i} \qquad (9)$$

$$= -\frac{a}{c} \sum_i (CS_j + \delta_i) \left[\frac{L_{ji}}{V_{aj}} (1 + \Delta_i)\right]$$

Because a and Δ_i are small, any term containing the product of the two can be neglected. Then, since

$$\sum_i L_{ji} \equiv L_j \qquad \text{and} \qquad \sum_i \delta_i L_{ji} \equiv 0 \ ,$$

the cosine term is reduced to $-\frac{a}{c} \ L_j \ CS_j / V_{aj}$, where CS_j is the average value of cos 2θ over the entire length of the path. The same simplification applies to the sine term.

Assuming constant a/c and b/c, the theoretical travel time is

$$T_j = \sum_i \frac{L_{ji}}{c_i} - \frac{a}{c}\frac{L_j CS_j}{V_{aj}} - \frac{b}{c}\frac{L_j SN_j}{V_{aj}} \qquad (10)$$

The least squares problem is linear in the regional phase or group slownesses $1/c_i$ and in the fractional azimuthal terms a/c and b/c. The approximations made in this section are justified by the experimental results which indicate the maximum value of a/c or b/c is only 0.01 and the maximum variation in phase velocity is only about 5%.

3.5 Regional velocities and anisotropy

Regional variation and anisotropy are both statistically required to explain the observed single-station measurements. The pure-path method was applied to many models with different combinations of the regional and anisotropy terms described in the previous sections. Starting with an initial model which considered only two possible regions, one continental and one oceanic, additional parameters were introduced until the effective travel times observed over each of the individual paths could be adequately predicted by the theoretical regionalized model. At each step, an F-test was applied to evaluate whether the newly added variables significantly reduced the sum of the squares of the errors between the observed and theoretical travel times. The results for some of the models are summarized in Table 5 which evaluates the ability of the theoretical models to predict the observed phase velocity data at 40 sec.

Model 1, which implies the oceanic crust and mantle is uniform and that western South America is similar to western North America, is totally inadequate. It predicts the observed travel times with an RMS error of 15.1 sec., much greater than the 5 sec. which was expected from the analysis of possible random errors. Dividing the ocean into two zones of 0-10 m.y. age and older than 10 m.y. age and separating North America from South America significantly improves the fit (model 2).

Including only the possible sin 2θ and cos 2θ terms also improves the model (3), but not to the same degree as the regional terms. Using all four age divisions (0-5, 5-10, 10-20, and greater than 20 m.y.) leads to only a slight improvement over the model with only two age zones. However, if both anisotropy and variation with age are allowed, the improvement is significant at the 99% confidence level (models 6-10). The RMS error for a model with anisotropy and four age zones is only 4.8 sec., close to the value predicted from error analysis.

No statistical distinctions can be made between model 10 with 4 age zones, model 7 with 3 age zones (0-10, 10-20, greater than 20 m.y.) or model 8 with 3 zones based on the bathymetry (less than 3500 m, 3500-4000 m, greater than 4000 m). The velocities deduced for the three bathmyetric zones are quite similar to the velocities in the roughly corresponding three age zones, so no conclusion about the relative validity of the two techniques employed in measuring the age of the sea floor can be made form this study. Model 10 is somewhat better than model 6 (0-10, older than 10 m.y.), but the improvement is significant only at the 80% level, and this only when the improvement over the entire range of periods is considered. However, there is other justification for considering a model with more than two oceanic divisions. The phase and group velocities of Rayleigh waves are sensitive to the thickness of

the water layer. If the crust and mantle are identical in two regions with different water depths, the phase and group velocities will be lower in the region with deeper water. Although there is a general tendency toward increasing depth with increasing age of the sea-floor, the observed velocities also increase with age (see Table 7). This means that the difference between the regions has been underestimated due to the effect of the increased thickness of the water layer. An interesting point is that the F-test is a much more rigorous test than is generally applied to geophysical data. For example, figures 17 and 18 show the standard deviations of c_i for phase and group velocity, respectively, of an anisotropic model with 3 oceanic age zones and 2 continental divisions. The 10-20 m.y. and older than 20 m.y. curves appear to be well-separated, but if they were replaced by a single curve and if the values of the 0-10 m.y. curve, the two continental curves, and the anisotropy coefficients are all properly adjusted, the fit to the data is only slightly degraded. I prefer to use a double approach: the data strictly require two oceanic divisions and anisotropy, so I will base models of the upper mantle on the velocities from model 6 of Table 5. But, as outlined above, I also have a priori reasons to believe that a model with 4 oceanic regions may be physically meaningful, therefore I will also construct earth models based on the data from model 10.

Model 5 is a test for possible mislocation of the earthquakes

and is discussed in the section on systematic errors. An attempt was made with model 9 to measure regional changes in anisotropy. Unfortunately, when the anisotropy is allowed to vary separately within each zone, there are built in correlations between variables, leading to large individual variances. Because the propagation angle Θ varies only slowly along the length of the path, the average value of sin 2Θ or cos 2Θ is nearly the same within each region for any one path. A high value for the cosine term in one region can be balanced by a low value in another region to produce the same net effect. There is not a sufficient number of paths traveling at different angles within only a single province to provide good resolution. For example, at 50 sec. the values of $a/c \times 10^2$ for the three ocean regions are -1.37 ± 0.75, -0.89 ± 0.77, and -1.024 ± 0.46, in order of increasing age. No improvement in fit resulted (Table 5) and there is no significant difference between zones. In fact, at this period, only the oldest zone can individually be said to be anisotropic. For the remainder of this study, I assume the degree of anisotropy is uniform throughout the entire ocean.

The degree of anisotropy as a function of period is shown in figures 19 and 20. The values shown are for model 7, but the coefficients remain nearly the same when 2 or 4 age divisions are allowed, or when the regionalization is based on bathymetry. The anisotropy is frequency dependent, with the maximum anisotropy

occurring in the 50 to 90 sec. period range. In this range, a/c is roughly -.01 and b/c is approximately zero. This means that the direction of maximum velocity is parallel to the direction of spreading, and that a wave traveling perpendicular to the ridge will be about 2% faster than a wave traveling parallel to the ridge. In the 50 to 80 sec. range, the azimuth of maximum velocity is 91° $\pm$ 9° clockwise from the pole of rotation. Seismic refraction measurements of the anisotropy in compressional velocity at the M-discontinuity have found the direction of maximum velocity to be roughly in the direction of spreading. Values for Θ of 61° in the Atlantic (Keen and Tramontini, 1970), and 79°, 88° (Raitt et al., 1969), 100° (Morris et al., 1969), and 107° (Keen and Barrett, 1971) in the Pacific have been reported. These directions are expressed relative to the poles of rotation or strikes of fracture zones and therefore differ from the angles relative to north given in the original references. In addition, Raitt et al.(1971) and Bishop and Lewis (1973) show the maximum P-velocity is perpendicular to the ridge at several points within the area covered by this surface wave study. The agreement between the surface wave results and the seismic refraction experiments, and the alignment with the spreading direction, suggests that there may be a common origin for the two effects which is related to either the original formation of the lithosphere or to current

tectonic processes associated with plate motions. Because both the magnitude and direction of anisotropy at the M-discontinuity vary from location to location, the surface wave observations should be regarded as an average of the anisotropy over the entire area and over a considerable depth range and therefore may not be representative of the anisotropy at any one location.

Figure 21 shows the increase in phase velocity across the four age zones, approximately corrected for water depth. The observed changes are consistent with plate tectonic theory. The greatest change at short periods occurs within the first few million years after the sea floor is generated at the ridge axis, probably due to the rapid cooling of the upper part of the lithosphere. In the older age zones, the greatest change occurs at around 40 sec., for which the maximum sensitivity to the shear velocity structure occurs at about 50 to 60 km. (figure 1). This may be indicative of a continued cooling and gradual thickening of the lithosphere. At longer periods, the curves tend to converge, indicating that most of the changes occur within the upper 100 km. of mantle. Some difference, however, does persist to at least 125 sec. (table 6). Wu (1972) demonstrated that the ridge velocities are lower than standard ocean velocities by about 0.015-0.035 km/sec. in the 175 to 300 sec. range. This degree of separation could not be detected by this experiment due to long period noise, but it is consistent

with confinement of the changes in mantle structure to the upper 100 km.

The maximum of the pure-path group velocity increases with age, and the period at which the maximum occurs shifts to longer periods in the older sea floor (figure 18 and table 7), as described by Savage and White (1969). Although their survey may be slightly biased by a predominance of east-west paths, they find an average group velocity maximum in the Nazca plate of about 4.0 km/sec. at about 30 sec., which roughly agrees with my results. The average group velocity for 0-10 m.y. is similar to curve A of Santo and Sato (1966) which describes the characteristic group velocity of the crest of the East Pacific rise in the 20-35 sec. range. Curve A has a maximum velocity of about 3.85 km/sec at 25 sec. In both of these earlier studies of the regional variation of group velocity dispersion, it was suggested that the depth to the low velocity zone could be the source of the variations, but the investigators did not have observations over a broad enough period range to adequately test the hypothesis.

The azimuthal coefficients, the regional phase and group velocities, and the standard deviation of each coefficient are given in tables 6 and 7 for models 6 and 10 of table 5, with two and four oceanic age divisions, respectively. In a later section, these measured values will be used to obtain models

of the anisotropy and of the change is mantle structure with age. The Rayleigh wave dispersion observed in this study requires a significant change in the structure of the upper mantle as the age of the sea floor increases. In addition, the upper mantle must be anisotropic. In this section, I have attributed the features of the Rayleigh wave propagation to the structure of the mantle. In the next section, the possibility that any of these features could be due to systematic experimental errors is examined.

Table 5. Root-mean-square residual errors in regional models of Rayleigh wave propagation.

Model	Description	40 sec.	F-test*
1.	1 cont. 1 ocean	15.1+	99
2.	2 cont. 2 ocean	7.6	99
3.	1 cont. 1 ocean aniso.	9.3	99
4.	2 cont. 4 ocean	7.0	99
5.	2 cont. 3 ocean mislocation	7.1	99
6.	2 cont. 2 ocean aniso.	5.2	(80)
7.	2 cont. 3 ocean aniso.	4.9	
8.	2 cont. 3 ocean (bath.) aniso.	4.8	
9.	2 cont. 3 ocean aniso. different each zone	4.8	
10.	2 cont. 4 ocean aniso.	4.8	

* Relative to model 10

+ RMS error in phase velocity expressed in seconds.

TABLE 6. RAYLEIGH WAVE PURE-PATH VELOCITIES; TWO OCEANIC AGE ZONES AND ANISOTROPY

PERIOD	0-10 M.Y.		GT 10 M.Y.	
	PHASE VELOCITIES			
16.7	3.8133	±0.0211	3.9296	±0.0101
20.0	3.8197	0.0185	3.9577	0.0086
25.0	3.8080	0.0154	3.9647	0.0071
33.3	3.8051	0.0128	3.9485	0.0059
40.0	3.8104	0.0114	3.9398	0.0053
50.0	3.8246	0.0108	3.9370	0.0049
58.8	3.8448	0.0109	3.9455	0.0049
66.7	3.8832	0.0123	3.9571	0.0054
77.0	3.9241	0.0146	3.9873	0.0062
90.9	3.9695	0.0183	4.0275	0.0073
100.0	3.9995	0.0215	4.0591	0.0085
111.1	4.0496	0.0256	4.1019	0.0096
125.0	4.0983	0.0379	4.1638	0.0143
142.8	4.2870	0.0816	4.2424	0.0266
	GROUP VELOCITIES			
16.4	3.7974	±0.0577	3.7305	±0.0225
18.7	3.7468	0.0390	3.8625	0.0180
21.5	3.8110	0.0326	3.9106	0.0147
23.9	3.8042	0.0258	3.9495	0.0122
27.1	3.8126	0.0245	3.9743	0.0117
30.8	3.8061	0.0243	3.9873	0.0117
34.8	3.7882	0.0232	3.9813	0.0113
39.4	3.7686	0.0214	3.9597	0.0105
44.6	3.7452	0.0197	3.9298	0.0094
50.8	3.7134	0.0180	3.8971	0.0087
57.5	3.6798	0.0160	3.8528	0.0076
64.9	3.6571	0.0165	3.8130	0.0078
73.5	3.6369	0.0195	3.7808	0.0091
83.3	3.6286	0.0241	3.7542	0.0106
94.3	3.6280	0.0359	3.7183	0.0152
107.5	3.6756	0.0380	3.6643	0.0152
122.0	3.5908	0.0610	3.6507	0.0233
137.0	3.4771	0.0874	3.5968	0.0321

TABLE 6. CONT.

PERIOD	SOUTH AMER.		NORTH AMER.		A/C		B/C		RMS ERROR
	PHASE VELOCITIES								
16.7	3.4118	± 0.0674	3.3412	± 0.0522	-0.0069	± 0.0021	-0.0007	± 0.0019	7.9
20.0	3.4821	0.0486	3.3978	0.0480	-0.0054	0.0018	-0.0002	0.0017	7.7
25.0	3.5557	0.0439	3.5346	0.0450	-0.0073	0.0016	-0.0004	0.0015	7.0
33.3	3.7348	0.0402	3.6551	0.0400	-0.0088	0.0013	-0.0009	0.0012	5.8
40.0	3.8332	0.0374	3.7016	0.0362	-0.0098	0.0011	-0.0007	0.0011	5.2
50.0	3.9464	0.0374	3.7644	0.0353	-0.0102	0.0011	-0.0009	0.0010	4.9
58.8	3.9973	0.0383	3.8036	0.0357	-0.0098	0.0011	-0.0012	0.0011	4.8
66.7	4.0404	0.0433	3.7937	0.0394	-0.0094	0.0012	-0.0011	0.0012	5.3
77.0	4.0919	0.0487	3.8340	0.0462	-0.0102	0.0013	-0.0008	0.0013	5.7
90.9	4.1139	0.0568	3.9143	0.0589	-0.0095	0.0016	0.0010	0.0015	6.2
100.0	4.1043	0.0611	3.9333	0.0669	-0.0072	0.0021	0.0033	0.0017	6.4
111.1	4.1720	0.0648	3.8973	0.0717	-0.0043	0.0026	0.0036	0.0019	6.2
125.0	4.2037	0.1019	3.9805	0.1069	-0.0045	0.0040	0.0034	0.0030	8.4
142.8	4.3837	0.1728	3.7073	0.1829	-0.0021	0.0072	0.0004	0.0051	10.1
	GROUP VELOCITIES								
16.4	3.2230	± 0.1733	2.8457	± 0.0921	-0.0030	± 0.0046	0.0001	± 0.0043	17.7
18.7	3.0795	0.1034	2.9723	0.0813	-0.0001	0.0037	-0.0032	0.0035	16.2
21.5	3.0797	0.0673	2.9327	0.0645	0.0023	0.0030	-0.0030	0.0029	13.7
23.9	3.0808	0.0557	3.0740	0.0577	0.0005	0.0026	-0.0014	0.0025	11.8
27.1	3.1300	0.0543	3.1351	0.0567	0.0002	0.0025	-0.0010	0.0024	11.1
30.8	3.1806	0.0558	3.2360	0.0601	-0.0017	0.0025	-0.0011	0.0024	11.1
34.8	3.2561	0.0565	3.3375	0.0618	-0.0024	0.0024	-0.0017	0.0023	10.7
39.4	3.3425	0.0559	3.4250	0.0610	-0.0041	0.0022	-0.0021	0.0022	10.1
44.6	3.4557	0.0543	3.4902	0.0576	-0.0070	0.0020	-0.0026	0.0019	9.2
50.8	3.5544	0.0538	3.5392	0.0555	-0.0083	0.0019	-0.0019	0.0018	8.6
57.5	3.6946	0.0525	3.6175	0.0520	-0.0096	0.0017	-0.0027	0.0016	7.6
64.9	3.7226	0.0555	3.6490	0.0552	-0.0105	0.0017	-0.0024	0.0017	7.9
73.5	3.7485	0.0669	3.6713	0.0664	-0.0111	0.0020	-0.0029	0.0020	9.4
83.3	3.7612	0.0808	3.6614	0.0818	-0.0113	0.0024	-0.0026	0.0024	10.9
94.3	3.8209	0.1154	3.5674	0.1161	-0.0071	0.0037	-0.0025	0.0034	14.1
107.5	3.9100	0.1163	3.4876	0.1091	-0.0075	0.0042	-0.0036	0.0033	13.0
122.0	3.6485	0.1506	3.5481	0.1840	0.0005	0.0071	0.0037	0.0050	17.8
137.0	4.0287	0.2875	4.1943	0.4249	0.0047	0.0094	0.0018	0.0072	20.2

TABLE 7. RAYLEIGH WAVE PURE-PATH VELOCITIES;
FOUR OCEANIC AGE ZONES AND ANISOTROPY

PERIOD	0-5 M.Y.		5-10 M.Y.		10-20 M.Y.		GT. 20 M.Y.	
	PHASE VELOCITIES							
16.7	3.7712	± 0.0270	3.8882	± 0.0430	3.9404	± 0.0199	3.9229	± 0.0148
20.0	3.7885	0.0212	3.9032	0.0360	3.9484	0.0174	3.9596	0.0128
25.0	3.7840	0.0168	3.8865	0.0313	3.9385	0.0141	3.9798	0.0115
33.3	3.7945	0.0151	3.8522	0.0258	3.9209	0.0117	3.9667	0.0096
40.0	3.8039	0.0132	3.8483	0.0225	3.9111	0.0102	3.9595	0.0084
50.0	3.8228	0.0129	3.8468	0.0218	3.9145	0.0098	3.9529	0.0081
58.8	3.8436	0.0129	3.8625	0.0219	3.9247	0.0098	3.9604	0.0081
66.7	3.8854	0.0149	3.8909	0.0250	3.9387	0.0111	3.9707	0.0091
77.0	3.9256	0.0173	3.9301	0.0286	3.9715	0.0127	3.9988	0.0102
90.9	3.9671	0.0221	3.9755	0.0387	4.0296	0.0157	4.0251	0.0134
100.0	4.0127	0.0251	3.9610	0.0412	4.0699	0.0174	4.0536	0.0149
111.1	4.0722	0.0286	3.9993	0.0434	4.1204	0.0189	4.0895	0.0179
125.0	4.1313	0.0413	4.0442	0.0621	4.2052	0.0276	4.1316	0.0261
142.8	4.3382	0.0875	4.1741	0.1003	4.2420	0.0568	4.2546	0.0528
	GROUP VELOCITIES							
16.4	3.8280	± 0.0777	3.8305	± 0.1034	3.6613	± 0.0428	3.7789	± 0.0353
18.7	3.7628	0.0474	3.6946	0.0744	3.8815	0.0357	3.8498	0.0305
21.5	3.8295	0.0404	3.7521	0.0625	3.9358	0.0303	3.8936	0.0250
23.9	3.7742	0.0315	3.8753	0.0541	3.9517	0.0256	3.9438	0.0216
27.1	3.7693	0.0285	3.9250	0.0523	3.9628	0.0236	3.9776	0.0201
30.8	3.7627	0.0285	3.9222	0.0517	3.9711	0.0235	3.9939	0.0202
34.8	3.7560	0.0278	3.8850	0.0494	3.9508	0.0226	4.0011	0.0197
39.4	3.7531	0.0264	3.8278	0.0454	3.9231	0.0211	3.9868	0.0185
44.6	3.7290	0.0230	3.8105	0.0399	3.8857	0.0184	3.9630	0.0162
50.8	3.6940	0.0200	3.7935	0.0349	3.8416	0.0159	3.9393	0.0142
57.5	3.6689	0.0181	3.7235	0.0315	3.8120	0.0146	3.8846	0.0129
64.9	3.6506	0.0195	3.6905	0.0331	3.7778	0.0153	3.8406	0.0135
73.5	3.6436	0.0230	3.6369	0.0388	3.7473	0.0182	3.8089	0.0161
83.3	3.6257	0.0287	3.6462	0.0476	3.7263	0.0219	3.7764	0.0192
94.3	3.6130	0.0417	3.6729	0.0750	3.6747	0.0300	3.7555	0.0290
107.5	3.6438	0.0417	3.7533	0.0750	3.6269	0.0295	3.6930	0.0289
122.0	3.5844	0.0697	3.5685	0.1080	3.6182	0.0458	3.6840	0.0455
137.0	3.4762	0.0950	3.4931	0.1326	3.6587	0.0708	3.5396	0.0622

TABLE 7. CONT.

PERIOD	SOUTH AMER.		NORTH AMER.		A/C		B/C		RMS ERROR
	PHASE VELOCITIES								
16.7	3.4048	± 0.0671	3.3094	± 0.0524	-0.0058	± 0.0021	-0.0015	± 0.0020	7.5
20.0	3.4754	0.0473	3.3906	0.0477	-0.0046	0.0017	-0.0002	0.0017	7.2
25.0	3.5334	0.0424	3.5429	0.0442	-0.0063	0.0015	0.0003	0.0015	6.5
33.3	3.7082	0.0391	3.6719	0.0398	-0.0080	0.0013	0.0001	0.0013	5.5
40.0	3.8036	0.0359	3.7222	0.0355	-0.0090	0.0011	0.0003	0.0011	4.8
50.0	3.9217	0.0369	3.7827	0.0355	-0.0097	0.0011	-0.0000	0.0011	4.6
58.8	3.9747	0.0379	3.8230	0.0365	-0.0094	0.0011	-0.0004	0.0011	4.6
66.7	4.0201	0.0437	3.8124	0.0409	-0.0090	0.0012	-0.0003	0.0012	5.1
77.0	4.0753	0.0497	3.8508	0.0485	-0.0099	0.0014	-0.0002	0.0014	5.6
90.9	4.1169	0.0603	3.9100	0.0626	-0.0095	0.0017	0.0009	0.0016	6.2
100.0	4.1129	0.0648	3.9270	0.0696	-0.0077	0.0022	0.0030	0.0018	6.3
111.1	4.1910	0.0687	3.8830	0.0742	-0.0056	0.0027	0.0031	0.0019	6.0
125.0	4.2677	0.1117	3.9455	0.1059	-0.0079	0.0043	0.0018	0.0030	7.8
142.8	4.3641	0.1799	3.6788	0.1761	-0.0014	0.0088	0.0004	0.0050	9.3
	GROUP VELOCITIES								
16.4	3.1743	± 0.1684	2.8647	± 0.0931	-0.0015	± 0.0047	0.0041	± 0.0047	17.0
18.7	3.0990	0.1105	2.9693	0.0841	-0.0010	0.0039	-0.0037	0.0037	16.1
21.5	3.0961	0.0706	2.9255	0.0662	0.0013	0.0031	-0.0037	0.0031	13.5
23.9	3.0829	0.0577	3.0620	0.0590	0.0010	0.0027	-0.0018	0.0026	11.5
27.1	3.1229	0.0543	3.1262	0.0563	0.0014	0.0025	-0.0012	0.0025	10.6
30.8	3.1701	0.0555	3.2292	0.0596	-0.0005	0.0025	-0.0011	0.0024	10.5
34.8	3.2339	0.0562	3.3449	0.0622	-0.0010	0.0024	-0.0011	0.0023	10.2
39.4	3.3137	0.0559	3.4449	0.0624	-0.0029	0.0023	-0.0010	0.0022	9.7
44.6	3.4179	0.0527	3.5168	0.0576	-0.0056	0.0020	-0.0013	0.0019	8.6
50.8	3.5034	0.0488	3.5749	0.0525	-0.0065	0.0018	-0.0002	0.0017	7.6
57.5	3.6545	0.0498	3.6515	0.0517	-0.0084	0.0016	-0.0014	0.0016	7.0
64.9	3.6866	0.0543	3.6807	0.0563	-0.0095	0.0017	-0.0013	0.0017	7.5
73.5	3.7132	0.0666	3.7108	0.0692	-0.0104	0.0021	-0.0016	0.0021	9.1
83.3	3.7315	0.0822	3.6915	0.0868	-0.0105	0.0025	-0.0017	0.0025	10.7
94.3	3.7697	0.1162	3.6163	0.1236	-0.0054	0.0038	-0.0015	0.0034	13.7
107.5	3.8637	0.1188	3.5189	0.1138	-0.0050	0.0045	-0.0024	0.0034	12.4
122.0	3.5995	0.1606	3.5963	0.2020	0.0032	0.0080	0.0049	0.0053	17.6
137.0	4.1309	0.3280	4.1559	0.4293	-0.0105	0.0111	0.0003	0.0076	19.6

3.6 Possible systematic errors

Mislocation. Mislocation of the epicenter of the source events is potentially the greatest source of error. Mislocation by 20 km in the direction of a station will produce an error of about 5 sec. in the effective travel time (assuming phase or group velocity is roughly 4 km/sec). If the direction of mislocation is perpendicular to the propagation path, no significant error will be introduced. In addition to introducing scatter into the data, the systematic mislocation of several events can create serious bias in the interpretation of the observed velocities. For example, if the events are systematically located northwest of their actual positions, velocities observed over paths from west to east will appear to be anomalously fast, while the velocities to stations north of the events will appear to be anomalously slow, thus producing an azimuthal effect which can simulate anisotropy. In order to estimate the magnitude of the possible random and systematic errors due to mislocation, I have examined the earthquake swarm associated a caldera collapse in the Galapagos Islands, measured the phase velocity between two seismic stations, and examined the possibility of producing the observed anisotropy by a systematic mislocation error.

In June, 1968 the floor of the volcano in Isla Fernandina in the Galapagos Islands collapsed, generating a swarm of hundreds of earthquakes of magnitude 4.0 or greater (Simkin and Howard, 1970). Since the waveforms from all the events observed

at WWSSN stations are nearly identical and there was a regular time interval between events, (Simkin and Howard, 1970) it is probable that all the earthquakes occurred at the same spot. Assuming that the location of the events was the caldera, one can obtain an estimate of the epicentral location capability in this area. Figure 22 shows the location of the 15 largest events as determined by the USCGS. The average location is roughly 13.5 km northeast of the caldera with an RMS scatter of 23.1 km around the average position. The average magnitude of these events (5.1 m_b) is significantly smaller than the average size of the events used in this study, so it is reasonable to assume that the random component of mislocation in this study is roughly 20 km. The systematic bias indicated by the Galapagos swarm is only 0.3% of the average path length and too small to produce the observed anisotropy.

Two of the paths listed in Table 2, GI-PEL and GI-ANT, are two-station measurements for which no mislocation is possible. Using two shallow events off the coast of Mexico as sources, the phase and group velocities between the station on the Galapagos (GIE) and two South American stations (PEL and ANT) were measured. The results agree very well with the regional velocity predicted from all the data plus the slowness indicated by the anisotropic term for paths nearly perpendicular to the direction of spreading. In particular, there is very good agreement between GI-PEL and the single

station velocities measured over the similar path 1-PEL (Tables 3 and 4).

The final experiment on mislocation is a test of the possibility that the observed anisotropy is merely an artifact of the measurement technique, produced by a systematic mislocation of the sources. In this paragraph, systematic mislocation means that all the events are mislocated in the same direction and to the same degree. The effect of mislocation on velocity is nearly independent of period, inversely proportional to the path length (the time error will be independent of length), and approximately the same for both the phase and group velocity of Love and Rayleigh waves. The effect of anisotropy is independent of path length (the time error will be proportional to length), and, in general, frequency dependent and different for Love and Rayleigh waves. The observed effect does appear to be frequency dependent and different for Love and Rayleigh waves, but there is a more rigorous test available. If the mislocation is small compared to path length and if the velocity in the source region and the average velocity V_a over the entire path are approximately equal, then the time error ΔT introduced by mislocation is

$$\Delta T = \frac{a \cos\theta}{V_a} + \frac{b \sin\theta}{V_a} \qquad (11)$$

where Θ is the azimuth of the path from the event to the station, measured clockwise from north at the source. a is the amount of mislocation north and b is the amount of mislocation east. By considering simultaneously all the effective travel times, the optimum values of a and b can be determined for the region; i.e., we ask, what values of a and b minimize the errors in the data in the least squares sense. We then compare the fit to the data of a model with anisotropic terms with the fit of a model with mislocation terms of the form of (11). In the mislocation model, the theoretical travel times T_j for each path are given by

$$T_j = \sum_i \frac{L_{ji}}{c_i} + \frac{a \cos\theta_j}{V_{aj}} + \frac{b \sin\theta_j}{V_{aj}} \qquad (12)$$

This is a completely linear problem in the unknowns, a, b, and the slownesses in each region $1/c_i$. The least squares problem was performed independently for each period using the observed Rayleigh wave phase velocities. The results are somewhat frequency dependent, but the mislocation given is in the southeast quadrant in every case. On the average, the data indicate that the events are located 4.3 ± 4.2 km too far south and 5.2 ± 5.5 km too far east. This mislocation is not significant. The fit to the data at 40 secs of a model with three oceanic and two continental divisions, plus the mislocation terms, is given in Table 5. The same regional

model with anisotropy included, is a significantly better fit to the data at the 99% confidence level.

Based on the experiments described above, I conclude there is no significant bias in the data due to the systematic mislocation of the source events. Mislocation will introduce some scatter in the data. The RMS time error is expected to be roughly equal to (20 km)/($\sqrt{2}$ x 4 km/sec) or 3.5 sec ($\sqrt{2}$ enters the expression because of the azimuthal variation of error).

Figure 22. Reported epicenters associated with a caldera collapse in the Galapagos Islands. Cross-hatched area indicates location of caldera. Crosses are individual epicenters and the triangle is the average location.

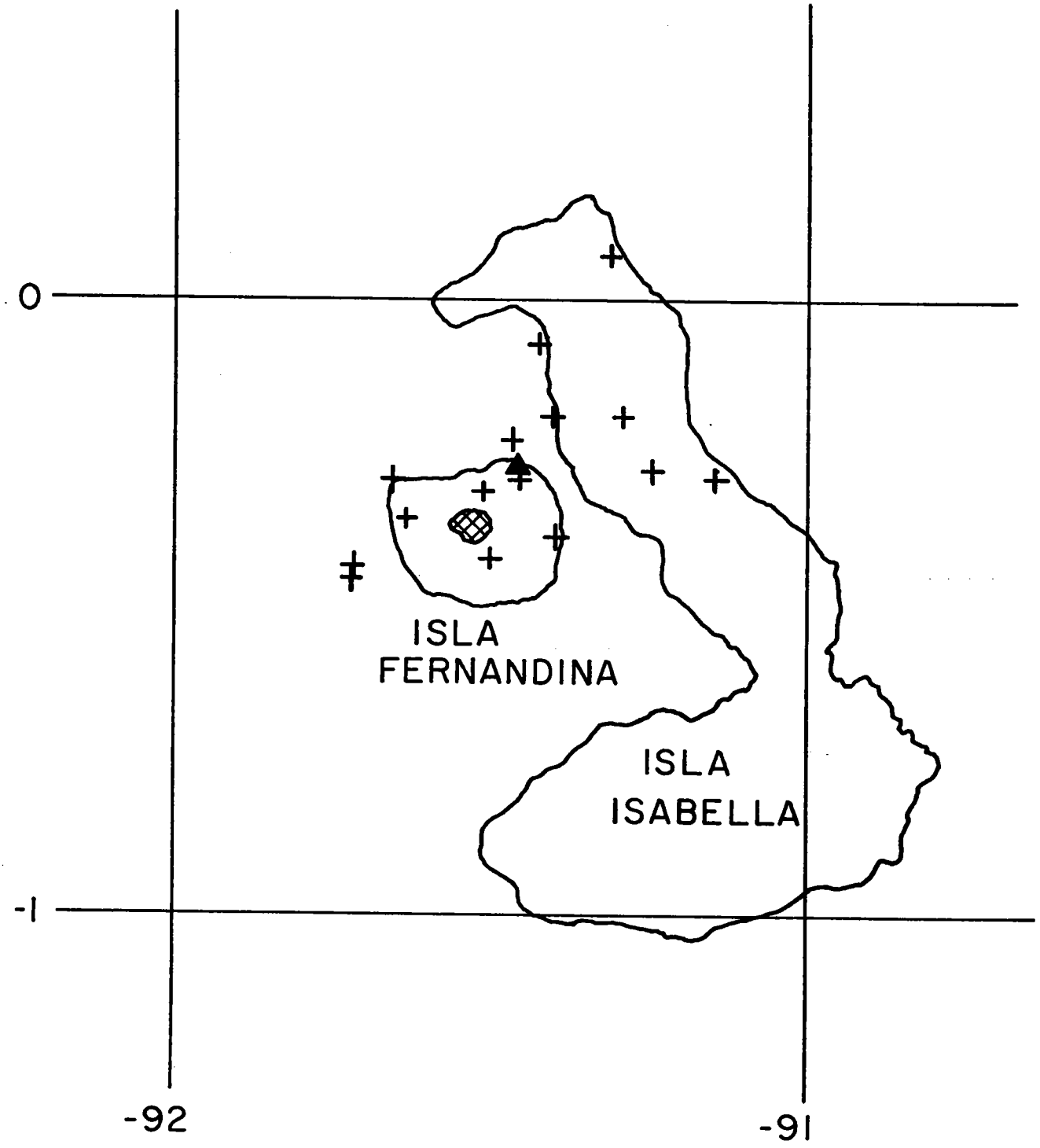
0
-1
-92
-91
ISLA
FERNANDINA
ISLA
ISABELLA

Origin time and finiteness. Errors in the assigned origin time of the source events may lead both to increased scatter in the data and to a systematic shift in the regional velocities. Some degree of uncertainty in the origin time is due to scatter in the reported P-arrival times used to locate the event. For the events used in this study, USCGS reports standard deviations in the origin time ranging from 0.6 to 1.6 sec. Although the average reported standard deviation is 1.1 sec., I assign an RMS uncertainty of 1.5 sec. to this parameter. The origin times listed in Table 1 and the standard deviations quoted are for hypocenter determinations in which the depth is constrained at 33 km. The actual depth as deduced from the radiation patterns is about 8 km including the water layer. The actual origin time should be the reported origin time minus whatever time it takes for compressional waves to travel from the focus to the 33 km deep reference level. For these events, the true origin time should be about 3.0 sec earlier than the reported time (the origin time of events computed for depths other than 33 km have been corrected to this reference level in Table 1). In addition, a regional delay of up to 1.5 sec may be possible due to anomalously low compressional velocities in the upper mantle beneath a mid-ocean ridge (Forsyth and Press, 1971; Long and Mitchell, 1970). The favored estimate of a 3.5 to 4.0 sec correction in origin time would lower the reported phase velocities. However, this correction has

not been made, because the shift toward earlier origin times is balanced by the effects of the finite fault length and finite rise time of the source.

The phase delay ϕ_d caused by the finite length b of a vertical strike slip source is

$$\phi_d = \frac{\omega b}{2V} - \frac{\omega b}{2c} \cos \phi \qquad (13)$$

where ϕ is the angle counter clockwise from the strike of the fault in the direction of rupture to the observation point, V is the rupture velocity and c the phase velocity of the medium (Ben-Menahem, 1961). The first term is of the form of a time delay; it is independent of propagation direction and, when converted into equivalent seconds of error, is independent of frequency. The contribution of the second term summed over all propagation directions is zero. It should appear to be a source of random scatter when a number of events and propagation directions are considered. If, by chance, most of the rupture directions are similar, the angular term would no longer be random because most of the stations are to the north or east of the events rather than uniformly distributed in azimuth. However, if this is the case, ϕ is then measured from approximately the same direction for each event and the angular term takes the form of a mislocation in the direction of rupture. Any such systematic

effect would show up in the numerical test for systematic mislocation. If the horizontal extent (perpendicular to the slip vector) of a dip-slip event is much greater than the vertical extent, only the directional component will be important. With a stress drop of 10 bars and the average seismic moment of the events in this study, an earthquake could be expected to have a characteristic fault length of about 20 km (Hanks and Thatcher, 1972). Assuming a rupture velocity of 3 km/sec (Kanamori, 1970) yields a time delay of about 3 sec. In addition, an error is introduced by assuming the source-time function is a step function. Although few studies of this parameter have been made, the existing evidence suggests the additional delay will be less than 1 sec (Tsai and Aki, 1970). Thus, to a first approximation, the error introduced by computing the origin time based on a 33 km reference depth will be canceled by the effects of finiteness. The RMS scatter introduced by the second finiteness term is approximately $20 \text{ km}/(2\sqrt{2} \times 4 \text{ km/sec}) = 1.75$ sec.

If the earthquakes are characterized by a very low stress drop, the characteristic size could be on the order of 50 km. If, in addition, the rupture velocity is as low as 2.2 km/sec (Eaton, 1967) a substantial error is possible. I have explored this possibility in a numerical experiment by examining the Rayleigh wave phase velocities for a systematic source-time

effect. If there is a systematic source-time error t, common to all the source events, due to finiteness or any other cause, the effective travel times T_j will best be described by

$$T_j = t + \sum_i \frac{L_{ji}}{c_i} - \frac{a}{c} \frac{L_j CS_j}{V_{aj}} - \frac{b}{c} \frac{L_j SN_j}{V_{aj}} \qquad (14)$$

for each frequency, where the regional and anisotropic terms are defined as before and c is the phase velocity. A simultaneous least squares solution for c_i, a/c, b/c, and t in the 20-100 second range yielded t = 1.0 ± 1.7 sec. A positive t means the effective origin time is earlier than the assumed origin time. This experimental value of t agrees with the conclusions of Weidner and Aki (1973), who found that the net timing error did not exceed 2 sec for a pair of mid-Atlantic ridge events. I conclude that the assumption of a 20 km fault length is reasonable, and that the net effect of finiteness and origin time error is negligibly small.

Non-horizontally layered media. In the vicinity of a transition zone between two different horizontally layered media, the apparent phase velocity of a surface wave travelling in one direction may be different from the apparent velocity over the same path in the opposite direction. This effect has been measured experimentally (Abe and Suzuki, 1970) and reported for a reversed profile in Western Canada (Wickens and Pec, 1968). At the boundary between two different structures some of the incident fundamental mode energy will be reflected, converted to higher modes, and reflected as body wave energy (McGarr and Alsop, 1967; Mal and Knopoff, 1965). Although the velocity of the fundamental mode itself is independent of propagation direction (Drake, 1972a), the interference of the reflected and converted waves will be directionally dependent, leading to apparent anisotropy in the measured phase velocities. No simple correction to the data can be made for this effect, because not even the sign of the phase shift can be predicted without precise knowledge of the geometry of the interface (Knopoff and Mal, 1967). In addition, all the theoretical model studies to date have examined only propagation perpendicular to the strike of the boundary. However, phase shifts due to non-horizontal layering are not likely to introduce significant error into this study.

There should be very little interference for waves

travelling down-dip (Knopoff and Mal, 1967; Boore, 1970; and Drake, 1972a). For the paths used in this study, propagation is predominantly down-dip. From a ridge event to the ocean basin, the water depth and the depth to the low velocity zone increase; both are down-dip geometries. From ocean basin to continent is up-dip for water depth but down-dip for the thickening of the crust. In a numerical study of the ocean basin to continent transition, Drake (1972b) demonstrated that 96% of the incident fundamental mode Rayleigh wave energy was transmitted as the fundamental mode; thus interference should be insignificant. Conversions of fundamental mode Love wave energy is much greater (Lysmer and Drake, 1971), yet Boore estimated the maximum apparent group delay for Love waves across the continent to ocean transition to be only 2 seconds, with a maximum phase shift corresponding to an error of one second. In the future, it may be possible to detect the effect of the shape of the low velocity zone under the ridge by measuring phase velocities over paths from events along the west coast of South America to stations on the East Pacific Rise, and comparing the results with similar paths reported in this study. But, unless the experiment proves otherwise, I believe the effect of non-horizontally layered media can be safely neglected.

Horizontal refraction. When there are lateral variations in structure, surface waves will follow a path determined by Snell's law for the phase velocities (Bullen, 1953). Horizontal refraction in an inhomogeneous medium can cause multiple arrivals of energy (Capon, 1970, 1971), beating (Pilant and Knopoff, 1964), unusual amplitude variations (McGarr, 1969), and systematic errors in the determination of phase velocities. The primary interest here is in velocity errors, but the other effects must also be considered in selecting and processing the data. In computing phase and group velocities, it is nearly always assumed, as in this paper, that the wave travels a great circle (least distance) path. This assumption is strictly correct only when the medium is laterally homogeneous or if the great circle path is normal to all boundaries between inhomogeneities. However, the difference in travel time between a least distance path and a least time path is a second-order effect and can often be neglected. The refracted path is longer, but a greater proportion is within the high velocity region, so that the net effect is a slight decrease in travel time. Whenever the error is significant, the great circle path assumption will lead to an over-estimate of the velocity of the low-velocity region and an underestimate of the velocity contrast between the two regions. I have performed a number of simple model studies, some of which are presented in Appendix 3, in order to illustrate the errors that may be encountered in the study of the low

velocity region associated with a mid-ocean ridge.

If the phase velocity increases gradually with distance from the axis of the low velocity region and if the distance over which this change occurs is on the order of the length of the path, then the deviation from a great circle path can be completely neglected. A low velocity region which is very narrow compared to the typical path length will be masked by refraction. The correct velocity may still be deduced by using paths which cross the zone at high angles, but this would require extremely accurate measurements because only a small proportion of the path would be within the narrow zone. The results in Table 7 indicate a gradual 5.2% increase in phase velocity across the entire ocean region covered in this study (maximum at 25 sec.), with a fairly rapid change of about 3% within the first 5 million years (maximum at 20 secs.). The average velocity calculated for the 0-5 m.y. zone may possibly be as much as 0.5% too fast (at 20 sec.), but there should be no significant bias due to refraction in the velocities deduced for the other regions. If there is a narrow, very low velocity region centered at the ridge axis, this experiment will not detect it. In the North Atlantic, at sea-floor spreading rates of 1.0 to 1.5 cm/yr, the half-width of the 0-5 m.y. zone is only 50 to 75 km. The masking effects of refraction associated with such a narrow zone may account for the results of surface wave studies in that ocean, which report either no anomalously low

velocities associated with the Mid-Atlantic ridge (Tarr, 1969; Ossing, 1964) or velocities significantly higher than those found in this study (Weidner, 1972; Taylor, 1972).

Multiple arrivals of refracted surface wave energy are another possible source of error. Pilant and Knopoff (1964) showed that the simultaneous arrival of wave trains that have traveled slightly different paths can cause interference resulting in amplitude modulation or "beating". In less severe cases, this amplitude modulation will appear to be a focusing or defocusing phenomena (McGarr, 1969). There are pronounced minima in the amplitude spectra of records showing beating and often there are phase shifts associated with these minima. Most of the observed cases of beating in this study occurred at periods of less than 20 sec. and are thought to be due to refraction at continental margins. Interference at periods greater than about 25 seconds was generally found only for azimuths close to nodes in the radiation pattern, where the energy content of the primary signal is low. Due to the rapid phase shifts near nodes, two arrivals traveling slightly different paths may be out of phase, even though they would be in phase under ordinary circumstances. Two exceptions to this general rule were observed. There are two clearly separated arrivals of Rayleigh waves observed at Albuquerque (ALQ) for the paths along the East Pacific Rise from events 8 and 9. The second arrival at an apparent velocity of 3.4 km/sec can be seen in the energy versus time plot (figure 8)

of the Oct. 12, 1964 record shown in figure 11. The amplitude and phase spectra, figures 9 and 10, show decreasing interference up to nearly 50 second period. Because the interference in this case is due to a clearly separated arrival of energy, it can be eliminated by time-variable filtering. The December 29, 1966 record is nearly identical. These are the only two records used which showed any significant late arrival of energy, and were the only two records which were time-variable filtered. It is not known whether the late arrivals are due to energy trapped by the wave-guide effect of the low velocity zone of the East Pacific Rise, or due to refraction at some point along continental margin.

Capon (1970) demonstrated through a detailed study of the multiple path propagation of Rayleigh waves at LASA that most of the late arrivals of energy could be attributed to refraction at the continental margins. Three events (21, 23 and 24 in his Table 2) on the East Pacific Rise were examined. Very little azimuthal deviation of the first arrivals was observed and no second arrivals at periods greater than 25 records were observed, suggesting that the effects of refraction may largely be ignored for the paths to North America considered in this study. In addition, the possibility of errors due to refraction at the continental margin is reduced by choosing primarily paths which cross the continental margins at high angles, and using only those portions of the records which show no significant beating.

The neglect of lateral refraction cannot be the source of the apparent anisotropy found in this paper. Waves traveling along the ridge, taking the least time path, will always arrive at the station somewhat sooner than they would if a great circle path was followed. This error will tend to make velocities perpendicular to the ridge appear too slow rather than fast as is observed. If the medium is anisotropic and laterally homogeneous, energy will propagate in a straight line (Lighthill, 1964), hence the presence of anisotropy does not affect the propagation path.

4. Love wave data

Love wave phase velocities should provide information which can not be obtained from Rayleigh wave measurements alone. In addition to the different averaging of the shear velocity structure (figure 1), Love waves sample SH velocity rather than the SV sampled by Rayleigh waves. In an anisotropic medium, SH velocity will not generally be the same as SV and consequently the observed Love wave velocities may appear to be inconsistent with the observed Rayleigh wave velocities. Aki and Kaminuma (1963) and McEvilly (1964) found apparently high Love wave phase velocities in Japan and central United States which could not be explained by any simple, isotropic model also consistent with the Rayleigh wave velocities. McEvilly (1964) and Kaminuma (1966) showed that the observations could be explained by a model in which SH velocity is 6-10% faster than SV. Aki (1968) suggested that thin, soft layers or pockets of magma under Japan produce the apparent difference between SH and SV. His laminated model is equivalent to a transversely isotropic medium with a vertical symmetry axis. However, Thatcher and Brune (1969) have proposed that the anomalous Love wave observations are the result of higher mode interference. This explanation is now widely accepted and has been experimentally confirmed by James (1971) for one two-station path in South America. The use of Love waves with periods less than 100 sec. has been largely abandoned due to the difficulty of dealing with the higher mode contamination. In this section, I present a general method that can be used to

measure the phase velocity of the fundamental and the higher modes even when the degree of contamination is severe. Secondly, I show that, to first order, the contamination of the fundamental mode Love wave by the first higher mode can be neglected when the source is located on a mid-ocean ridge and the path is a few thousand kilometers long.

4.1 Method. In oceanic areas, the group velocities of the fundamental and the first and second higher Love modes nearly overlap in a broad frequency range (Thatcher and Brune, 1969; Boore, 1969). As a result, the Love wave observed for a predominately oceanic path is actually a composite of several signals which arrive simultaneously. There is no way to separate these signals for any single record. However, it is possible to determine the regional average of the phase velocity of each component signal if measurements are made over many paths of varying lengths with earthquake sources of known focal mechanism. The phase velocity of each of the modes is different, so the way in which the signals interfere will vary with length of the path. If two modes are in phase at one point along a great circle path, they will be out of phase at some later point along the same path. This fact forms the basis of the method. The phase of the total signal at station j due to the superposition of k signals of frequency ω is given by

$$\phi_j(\omega) = \tan^{-1} \left\{ \sum_{\ell=1}^{k} \lambda_{\ell j} \sin\beta_{\ell j} \Big/ \sum_{\ell=1}^{k} \lambda_{\ell j} \cos\beta_{\ell j} \right\} \qquad (15)$$

where $\lambda_{\ell j}$ is the frequency-dependent amplitude of each signal and $\beta_{\ell j}$ is the frequency-dependent phase of each signal. In practice, the amplitude λ_{oj} of the fundamental mode is normalized to 1.0 and the $\lambda_{\ell j}$ give the relative excitation of the other modes. By analogy with the Rayleigh wave case, the theoretical phase shift of the fundamental mode is given by

$$\beta_{oj}(\omega) = \omega \left\{ \sum_i \frac{L_{ji}}{c_{oi}} - \frac{a}{c} \frac{L_j CS_j}{V_{aj}} - \frac{b}{c} \frac{L_j SN_j}{V_{aj}} \right\} + \phi_f(\omega) \qquad (16)$$

where the terms are defined as in (1) and (10). A similar relation applies to each of the other modes. The regional phase velocities are determined by minimizing the sum of the squares of the differences between the observed phase and the theoretical phase ϕ_j with respect to the slownesses $1/C_{\ell i}$ in each region. The observed phase ϕ_{ob} here is redefined to include corrections for origin time and instrument response, and is given in terms of the variables defined in (1) and (2),

$$\phi_{ob}(\omega) = \phi_{obs}(\omega) + \omega t_1 - \phi_{inst}(\omega) \qquad (17)$$

If only one mode is present, this method is exactly equivalent to the least squares method used to determine the pure-path Rayleigh wave velocities. If a second mode is added

which is significantly smaller in amplitude than the first, it will cause only a perturbation in the phase of the original signal. The degree of perturbation will depend on the relative amplitude of the signals, the distance to the station, and the phase velocity contrast between the two modes. Figure 23 illustrates the effect a higher mode signal with half the amplitude of the fundamental mode would have on the phase of the original signal. The maximum phase shift is only 1/12 circle. At 40 sec., neglecting the higher mode leads to a maximum error of only 3.33 sec. in the phase of the fundamental mode. Over many paths of sufficiently different lengths, the average error will be zero and the RMS error less than 2.4 sec., or about 0.01 km/sec for the average path length in this study. Thus, if the relative amplitude of the higher mode is 0.5 or less, to first order it can be neglected when considering only the velocity of the fundamental mode at periods less than about 100 sec.

In the complete least squares problem, λ_{ij} should include variable terms for the relative attenuation of the modes along the path and for the relative amplification at the ocean-continent transition. Anisotropy should be allowed to be different in each zone and for each mode. Thus for 2 modes and 3 regions, a complete description would require 20 variables. This is highly impractical because the amount of data and the computing time required to solve the problem are prohibitive.

Equation (15) is non-linear, resulting in local minima in the least squares problem. In order to find the absolute minimum, a grid of possible values of the parameters must be searched. If there are m observations, n possible values of each parameter, parameter, and k parameters, expression (15) must be evaluated mn^k times in a grid search. Even if a quasi-linear approximation scheme is employed, the full problem is impractical. In this study, it is found that a model with only two oceanic and two continental regions for the fundamental mode, anisotropy of the fundamental mode, and one average velocity for the first higher mode provides an adequate description of the data.

4.2 Higher mode excitation. The excitation of the higher modes relative to the fundamental mode for very shallow sources depends primarily on the structure of the medium and the frequency of the wave. The source geometry and azimuth are unimportant for the shallow sources used in this study. Using the equations given in Appendix 1 for the excitation of Love waves in a spherical earth, I have computed the relative excitation of the first and second higher modes for earth models which fit the Rayleigh wave pure-path velocities in each age zone. The results are shown in figure 24. For an earthquake occurring on the ridge (0-10 m.y. age zone), the excitation of the first higher mode is less than half the excitation of the fundamental mode at periods greater than about 35 sec. In older areas of the sea floor, the excitation of the higher modes is greater, as indicated by the curve for the 10-50 m.y. zone (average age about 22 m.y.). Not shown here are the results for the Harkrider and Anderson (1966) oceanic model, which represents the structure in an average ocean basin older than the area considered in this study. Their model gives a relative excitation greater than 1.0 for periods less than about 60 sec. Thus, as the age of the sea floor increases, the excitation of the higher modes become more important. All the sources used in this study are within the 0-10 m.y. zone except events 15 and 17, which are in 10-15 m.y. crust. Consequently, the higher modes will contribute to the noise, but neglecting their

contribution to the signal should not seriously bias the measurement of the phase velocity of the fundamental mode at periods greater than 35 seconds.

The relative amplitudes can be altered by the transmission characteristics of the path between source and receiver: factors which are not well-known and difficult to predict. It is important, then, to confirm the predicted amplitudes by actual observations. This is accomplished using a technique similar to one originally suggested by Thatcher and Brune (1969). In normal oceanic areas, the group velocities of the fundamental and first higher modes are similar, creating the problem of simultaneously arriving signals. But for a continental structure, the group velocities are similar only at periods greater than 60 sec. At shorter periods, the fundamental mode energy travels much more slowly, so that the two signals will separate. By choosing a path which starts on a mid-ocean ridge and later crosses a substantial length of continent, it should be possible to observe separate signals from the first and fundamental modes, whose amplitudes can then be compared. For example, figure 25, shows the transverse (east-west) component of motion observed at four stations in North America generated by event 10 on the Chile fracture zone. The seismogram from station TUC shows a wave-form which has dispersed very little, typical of predominately oceanic paths (see figure 26). Stations ALQ, GOL, and RCD show

progressively greater dispersion of the fundamental mode as the length of the continental portion of the path increases. The higher mode remains relatively undispersed and gradually separates from the fundamental mode. From the computation of the group velocities for the ridge model, some separation is also expected for paths travelling along the ridge axis.

Figure 25 demonstrates the chief problem with this approach. Multiply-reflected S waves can be quite large and may be mistakenly identified as higher modes (Richter, 1956). Even when a higher mode is correctly identified, it may be contaminated by one of the multiply-reflected body waves. In the case shown here, SSSS is a likely contaminant. The arrivals I have identified as higher modes typically have greater amplitudes than the earlier arrivals of S, SS, or SSS; often are polarized differently than the S phases; show the expected rate of separation from the fundamental mode; have the expected shape of the relative amplitude-versus-period curve; and show the expected increase in amplitude of the higher mode for a source located off the ridge system. Figure 27 compares the seismograms from 2 stations nearly the same distance away from the intra-plate event 15. The path to BKS is almost entirely oceanic and the Love wave is clean and only slightly dispersed. The first higher mode at DUG arrives at nearly the same time as the Love wave at BKS (the delay is appropriate for the 100 km greater epicentral distance) followed by the fundamental mode, which is dispersed due to the continental

portion of the path. The north-south and vertical components of motion show no SV arrival at the time of the higher mode, even though SV is larger than SH for SS and SSS. The north component is primarily SV or P because the propagation direction is nearly north-south. The relative amplitudes measured using the moving-window analysis technique are shown in figure 24. The relative amplitudes have roughly the same frequency dependence as the theoretical curves, but show more variability in level than expected. This may be due to differences in focusing and defocusing of the two modes by lateral inhomogeneities. However, the two most clearly separated observations, RCD for event 10 and DUG for event 15 agree well with the theoretical predictions for events on the ridge system and within the plate, respectively.

The observed relative amplitudes are roughly consistent with the theoretical relative excitation and support the hypothesis that the higher modes can be neglected at periods greater than about 35 sec. I therefore use two different approaches for determining the pure-path phase velocities. The first method is to treat the higher modes as just another contributor to the noise and proceed with the linear, least squares problem for the fundamental mode exactly as was done for the Rayleigh waves. The second method is to consider both the fundamental and first higher modes simultaneously using the theoretical excitations and the non-linear, least squares

technique described earlier in this section. It should be mentioned that, using the first method, the possibility that the observed separated signals are contaminated by multiple S phases is unimportant. The higher mode, if present, will separate out as indicated. The experiment shows that the interfering signal, whether higher mode, S phase or a combination of both, is less than half the amplitude of the fundamental mode at sufficiently long periods. The interference will therefore have an acceptably small effect on the measured phase velocities over paths of the length used in this study.

Figure 23. Phase shift caused by addition of a higher mode signal to the fundamental mode versus phase velocity of the higher mode. Computed for 40 sec. period waves at an epicentral distance of 4500 km. and with a relative excitation of the higher mode of 0.5.

Figure 24. Theoretical and observed relative excitation of higher mode Love waves. Curve labeled 1_R is the theoretical excitation of the first higher mode relative to the fundamental mode for a shallow earthquake in the 0-10 m.y. zone. 1_B is the relative excitation of the second higher mode in the 0-10 m.y. zone. Individual symbols are observed relative amplitudes: filled squares, path 15-DUG; open triangles, 6-TUC; stars, 10-RCD; filled circles, 10-ALQ; open squares, 5-ALQ; filled triangles, 10-GOL; and open circles, 7-ALQ.

Figure 25. Progressive separation of the first higher Love mode from the fundamental mode. Traces shown are the east-west component of motion observed at the four stations shown in figure 26.

Figure 26. Continental portion of great circle paths from event 10 to stations in North America.

Figure 27. Comparison of an oceanic path with a partly continental path for Love waves from an intra-plate event. Source event occurred on May 9, 1971. The path to DUG includes about 1500 km continent. Epicentral distances are 8780 km to BKS and 8893 km to DUG.

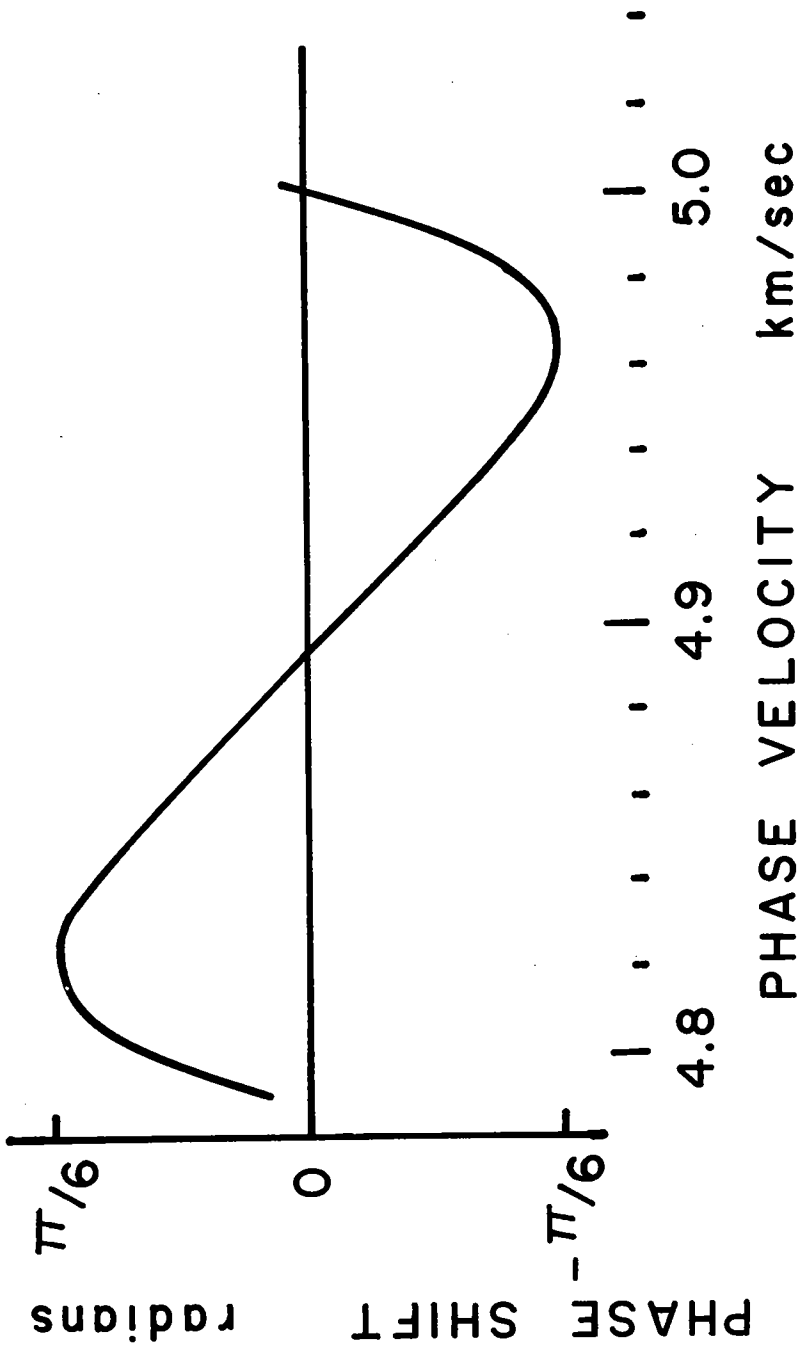
PHASE SHIFT radians
π/6
0
-π/6
4.8
4.9
5.0
PHASE VELOCITY km/sec

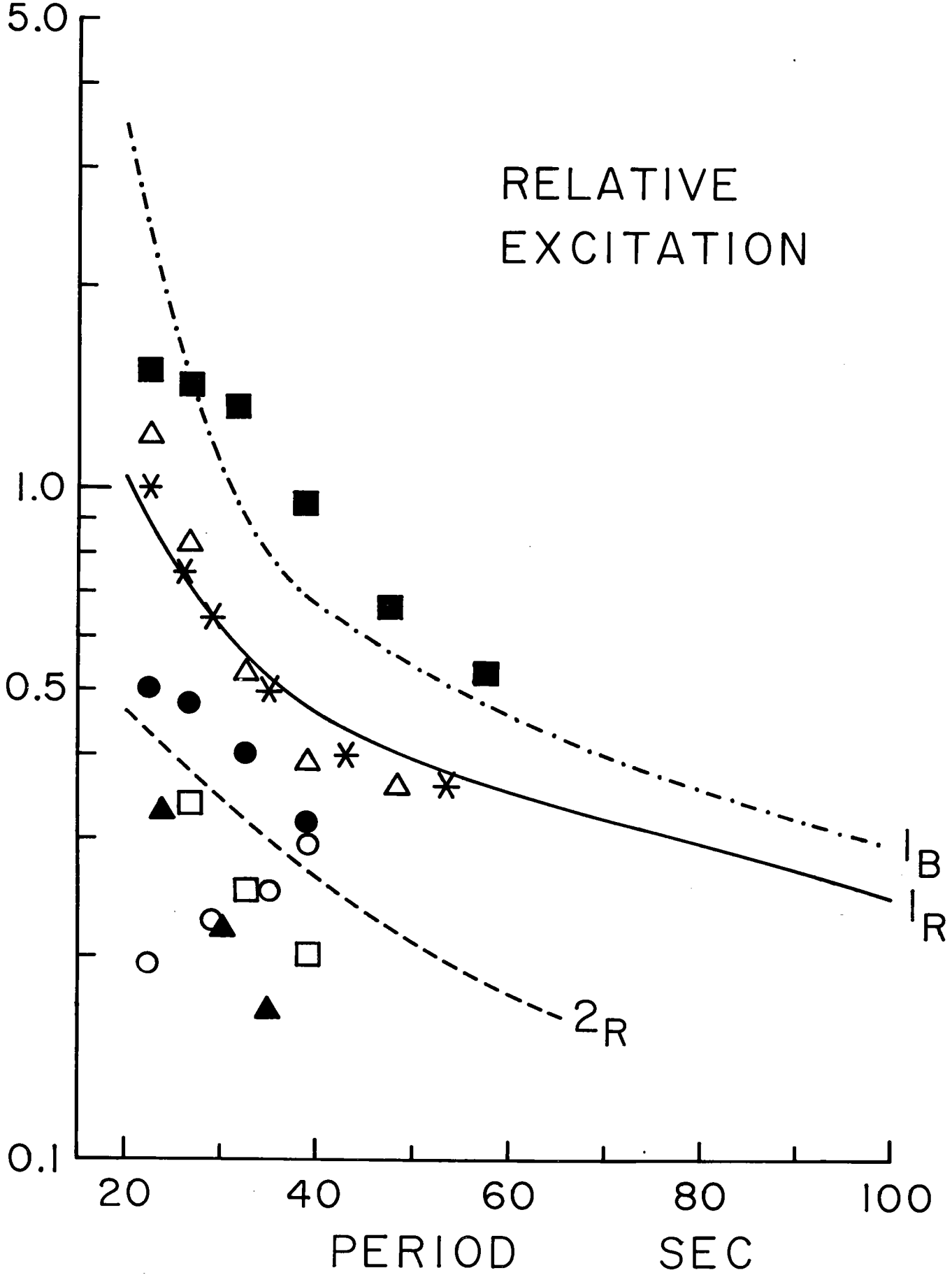
5.0
1.0
0.5
0.1
RELATIVE
EXCITATION
I_B
I_R
2_R
20
40
60
80
100
PERIOD SEC

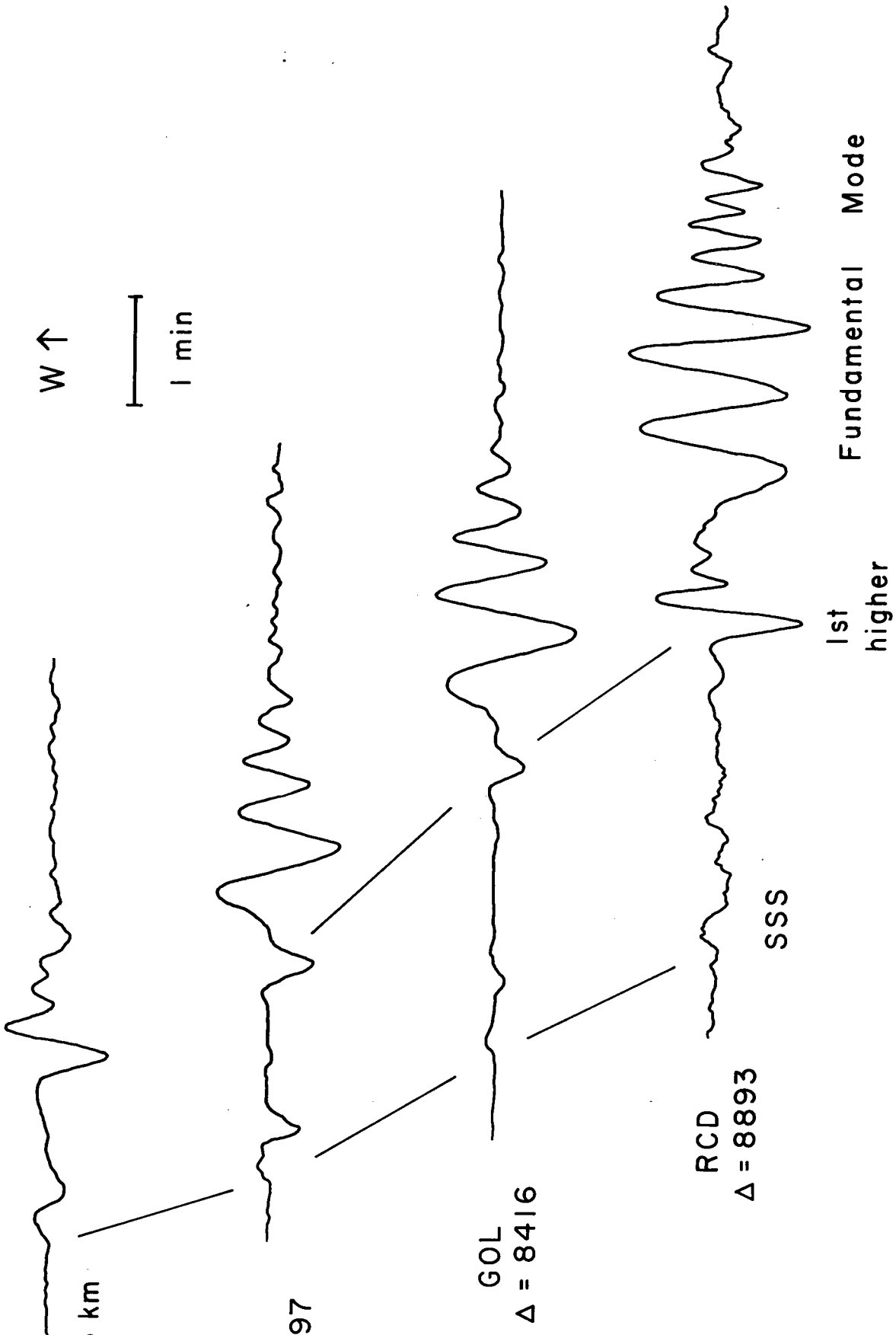
W ↑
1 min
TUC
Δ = 7653 km
ALQ
Δ = 7897
GOL
Δ = 8416
RCD
Δ = 8893
SSS
1st
higher
Fundamental Mode

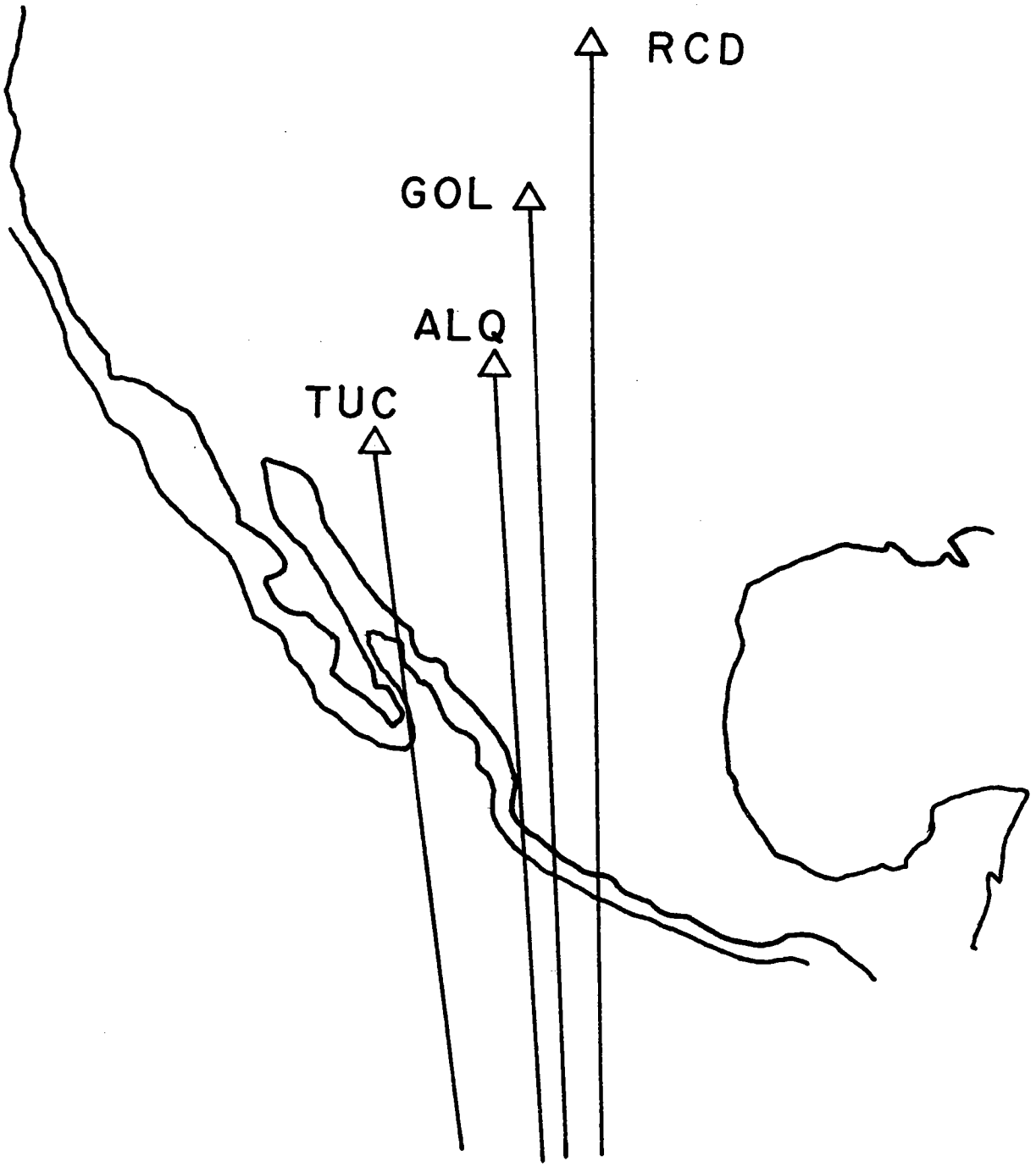

to event IO

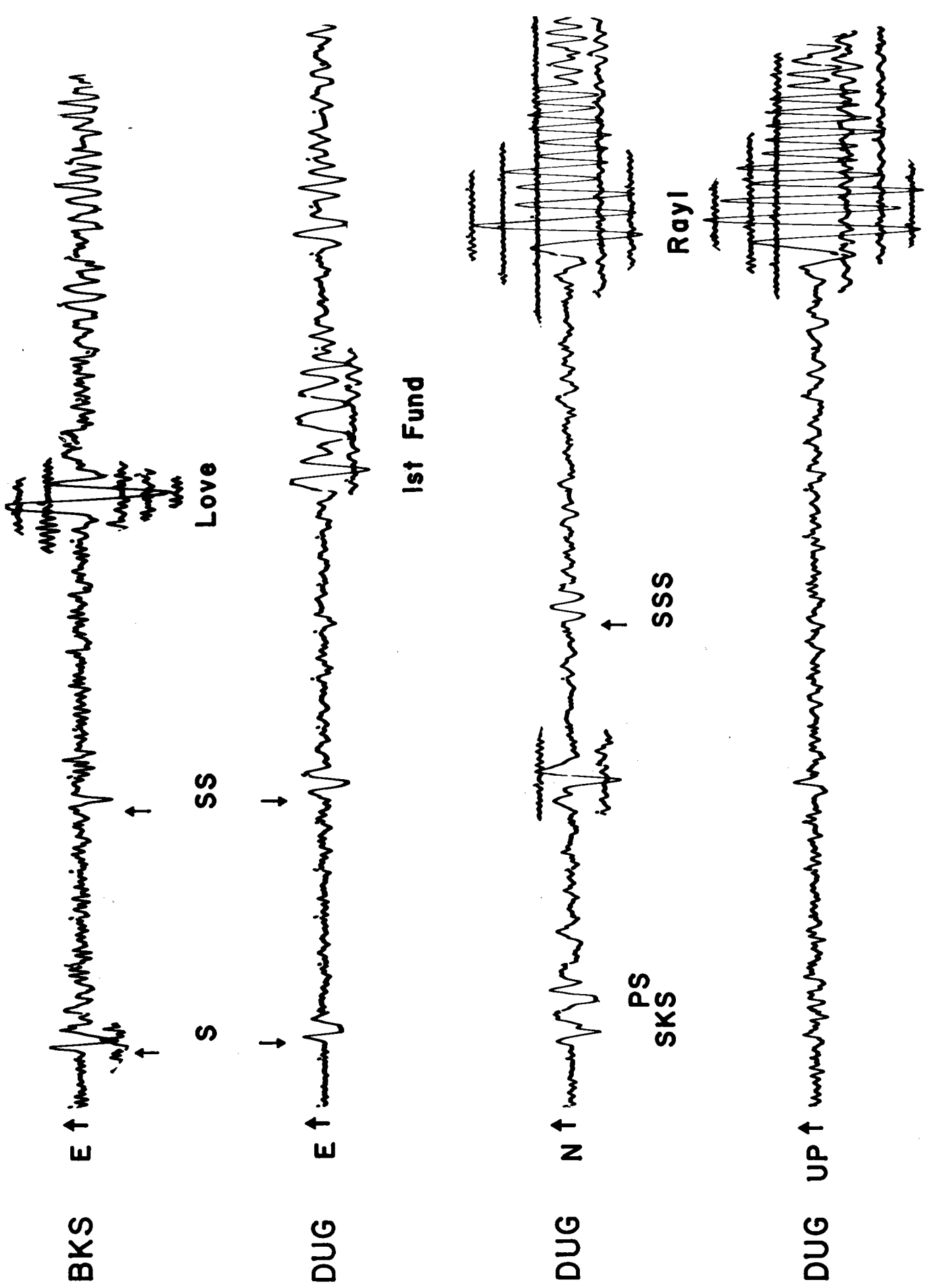
BKS
E
S
SS
Love
DUG
E
1st Fund
DUG
N
PS
SKS
SSS
Rayl
DUG
UP

4.3 Data selection and processing. The acceptable paths are chosen on the basis of percentage of the path within oceanic areas and proximity to a node in the Love wave radiation pattern, as discussed in the selection of Rayleigh wave data. Thatcher and Brune (1969) suggest that the normal procedures used in selecting high quality data may result in a biased set of measurements if a higher mode is present. The interference of a higher mode may produce beating phenomena or phase shifts normally attributed to multipath effects. The interference may also cause an unusually low amplitude arrival or a signal which just doesn't "look good". Omitting records showing these phenomena, if they are actually due to higher modes, may prejudice the results. Consequently, the records were not pre-selected on the basis of their apparent quality. Other selection criteria which were applied to the Rayleigh wave data, but not used for Love data are apparent anomalous amplitudes, shifts in the apparent group velocity, and smoothness of the phase and amplitude spectra. As a result, some records were used which would ordinarily be rejected.

The apparent phase velocities for every record were computed over the entire period range from 33 sec. to 167 sec., because the selection criteria which could be used to choose only a portion of the data have been eliminated. To avoid gross errors, the data were pre-selected on the basis of the level of the background noise. The 45 paths listed in Table 8 and shown in figure 28 were finally accepted. The fact

that fewer acceptable Love wave records were found than Rayleigh wave records is partially due to the difference in radiation patterns, but is primarily a result of a much greater incidence of unacceptable noise levels on the horizontal components and the need to have both horizontal components working at the same time in order to synthesize the transverse component of motion. Listed in Table 9 are the Love wave phase velocities computed with the assumption that the higher mode is unimportant. I call these velocities the "apparent phase velocity" of the fundamental mode. They can easily be converted to effective travel time or to the observed phase, ϕ_{ob}. Velocities for periods less than 33 seconds were not computed because the amplitude of the first higher mode is expected to be comparable to the fundamental mode.

4.4 Error analysis. The sources of error in the Love wave analysis are similar to those discussed for Rayleigh waves. The phase velocity of Love waves is higher than the phase velocity of Rayleigh waves, so the mislocation and finiteness errors, expressed in seconds, are reduced in proportion to the ratio of the velocities. Because the effective travel times are also reduced, the fractional error remains the same. The signal-to-noise ratio for signals of equal energy should be increased by a factor of two for Love waves. The Love wave is usually only slightly dispersed, with most of the energy concentrated into a short time interval. As a result, only four to five minutes of the average

record must be digitized. Decreasing the record length reduces the amount of background noise included with the signal, thus increasing the signal-to-noise ratio. The effect of greater noise levels on horizontal than vertical components has been largely eliminated by the pre-selection of records.

The initial phase of the Love wave is much less sensitive to changes in depth or focal mechanism than the initial phase of Rayleigh waves. If the source is shallow, the initial phase of the higher modes will be the same as the fundamental mode and will be close to either 1/8 or 5/8 circle, depending on the azimuth to the station. Except for possible interference from multiple S-phases and higher modes, each of the possible errors are either less than or equal to the errors expected for Rayleigh waves. Thus, if the higher modes are properly included in the analysis, it should be possible to predict the observed phase of the Love wave with an RMS scatter of less than 5 seconds.

Table 8 Path characteristics; Love waves

PATHID	TOTAL LENGTH	AGE ZONES M.Y. 0-5	5-10	10-20	GT 20	BATHYMETRIC ZONES KM. LT 3.5	3.5-4.0	GT 4.0	AZIMUTHAL CS	SN	CONTINENTAL S.A.	N.A.
2-BOG	3013.3	1525.9	564.4	0.0	506.2	2596.5	0.0	0.0	0.858	-0.079	416.9	0.0
2-QUI	2517.4	1784.3	280.0	0.0	183.8	2248.1	0.0	0.0	0.730	0.158	269.4	0.0
3-ANT	4366.9	316.6	316.6	1179.1	2489.1	301.1	1144.2	2856.1	-0.496	-0.846	65.5	0.0
4-QUI	4527.4	633.8	498.0	1442.5	1553.0	648.0	1679.8	1799.5	-0.277	0.865	400.1	0.0
4-PEL	4389.6	566.8	482.9	1484.4	1696.5	389.2	2953.0	888.4	-0.838	-0.474	159.0	0.0
5-ALQ	6389.3	2079.7	891.3	2172.4	0.0	1995.6	2659.1	488.6	0.780	-0.036	0.0	1245.9
5-QUI	4558.3	639.3	523.1	1435.9	1572.6	684.0	1630.8	1856.0	-0.277	0.868	387.5	0.0
5-NNA	4101.4	541.5	442.8	1476.5	1497.0	273.5	320.2	3364.1	-0.758	0.593	143.5	0.0
5-ARE	4495.8	535.5	420.7	1495.1	1817.3	264.7	354.3	3649.7	-0.893	0.317	227.2	0.0
6-TUC	6556.2	1925.5	992.0	2589.7	0.0	2621.4	2158.8	726.9	0.815	-0.157	0.0	1049.0
7-ALQ	7075.3	2702.6	1103.9	1981.1	0.0	2951.7	2529.2	306.7	0.800	0.022	0.0	1287.7
8-TUC	7051.6	2513.9	1540.8	1939.2	0.0	2409.5	3200.7	383.6	0.814	-0.204	0.0	1057.7
8-QUI	4851.2	348.7	481.6	1868.1	1631.0	822.6	1450.3	2056.5	0.090	0.887	521.9	0.0
8-NNA	4095.4	320.5	375.7	1556.3	1699.6	1027.5	711.4	2213.2	-0.377	0.888	143.3	0.0
8-ARE	4304.9	310.1	335.6	1463.7	2023.3	578.6	1487.8	2066.3	-0.665	0.692	172.2	0.0
8-LPB	4616.7	299.0	324.3	1477.3	2054.4	548.5	2152.3	1454.2	-0.676	0.593	461.7	0.0
9-LPS	5740.5	1420.4	904.5	2210.1	1004.6	1612.0	1994.3	1933.3	0.504	0.534	200.9	0.0
9-BHP	5747.4	1210.7	772.2	1982.9	1505.8	2462.2	1466.4	1543.0	0.272	0.591	275.9	0.0
9-QUI	5017.3	476.8	476.9	1881.5	1650.7	1031.7	919.5	2534.3	0.112	0.886	531.8	0.0
9-BOG	5743.3	459.4	459.5	1895.3	1636.8	1023.7	912.5	2514.8	0.090	0.768	1292.2	0.0
9-NNA	4239.0	405.0	373.8	1551.7	1765.7	737.3	1146.9	2211.9	-0.331	0.907	142.7	0.0
9-ARE	4426.4	413.5	413.5	1392.2	2028.8	666.9	1669.5	1911.6	-0.622	0.731	178.5	0.0
9-GIE	4202.5	754.6	569.2	2878.7	0.0	1260.7	1517.1	1424.6	0.555	0.758	0.0	0.0
9-LPB	4732.1	423.1	423.2	1251.6	2169.3	682.8	2261.6	1322.8	-0.642	0.633	464.9	0.0
10-TUC	7653.4	1198.0	2399.1	3137.9	0.0	1576.0	3374.2	1784.8	0.804	-0.318	0.0	918.4
10-ALQ	7896.9	2320.2	3869.5	2448.0	0.0	2192.2	2337.5	1787.9	0.760	-0.147	0.0	1579.4
10-GIE	4077.1	113.1	229.6	3060.8	673.6	448.5	1961.1	1667.5	0.850	-0.406	0.0	0.0
10-BHP	5476.9	205.4	205.4	2136.0	2700.1	1411.4	1642.3	2193.2	0.586	0.642	230.0	0.0
10-LPB	3903.3	154.7	154.7	833.0	2296.8	223.5	2283.6	932.0	-0.410	0.780	464.1	0.0
11-ARE	3040.0	124.2	0.0	366.7	2348.1	51.1	871.6	1916.3	0.489	0.796	201.1	0.0
11-NNA	3362.0	112.1	0.0	507.2	2548.1	57.0	1111.8	1998.6	0.787	0.518	194.6	0.0
13-GIE	1776.4	720.8	442.7	612.9	0.0	923.7	852.7	0.0	0.673	0.532	0.0	0.0
13-ARE	3970.7	297.8	297.8	913.3	1985.3	314.5	950.4	2229.3	-0.686	-0.543	476.5	0.0
14-NNA	3325.2	343.3	343.4	775.1	1655.6	358.5	713.9	2045.0	-0.826	-0.431	207.8	0.0
14-ARE	4004.2	310.4	310.4	895.6	2002.2	355.4	953.5	2209.7	-0.675	-0.553	485.6	0.0
15-BKS	8780.5	2558.3	1041.7	2985.4	1756.1	2027.0	3912.2	2402.4	0.590	-0.681	0.0	439.0
15-TUC	8004.8	4402.0	841.1	1841.1	0.0	2274.0	3620.0	1190.1	0.826	-0.281	0.0	920.6
15-GIE	4569.1	143.3	290.8	3655.3	479.8	685.4	2627.3	1256.5	0.843	0.490	0.0	0.0
15-BHP	5993.1	269.7	269.7	2547.1	2666.9	1455.6	2157.5	2140.3	0.617	0.733	239.7	0.0
15-ARE	4131.6	165.2	165.3	1322.1	2313.7	245.9	2609.8	1110.5	-0.246	0.928	165.3	0.0
15-LPB	4384.7	153.4	153.4	1315.4	2302.0	306.1	2833.3	784.8	-0.335	0.830	460.4	0.0
15-ANT	3684.9	184.2	184.3	1197.6	2045.1	260.0	3087.6	263.6	-0.560	0.804	73.7	0.0
16-NNA	3761.8	376.2	376.2	1365.5	1482.1	324.0	1321.2	1954.8	-0.940	0.156	161.8	0.0
16-ARE	4309.2	366.3	366.3	1443.6	1853.0	282.0	854.2	2893.0	-0.924	-0.112	280.1	0.0
16-LPB	4671.2	373.7	373.7	1448.1	1845.1	282.8	856.6	2901.1	-0.854	-0.110	630.6	0.0

Table 9 Apparent Love wave phase velocities

PATHID	33.3	40.0	50.0	58.8	66.7	76.9	90.9	100.0	111.1	125.0	142.9	166.7
2-BOG	4.222	4.240	4.300	4.338	4.363	4.389	4.402	4.402	4.408	4.418	4.431	4.445
2-QUI	4.226	4.261	4.322	4.369	4.405	4.447	4.497	4.527	4.561	4.600	4.646	4.706
3-ANT	4.465	4.478	4.495	4.512	4.529	4.552	4.583	4.603	4.627	4.656	4.692	4.738
4-QUI	4.397	4.410	4.437	4.457	4.475	4.500	4.537	4.562	4.597	4.649	4.736	4.884
4-PEL	4.422	4.436	4.460	4.477	4.500	4.531	4.567	4.590	4.623	4.672	4.746	4.857
5-ALQ	4.298	4.324	4.359	4.388	4.414	4.449	4.495	4.525	4.563	4.612	4.678	4.769
5-QUI	4.405	4.426	4.451	4.474	4.488	4.514	4.558	4.585	4.607	4.610	4.613	4.642
5-NNA	4.430	4.445	4.462	4.484	4.506	4.537	4.578	4.604	4.635	4.672	4.717	4.776
5-ARE	4.440	4.453	4.474	4.494	4.512	4.538	4.575	4.599	4.630	4.670	4.721	4.793
6-TUC	4.300	4.324	4.361	4.388	4.405	4.425	4.458	4.481	4.509	4.540	4.576	4.625
7-ALQ	4.280	4.312	4.332	4.354	4.379	4.416	4.468	4.498	4.532	4.575	4.641	4.750
8-TUC	4.315	4.331	4.344	4.358	4.380	4.419	4.460	4.482	4.506	4.534	4.570	4.617
8-QUI	4.389	4.420	4.459	4.483	4.499	4.521	4.552	4.575	4.604	4.642	4.694	4.765
8-NNA	4.440	4.449	4.461	4.473	4.487	4.508	4.538	4.558	4.582	4.613	4.652	4.705
8-ARE	4.437	4.449	4.462	4.476	4.491	4.512	4.541	4.559	4.581	4.609	4.644	4.690
8-LPB	4.390	4.414	4.442	4.465	4.484	4.508	4.543	4.565	4.594	4.631	4.679	4.746
9-LPS	4.377	4.395	4.409	4.421	4.438	4.461	4.495	4.517	4.545	4.579	4.623	4.682
9-BHP	4.406	4.423	4.449	4.468	4.483	4.503	4.529	4.547	4.570	4.598	4.636	4.686
9-QUI	4.412	4.427	4.458	4.498	4.523	4.544	4.562	4.576	4.600	4.634	4.681	4.747
9-BOG	4.345	4.384	4.432	4.466	4.489	4.520	4.560	4.582	4.606	4.633	4.679	4.762
9-NNA	4.461	4.475	4.495	4.505	4.518	4.543	4.583	4.610	4.644	4.690	4.757	4.876
9-ARE	4.450	4.467	4.491	4.507	4.520	4.540	4.571	4.593	4.622	4.662	4.722	4.822
9-GIE	4.401	4.416	4.432	4.449	4.466	4.492	4.528	4.553	4.584	4.625	4.681	4.766
9-LPB	4.387	4.427	4.467	4.496	4.518	4.542	4.575	4.598	4.630	4.673	4.737	4.838
10-TUC	4.371	4.388	4.400	4.411	4.424	4.443	4.472	4.491	4.515	4.545	4.584	4.638
10-ALQ	4.286	4.313	4.362	4.389	4.409	4.434	4.471	4.494	4.524	4.560	4.607	4.668
10-GIE	4.433	4.449	4.468	4.478	4.490	4.511	4.541	4.559	4.580	4.603	4.632	4.672
10-BHP	4.444	4.458	4.481	4.502	4.521	4.544	4.575	4.593	4.615	4.642	4.675	4.718
10-LPB	4.385	4.409	4.433	4.451	4.467	4.489	4.522	4.545	4.574	4.613	4.667	4.745
11-ARE	4.478	4.496	4.469	4.491	4.537	4.586	4.630	4.657	4.691	4.738	4.804	4.897
11-NNA	4.399	4.425	4.467	4.492	4.508	4.525	4.544	4.556	4.570	4.588	4.612	4.647
13-GIE	4.303	4.319	4.337	4.357	4.377	4.398	4.416	4.421	4.423	4.420	4.411	4.394
13-ARE	4.415	4.422	4.453	4.475	4.489	4.510	4.546	4.572	4.607	4.655	4.726	4.847
14-NNA	4.391	4.419	4.456	4.475	4.489	4.514	4.556	4.586	4.624	4.674	4.747	4.870
14-ARE	4.408	4.421	4.445	4.470	4.491	4.514	4.541	4.559	4.583	4.614	4.657	4.716
15-BKS	4.413	4.425	4.441	4.454	4.464	4.483	4.515	4.537	4.565	4.597	4.637	4.687
15-TUC	4.347	4.360	4.387	4.402	4.430	4.448	4.462	4.476	4.500	4.541	4.603	4.683
15-GIE	4.447	4.461	4.483	4.501	4.517	4.540	4.576	4.600	4.630	4.665	4.709	4.766
15-BHP	4.442	4.458	4.472	4.487	4.504	4.529	4.563	4.584	4.611	4.643	4.692	4.735
15-ARE	4.421	4.439	4.463	4.483	4.501	4.524	4.554	4.574	4.599	4.629	4.667	4.718
15-LPB	4.393	4.412	4.435	4.459	4.480	4.509	4.546	4.570	4.598	4.632	4.675	4.730
15-ANT	4.425	4.440	4.445	4.458	4.476	4.499	4.529	4.548	4.569	4.596	4.631	4.679
16-NNA	4.505	4.516	4.533	4.549	4.566	4.590	4.631	4.662	4.701	4.750	4.803	4.844
16-ARE	4.446	4.466	4.489	4.503	4.527	4.542	4.584	4.609	4.646	4.702	4.767	4.792
16-LPB	4.379	4.409	4.466	4.491	4.518	4.543	4.580	4.607	4.640	4.678	4.720	4.779

4.5 Fundamental mode phase velocity

The observed phases at each station are best described by a model of the propagation in which the ocean floor is anisotropic and regionalized, and in which the first higher mode makes a significant contribution to the signal (Table 10). However, unlike Rayleigh waves, the azimuthal variation of velocity described by the anisotropy terms is not statistically required by the data. The fit to the data at periods of 33, 67, and 100 seconds, and the results of an F-test on the significance of the fit for a variety of propagation models are summarized in Table 10. The RMS errors in predicting the observed phase were converted to the equivalent errors in seconds for presentation in the table.

Model 1, which allows for only one continental and one oceanic region, does not adequately describe the observed phases. The 10 second RMS error is much larger than the expected 5 second error and the regionalized models are better descriptions of the data at the 99% confidence level. Dividing the ocean into 2 regions (0-10 m.y., and older than 10 m.y., model 2) dramatically improves the fit. With only three regional velocity parameters, this model explains the observed, "apparent" Love wave phase velocities in the 33 to 100 second range with an RMS error of less than 0.6%. Adding more regional parameters does not significantly improve the fit (models 3 and 4). Two

continental divisions are used in other models only to avoid any possible bias in the oceanic velocities. Adding the anisotropic terms,improves the fit somewhat, but the improvement is not statistically significant. From the Rayleigh wave analysis, we know that the region is anisotropic: the lack of significant improvement in the Love wave data is probably due to small sin 2θ and cos 2θ coefficients for Love wave propagation in the real earth, rather than insufficient sampling or some other experimental defect. Because Love waves effectively sample SH velocity while Rayleigh waves sample SV velocity, there is no physical requirement that the anisotropy of the two surface waves be similar. In fact, Wang (1973) has shown that in a model in which the "a" axis of olivine is preferentially aligned perpendicular to a mid-ocean ridge axis and the "b" and "c" axes are randomly distributed about the "a" axis, SH anisotropy will be very small and will appear only as a 4θ variation, while SV will be large and vary as the cosine of 2θ. Thus the results qualitatively fit a mineralogical model which has been proposed to explain the anisotropy of P-waves (Francis, 1969).

Although the degree of fit is similar, close examination reveals that the models with regions based on magnetic anomalies are not equivalent to regionalized models based on the bathymetry. The anisotropy in both model 6 and 8 is small (figure 29 and 30), but there are differences, particularly in the coefficient of

the sin 2θ term. This discrepancy did not exist for Rayleigh waves. The difference is probably due to a more limited azimuthal and regional sampling for Love waves than for Rayleigh waves. The southeastern corner of the Nazca plate is not as well sampled, and, outside of the ridge area, there are fewer north-south paths. Another possibility is that the 2θ terms may not provide an adequate description of the azimuthal variation. For Rayleigh waves, Smith and Dahlen (1973) showed that only the 2θ terms should be important. But for Love waves, they predict that the 2θ terms will be small at long periods and that the 4θ terms may be significant at all periods. The fact that the azimuthal terms appear to increase at the longer periods, rather than decrease as predicted by Smith and Dahlen, implies the degree of anisotropy in the earth changes with depth. However, the presence of unmodelled 4θ terms in the real earth could hinder the attempt to precisely measure the regional and 2θ terms.

The difference between the two methods of regionalization is not confined to the anisotropy terms alone. Although the velocities of the youngest zones (0-10 m.y. and less than 3500 m.) in each model agree, the relative velocities in the two older zones of each model show contrasting frequency dependence (figure 31). It must be emphasized that these are fairly small details which are not quite statistically significant. In the bathymetry model, the phase velocity in the oldest zone

(>4000 m water depth) is consistently faster by about 0.07 km/sec than the velocity in the intermediate zone (3500-4000 m). Qualitatively, this increase in velocity with age is what one would expect and tends to favor this model over the model based on the identification of linear magnetic anomalies. However, the 0.07 km/sec increase is about twice that predicted from earth models that fit the pure-path Rayleigh wave data for the same zones and in addition, the magnetic anomaly model fits the data better at long periods. It may be possible that, in the Nazca plate, the phase velocities at long periods really are lower in the 20-50 m.y. age zone than in the 10-20 m.y. zone. Note that the same effect appears for Rayleigh waves in the 90 to 125 sec. period range (see figure 17). In order to resolve these details of the pure-path velocities, discriminate between the two methods of regionalization, and measure the 4θ coefficients, much more high quality data is needed. Because the 2θ terms are not statistically required and may be confused with 4θ variation, they will not be used in subsequent modelling except as a speculative guide. The azimuthal terms and the pure-path phase velocities for the two oceanic regions, 0 to 10 m.y. and older than 10 m.y. (model 5) are listed in Table 11 along with the standard deviation of each parameter. These parameters, in combination with the equivalent Rayleigh wave velocities (table 6), are used in the section on mantle models

to obtain rigorous limits on the possible structure of the oceanic upper mantle.

4.6 Higher mode velocity

In the models of the fundamental mode phase velocity, the higher modes were considered to be just another contributor to the noise. If the higher modes are present, there should be systematic information about their velocity buried within the residual errors of those models. For example, the RMS residual to model 3 at 33 seconds period is 6.0 sec. If a signal with an RMS value of 2.5 sec. is contained within the residuals, removal of the signal will reduce the apparent noise level to about 5.4 sec. With a theoretical relative excitation of 0.54 for a source on the ridge, the first higher mode will produce a maximum phase shift equivalent to a 3.05 sec. error at 33 second period. The RMS error is about 2.2 sec.; thus a higher mode signal may easily be contained within the level of noise observed for the models of the fundamental mode propagation.

The higher mode signal is extracted from the noise using equations 15 and 16 in a search for the minimum sum of the squares of the residuals. A detailed description of the procedure involved in such a search is given in a later section. For simplicity, I assume that for all earthquakes the amplitude is equal to the theoretical relative excitation of the first higher mode in the 0-10 m.y. model. Because the first higher

mode is most sensitive to the structure in the low velocity zone, its velocity is only slightly affected by changes in the shear velocity structure of the upper 100 kilometers of the mantle. Consequently, little regional variation in velocity is expected. I therefore model the first higher mode with only a single parameter, which represents the average phase velocity in the entire area of study. The sum of the squares of the residuals as a function of this velocity is shown in figure 32 for 67 second period waves. The dotted line indicates the sum of the squares of the errors for model 3 in Table 10. The solid line represents the sum for the same model, but with the theoretical contribution of the higher mode included. The regional velocities of the fundamental mode are fixed at the values derived for model 3 and only the model phase velocity of the higher mode is allowed to vary. The phase velocity is given by the minimum in the curve at about 5.22 km/sec. The uncertainty in this velocity is defined by an F-test on the ratio of the sum of the squares of the errors at other trial values to the minimum sum at 5.22 km/sec. These bounds are somewhat asymmetrical as indicated by the arrows at the 95% confidence limit. There are local minima on either side of the central minimum, which do not reach as low a level and do not yield reasonable phase velocities at long periods. The problem of choosing the correct local minimum stems from the large number of paths in the limited distance range of 4 to 5 thousand kilometers, and is analogous

to choosing the correct value of N in the usual phase velocity measurements.

The minimum at 5.22 km/sec corresponds to an RMS error of 4.4 sec. (model 10, table 10). The theoretical relative amplitude at 67 seconds would produce a maximum phase shift of 3.62 sec. and a RMS shift of about 2.6 sec. Removing a 2.6 sec. signal from a noise level of 5.1 sec. (model 3) would theoretically reduce the error to 4.4 sec. At 100 seconds, removal of the theoretical 2.75 sec. RMS signal would reduce the 5.7 sec. error to 5.1 sec. In both cases, the agreement with the predicted reduction is remarkable considering the simplicity of the model. I believe this agreement provides very strong support for the validity of the phase velocities derived for the first higher mode.

The reduction of the error at 33 seconds is not as large as theory predicts. One possible explanation is that the relative amplitudes may vary more at short periods: the effect of lateral inhomogeneities on the fundamental mode Love wave amplitudes should be greater at short periods, and the relative excitation is more sensitive to the structure at 33 seconds than at 67 seconds. Also, at short periods the total phase shift is more sensitive to small changes in velocity, so a regionalized or anisotropic model may be required. The error was reduced to the theoretical 5.6 sec level in a model with 1% anisotropy of the first higher mode, but no reasonable uncertainty limits can be placed on that value, so the experiment is of little

practical value.

The first higher mode phase velocity in the period range 33 to 100 seconds is shown in figure 33. The uncertainty indicated is the 95% confidence limit. At 40 seconds, the local maxima on either side of the minimum were below the 95% confidence level, so the uncertainty indicated in the figure corresponds to the velocity at each maximum in the sum of the squares. At 33 seconds, one of the local minima is indicated, but no uncertainty limits could be assigned with confidence. As indicated by the dotted curve in the figure, the measured phase velocity agrees reasonably well with that predicted from the mantle model based on the Rayleigh wave observations. Because the majority of the paths are outside the youngest zone, the observed phase velocity of the first higher mode will be used as a constraint in constructing models of the mantle only for the zone which is older than 10 m.y. in age. These velocities were derived with the assumption that the apparent Love wave phase velocities are not systematically biased by the presence of the higher mode, and that, therefore, the regional velocities of the fundamental mode found by ignoring the higher modes are correct. The validity of this assumption can be tested by searching for the minimum of the sums of the squares of the residuals in a multidimensional space in which both the regional velocities of the fundamental mode and the velocity of the first higher mode are allowed to vary. If the apparent velocities are systematically

biased, it should be possible to find another set of fundamental and higher mode velocities which fit the data equally well.

Table 10. Root-mean-square residual errors in regional models of Love wave propagation

Model	Description	33 sec.	67 sec.	100 sec.	F-test*
1.	1 cont. 1 ocean	8.7+	9.5	10.1	99
2.	1 cont. 2 ocean	6.0	5.5	5.8	90
3.	2 cont. 2 ocean	6.0	5.1	5.7	
4.	2 cont. 4 ocean	6.0	5.1	5.7	
5.	2 cont. 2 ocean aniso.	5.6	4.8	5.3	
6.	2 cont. 3 ocean aniso.	5.6	4.8	5.2	
7.	2 cont. 2 ocean (bath.) aniso.	5.2	5.1	6.2	90
8.	2 cont. 3 ocean (bath.) aniso.	5.0	4.7	5.9	
9.	2 cont. 2 ocean aniso. 1st higher mode	5.5	4.2	4.8	
10.	2 cont. 2 ocean 1st higher	5.9	4.4	5.1	

* F-test computed relative to model 9

+ RMS error in sec.

TABLE 11. LOVE WAVE PURE-PATH VELOCITIES; TWO OCEANIC AGE ZONES AND ANISOTROPY

PERIOD	0-10 M.Y.		GT 10 M.Y.	
	PHASE VELOCITIES			
33.3	4.3349	± 0.0245	4.4917	± 0.0112
40.0	4.3406	0.0222	4.5022	0.0101
50.0	4.3587	0.0206	4.5117	0.0094
58.8	4.3706	0.0208	4.5226	0.0095
66.7	4.3925	0.0215	4.5343	0.0098
77.0	4.4129	0.0205	4.5542	0.0093
90.9	4.4305	0.0216	4.5884	0.0100
100.0	4.4443	0.0243	4.6116	0.0112
111.1	4.4660	0.0279	4.6408	0.0129
125.0	4.4991	0.0336	4.6763	0.0155
142.8	4.5471	0.0447	4.7188	0.0205
166.7	4.6100	0.0655	4.7710	0.0298

TABLE 11. CONT.

PERIOD	SOUTH AMER.		NORTH AMER.		A/C		B/C		RMS ERROR
	PHASE VELOCITIES								
33.3	3.9604	±0.0698	3.9744	±0.0693	-0.0020	±0.0018	-0.0035	±0.0019	5.6
40.0	4.0636	0.0661	4.0636	0.0652	-0.0019	0.0017	-0.0028	0.0018	5.1
50.0	4.2484	0.0666	4.1519	0.0627	-0.0021	0.0016	-0.0030	0.0016	4.7
58.8	4.3697	0.0709	4.2131	0.0649	-0.0020	0.0016	-0.0025	0.0016	4.7
66.7	4.4271	0.0745	4.2582	0.0679	-0.0022	0.0016	-0.0020	0.0017	4.8
77.0	4.4772	0.0721	4.3346	0.0666	-0.0024	0.0015	-0.0012	0.0016	4.7
90.9	4.5206	0.0769	4.4630	0.0738	-0.0034	0.0016	-0.0007	0.0017	4.8
100.0	4.5369	0.0864	4.5375	0.0851	-0.0042	0.0018	-0.0004	0.0019	5.3
111.1	4.5538	0.0994	4.6198	0.1007	-0.0053	0.0021	-0.0004	0.0022	6.0
125.0	4.5663	0.1188	4.7203	0.1252	-0.0071	0.0025	-0.0005	0.0026	7.1
142.8	4.6145	0.1586	4.8689	0.1741	-0.0094	0.0032	-0.0001	0.0034	9.2
166.7	4.7467	0.2421	5.1177	0.2781	-0.0125	0.0047	0.0016	0.0049	13.1

Figure 28. Great circle paths of Love waves considered in this study. Shaded portion indicates sea-floor which is less than 10 m.y. old.

Figure 29. Sin 2θ coefficient of anisotropy for Love waves. Solid circles represent measured values and continuous lines are one standard deviation limits for a regionalized model based on bathymetry. Open circles and dashed lines represent measured values and one standard deviation limits for a regionalized model based on magnetic anomalies.

Figure 30. Cos 2θ coefficient of anisotropy for Love waves. Symbols as in figure 29.

Figure 31. Pure-path phase velocities of the fundamental Love mode. Solid symbols indicate measured velocities for a regionalized model based on magnetic anomalies. Vertical bars indicate one standard deviation from the velocities for the 0 to 10 m.y. zone. Standard deviations of the other curves are approximately the same size.

Figure 32. Sum of the squares of the residuals as a function of the model phase velocity of the first higher mode. The best fit to the 67 sec. period Love wave data is found at 5.22 km/sec. The dashed line indicates the fit to the data if only the

fundamental mode is considered. Arrows indicate 95% confidence limits.

Figure 33. Phase velocity of the first higher Love mode. Error bars indicate 95% confidence limits. Dashed line represents predicted higher mode velocities based on Rayleigh wave earth model for 10-50 m.y. zone.

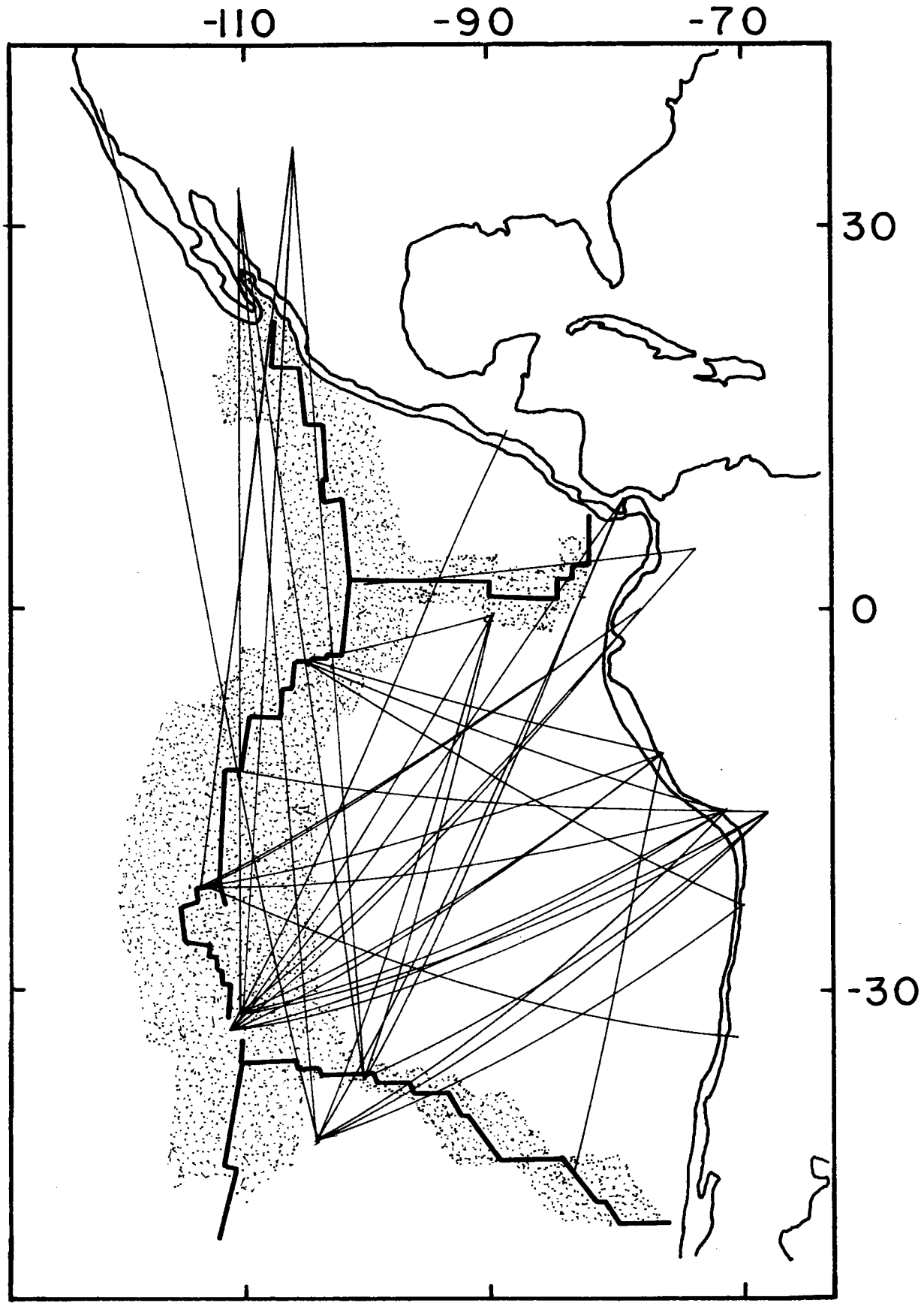
-110
-90
-70
30
0
-30

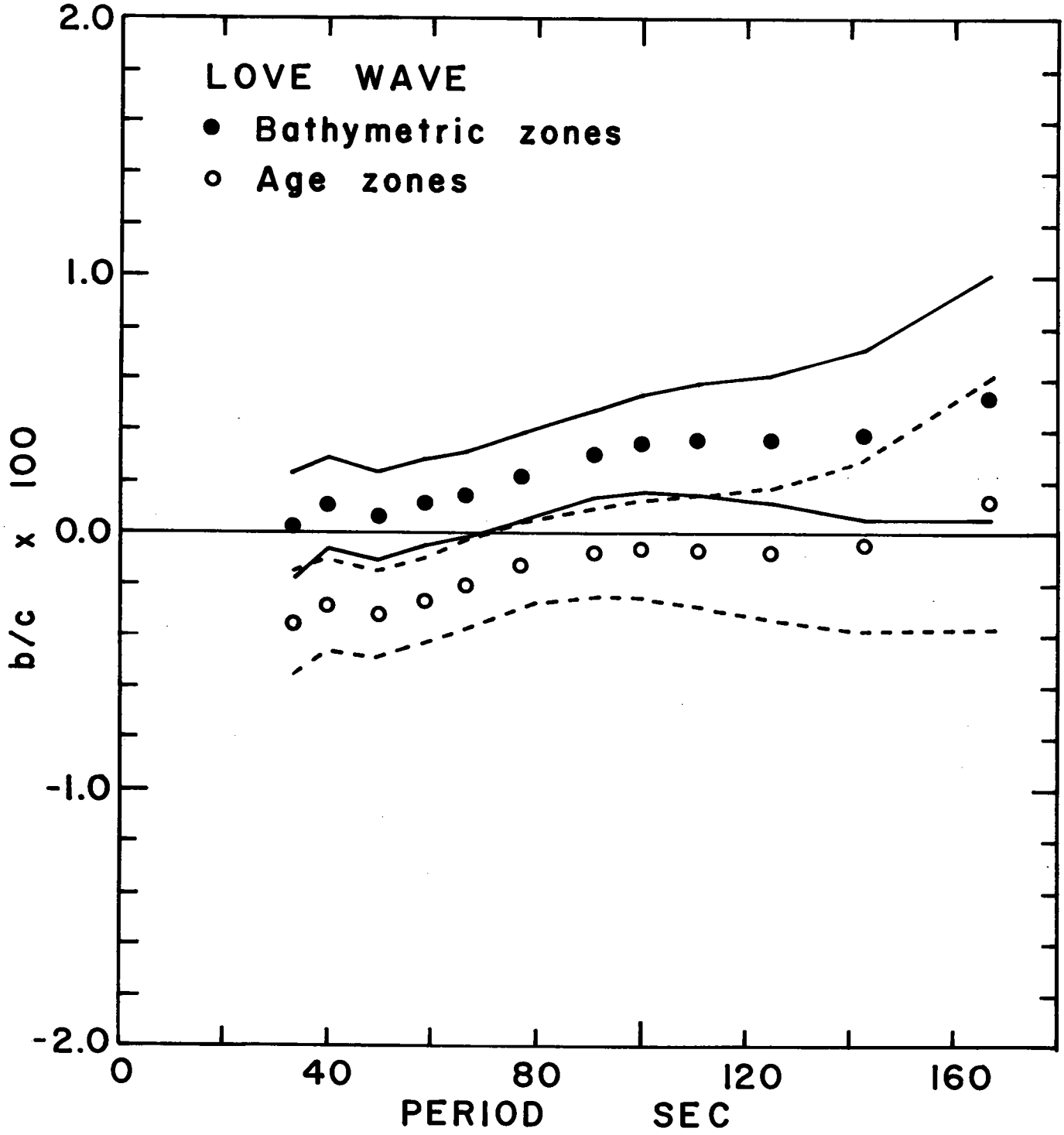
LOVE WAVE
Bathymetric zones
Age zones
2.0
1.0
0.0
-1.0
-2.0
b/c x 100
0
40
80
120
160
PERIOD SEC

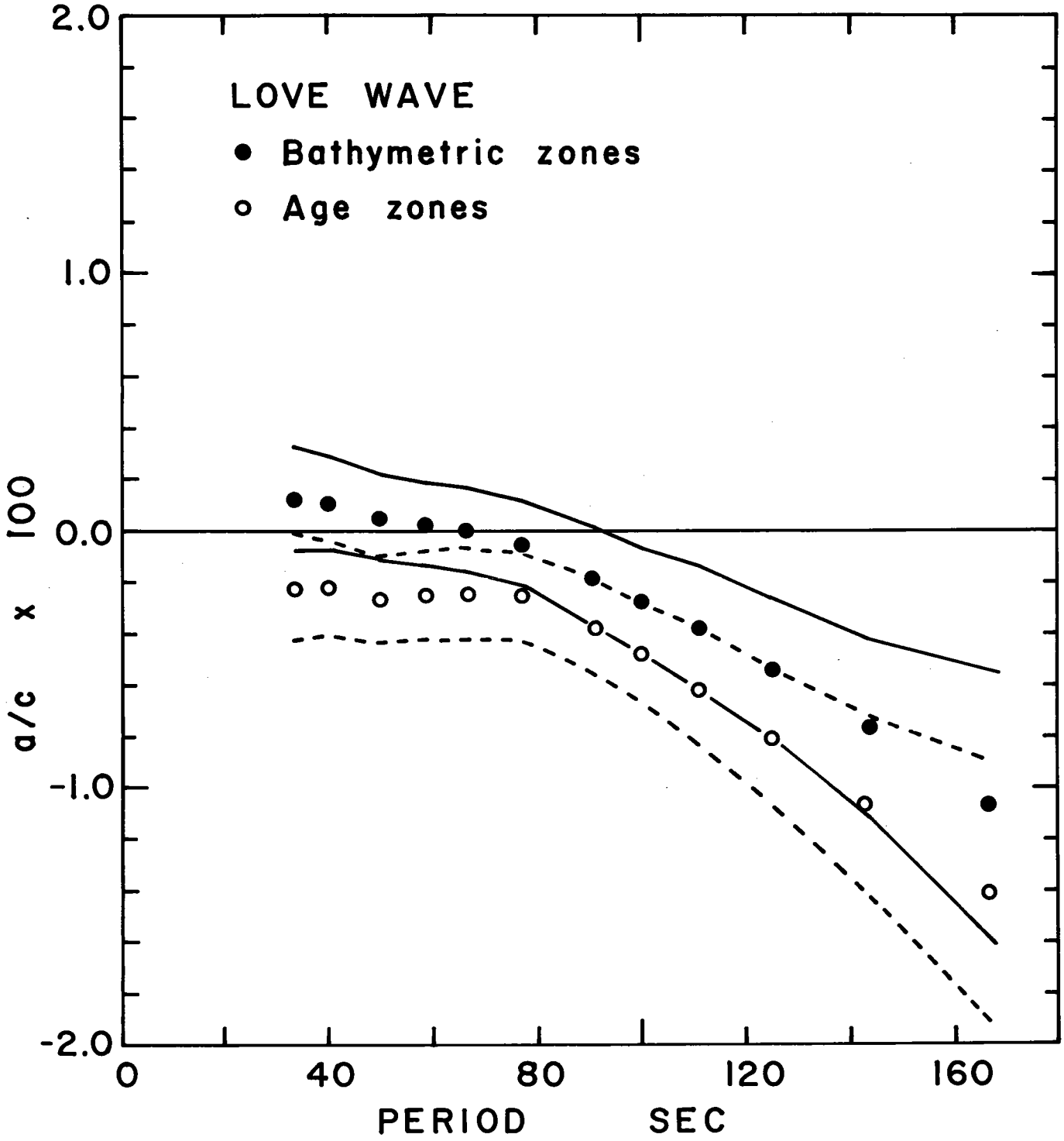
LOVE WAVE
Bathymetric zones
Age zones
2.0
1.0
0.0
-1.0
-2.0
a/c x 100
0
40
80
120
160
PERIOD SEC

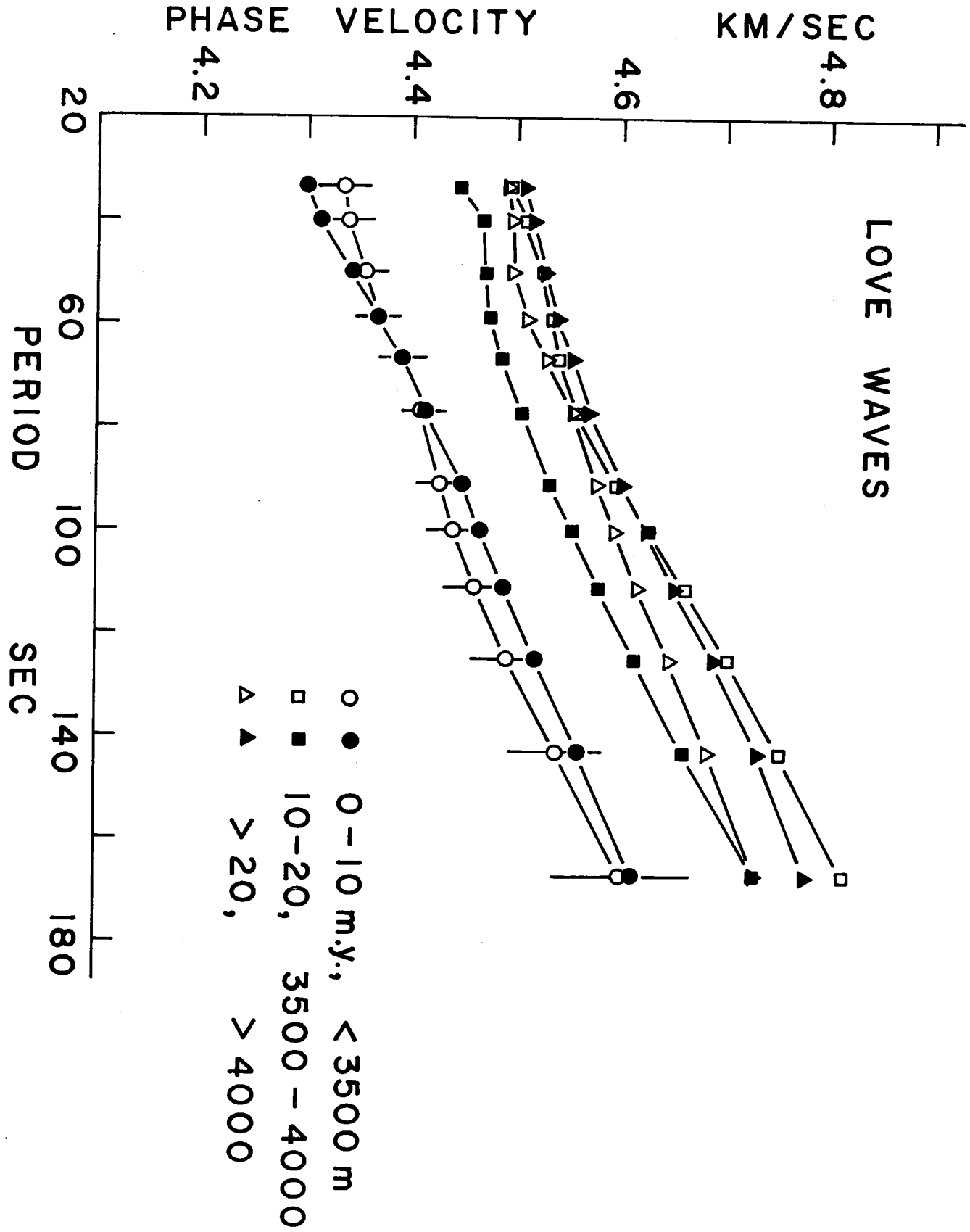
PHASE VELOCITY
KM/SEC
4.2
4.4
4.6
4.8
20
60
100
140
180
PERIOD
SEC
LOVE WAVES
○ ● 0-10 m.y., < 3500 m
□ ■ 10-20, 3500-4000
△ ▲ > 20, > 4000

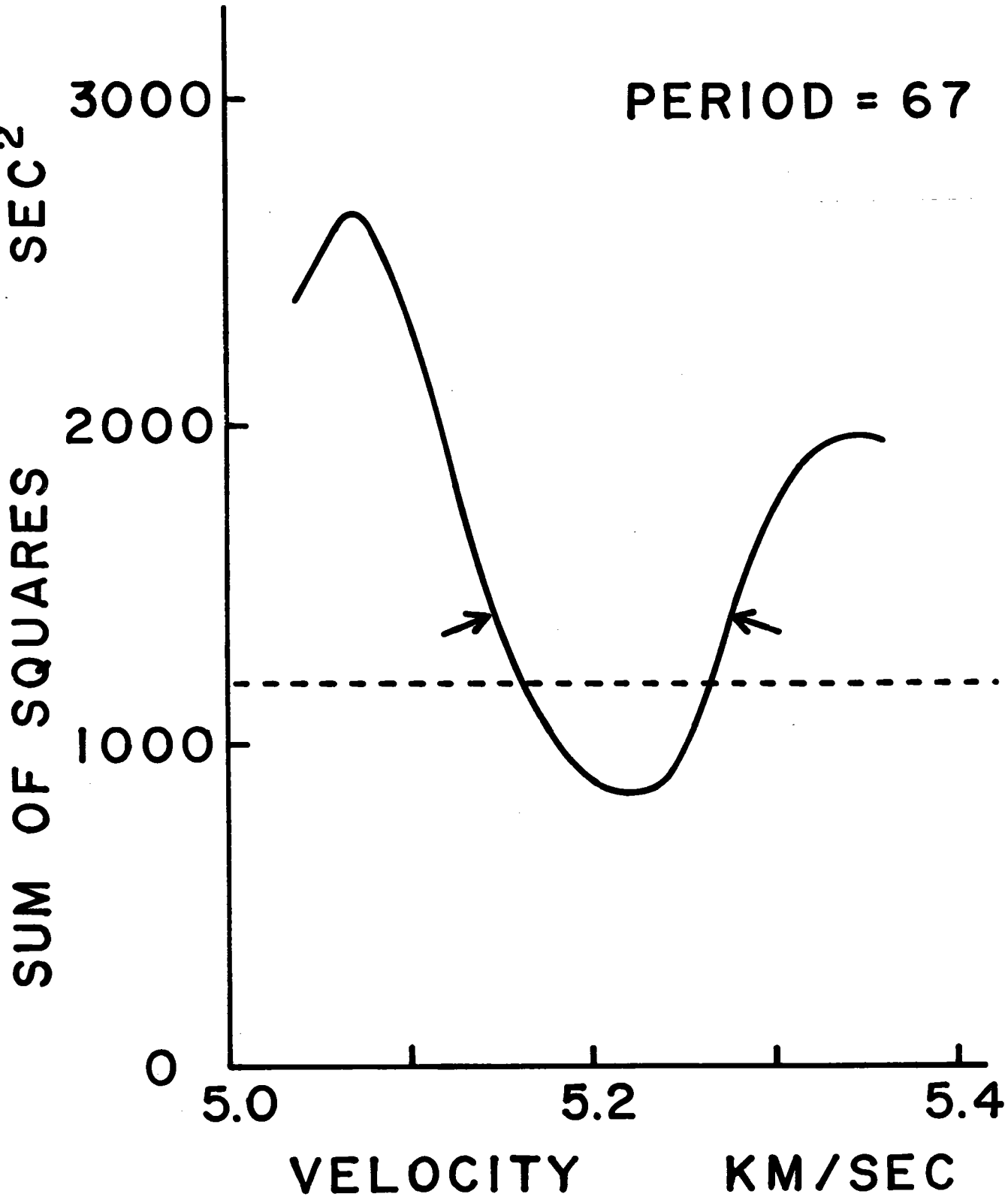
PERIOD = 67
3000
2000
1000
0
SEC2
SUM OF SQUARES
5.0
5.2
5.4
VELOCITY
KM/SEC

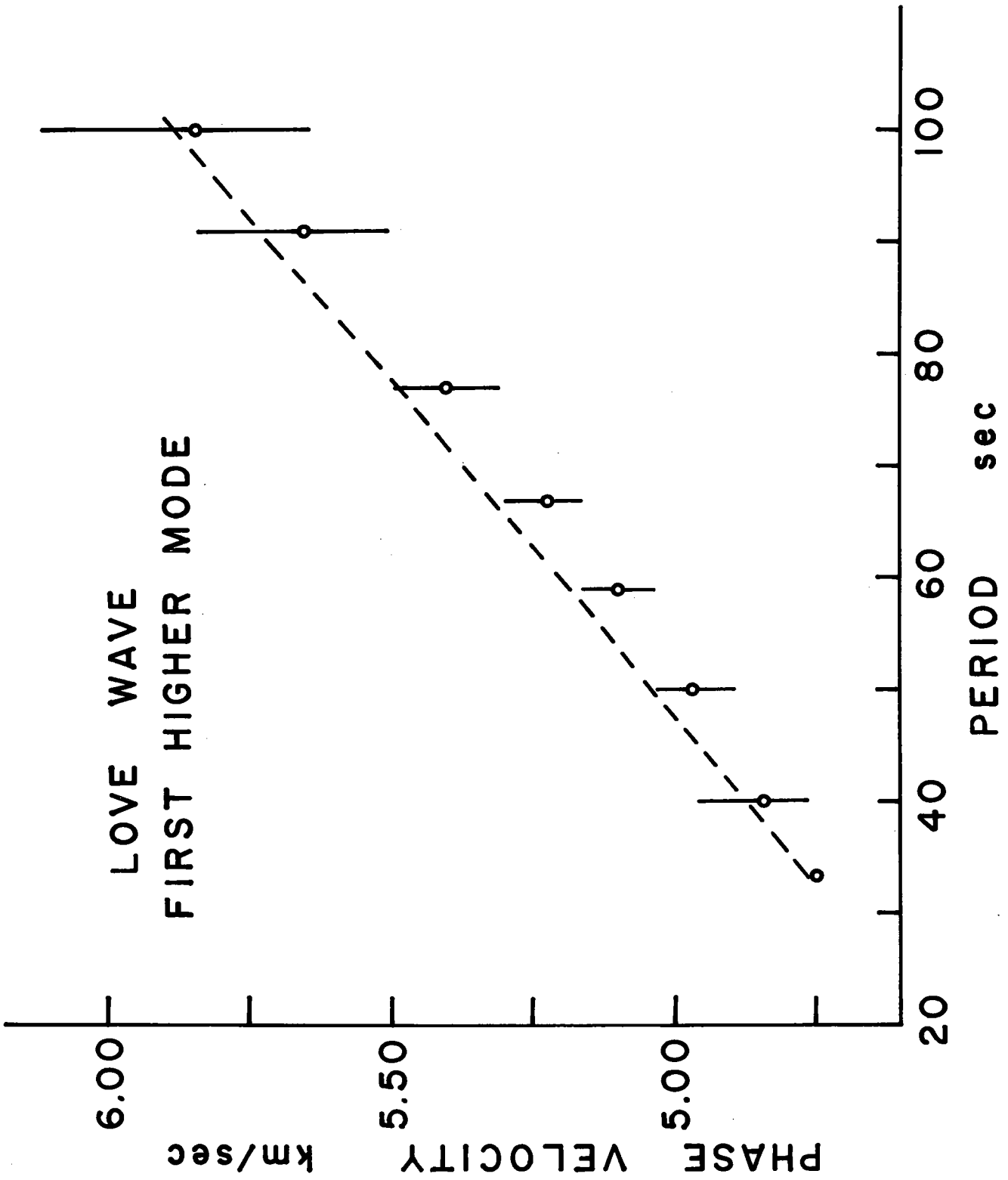
LOVE WAVE
FIRST HIGHER MODE
PHASE VELOCITY km/sec
6.00
5.50
5.00
20
40
60
80
100
PERIOD sec

4.7 Search for contamination of the fundamental mode

The fact that a very simple regional model with only two oceanic and one continental division explains the observed phases at each station with an RMS error of less than six seconds is strong evidence, in my opinion, that the phase velocity fundamental mode is not significantly biased by contamination with higher modes. If this contamination were important, such precision would not be expected. However, a thorough search for such bias has been carried out. The procedure is as follows.

The phase velocity of the fundamental mode is modelled in four different regions; 0-10 m.y. old, older than 10 m.y. ocean, North America, and South America. In addition, the average first higher mode phase velocity is modelled, with a relative amplitude equal to the theoretical relative excitation given in figure 24 for 0-10 m.y. sea floor. A five-dimensional grid of possible values of each of these parameters is searched for minima in the sum of the squares of the residual phases. At each grid point, the theoretical phase expected at each station is computed according to equation 15 with the appropriate values of each parameter. The square of the difference between this theoretical phase and the observed phase is then summed over all paths. This process is repeated for every grid point, building up a map of the sums of the squares of the errors in five-dimension space. This map is

then examined for local minima. At first, a coarse grid is used merely to determine the approximate location of the local minima. Then finer grids are employed in the vicinity of each of these approximate locations to more precisely locate the minima and to determine the lowest value reached within each minima.

The results of a small part of this search in the vicinity of the best fitting model are shown in figure 34. In this particular portion of the grid space, the continental phase velocities are held equal to the values found for model 3 Table 10. In the left hand side of the figure, the test value of the fundamental mode phase velocity in the older than 10 m.y. zone is 4.55 km/sec. On the right, it is changed to 4.53 km/sec. Thus, these two contour plots show the variation of the sum of the squares of the errors in three dimensions. Two local minima are found within this region. The absolute minimum occurs at a phase velocity of about 4.55 km/sec in the older than 10 m.y. zone, 4.41 km/sec in the 0-10 m.y. zone, and 5.40 km/sec for the higher mode. The grid point with the smallest sum is the best model of the phase velocities. An F-test is used to compare the fit of the best model with the fit of all other models. The two local minima shown here are the only two which fall within the 95% confidence limit of the F-test. The

minimum reached in the upper region is smaller than the minimum in the lower region and the phase velocity of the first higher mode required by the lower region is unreasonably slow. These minima can be followed in similar plots to other periods; the upper local minimum gives consistently better results. We can therefore be confident in choosing 5.40 km/sec as the approximate phase velocity of the first higher mode at 77 seconds period. By searching out the boundaries of the region within the 95% confidence level, limits can be placed on the possible phase velocities. For example, with the phase velocity in the older than 10 m.y. zone reduced to 4.53 km/sec, the acceptable region has almost disappeared. At velocities a little slower than 4.53 km/sec, no acceptable models are found. The limits are larger than those given in Table 11 because they are at the 95% level, or about 2 standard deviations away from the central value in a linear problem.

The net result of the five-dimensional grid search performed at each frequency is that the limits placed on the higher mode velocities in figure 33 are correct, and that there is no significant error in the fundamental mode Love wave phase velocities found by ignoring the effect of the higher modes. As stated previously, 95% confidence limits can not be placed on the phase velocity of the higher mode at periods less than 50 seconds. Thus, although

there is no positive evidence of such a bias, it may be possible that there is a small degree of systematic contamination of the fundamental mode at periods less than 50 seconds.

Figure 34. Search for the minimum sum of the squares of the residuals. Contour lines mark equal error levels in the attempt to predict the observed Love wave phase simultaneously at all stations. The dots mark the position of local minima. Numbers labelling the minima and contours are proportional to the sum of the squares of the errors. Heavy line marks the 95% confidence level. C_{1st} is the average phase velocity of the first higher Love mode; C_{0-10} and $C_{>10}$ are the phase velocities of the fundamental mode in the 0 to 10 m.y. and 10 to 50 m.y. age zones, respectively. The period is 77 seconds.

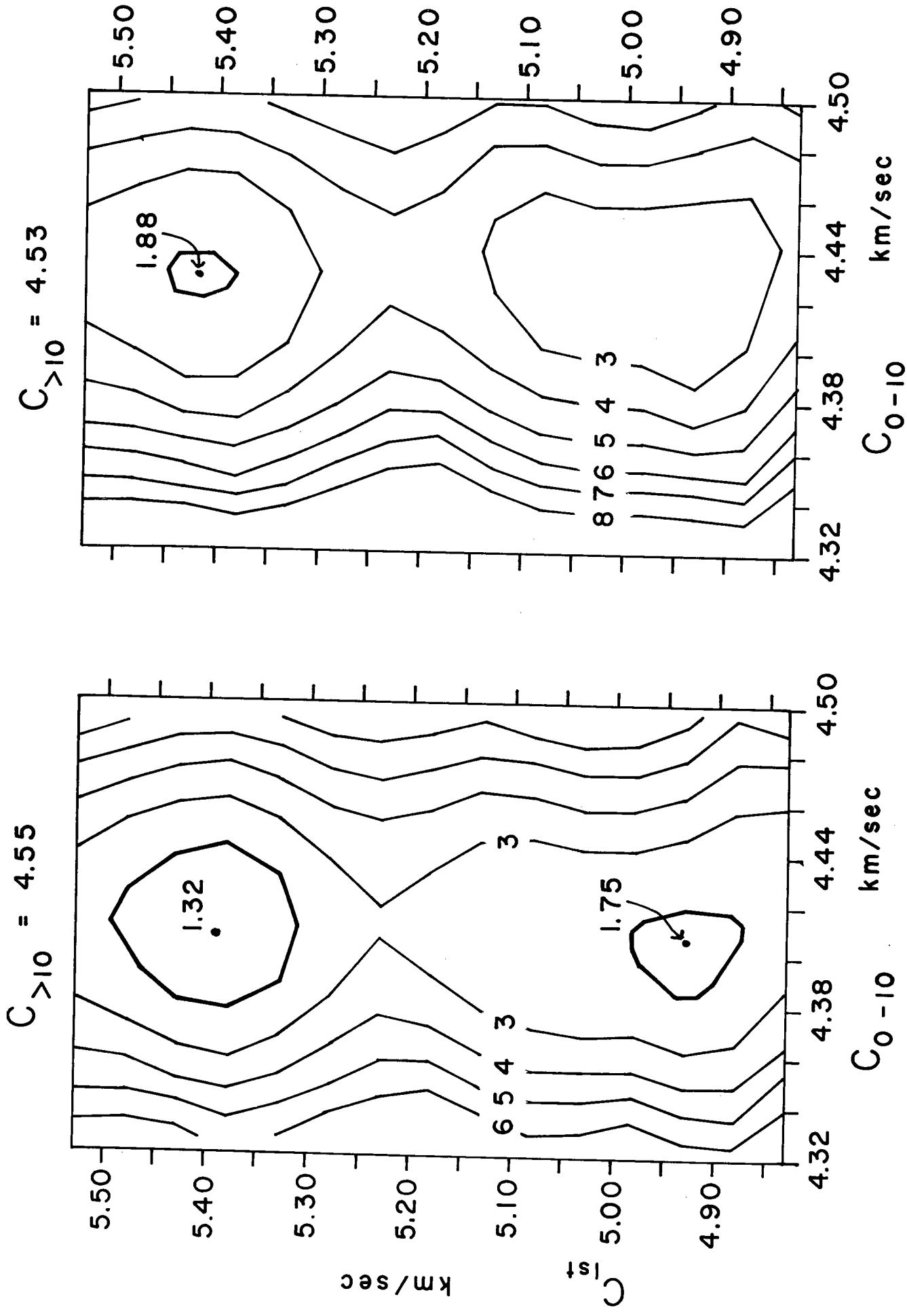
$C_{>10}$ = 4.55
1.32
1.75
3
6 5 4 3
C_{0-10}
km/sec
4.50
4.44
4.38
4.32
5.50
5.40
5.30
5.20
5.10
5.00
4.90
C_{1st}
km/sec
$C_{>10}$ = 4.53
1.88
8 7 6 5 4 3
C_{0-10}
km/sec

5. Models of the upper mantle

The regionalized surface wave data require lateral variations in the structure of the oceanic upper mantle. In this section, a structural model is presented for each age zone, showing that the primary changes are confined to the upper 80 km of the mantle. In addition, possible models of the source of the observed anisotropy are given. Until recently, most studies of the earth structure using surface waves have reported a model which fit the data, without indicating which features of the model were actually required. Backus and Gilbert (1967, 1968, 1970) have presented a formalism for treating this inverse problem, demonstrating that although an exact, unique solution is not possible because of insufficient information, unique linear averages of the solutions can be computed. They have also shown that there is a tradeoff between the ability to resolve detail and the accuracy to which this detail can be estimated. Their method is based on the fact that the inverse problem for surface waves is an approximate linear problem: changes in surface wave velocities are nearly linear with respect to small changes in the earth model. A starting model is established which comes close to fitting the data. The linear approximation then reduces the problem to solving an under-determined set of linear equations for the first order corrections to the starting model. The starting model is

corrected as indicated by the linearized equations; the exact velocities are computed for the corrected model, which is then used as a new starting model. This iterative procedure insures that the final model will not be in error due to the nonlinearity of the derivatives. I have used the matrix formulation of the general inverse problem presented by Wiggins (1972) and the discussion and notation in the brief review below closely follows that of Wiggins.

5.1 Inversion technique. A set of m observations O_j and model parameters P_i leads to a set of m linear equations in n unknowns

$$\underset{m \times n}{A'} \quad \underset{n \times 1}{\Delta p'} = \underset{m \times 1}{\Delta c'} \qquad (18)$$

Each member of the column vector $\Delta c'$ corresponds to the difference between one observed velocity O_j and the corresponding velocity C_j calculated for the starting model. The matrix A' contains the partial derivatives $\partial C_j/\partial P_i$ of the velocities C_j with respect to the model parameters. The generalized inverse minimizes both $|A' \Delta p' - \Delta c'|^2$ and $|\Delta p'|^2$, thus finding the smallest set of parameter changes $\Delta p'$ that will solve the simultaneous equations.

The columns of the derivative matrix A' and the parameter

changes $\Delta p'$ are weighted by terms proportional to the average value of the parameter in each layer divided by the thickness of the layer, so that inverse will not be sensitive to the particular layer parametization chosen. The observations and the rows of A' are weighted proportionally to the certainty of the observations (inversely proportional to the standard deviation). In the weighted system, we have

$$A \, \Delta p = \Delta c \qquad (19)$$

The matrix A can be factored as

$$\underset{m \times n}{A} = \underset{m \times k}{U} \; \underset{k \times k}{\Lambda} \; \underset{k \times n}{V^T} \qquad (20)$$

if there are k independent equations among the m equations of (19). Λ is a diagonal matrix containing the k eigenvalues λ_i of A. The observations are reordered into a new set of k linear combinations of the data, with each combination providing independent data about the structure. Similarly, the model correction parameters are recombined into a new set Δp^* of linear combinations of the old parameters, with each new parameter correction being determined by one of the independent observations. With the new parametization

$$\Delta p = V\Delta p^*$$

the solution or generalized inverse is

$$\Delta p^* = \Lambda^{-1} U^T \Delta c \qquad (21)$$

The standard deviations of Δp_i^* are reciprocals of the eigenvalues λ_i. By convention, the eignevalues are numbered in descending order of their size, so that the corrections Δp^* are ranked in order of their certainty.

In practice, since the data are imperfect, it is difficult to tell exactly how many independent equations are present (or equivalently, how much independent information is contained in the data). In the Wiggins formulation, the number k is limited by the acceptable level of standard deviations to the parameter corrections $\Delta p'$. The variance of the parameter changes to the original model is expressed in terms of the variance of Δp^*, and the largest value of k is found which yields acceptable variance in $\Delta p'$. The linear combinations of Δp that are well-determined are given by the resolution matrix VV^T. If we can resolve a linear combination of physically adjacent parameters, such as the shear velocity in three consecutive layers, then we have compact resolution and the average shear velocity over the three layers can be determined.

However, as will be seen later in the inversion of anisotropy, the resolvable combination may consist of parameters from separate parts of the model, or parameters of different types, such as β and ρ. If the resolution is not compact, the resolution matrix defines a family of possible earth structures in which there is a tradeoff between the parameter values in two or more different parts of the model.

5.2 The starting model. Crust. The same crustal section (table 12) was used in every inversion, except for variation allowed in the thickness of the water and sediment layers. The compressional velocities and layer thicknesses represent a composite of 9 crustal sections in the Nazca plate (Hussong, et al., 1972). Distributed across the Nazca plate at about 10°S, the crustal sections were measured using two-ship, reversed, seismic refraction profiles. There is little apparent variation with age. Shear velocities given in table 12 are derived from the observed compressional velocities assuming a Poisson's ratio of 0.25. The density is arbitrarily set at 2.84 g/cm^3. Sediment cover in the Nazca plate is quite thin and increases with distance from the East Pacific rise (Ewing, et al., 1969, and S. Johnson, personal communication). Water and sediment thicknesses used in this study are: 0-10 m.y., 3.25 km and no sediment; 0-5 m.y., 3.2 km and no sediment; 5-10 m.y., 3.4 km and no sediment; 10-20 m.y., 3.75 km and 100 m; older than 10 m.y., 4.0 km and 100 m; and older than 20 m.y., 4.15 km and 200 m. Sediment thickness is somewhat greater in a few areas such as the Panama Basin (Van Andel, et al., 1971), but this increase was not considered in the inversion of the surface wave data.

Mantle. The partial derivatives or variational parameters are not recomputed after each iteration. Therefore, it is important that the starting model be close to the final

model. The initial set of derivatives used for all regions was generated for a single model with a standard crustal section and water depth 4.0 km. β was assigned a value of 4.50 km/sec from the base of the crust to 60 km depth, 4.10 km/sec from 60 km to 125 km, 4.30 km/sec from 125 km to 250 km, and 4.65 km/sec from 250 km to 380 km. Below 380 km, model O1 of Dziewonski (1971) was used and no variation was allowed, as the data is quite insensitive to changes at this depth. Figure 1 demonstrates the nonlinearity of the problem. The derivatives are model dependent as is shown by the discontinuity of the derivatives at 60, 125 and 250 km caused by the shear velocity discontinuities in the model.

A uniform density of 3.40 g/cm^3 (Dziewonski, 1971) was assigned to the upper mantle down to 380 km for the purposes of computing derivatives. (Jordan and Anderson (1973) suggest an average of 3.42 g/cm^3 for the upper 400 km.) However, a preliminary inversion showed the combined Love and Rayleigh wave data contain no independent information about density, so, in subsequent modeling, the density of the mantle in each age zone was fixed by a simple isostatic model. The mid-ocean ridge system is thought to be essentially in isostatic equilibrium (Sclater and Francheteau, 1970), thus I require constant mass in a column above a compensation depth of 100 km. 100 km was chosen because it is expected to be the maximum possible thickness of the lithosphere. If the density of the

uppermost mantle is uniform within any one column, then

$$\rho_w d_w + \rho_c t_c + \rho_m (d_c - t_c - d_w) = M \qquad (22)$$

where d_w is the depth of water, t_c is the crustal thickness, d_c is the compensation depth, and ρ_w, ρ_c, ρ_m are the densities of sea water, crust, and mantle, respectively. ρ_m was taken as 3.40 g/cm^3 in the oldest zone, and the total mass, M, is constant, independent of the age of the sea floor. The absolute density may not be correct, but, with this adjustment, the lateral changes in density should be correct to first order and thus will not significantly bias the relative changes in shear velocities deduced for each age zone.

Rayleigh wave velocities also depend to some extent on the distribution of compressional velocity, α. α was arbitrarily set at 8.0 km/sec if β was greater than or equal to 4.4 km/sec or 7.7 km/sec if β was less than 4.4 km/sec. Except in the uppermost 25 to 30 km of mantle, the partial derivatives are an order of magnitude greater for β than α. Consequently, small errors in the compressional velocity will not significantly affect the inversion, and, conversely, the data contain very little information on the distribution of α.

After the first iteration, the solution was smoothed so that the sharp discontinuity at 60 km in the initial model was

not a required feature of the final model. Because the final model for the youngest zone is not close to the original model, a new set of derivatives were calculated using the results of the second iterative step as a new starting model. Two other alterations in the inversion procedure were found to be necessary in the course of the inversion. First, the shear velocity in the uppermost 10 km of mantle is very poorly resolved and also does not exhibit compact resolution (see resolution diagram, figure 36). In order to be consistent with the mantle at compressional velocities observed at the M-discontinuity in seismic refraction experiments and to reduce the uncertainty in deeper structure, β was held at 4.60 km/sec in the top 10 km, except in the youngest zone. In the youngest zone, β in the upper 10 km was required to be the same as in the next 10 km. The second alteration involves a change in the weighting of the parameter corrections. In general, the standard deviations of the parameter corrections are not uniform. As suggested by Wiggins (1972), I equalize the standard deviations by modifying the weighting matrix. In effect, changes in the parameters with large σ are penalized in the attempt to minimize the model changes required to fit the data. With these additions to the technique, inversion typically involved five or six iterations.

Table 12. Standard Crustal Section

h km	α km/sec	β km/sec
4.0*	1.50	0
0.13*	1.70	0.1
0.45	4.20	2.42
1.06	5.81	3.35
1.72	6.53	3.76
2.92	7.38	4.25

*Variable, see text

5.3 The evolving structure of the mantle. The change in shear velocity structure with age are derived from the average phase and group velocities of Rayleigh waves within each zone, as represented by the terms which are independent of azimuth. However, because anisotropy has been shown to be significant, interpretation of the aging process in terms of the cooling of the upper mantle requires the additional assumption that the degree of anisotropy is independent of age. In an isotropic medium, surface wave propagation will be independent of direction and the effective shear velocity structure will be the same for both Love and Rayleigh waves. In general, if this isotropic medium is perturbed by the addition of slight anisotropy, not only will directional variation in velocity be created, but the overall average velocity will be altered. In the case of transverse isotropy with the symmetry axis parallel to the free surface, no azimuthal terms are introduced: the only change which can be detected by surface waves is in the average velocity of the Love and Rayleigh waves. Thus, a change in Rayleigh wave dispersion which may appear to be due to the change in shear velocity accompanying the cooling of the lithosphere may actually be due to a change in the degree or form of anisotropy. Also, unless the exact form of the anisotropy is known, the effective shear velocity distribution felt by the Rayleigh waves can not be interpreted

directly in terms of the pressure and temperature derivatives of known mineral assemblages. However, if the degree of anisotropy is independent of age, the relative changes in the effective shear velocity may be representative of the changes in the in situ shear velocity averaged over all directions. I therefore examine the evolution of the mantle, assuming the degree and form of the anisotropy remain unchanged.

The final models of the shear velocity structure in the 0-10 m.y. and 10-50 m.y. zones are shown in figure 35. The thirteen layers used in the inversion of the average Rayleigh velocities are described in the caption to figure 36. The degree of uniqueness in these models is determined by the resolution matrix. With standard deviations in the corrections to the shear velocity of 0.02 km/sec in the older zone and 0.04 km/sec in the younger, there are five independent pieces of information about the shear velocity structure contained in the Rayleigh wave data. The distribution of this information is illustrated by the averaging kernels shown in figure 36. Each histogram corresponds to one row of the resolution matrix, giving the averaging kernel centered on one layer. The resolution matrices for the two regions are nearly identical, although the standard deviations are different.

The most important feature of the resolution matrix is that it is reasonably compact. There is little possible tradeoff between separate parts of the mantle. This permits

the resolution of a unique average of the shear velocity over a continuous depth interval. The resolution length, or depth interval in which the average shear velocity can be computed, can be estimated from the diagonal of the resolution matrix. The sum of the diagonal terms is k, the number of independent data. If the sum of the diagonal elements of sequential rows is one, then the combination of the layers represented by those rows will be resolved and the sum of the layer thicknesses gives the resolution length (Wiggins, 1972). I have used fractional layers, when necessary, to obtain more accurate estimates of the resolution length, so the depth intervals in Table 13 do not always correspond to an integral number of layers. The required features of the models can be deduced from Table 13, which gives the average shear velocity over various depth ranges corresponding to the resolution length in each section of the model. The shear velocity in the uppermost layer is not very well resolved (see figure 36). For this reason, the velocity was constrained during inversion as discussed in the previous section.

The resolution length varies from 20 km centered at a depth of about 30 km, to 180 km centered at about 300 km (Table 13). The low velocity zone is well resolved. The 4.1 km/sec minimum is much lower than the global average, which reaches a minimum of about 4.35 km/sec at roughly 200 km according to Jordan and Anderson (1973). Below 150 km

the model required by the Rayleigh wave data is nearly the same as their model B1. From 146 to 371 km depth, the average shear velocity in B1 is 4.48 km/sec. From 150 to 380 km in the 0-10 m.y. zone the average is 4.50 km/sec; in the 10-50 m.y. zone, it is 4.54 km/sec. Although other gross earth, average models are slightly different, the agreement is remarkable. Comparison with the Canadian shield model of Brune and Dorman (1963), which averages 4.59 km/sec from 150 to 380 km, suggests there is little or no change in the upper mantle below about 150 km from the youngest sea floor to an old, Pre-Cambrian shield. Within the area of this study, there is no significant difference deeper than 80 km between the two age zones. The average ages of the two zones considered here are about 4 m.y. for the younger zone and 22 m.y. for the older. In the following discussion, the lithosphere-asthenosphere boundary is considered to be the top of the low-velocity zone. The asthenosphere continues deeper than the zone of very low velocities, down to about 250 km.

The similarity in shear velocity implies a lateral uniformity of temperature with the low velocity zone beneath the ocean. If this uniformity continues into older sections of the sea floor, it strongly supports a class of geochemical and thermal models in which efficient, small-scale convection beneath the continents and oceans maintains

a uniform, nearly adiabatic temperature gradient under the lithosphere (Sclater and Francheteau, 1970). The small-scale convection which could maintain uniform temperatures could not be part of a large-scale convective overturn coupled with the lateral plate motions. If the mantle convection is strongly coupled to the plate motion, the asthenosphere would grow old along with the surface plates. It would cool off, the low velocity zone would gradually disappear, and the lithosphere would continue to increase in thickness. Leeds (1973) has suggested that the 4.1 km/sec low velocity zone disappears and that the lithosphere increases in thickness to about 160 km in sea floor 150 million years old. However, Leeds did not have sufficient data to constrain this thickness precisely, and did not allow changes in velocity within the lithosphere or the possibility of anisotropy. At 100 m.y., with better data coverage, he found that an 85 km lid with a 4.1 km/sec low velocity zone explained the Rayleigh wave phase velocities. Within the uncertainty of the data, this is consistent with the hypothesis that no change occurs in the oceanic mantle deeper than about 80 km. The final resolution of this problem requires more data in the oldest parts of the oceans, possibly with a density of coverage comparable to that employed in this study.

There is another possible explanation for absence of change in the low velocity zone other than uniformity of

temperature. It may be that a sharp reduction in shear velocity occurs at the onset of melting and that increased melting at higher temperatures only gradually reduces velocities (Spetzler and Anderson, 1968). A sharp drop in velocity would then occur at the base of the lithosphere; as the asthenosphere cooled off, the boundary between lithosphere and asthenosphere would deepen, but no significant change would occur in the velocity of the low velocity zone. This is, in fact, probably a valid mechanism. However, if there were significant lateral variations in temperature within the asthenosphere and this mechanism were operative, then the lower boundary of the 4.1 km/sec low velocity zone would be highly variable. Because the vertical temperature gradient within the mantle at a depth of 150 to 200 km can not be as great as in the upper 50 km, a relatively small change in temperature can cause a large change in the depth to the solidus. As we have seen, there is no significant change in the mantle below 150 km that would reflect the downward migration of the solidus.

Although it is always difficult to pinpoint velocity discontinuities in the inversion of surface wave data, a pronounced decrease in shear velocity must occur near a depth of 60 to 70 km in the 10-50 m.y. zone. The average velocity from 30 to 55 km is 4.42 ± .02 km/sec, which is very similar to the 20 to 40 km average (Table 13). The

60 to 100 km average is 0.24 km lower. It is unlikely that the 4.4 km/sec layer continues much deeper than 70 km, because the average velocity between 50 and 90 km is also significantly lower than the 30 to 55 km average. I associate the sharp drop in velocity with the beginning of a partially molten zone and conclude that the thickness of the lithosphere in the 10-50 m.y. zone is about 60 to 70 kilometers. For the 0-10 m.y. zone, the velocity averages are less than 4.30 km/sec everywhere above 150 km. Consequently, the lithosphere must be very thin. The lithosphere is expected to grow very rapidly in the first few million years (Parker and Oldenburg, 1973), so the lack of a well-defined discontinuity may be due to the averaging of a wide range of structures within the younger zone. The pure-path velocities for each of the four age zones listed in Table 7 have been inverted to obtain more detailed information about the evolution of the lithosphere.

The shear velocity structure of the mantle shallower than 100 km is shown in figure 37 for the age zones 0 to 5 m.y., 5 to 10 m.y., 10 to 20 m.y., and 20 to 50 m.y. In each inversion, only the shear velocity from the base of the crust to a depth of 80 km was allowed to vary. Below 80 km, the structure of the mantle was fixed at an average of the structures deduced for the 0 to 10 and 10 to 50 m.y. zones.

The average was weighted 2:1 in favor of the older zone, i.e. in inverse proportion to the standard deviations of the velocity averages. This procedure formalizes the hypothesis that no changes occur deeper than 80 km. The ability to fit the data was not damaged by this restriction. Figure 38 shows the difference between the observed pure path velocities in the 0-10 and 10-50 m.y. zones and the corresponding theoretical velocity computed for the models shown in figure 35. At every frequency, the misfit is less than 2 standard deviations, and more than two thirds of the data are fit within $\pm 1\sigma$. Both models are excellent fits to the data. The quality of the fit obtained is comparable for all four of the models in figure 36. As demonstrated in figure 39, all residuals are less than two standard deviations and more than two thirds of the data for each age zone are fit within one standard deviation.

The resolution lengths in the 0-5, 10-20, and 20-50 m.y. zones are 20 to 25 km with a standard deviation in shear velocity of about 0.05 km/sec. For the same accuracy, the resolution length in the 5-10 m.y. zone is about 35 km. The structure required to fit the data in this zone is rather odd and may be due to errors in the data caused by the rapid change in lithospheric thickness in this age range. Because not every path covers the same frequency range, the spatial

distribution of coverage of each age zone will vary a little with frequency. If the zones are not fairly homogeneous, some unusual aliasing effects may be introduced in which the lower frequencies may be sampling a younger mantle than the high frequencies, or vice versa. However, I believe that the gross structure is probably a representative average of the structure in the 5 to 10 m.y. zone.

The dividing point between lithosphere and asthenosphere is chosen to be at about 4.3 km/sec. In peridotite under constant pressure, an increase in temperature of 1000°C, while remaining below the temperature at the solidus, will cause a decrease in shear velocity of about 7% (Birch, 1969). Thus, a lateral shear velocity contrast of 0.3 km/sec is possible in a cross-section of the mantle without necessarily indicating partial melting. Somewhat greater contrast is possible if solid-solid phase changes occur. As the depth within the section increases, the pressure tends to raise the shear velocities. A decrease in shear velocity of more than 0.25 km/sec from the top of the lithosphere to a depth of 70 km is unlikely without the occurrence of partial melting (see Forsyth and Press (1971) for examples of the competing effects of temperature and pressure within lithospheric slabs). The maximum shear velocity in any of the models presented in figure 37 is 4.5 to 4.6 km/sec. The 4.3 km/sec layer in the 0-5 and 5-10 m.y. models may be solid, but shear velocities

below 4.3 km/sec anywhere else probably indicate partial melting.

The lithosphere apparently reaches a thickness of about 60 km within only a few million years and subsequently only grows gradually, reaching a thickness of 70 km in the 20 to 50 m.y. age zone. The lithosphere in the 0-5 m.y. zone can be no thicker than 30 km, including the water and crustal layers. In addition to the growth of the lithosphere at the expense of the low velocity zone, the average shear velocity within the lithosphere increases with age. This is the expected behavior. As the lithosphere cools, the velocity should continue to increase beyond the oldest zone considered in this study. In the cooling slab type of lithospheric model (Langseth, 1966; McKenzie, 1967; Sleep, 1969), with thicknesses of 70 to 100 km, the minimum age in which equilibrium is reached is 50 m.y. (Forsyth and Press, 1971). In most models, changes continue to occur in the shear velocity for more than 50 m.y. If eclogite is present, transformation to the densest phase may not be completed within the first 100 m.y. (see figures 8 and 9 in Forsyth and Press). In this study only two changes in the structure of the mantle have been found: the lithosphere grows in thickness, and the average shear velocity within the lithosphere increases with age. There is no significant change in the mantle deeper than 80 kilometers.

Table 13. Mantle shear velocity structure from Rayleigh waves

Depth range	0-10 m.y.	10-50 m.y.
km	β, km/sec	β, km/sec
20-40	4.26 ± .04	4.46 ± .02
30-55	4.21	4.42
40-73	4.10	4.35
50-87	4.03	4.26
60-102	4.04	4.18
70-123	4.07	4.13
80-138	4.10	4.11
100-163	4.17	4.17
125-218	4.30	4.33
150-247	4.35	4.41
200-380	4.54	4.58

Figure 35. Shear velocity within the upper mantle. Left hand figure based on Rayleigh wave data, right hand on Love wave data. Dotted line, 0-10 m.y. zone; solid line, 10-50 m.y. zone. Deepest layer extends from 250 km to 380 km.

Figure 36. Rows of the resolution matrix for Rayleigh waves with 5 independent pieces of information. Arrows mark the layer on which each row is centered. The shear velocities in thirteen layers are used in the inversions. The first layer is roughly 10 km thick, extending from the base of the crust to 20 km below the sea surface. The next six layers are each 10 km, followed by layers of 20, 25, 25, 50, 50 and 130 km.

Figure 37. Thickness of the lithosphere and shear velocity versus age of the sea floor. The break between lithosphere and asthenosphere is taken to be 4.30 km/sec. Below 80 km, all models are identical.

Figure 38. a. Residuals of the fit of the final model to the pure-path, Rayleigh wave phase and group velocities, 0-10 m.y. zone. Positive residual means model velocity is too low. Vertical bars indicate one standard deviation limits.
b. Residuals to pure-path Rayleigh data, 10-50 m.y. zone. Models shown in fig. 35.

Figure 39 a,b. Residuals of the fit of the final models to the pure-path Rayleigh wave velocities in the 0-5, 5-10, 10-20, and 20-50 m.y. age zones. Models shown in fig. 37.

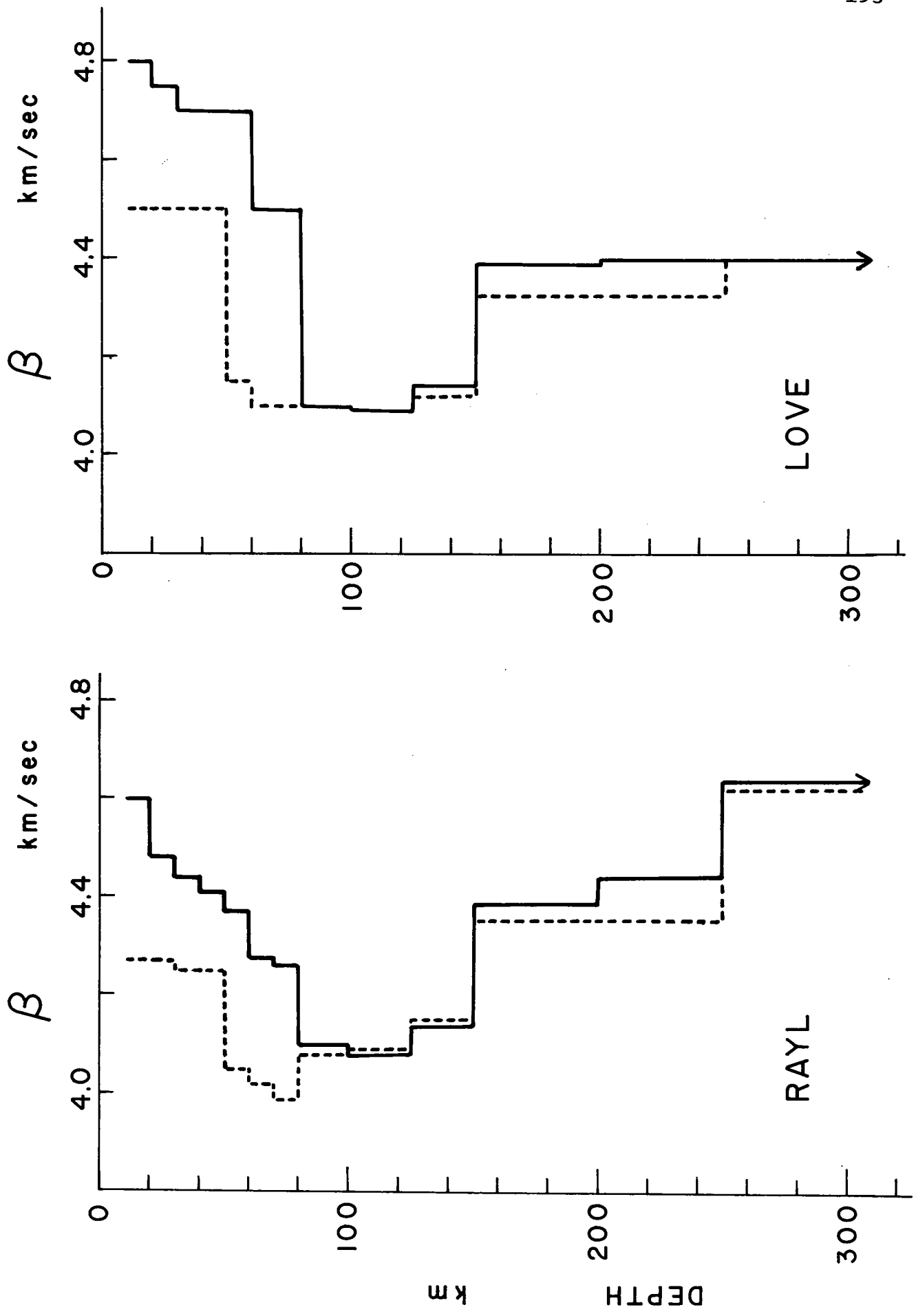
β
km/sec
4.8
4.4
4.0
0
100
200
300
LOVE
β
km/sec
4.8
4.4
4.0
0
100
200
300
RAYL
DEPTH
km

Resolution Matrix

Rayl > 10 m.y.

k = 5

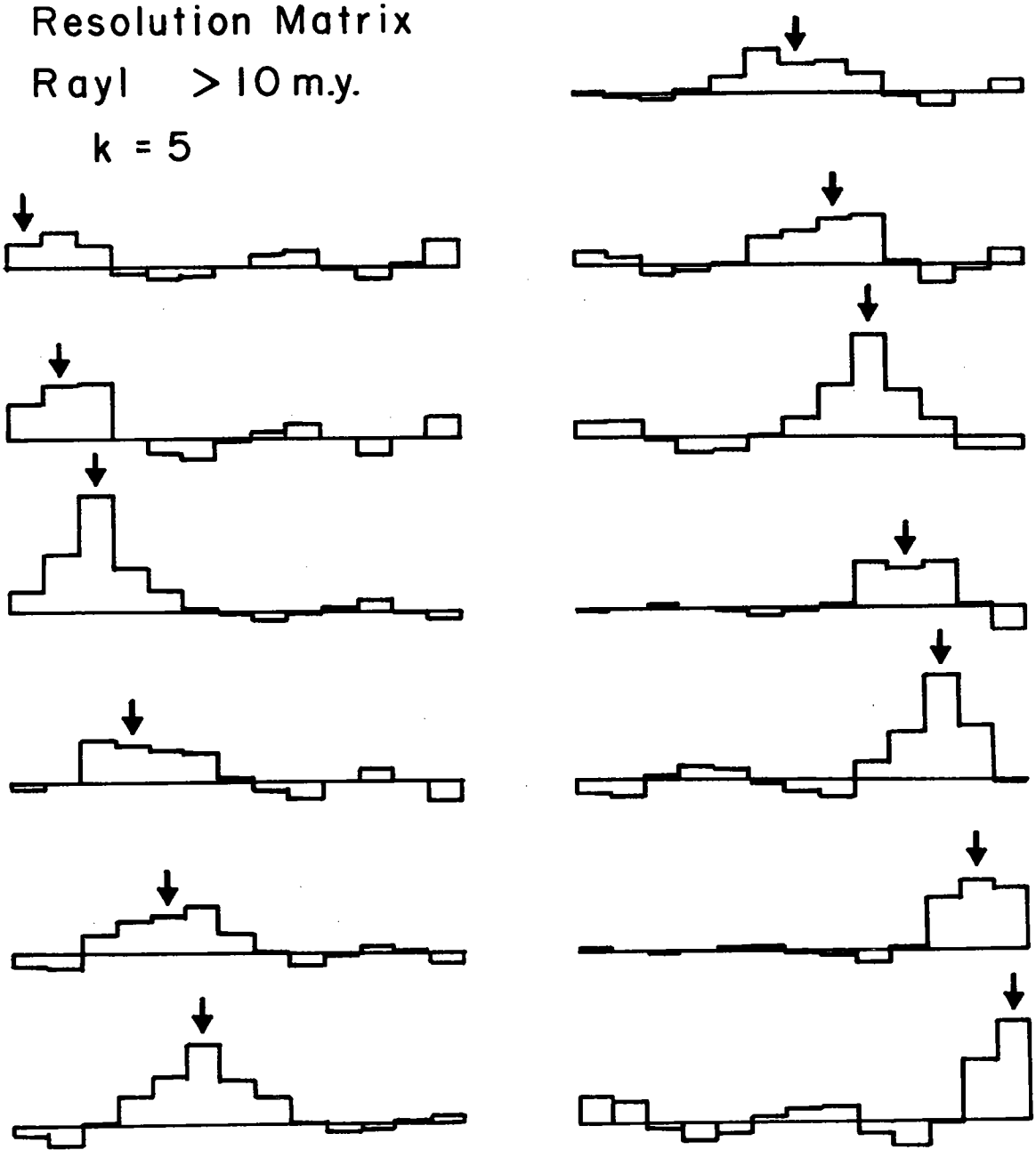

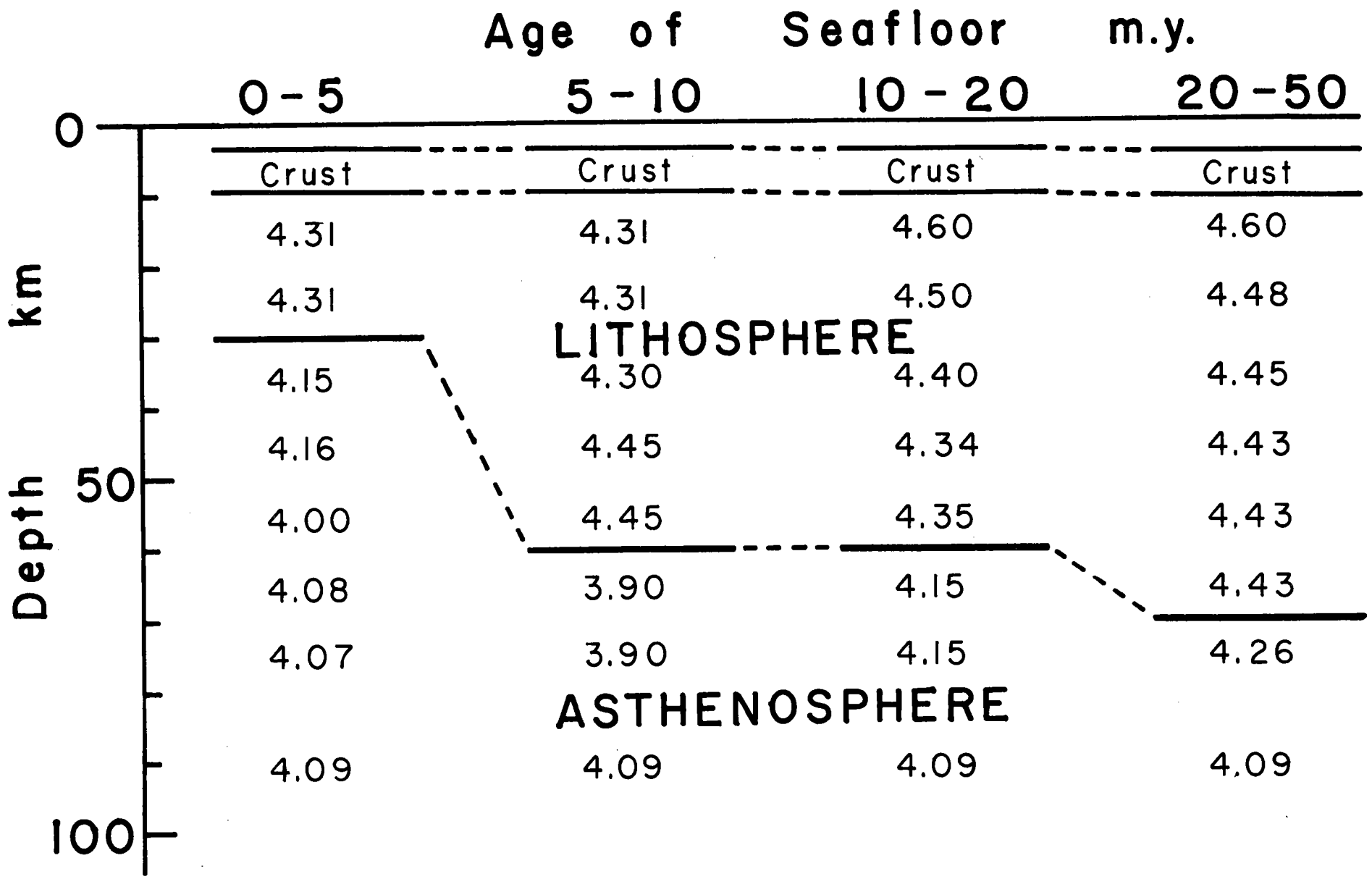
Age of Seafloor m.y.
0-5
5-10
10-20
20-50
0
50
100
Depth km
Crust
Crust
Crust
Crust
4.31
4.31
4.60
4.60
4.31
4.31
4.50
4.48
LITHOSPHERE
4.15
4.30
4.40
4.45
4.16
4.45
4.34
4.43
4.00
4.45
4.35
4.43
4.08
3.90
4.15
4.43
4.07
3.90
4.15
4.26
ASTHENOSPHERE
4.09
4.09
4.09
4.09

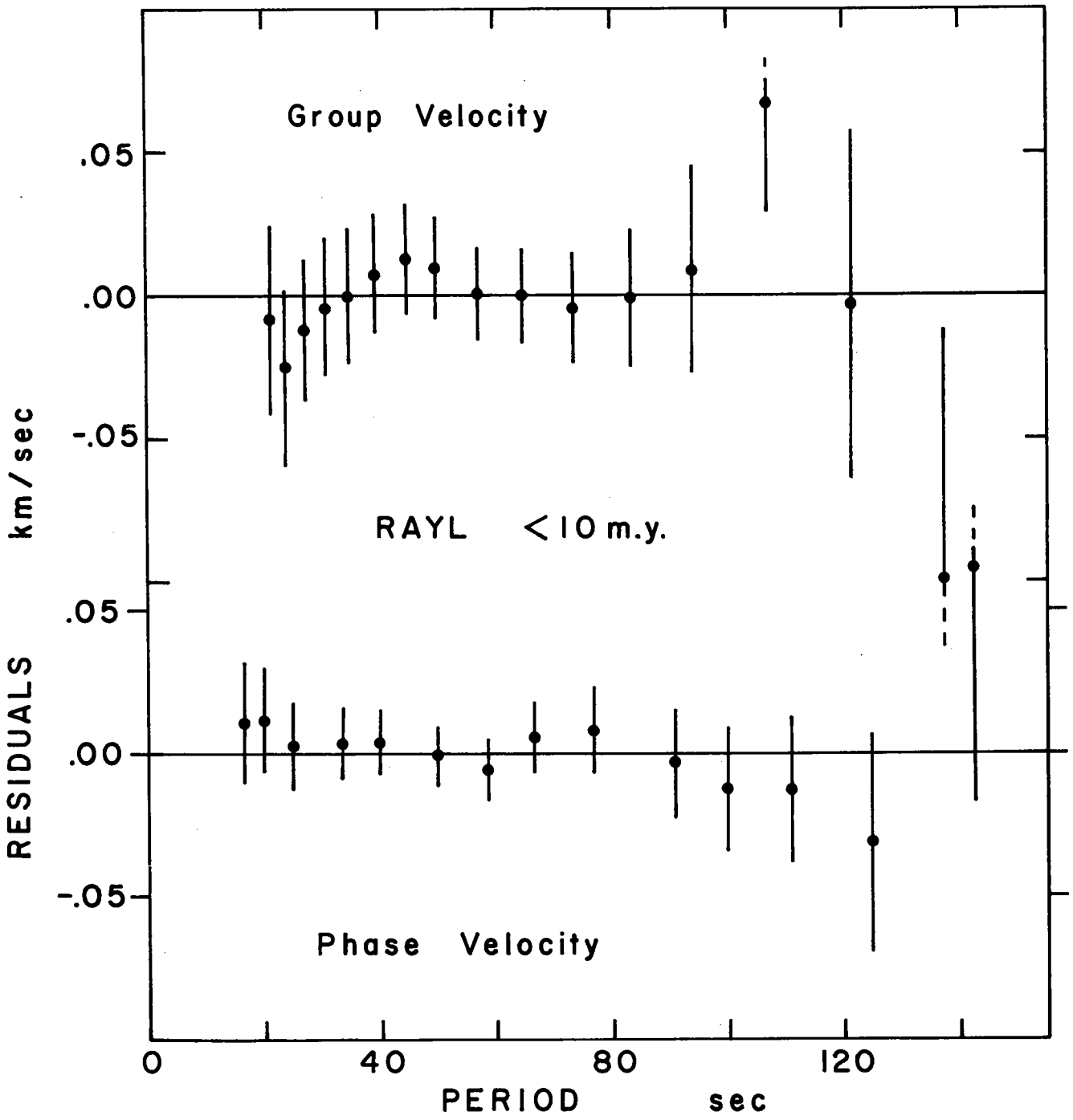
Group Velocity
.05
.00
-.05
RAYL < 10 m.y.
.05
.00
-.05
Phase Velocity
RESIDUALS km/sec
0
40
80
120
PERIOD sec

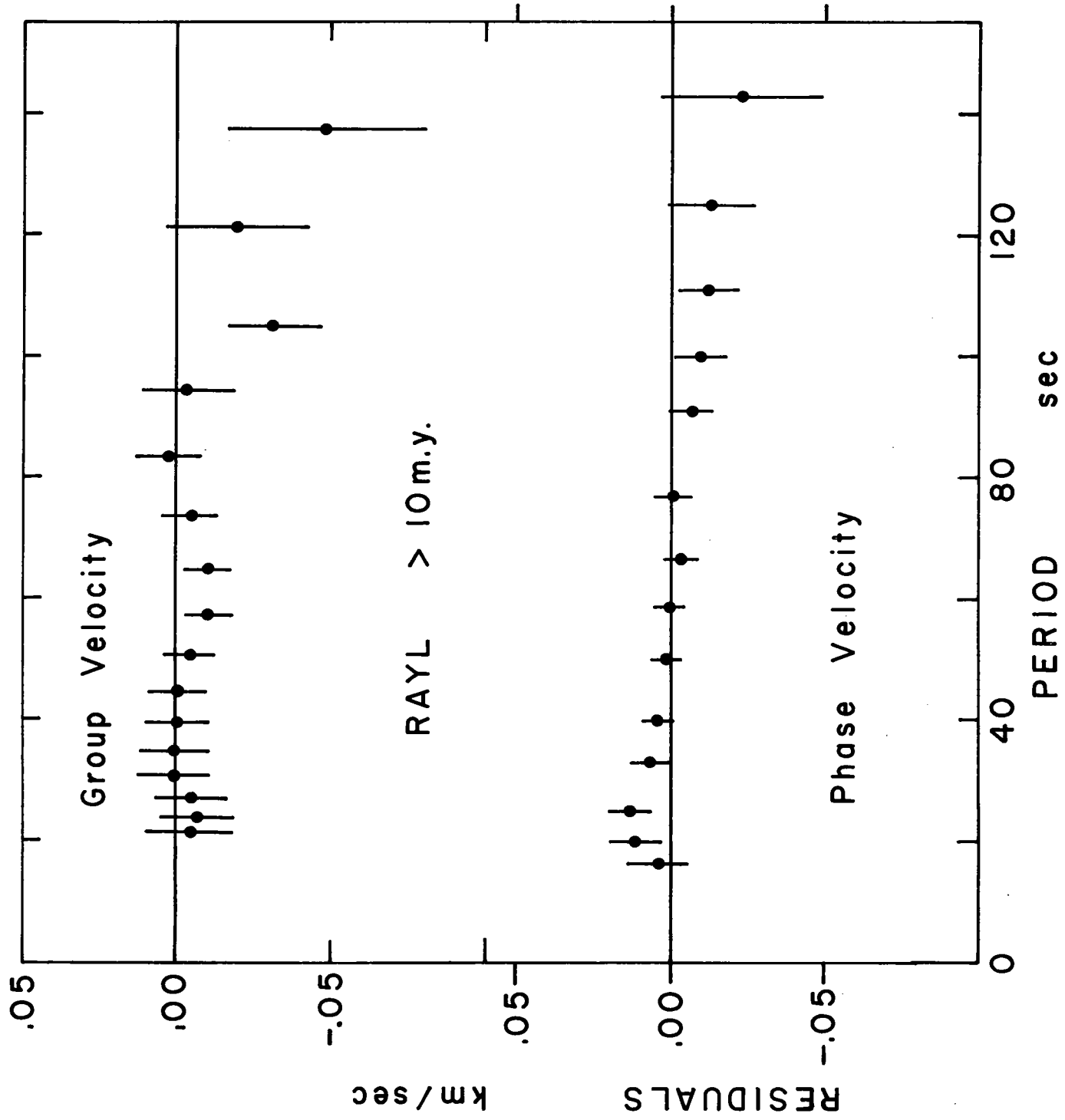
Group Velocity
RAYL > 10 m.y.
Phase Velocity
.05
.00
-.05
.05
.00
-.05
km/sec
RESIDUALS
0
40
80
120
PERIOD sec

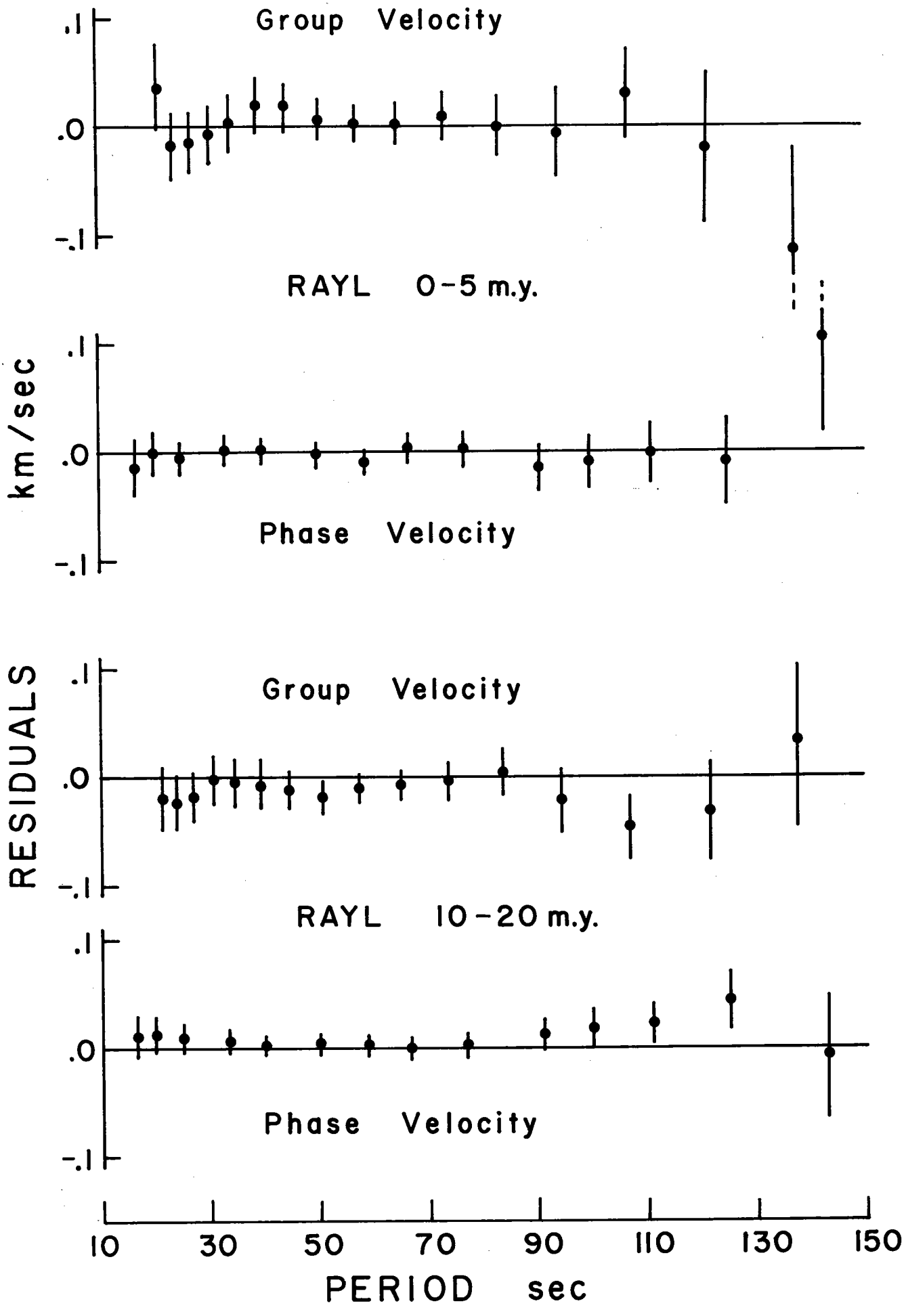
Group Velocity
.1
.0
-.1
RAYL 0-5 m.y.
km/sec
Phase Velocity
RESIDUALS
Group Velocity
RAYL 10-20 m.y.
Phase Velocity
10
30
50
70
90
110
130
150
PERIOD sec

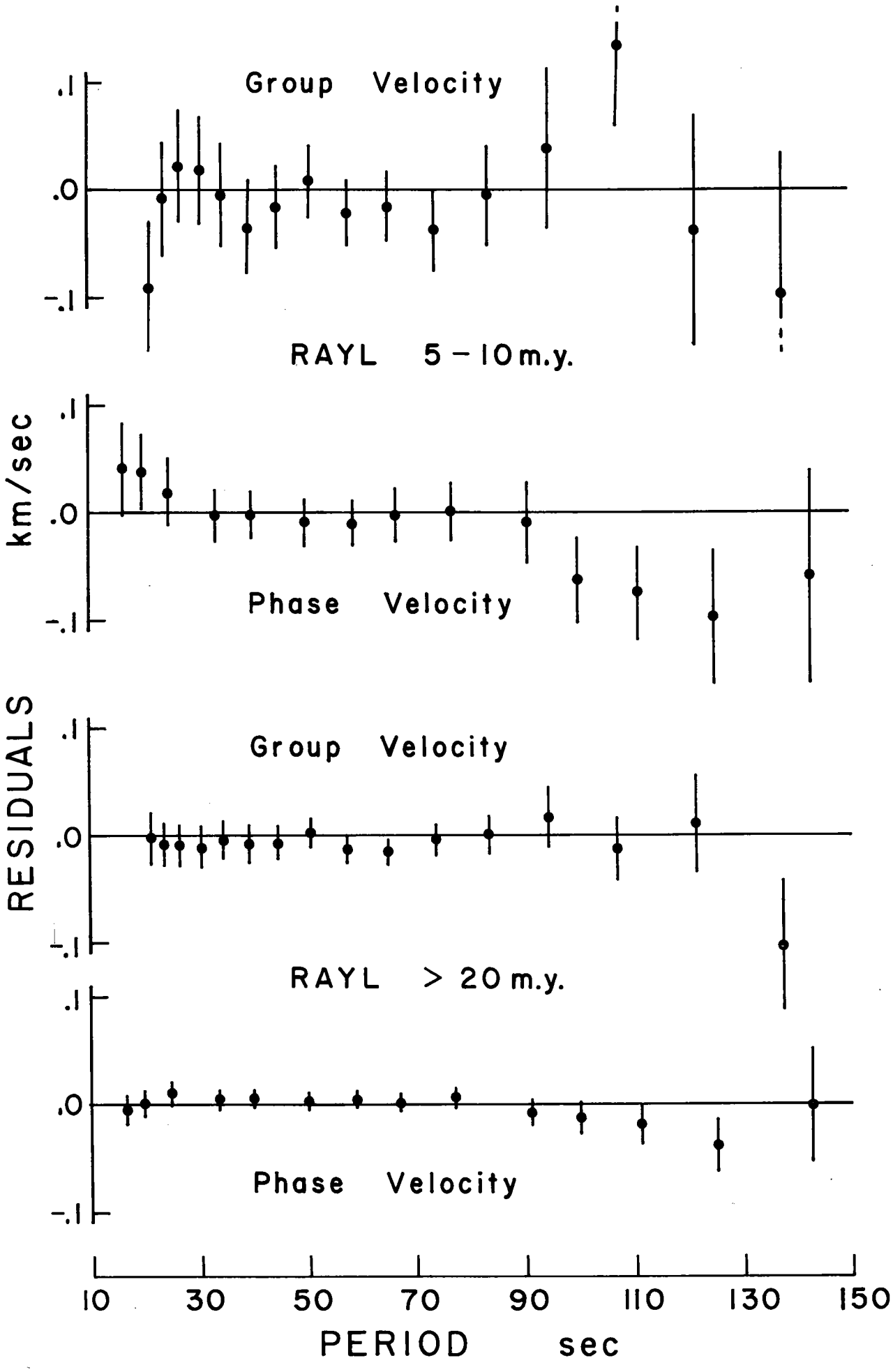
Group Velocity
.1
.0
-.1
RAYL 5 – 10 m.y.
km/sec
Phase Velocity
RESIDUALS
Group Velocity
RAYL > 20 m.y.
Phase Velocity
10
30
50
70
90
110
130
150
PERIOD sec

5.4 Anisotropy. The most general anisotropic medium has 21 independent elastic coefficients. Surface waves alone give information on only 10 combinations of these 21 coefficients. Even if the azimuthal dependence of propagation is perfectly known, Rayleigh waves yield only five pieces of information; the average velocity and the sin 2θ, cos 2θ, sin 4θ and cos 4θ coefficients. Love waves will provide data on another five combinations of the elastic constants. Higher mode data and the frequency dependence of the phase and group velocity coefficients help describe the depth distribution of the anisotropy, but do not give any more information on its form. In this study, the 4θ terms have been ignored, reducing the maximum available data to six. Rather than imposing arbitrary symmetry relations on the medium to reduce the number of unknowns, I have attempted to compute the effective structure of the mantle for waves traveling in different directions. In the previous section, I examined the structures felt by the average Rayleigh wave in each age zone. In this section, I consider what changes in these structures are required to explain the average Love wave phase velocities, the phase and group velocities of Rayleigh waves traveling perpendicular to the ridge, and the phase velocity of Love waves traveling perpendicular to the ridge.

The average Love wave phase velocities are faster than the predicted velocities of the earth models based on Rayleigh wave data. In the 10 to 50 m.y. zone, the predicted velocities of the fundamental mode are too slow by amounts ranging from 0.13 km/sec at 33 sec period to 0.03 km/sec at 167 sec. At 50 seconds, the discrepancy is more than 10 times the standard deviation of the data. An unsuccessful attempt was made to reconcile these differences by simultaneously inverting the Love and Rayleigh wave data. No isotropic structure was found which could explain both sets of data, even when density and shear velocity were allowed to vary simultaneously. An interesting phenomenon occurs when density is a free parameter. In the unsuccessful attempt to simulate the apparent effect of anisotropy, the most successful isotropic models had an unreasonably high density ($\sim$4.0 g/cm^3) in the lithosphere and a very low density in the low velocity zone. This apparent trade-off between anisotropy and density was noted by Mizutani and Abe (1972) who pointed out that if anisotropy is present in the low velocity zone, the high density lithosphere proposed by Press (1970) is not necessary. The possibility of a high density ($\sim$3.5 g/cm^3) lithosphere still exists, but at present, there is no surface wave or free oscillation data which requires it.

The Love and Rayleigh wave data are compatible only if the upper mantle is anisotropic. An estimate of the distribution of the anisotropy is obtained by inverting the Love wave data alone, then comparing the result with the Rayleigh wave structure. The model shown in figure 35 for the 10-50 m.y. age zone fits the data very well (fig. 40). The model is similar to the structure found for Rayleigh waves, except that shear velocity in the upper 80 km is higher, and below 250 km, it is lower. Unfortunately, features of this size are not adequately resolved. With a standard deviation of 0.05 km/sec for the parameter corrections, there are only 2 independent pieces of information about the structure contained in the Love wave data, including the higher mode phase velocities. The low information content is due to several factors. There is no peak in the fundamental Love mode derivatives comparable to the peak in sensitivity of the Rayleigh waves (figure 1). No group velocity measurements are available for Love waves because of the similar group travel-times of the fundamental and higher modes. There are no observations for periods shorter than 33 sec, thus limiting the information about the uppermost layers. Perhaps the most important factor is the large uncertainty assigned to the higher mode observations. Because the observations are given weights inversely proportional to their standard deviations, the higher mode

data contribute little information. The resolution matrix shown in figure 41 graphically illustrates the distribution of the information. The average shear velocity from the base of the crust to 125 km, and from 125 km to 380 km can be resolved with a standard deviation of 0.05 km/sec.

The average, effective shear velocity felt by Love waves in the upper 125 km is 4.41 ± .05 km/sec, compared to an average 4.26 ± .01 km/sec for Rayleigh waves. This means anisotropy exists somewhere in the upper 125 km of the mantle, but it is not necessarily confined to the upper 80 km as depicted in the model of figure 35. The mantle also appears to be anisotropic somewhere between 125 and 380 km. The average, effective shear velocities in this range are 4.37 ± .05 km/sec and 4.50 ± .015 km/sec for Love and Rayleigh waves, respectively. However, this discrepancy may be somewhat exaggerated. Because the Love wave data is more sensitive than the Rayleigh wave data to the structure deeper than 380 km, some of the apparent difference may be due to an error in the assumed structure below 380 km. Taken alone, this data suggests, but does not require, anisotropy deeper than 125 km. Additional evidence of anisotropy is provided by the apparent increase in the azimuthal variations of Love waves at long periods.

Although the change is not statistically significant

at the 95% confidence level, the cos 2θ term (fig. 30 and Table 11) shows that at long periods, the fundamental mode Love wave travels fastest in a direction roughly parallel to the direction of spreading. The shear velocity structure seen by Love waves evidently depends on the direction of propagation. The change in structure with azimuth is found by perturbing an exact model in such a way that the difference between the phase velocities of the perturbed and the original models duplicates the difference between the average, observed phase velocities and the velocities observed for paths perpendicular to the ridge axis. Stated in terms of the inversion notation, the procedure is as follows. We begin with an exact starting model which approximately fits the average Love wave phase velocities. The phase velocity of the model is C_j. $\Delta c_j'$ is established by multiplying C_j by the observed cos 2θ coefficient $(a/c)_j$. Equation 18 is then solved for the changes in structure, $\Delta P'$, in the same way in which the other inverse problems were solved. This same technique is used in a later paragraph to find possible sources of the Rayleigh wave anisotropy. The cos 2θ term for Love waves is explained reasonably well if the SH velocity from 200 to 380 km is 0.20 km/sec faster for Love waves traveling in the direction of spreading than for waves traveling perpendicular to the spreading. However,

taking into account the theoretical resolution, all that can be said is that the average SH anisotropy from 100 to 380 km is 0.13 ± .08 km/sec. This is not significant at the 95% confidence level, but, since the average SH velocity also seems to be faster than the SV velocity measured by Rayleigh waves, I think it is probable that the mantle is anisotropic below 125 km and possibly as deep as 380 km.

There is not much one can say about the structure within the 0-10 zone as seen by Love waves. Although the uncertainty in the fundamental mode phase velocity is fairly small, it is nearly twice the uncertainty in the 10-50 m.y. zone. Consequently, the only confident statements that can be made are that, for Love waves, the average shear velocity in the upper 380 km of the mantle beneath the 0-10 m.y. old sea-floor is less than the average shear velocity in the 10-50 m.y. zone, and the average SH velocity is greater than the average SV velocity seen by Rayleigh waves. Accurate, regionalized observations of the first and second higher Love modes are needed to provide more details, and will be particularly valuable in studying the structure below the low velocity zone.

The Rayleigh waves travel fastest perpendicular to the ridge axes. If only the shear velocity is allowed to vary, the structure which can produce the frequency-

dependent azimuthal variation is well-defined. With β the only parameter, the primary anisotropy must occur between 50 and 150 km, where the average SV velocity in the direction of spreading is 0.10 ± .03 km/sec faster than the average SV velocity perpendicular to the spreading direction. However, when the compressional velocity is allowed to vary, the solution becomes highly nonunique. As the rows of the resolution matrix (fig. 42) indicate, there is a tradeoff between P-wave velocity in the upper 50 km and S-wave velocity, particularly in the low velocity zone. The resolution is not compact. In figure 43, three radically different models are shown; each model is capable of explaining the difference between the average phase and group velocities, and the phase and group velocities of Rayleigh waves traveling in the direction of spreading. The data can be matched with changes in compressional velocities alone. However, this model (dashed line) requires nearly 25% P anisotropy starting a few kilometers beneath the M-discontinuity. The greatest, documented P_n anisotropy observed to date is about 8%, so this model is tentatively rejected as being improbable. The model indicated by the solid line is similar to the model in which only β is inverted. The third model demonstrates that the Rayleigh wave propagation can be explained by anisotropy confined

to the upper 50 kilometers of mantle, with a reasonable P_n anisotropy of about 8%. Even with the very simple models considered here, we are left with a bewildering array of possible forms of anisotropy within the oceanic mantle. Progress in unraveling this puzzle will depend on the acquisition of additional data and the testing of models based on knowledge gained in laboratory experiments.

Several possible mechanisms for producing anisotropy within the upper mantle have been proposed. The preferred orientation of olivine crystals was first suggested by Hess (1964) to explain the observed P-wave anisotropy at the M-discontinuity. Crystal reorientation within the mantle may be caused by syntectonic recrystallization, (Carter and Ave'Lallemant, 1970), by glide mechanisms (Francis, 1969), or by grain boundary slip with grain rotation (Crosson, 1972). The anisotropy of P waves observed in seismic refraction experiments determine only 5 of the 21 elastic coefficients (Backus, 1965) so the problem is underdetermined, but the most probable crystalline source of the P_n anisotropy is preferred orientation of the "a" axis of olivine perpendicular to the ridge axis (Ave'Lallemant and Carter, 1970). Olivine has 9 independent coefficients (Verma, 1960), but if the "b" and "c" axes are randomly oriented about the "a" axis, the number is reduced to five and takes the form of transverse

isotropy. However, preferred orientation of the "b" or "c" axes is also common in olivine rich ultramafic rocks (Birch, 1960, 1961; Christensen and Crosson, 1968) and will also produce transverse isotropy (Crosson and Christensen, 1969). These possible forms of preferred olivine crystal orientation can be tested by using the perturbation approach to surface wave anisotropy (Smith and Dahlen, 1973) assuming the appropriate symmetries, and then simultaneously inverting all the Love and Rayleigh wave data, including azimuthal coefficients. This will be done in a later paper. An additional complication is introduced by the possibility that each of the elastic parameters of olivine may have different pressure and temperature coefficients (Kumazawa and Anderson, 1969).

Thin layers or pockets of partial melt within the low velocity zone may be able to explain the discrepancy between Love and Rayleigh waves (Aki, 1968; and Takeuchi, et al., 1968). It is difficult to envision this mechanism producing the azimuthal variations, but it could act in concert with preferred crystal orientation to produce all the observed effects.

Nur and Simmons (1969) demonstrated that applying uniaxial stress to a rock with cracks will increase the elastic velocities in the direction of the stress and that in general, SH differs from SV, with the difference

increasing with increasing stress. With no confining pressure, a stress difference of 200 bars is enough to produce 12% anisotropy in P wave velocity. The size of the effect should decrease with depth, but it may be large enough to produce the observed Rayleigh wave anisotropy. The maximum compressive stress must be horizontal and perpendicular to the ridge axis in order to produce the observed effect. Thrust-faulting has been observed in two intraplate events used as surface wave sources in this study. In both cases, the apparent axis of maximum compressive stress was approximately horizontal and perpendicular to the ridge axis (Mendiguren, 1971; Forsyth, 1973). Stress-induced anisotropy is thus a possible mechanism for producing the observed surface wave anisotropy. This mechanism can not produce the apparent anisotropy found below 125 km.

Observations in other areas may reduce the uncertainty in both the form and cause of the anisotropy. If the anisotropy occurs in the upper 50 km and is due to preferred crystal orientation, it is probably "frozen in". The observed maximum velocity should then be found to be parallel to the direction of spreading at the time the sea-floor was created. If the anisotropy is due to horizontal compressive stress, the maximum velocity will be in the direction of the applied stress. If the anisotropy

occurs deeper than 50 km, it probably is maintained dynamically by some sort of shearing flow within the low velocity zone. In the Nazca plate, return flow in the asthenosphere is probably from the trench to the ridge axis or approximately east-west and parallel to the direction of spreading. By examining other areas in which the apparent stress or apparent return flow differs from the spreading direction, we may be able to distinguish between the possible mechanisms.

Figure 40. Residuals of the fit of the final model to the fundamental and first higher Love modes for the 10-50 m.y. region. Model is shown in fig. 35.

Figure 41. Rows of the resolution matrix for Love waves with 2 independent pieces of information. Symbols and layers as in fig. 36.

Figure 42. Selected rows of the resolution matrix for the Rayleigh wave cos 2θ term with 3 independent pieces of information. The first five columns correspond to the variables representing compressional velocity in the first 5 layers of the mantle. The next 13 columns correspond to the variables representing the shear velocity in the same 13 layers described in fig. 36.

Figure 43. Three possible models of the apparent change in structure producing the Rayleigh wave cos 2θ term. Solid line, Shear velocity and compressional velocity allowed to vary in all 13 layers. Dotted line, shear velocity and compressional velocity allowed to vary only in the top 5 layers. Dashed line, only compressional velocity allowed to vary, all 13 layers.

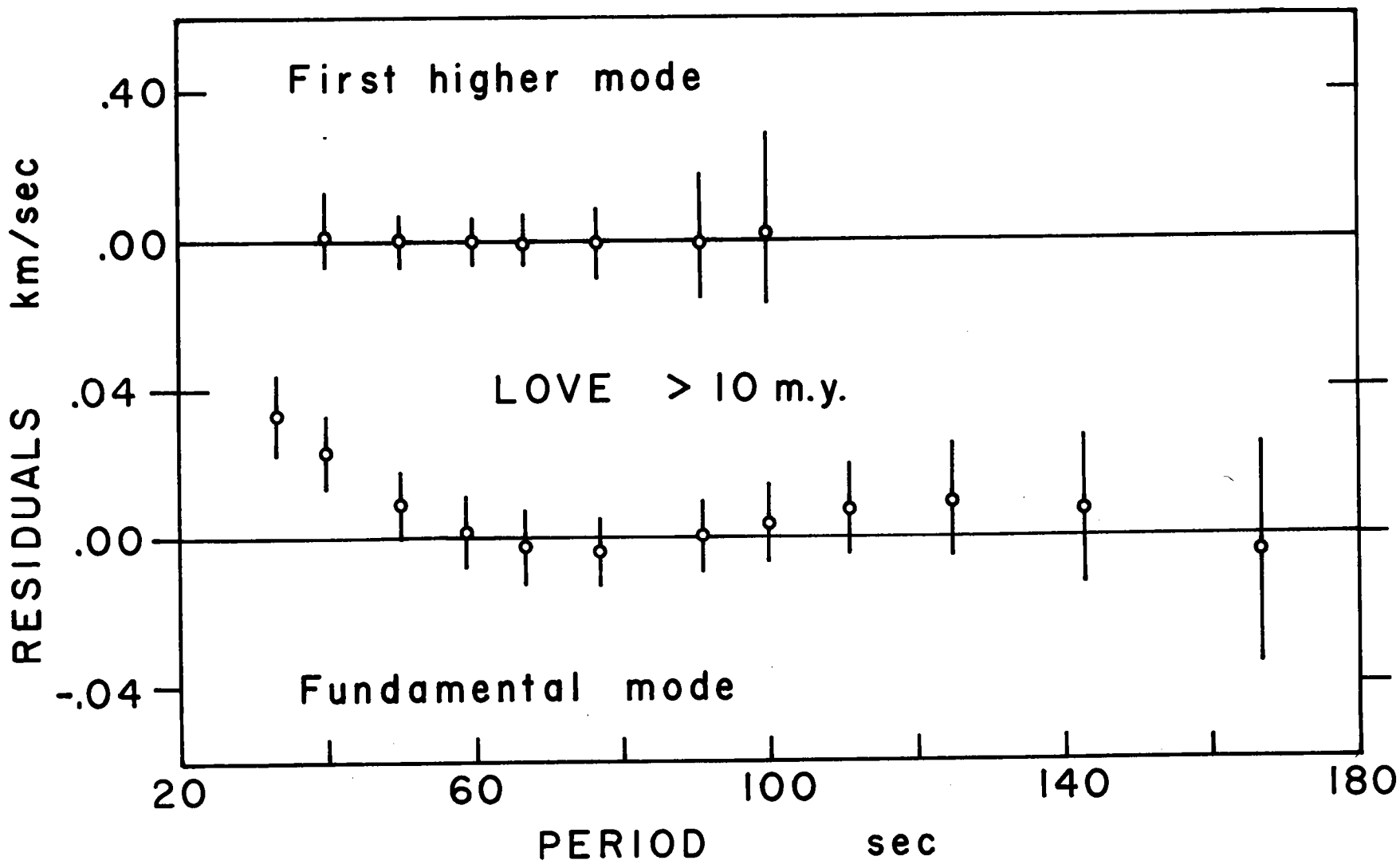
First higher mode
.40
.00
.04
LOVE > 10 m.y.
.00
-.04
Fundamental mode
RESIDUALS km/sec
20
60
100
140
180
PERIOD sec

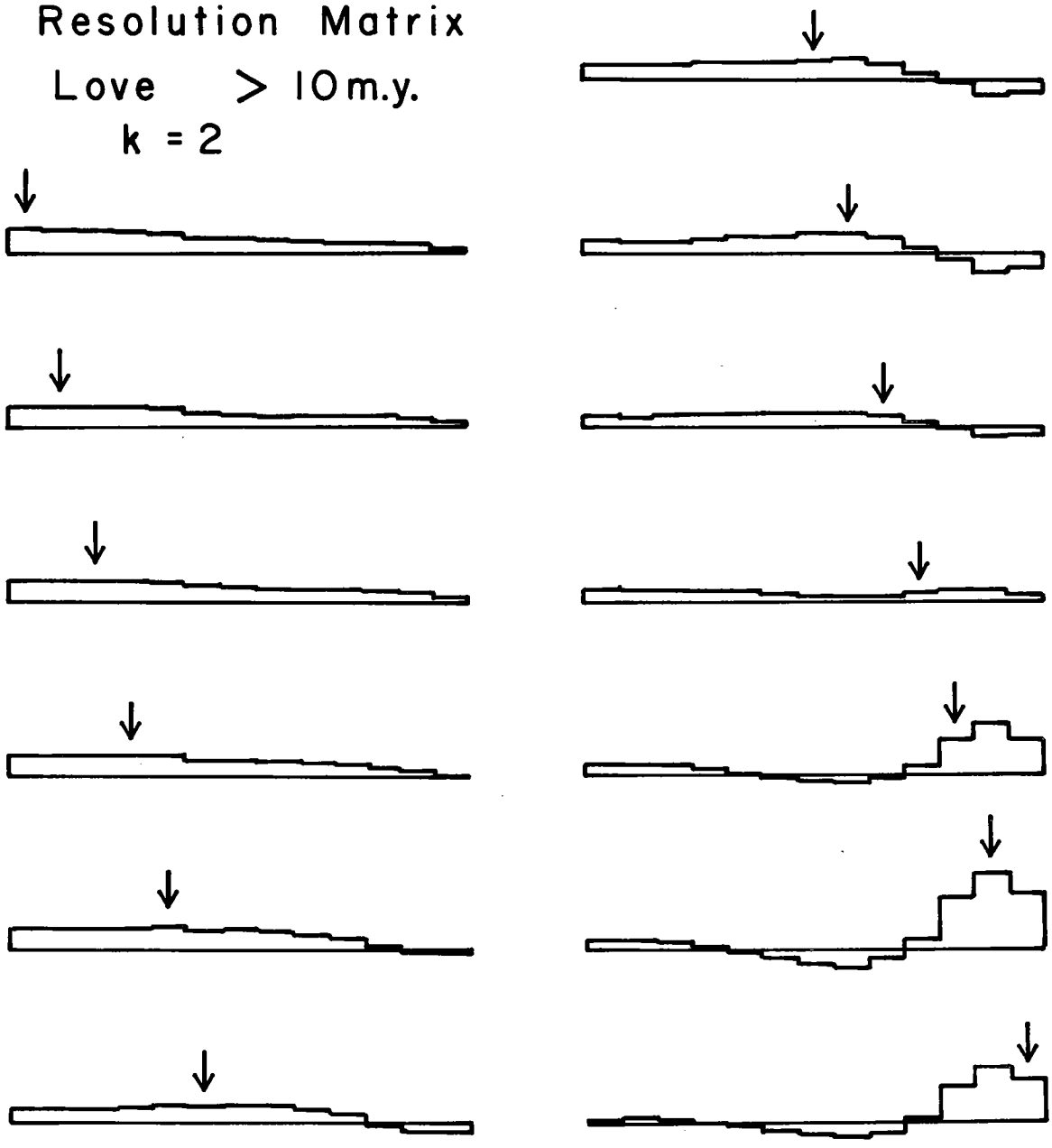
Resolution Matrix
Love > 10m.y.
k = 2

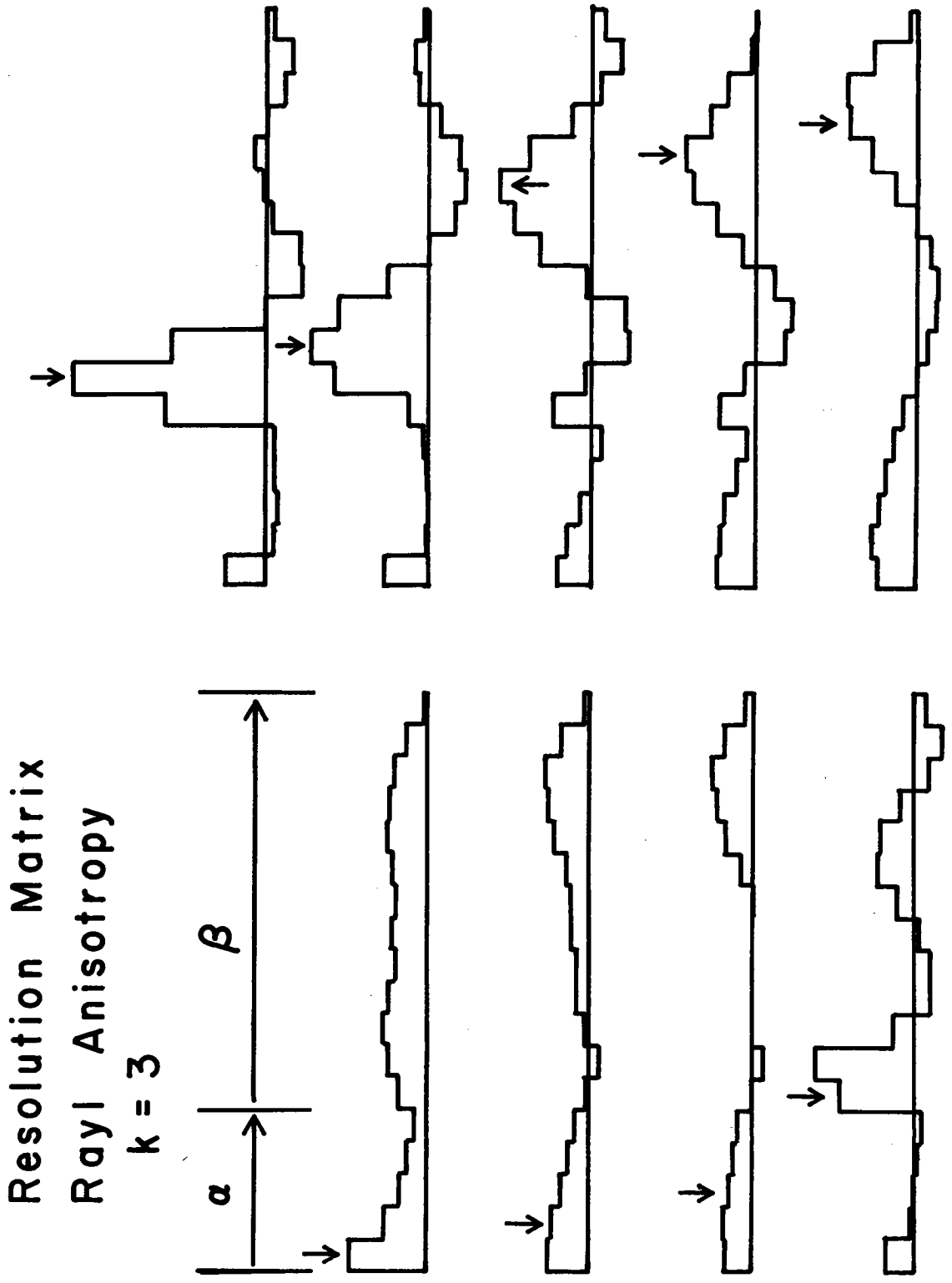
Resolution Matrix
Rayl Anisotropy
k = 3
α
β

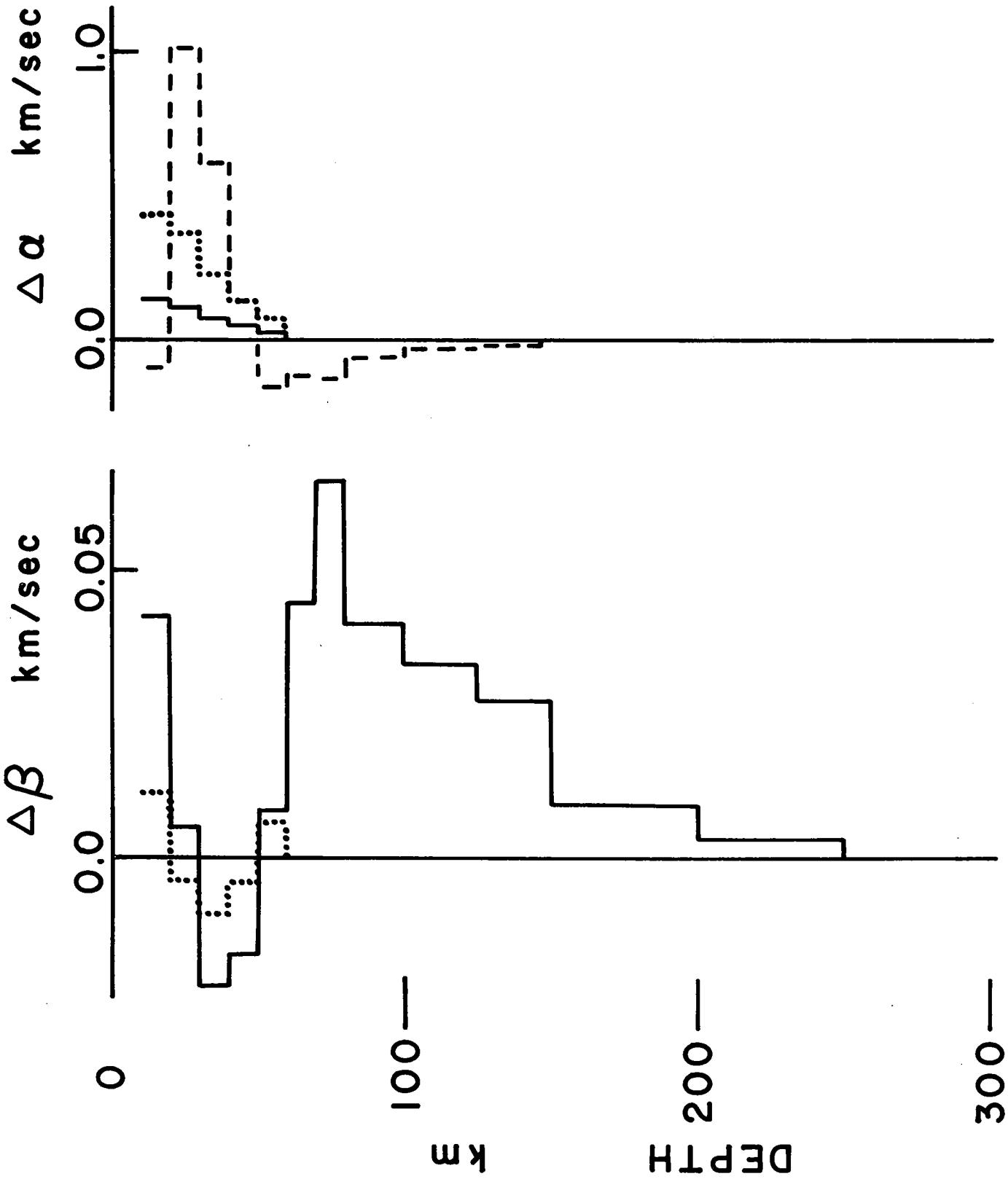
Δα km/sec
1.0
0.0
Δβ km/sec
0.05
0.0
0
100
200
300
km
DEPTH

6. Summary

The propagation of surface waves in the east Pacific has been studied in order to examine the early development of an oceanic plate. Using the single station method, the phase and group velocities of Rayleigh waves were measured for 78 great circle paths. Love wave phase velocities were measured for 45 paths. These investigations led to the following conclusions.

1. At each station, the observed phase of surface waves from events in the east Pacific can be predicted with great accuracy if a regionalized model of the propagation is used. The observed phase of Rayleigh waves in the period range 33 to 80 sec is predicted with an RMS error of about 5 sec. The phase of Love waves is explained with the same accuracy for periods up to 100 sec.

2. Rayleigh wave propagation within the ocean is anisotropic. The direction of maximum velocity is 91 ± 9° clockwise from the pole of relative motion between plates. The anisotropy is frequency-dependent, reaching a maximum of 2.0 ± 0.2 per cent at a period of about 70 sec.

3. The Rayleigh wave phase and group velocities increase systematically as the age of the sea-floor increases. The greatest change at short periods occurs within the first few million years after the sea-floor is formed. The velocity continues to increase in oceanic areas older than 20 million years, for a total change of about 5% at short periods.

4. Two methods of regionalization of the ocean were used. The surface wave data is unable to distinguish between a regionalized model based on bathymetry and a model based on the identification of magnetic anomalies.

5. It is possible to simultaneously measure the regional phase velocities of both the fundamental and first higher Love modes. Many observations over paths of varying length are required, and the initial phase at the source must be known. Using a new technique, the phase velocity of the first higher Love mode was measured for the first time in an oceanic area.

6. The phase velocities of the fundamental mode Love wave in the 0-10 m.y. age zone are 3 to 4 per cent lower than in the 10-50 m.y. age zone. Anisotropy is small for

Love waves, but the degree of anisotropy appears to increase at periods greater than 100 sec.

7. Inversion of the Rayleigh wave data shows that the low velocity zone is well-resolved. Deeper than 150 km, the structure is similar to the gross earth average found by Anderson and Jordan (1973) and to the Canadian shield model of Brune and Dorman (1963). Within the area of this study, no change takes place in the mantle deeper than about 80 km. It is suggested that this uniformity of structure is due to efficient thermal convection beneath the lithosphere and, therefore, no significant increase in the thickness of the oceanic lithosphere is expected in areas older than that considered in this study.

8. The average thickness of the lithosphere in the 0-5 m.y. age zone can be no greater than 30 km, including the water and crustal layers. Within 10 m.y. after the formation of the oceanic crust, the lithosphere reaches a thickness of about 60 km. Beyond 10 m.y., the average shear velocity within the lithosphere increases in age, and there may also be a small increase in the thickness to about 70 km in the 20-50 m.y. age zone.

9. The Love and Rayleigh wave data are compatible only if the upper mantle is anisotropic. If anisotropy is not considered in the simultaneous inversion of Love and Rayleigh wave observations, the lithosphere may erroneously be assigned a high density.

10. Models of the distribution of the anisotropy within the mantle are highly non-unique. The average SH velocity within the upper 125 km is 0.15 ± .05 km/sec faster than the SV velocity. The data strongly supports, but does not require, the existence of anisotropy deeper than 125 km and possibly as deep as 380 km. A wide variety of models can explain the Rayleigh wave anisotropy, including the possibilities that anisotropy is confined to either the upper 50 km or to the low velocity zone.

The existence of anisotropy within the oceanic upper mantle has been firmly established. The questions of the form of the anisotropy and the involvement of the asthenosphere in the aging process can not be fully settled without additional data from other areas.

References

Abe, M. and Z. Suzuki, A model-seismological study on the propagation of Rayleigh waves in a medium with a dipping boundary between a superficial layer and the basement, Sci. Rept. Tohoku Univ., Fifth Ser. 20, 1, 1970.

Aki, K., Generation and propagation of G waves from the Niigata earthquake of June 16, 1964: Part I and Part II, Bull. Earthq. Res. Inst. 44, 23, 1966.

Aki, K., Seismological evidence for the existence of soft thin layers in the upper mantle under Japan, J. Geophys. Res. 73, 585, 1968.

Aki, K. and K. Kaminuma, Phase velocity of Love waves in Japan, 1, Love waves from the Aleutian shock of March 9, 1957, Bull. Earthq. Res. Inst. 41, 243, 1963.

Anderson, R.N. and J.G. Sclater, Topography and evolution of the east Pacific rise between 5°S and 20°S, Earth Planet. Sci. Letters 14, 433, 1972.

Atwater, T., and H.W. Menard, Magnetic lineations in the northeast Pacific, Earth Planet. Sci. Letters 7, 445, 1970.

Ave'Lallemant, H.G. and N.L. Carter, Syntectonic recrystallization of olivine and modes of flow in the upper mantle, Geol. Soc. Amer. Bull. 81, 2203, 1970.

Backus, G.E., Possible forms of seismic anisotropy of the upper mantle under oceans, J. Geophys. Res. 70, 3429, 1965.

Backus, G.E., and J.F. Gilbert, Numerical application of a formalism for geophysical inverse problems, Geophys. J. R. Astr. Soc. 13, 247, 1967.

Backus, G.E., and J.F. Gilbert, The resolving power of gross earth data, Geophys. J.R. Astr. Soc. 16, 169, 1968.

Backus, G.E., and J.F. Gilbert, Uniqueness in the inversion of inaccurate gross earth data, Phil. Trans. Roy. Soc. London, Ser. A 266, 123, 1970.

Ben-Menahem, A., Radiation of seismic surface-waves from finite moving sources, Bull. Seism. Soc. Amer. 51, 401, 1961.

Ben-Menahem, A., Observed attenuation and Q values of seismic surface waves in the upper mantle, J. Geophys. Res. 70, 4641, 1965.

Ben-Menahem, A., and D.G. Harkrider, Radiation patterns of seismic surface waves from buried dipolar point sources in a flat stratified earth, J. Geophys. Res. 69, 2605, 1964.

Birch, F., The velocity of compressional waves in rocks to 10 kilobars, 1, J. Geophys. Res., 65, 1083, 1960.

Birch, F., The velocity of compressional waves in rocks to 10 kilobars, 2, J. Geophys. Res. 66, 2199, 1961.

Birch, F., Density and composition of the upper mantle: First approximation as an olivine layer, The Earth's Crust and Upper Mantle, Geophys. Monogr. Ser., vol. 13, edited by P.J. Hart, p. 18, AGU, Washington, D.C., 1969.

Bishop, T.N. and B.T.R. Lewis, Seismic refraction results

from the east Pacific rise near 14°N, 104°W, Trans. AGU, 54, 377, 1973.

Boore, D.M., Effect of higher mode contamination on measured Love wave phase velocities, J. Geophys. Res. 74, 6612, 1969.

Boore, D.M., Love waves in nonuniform waveguides: finite difference calculations, J. Geophys. Res. 75, 1512, 1970.

Brune, J.N., Correction of initial phase measurements for southeast Alaska earthquake of July 10, 1958, and for certain nuclear explosions, J. Geophys. Res. 67, 3643, 1962.

Brune, J.N. and J. Dorman, Seismic waves and earth structure in the Canadian shield, Bull. Seism. Soc. Amer. 53, 167, 1963.

Brune, J.N., J.E. Nafe, and J.E. Oliver, A simplified method for the analysis and synthesis of dispersed wave trains, J. Geophys. Res. 65, 287, 1960.

Bullen, K.E., An Introduction to the Theory of Seismology, Cambridge University Press, New York, 1963.

Capon, J., Analysis of Rayleigh-wave multipath propagation at LASA, Bull. Seism. Soc. Amer. 60, 1701, 1970.

Capon, J., Comparison of Love and Rayleigh wave multipath propagation at LASA, Bull. Seism. Soc. Amer. 61, 1327, 1971.

Carter, N.L. and H.G. Ave'Lallemant, High temperature flow of dunite and peridotite, Geol. Soc. Amer. Bull. 81, 2181, 1970.

Christensen, N.I. and R.S. Crosson, Seismic anisotropy in the upper mantle, Tectonophysics 6, 93, 1968.

Crosson, R.S., Symmetry of upper mantle anisotropy, Earth Planet. Sci. Letters 15, 423, 1972.

Crosson, R.S. and N.I. Christensen, Transverse isotropy of the upper mantle in the vicinity of Pacific fracture zones, Bull. Seism. Soc. Amer. 59, 59, 1969.

Drake, L.A., Love and Rayleigh waves in nonhorizontally layered media, Bull. Seism. Soc. Amer. 62, 1241, 1972a.

Drake, L.A., Rayleigh waves at a continental boundary by the finite element method, Bull. Seism. Soc. Amer. 62, 1259, 1972b.

Dziewonski, A.M., Upper mantle models from 'pure path' dispersion data, J. Geophys. Res. 76, 2587, 1971.

Eaton, J.P., Instrumental seismic studies, in the Parkfield-Cholame, California, Earthquakes of June-August, 1966. U.S. Geol. Surv. Prof. Pap., 579:57, 1967.

Ewing, M., R. Houtz, and J. Ewing, South Pacific sediment distribution, J. Geophys. Res. 74, 2477, 1969.

Forsyth, D.W., Mechanisms of earthquakes and plate motions in the east Pacific, Earth Planet. Sci. Letters 17, 189, 1972.

Forsyth, D.W., Compressive stress between two mid-ocean ridges, Nature, 243, 78, 1973.

Forsyth, D.W. and F. Press, Geophysical tests of petrological

models of the spreading lithosphere, J. Geophys. Res. 76, 7963, 1971.

Francis, T.J.G., Generation of seismic anisotropy in the upper mantle along the mid-ocean ridges, Nature 221, 162, 1969.

Grim, P.J., Connection of the Panama fracture zone with the Galapagos rift zone, eastern tropical Pacific, Mar. Geophys. Res. 1, 85, 1970.

Hagiwara, T., A note on the theory of the electromagnetic seismograph, Bull. Earthq. Res. Inst. 36, 139, 1958.

Hanks, T.C. and W. Thatcher, A graphical representation of seismic source parameters, J. Geophys. Res. 77, 4393, 1972.

Harkrider, D.G. and D.L. Anderson, Surface wave energy from point sources in plane layered earth models, J. Geophys. Res. 71, 2967, 1966.

Haskell, N.A., Radiation pattern of surface waves from point sources in a multi-layered medium, Bull. Seism. Soc. Amer. 54, 377, 1964.

Heirtzler, J.R., G.O. Dickson, E.M. Herron, W.C. Pitman III, and X. LePichon, Marine magnetic anomalies, geomagnetic field reversals, and motions of the ocean floor and continents, J. Geophys. Res. 73, 2119, 1968.

Herron, E.M., Crustal plates and sea-floor spreading in the southeastern Pacific, Am. Geophys. Union, Antarctic

Oceanology I, Antarctic Research Series, v. 15, 229, 1971.

Herron, E.M., Sea-floor spreading and the Cenozoic history of the east-central Pacific, Geol. Soc. Amer. Bull. 83, 1671 1972.

Herron, E.M. and D.E. Hayes, A geophysical study of the Chile ridge, Earth Planet. Sci. Letters 6, 77, 1969.

Herron, E.M. and J.R. Heirtzler, Sea-floor spreading near the Galapagos, Science 158, 775, 1967.

Hess, H., Seismic anisotropy of the uppermost mantle under oceans, Nature 203, 629, 1964.

Hey, R.N., K.S. Deffeyes, G.L. Johnson and A. Lowrie, The Galapagos triple junction and plate motions in the east Pacific, Nature 237, 20, 1972.

Hussong, D.M., S.H. Johnson, G.P. Woollard, and J.F. Campbell, Crustal structure of the Nazca plate; 1972 preliminary report (abs.), Trans., Amer. Geophys. Un. 53, 413, 1972.

James, D.E., Anomalous Love wave phase velocities, J. Geophys. Res. 76, 2077, 1971.

Jordan, T.H. and D.L. Anderson, Earth structure from free oscillations and travel times, preprint, 1973.

Kaminuma, K., The crust and upper mantle structure in Japan, 3, An anisotropic model of the structure in Japan, Bull. Earthq. Res. Inst. 44, 511, 1966.

Kanamori, H., Synthesis of long-period surface waves and its application to earthquake source studies - Kurile Islands earthquake of October 13, 1963, J. Geophys. Res. 75, 5011, 1970.

Kausel, E.G., Regionalization of the lithosphere and asthenosphere of the Pacific Ocean, Ph.D. thesis - 147 pp., Columbia Univ., New York, 1972.

Keen, C.E., and D.L. Barrett, A measurement of seismic anisotropy in the northeast Pacific, Can. J. Earth Sci. 8, 1056, 1971.

Keen, C.E. and C. Tramontini, A seismic refraction survey on the mid-Atlantic ridge, Geophys. J. R. Astr. Soc. 20, 473, 1970.

Knopoff, L., Phase and group slownesses in inhomogeneous media, J. Geophys. Res. 74, 1701, 1969.

Knopoff, L., Observation and inversion of surface wave dispersion, Tectonophysics, 13, 497, 1972.

Knopoff, L. and A.K. Mal, Phase velocity of surface waves in the transition zone of continental margins, J. Geophys. Res. 72, 1769, 1967.

Knopoff, L., J.W. Schlue, and F.A. Schwab, Phase velocities of Rayleigh waves across the east Pacific rise, Tectonophysics, 10, 321, 1970.

Kumazawa, M. and O.L. Anderson, Elastic moduli, pressure derivatives, and temperature derivatives of single-crystal olivine and single-crystal forsterite, J. Geophys. Res. 74, 5961, 1969.

Kuo, J., J. Brune, and M. Major, Rayleigh wave dispersion in the Pacific Ocean for the period range 20 to 140 seconds, Bull. Seism. Soc. Amer. 52, 333, 1962.

Landisman, M., A. Dziewonski and Y. Sato, Recent improvements in the analysis of surface wave observations, Geophys. J.R. Astr. Soc. 17, 369, 1969.

Langseth, M.G., X. LePichon, and M. Ewing, Crustal structure of mid-ocean ridges, J. Geophys. Res. 71, 5321, 1966.

Larson, R.L. and C.G. Chase, Relative velocities of the Pacific, North America and Cocos plates in the middle America region, Earth Planet. Sci. Letters 7, 425, 1970.

Lee, W.H.K. and S. Uyeda, Review of heat flow data, in Terrestrial Heat Flow, Geophys. Mon. 8, ed. W.H.K. Lee, AGU, Washington, D.C., 87, 1965.

Leeds, A.R., Rayleigh wave dispersion in the Pacific basin, Ph.D. thesis, 100 pp., Univ. of California, Los Angeles, 1973.

Lighthill, M.J., Group velocity, J. Inst. Maths. Applics. 1, 1, 1965.

Long, R.E. and M.G. Mitchell, Teleseismic P wave delay in Iceland, Geophys. J.R. Astr. Soc. 20, 41, 1970.

Lysmer, J. and L.A. Drake, The propagation of Love waves across nonhorizontally layered structures, Bull. Seism. Soc. Am. 61, 1233, 1971.

McEvilly, T.V., Central U.S. crust-upper mantle structure from Love and Rayleigh wave phase velocity inversion, Bull. Seism. Soc. Amer. 54, 19, 1964.

McGarr, A., Amplitude variations of Rayleigh waves--horizontal refractions, Bull. Seism. Soc. Amer. 59, 1307, 1969.

McGarr, A. and L.E. Alsop, Transmission and reflection of Rayleigh waves at vertical boundaries, J. Geophys. Res. 72, 2169, 1967.

McKenzie, D.P., Some remarks on heat flow and gravity anomalies, J. Geophys. Res., 72, 6261, 1967.

Mal, A.K. and L. Knopoff, Transmission of Rayleigh waves past a step change in elevation, Bull. Seism. Soc. Amer. 55, 319, 1965.

Mal, A.K. and L. Knopoff, A differential equation for surface waves in layers with varying thickness, J. Math. Anal. Appl. 21, 431, 1968.

Mendiguren, J.A., Focal mechanism of a shock in the middle of the Nazca plate, J. Geophys. Res. 76, 3861, 1971.

Mizutani, H. and K. Abe, An earth model consistent with free oscillation and surface wave data, Phys. Earth Planet. Interiors 5, 345, 1972.

Molnar, P., and J. Oliver, Lateral variations of attenuation in the upper mantle and discontinuities in the lithosphere, J. Geophys. Res. 74, 2648, 1969.

Morgan, W.J., Rises, trenches, great faults and crustal blocks, J. Geophys. Res. 73, 1959, 1968.

Morgan, W.J., P.R. Vogt, and D.F. Falls, Magnetic anomalies

and sea-floor spreading on the Chile rise, Nature 222, 137, 1969.

Morris, G.B., R.W. Raitt, and G.G. Shor, Jr., Velocity anisotropy and delay time maps of the mantle near Hawaii, J. Geophys. Res. 74, 4300, 1969.

Nur, A. and G. Simmons, Stress-induced velocity anisotropy in rock: an experimental study, J. Geophys. Res. 74, 6667, 1969.

Ossing, J., Dispersion of Rayleigh waves originating in the mid-Atlantic ridge, Bull. Seism. Soc. Amer. 54, 1137, 1964.

Parker, R.L. and D.W. Oldenburg, Thermal model of ocean ridges, Nature Physical Science 242, 137, 1973.

Pilant, W.L. and L. Knopoff, Observations of multiple seismic events, Bull. Seism. Soc. Amer. 54, 19, 1964.

Pitman, W.C., III, E.M. Herron, and J.R. Heirtzler, Magnetic anomalies in the Pacific and sea-floor spreading, J. Geophys. Res. 73, 2069, 1968.

Press, F., Regionalized earth models, J. Geophys. Res. 75, 6575, 1970.

Raitt, R.W., G.G. Shor, Jr., T.J.G. Francis, and G.B. Morris, Anisotropy of the Pacific upper mantle, J. Geophys. Res. 74, 3095, 1969.

Raitt, R.W., G.G. Shor, Jr., G.B. Morris, and H.K. Kirk, Mantle anisotropy in the Pacific Ocean, Tectonophysics 12, 173, 1971.

Saito, M., Excitation of free oscillations and surface waves by a point source in a vertically heterogeneous earth, J. Geophys. Res. 72, 3689, 1967.

Santo, T.A. and Y. Sato, World wide survey of regional characteristics of group velocity dispersion of Rayleigh waves, Bull. Earthq. Res. Inst. 44, 939, 1966.

Savage, J.C. and R.H. White, A map of Rayleigh wave dispersion in the Pacific, Con. J. of Earth Sci. 6, 1289, 1969.

Sclater, J.G., R.N. Anderson, and M.L. Bell, The elevation of ridges and the evolution of the central eastern Pacific, J. Geophys. Res. 76, 7888, 1971.

Sclater, J.G., and J. Francheteau, The implications of terrestrial heat flow observations on current tectonic and geochemical models of the crust and upper mantle of the earth, Geophys. J.R. Astr. Soc. 20, 509, 1970.

Simkin, T. and K.A. Howard, Caldera collapse in the Galapagos Islands, 1968, Science 169, 429, 1970.

Sleep, N.H., Sensitivity of heat flow and gravity anomaly to the mechanism of sea-floor spreading, J. Geophys. Res. 74, 542, 1969.

Solomon, S.C., Shear-wave attenuation and melting beneath the mid-Atlantic ridge, J. Geophys. Res. in press, 1973.

Spetzler, H., and D.L. Anderson, The effect of temperature and partial melting on velocity and attenuation in a simple binary system, J. Geophys. Res. 73, 6051, 1968.

Takeuchi, H., Y. Hamano, and Y. Hasegawa, Rayleigh and Love wave discrepancy and the existence of magma pockets in the upper mantle, J. Geophys. Res. 73, 3349, 1968.

Talwani, M., X. LePichon, and M. Ewing, Crustal structure of the mid-ocean ridges, 2, computed model from gravity and seismic refraction data, J. Geophys. Res. 70, 341, 1965.

Talwani, M., C.C. Windisch, M.G. Langseth, Jr., Reykjanes Ridge crest: a detailed geophysical study, J. Geophys. Res. 76, 473, 1971.

Tarr, A.C., Rayleigh wave dispersion in the North Atlantic Ocean, Caribbean Sea, and Gulf of Mexico, J. Geophys. Res. 74, 1591, 1969.

Taylor, R.W., Remote determinations of earth structure from relative event analysis with applications to the mid-Atlantic ridge, Ph.D. thesis, Penn. State Univ., 1972.

Thatcher, W., and J.N. Brune, Higher mode interference and observed anomalous apparent Love wave phase velocities, J. Geophys. Res. 74, 6603, 1969.

Thatcher, W., and J.N. Brune, Seismic study of an oceanic ridge earthquake swarm in the Gulf of California, Geophys. J. R. Astr. Soc., 22, 473, 1970.

Tsai, Y.-B., Determination of focal depths of earthquakes in mid-ocean ridges from amplitude spectra of surface waves, Ph.D. thesis, 144 pp. Mass. Inst. of Technol., Cambridge, 1969.

Tsai, Y.B. and K. Aki, Simultaneous determination of the seismic moment and attenuation of seismic surface waves, Bull. Seism. Soc. Amer. 59, 275, 1969.

Tsai, Y.B. and K. Aki, Precise focal depth determination from amplitude spectra of surface waves, J. Geophys. Res. 75, 5729, 1970.

Van Andel, T.H., G.R. Heath, B.T. Malfait, D.F. Heinrichs, and J.I. Ewing, Tectonics of the Panama basin, eastern equatorial Pacific, Geol. Soc. Amer. Bull. 82, 1489, 1971.

Verma, R.K., Elasticity of some high-density crystals, J. Geophys. Res., 65, 757, 1960.

Wang, C.-F., Elastic wave propagation in homogeneous transversely isotropic medium with symmetry axis parallel to the free surface, M.S. thesis, 89 pp., Mass. Inst. of Technol., Cambridge, Mass., 1973.

Weidner, D.J., Rayleigh waves from mid-ocean ridge earthquakes: source and path effects, Ph.D. thesis, 256 pp., Mass. Inst. of Technol., Cambridge, Mass., 1972.

Weidner, D.J. and K. Aki, Focal depth and mechanism of mid-ocean ridge earthquakes, J. Geophys. Res. 78, 1818, 1973.

Wickens, A.J., and K. Pec, A crust-mantle profile from Mould Bay, Canada, to Tucson, Arizona, Bull. Seism. Soc. Amer. 58, 1821, 1968.

Wiggins, R.A., The general linear inverse problem: implication of surface waves and free oscillations for earth structure,

Rev. Geophys. and Space Phys., 10, 251, 1972.

Wu, F.T., Mantle Rayleigh wave dispersion and tectonic provinces, J. Geophys. Res., 77, 6445, 1972.

Appendix 1. The excitation of surface waves in a layered medium.

This section contains no new contribution and is included for completeness only. The discussion closely follows Tsai and Aki (1970). The coordinate and fault plane geometry are given in fig. A1. The fault is located at depth h and strikes in the X direction. The dip angle d is measured downward from the positive Y direction. The slip angle s describes the motion of the block on the positive Y side of the fault plane, and is measured counterclockwise from a horizontal line on the fault plane. The finite length of the fault b and the rupture velocity V are neglected in the following discussion, r and ϕ represent the distance and azimuth from the epicenter to a point P on the free surface. ϕ is measured counterclockwise from the strike of the fault.

The Fourier spectrum of the vertical component of displacement due to Rayleigh waves observed at P can be written as

$$R_z(\omega,r,\phi/h,d,s) = \frac{Y_1(0)}{4\omega c U I_1}\left(\frac{2c}{\pi\omega r}\right)^{1/2} \exp\left[-i\left(\frac{\omega r}{c}-\frac{\pi}{4}\right)\right]$$

$$\cdot\left\{\left[\frac{\omega Y_3(h)}{c}\left(\frac{1}{2}\,\frac{3\lambda(h)+2\mu(h)}{\lambda(h)+2\mu(h)}\sin 2d\sin s-\frac{1}{2}\sin 2d\sin s\cos 2\phi\right.\right.\right.$$

$$\left.\left.\left.-\sin d\cos s\sin 2\phi\right)+\frac{Y_2(h)}{\lambda(h)+2\mu(h)}\sin 2d\sin s\right]\right.$$

$$\left.+i\,\frac{Y_4(h)}{\mu(h)}\left[\cos d\cos s\cos\phi-\cos 2d\sin s\sin\phi\right]\right\}$$

where C and U are phase velocity and group velocity respectively at angular frequency w. I_1 is defined as

$$I_1 = \int_{-\infty}^{0} \rho(z)\left[y_1^2(z) + y_3^2(z)\right] dz$$

$y_1(z)$, $Y_2(z)$, $y_3(z)$ and $Y_4(z)$ are the normal mode solutions satisfying the equations

$$\begin{vmatrix} \frac{dy_1}{dz} \\ \frac{dy_2}{dz} \\ \frac{dy_3}{dz} \\ \frac{dy_4}{dz} \end{vmatrix} = \begin{vmatrix} 0 & \frac{1}{\lambda(z)+2\mu(z)} & \frac{\omega}{c}\left[\frac{\lambda(z)}{\lambda(z)+2\mu(z)}\right] & 0 \\ -\omega^2\rho(z) & 0 & 0 & \frac{\omega}{c} \\ -\frac{\omega}{c} & 0 & 0 & \frac{1}{\mu(z)} \\ 0 & -\frac{\omega}{c}\left(\frac{\lambda(z)}{\lambda(z)+2\mu(z)}\right) & -\omega\rho(z) + \frac{4\omega^2}{c^2}\frac{\mu(z)\left[\lambda(z)+\mu(z)\right]}{\lambda(z)+2\mu(z)} & 0 \end{vmatrix} \begin{vmatrix} y_1 \\ y_2 \\ y_3 \\ y_4 \end{vmatrix}$$

and the boundary conditions $y_2(0) = y_4(0) = y_1(-\infty)$ $= y_2(-\infty) = y_3(-\infty) = y_4(-\infty) = 0$, where ρ, u, and λ are density, rigidity, and the Lame' constant, respectively, of the medium at depth z.

The Fourier spectrum of displacement due to Love waves observed at P can be written as

$$L_\phi(\omega, r, \phi/h, d, s) = \frac{Y_1(0)}{4\omega C U I_1}\left(\frac{2C}{\pi\omega r}\right)^{1/2} \cdot \exp\left[-i\left(\omega r/C - \frac{3\pi}{4}\right)\right]$$

$$\cdot\left\{\frac{\omega Y_1(h)}{C}\left(\sin d \cos s \cos 2\phi - \frac{1}{2}\sin 2d \sin s \sin 2\phi\right)\right.$$

$$\left. + i\,\frac{Y_2(h)}{\mu(h)}\left(\cos 2d \sin s \cos\phi + \cos d \cos s \sin\phi\right)\right\}$$

where C is the phase velocity and U the group velocity of Love waves at angular frequency w. I_1 is defined by

$$I_1 = \int_{-\infty}^{0} \rho(z)\, Y_1^2(z)\, dz$$

Y_1 and Y_2 are the normal mode solutions satisfying the equations

$$\begin{vmatrix} \frac{dY_1}{dz} \\ \frac{dY_2}{dz} \end{vmatrix} = \begin{vmatrix} 0 & \frac{1}{\mu(z)} \\ \frac{\omega^2}{C^2}\left[\mu(z) - C^2\rho(z)\right] & 0 \end{vmatrix} \begin{vmatrix} Y_1 \\ Y_2 \end{vmatrix}$$

and the boundary conditions $y_2(0) = y_2(-\infty) = y_1(-\infty) = 0$, where $\rho(z)$ is the density and $u(z)$ is the rigidity of the medium at depth z.

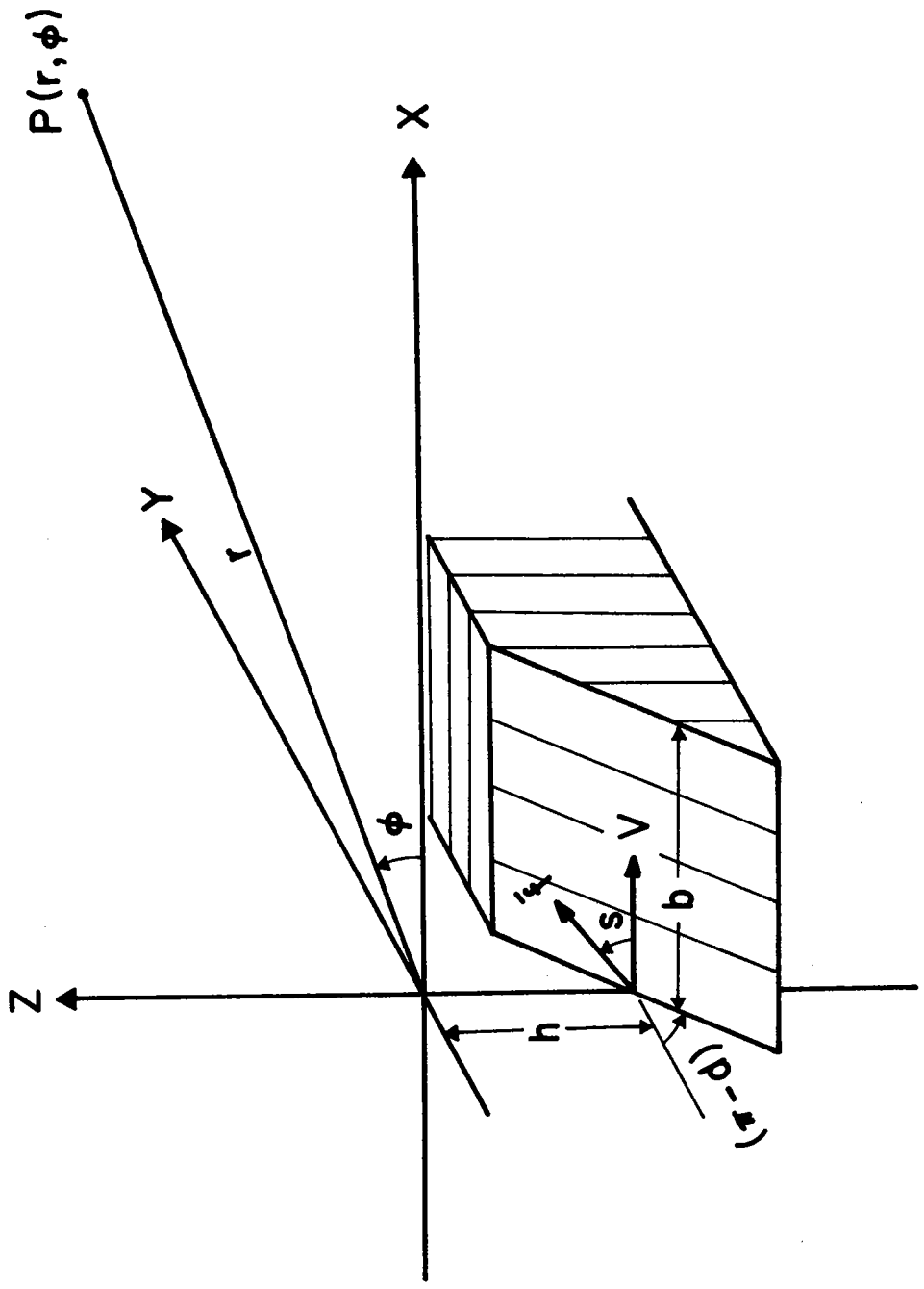

Figure A1

Appendix 2. Fault plane solutions. Symbols as in fig. 4.

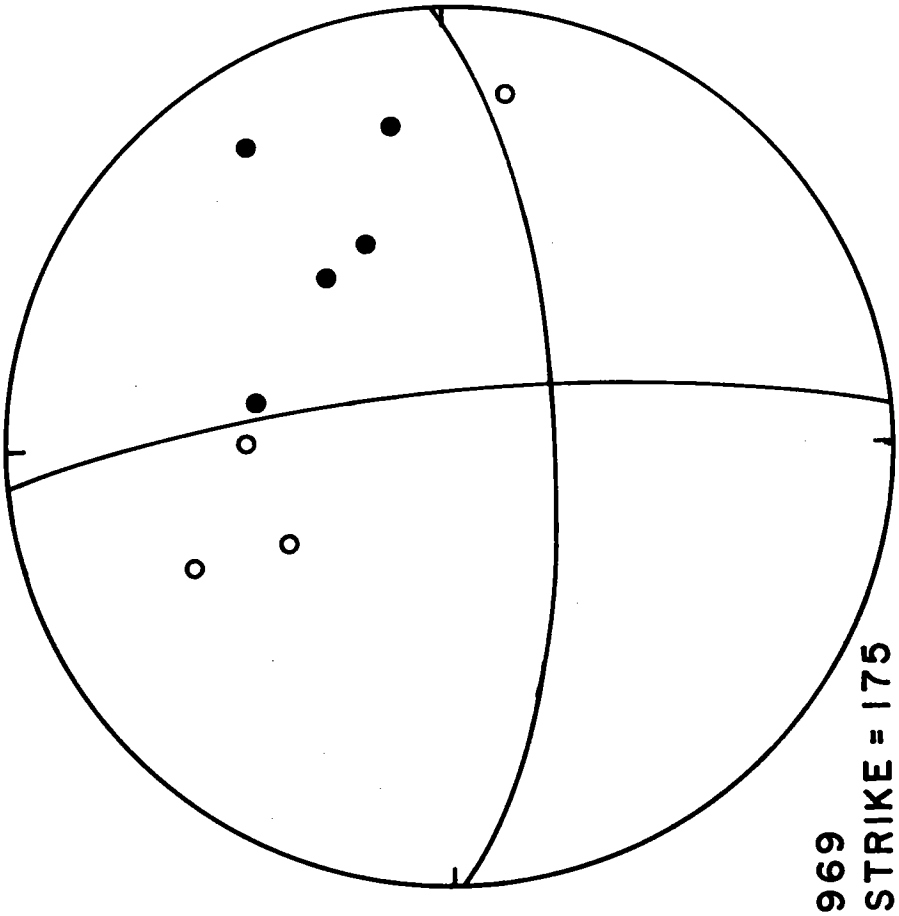

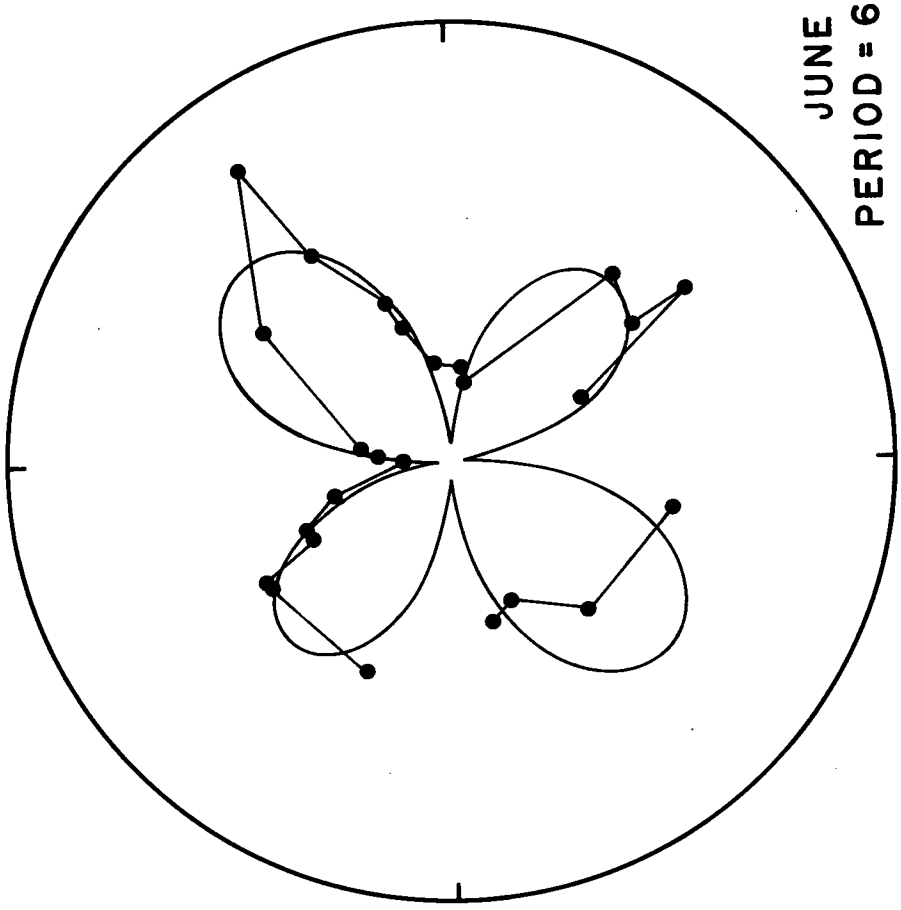

JUNE 26, 1969
PERIOD = 67
Q = 125
DEPTH = 5
STRIKE = 175
DIP = 80
SLIP = -160

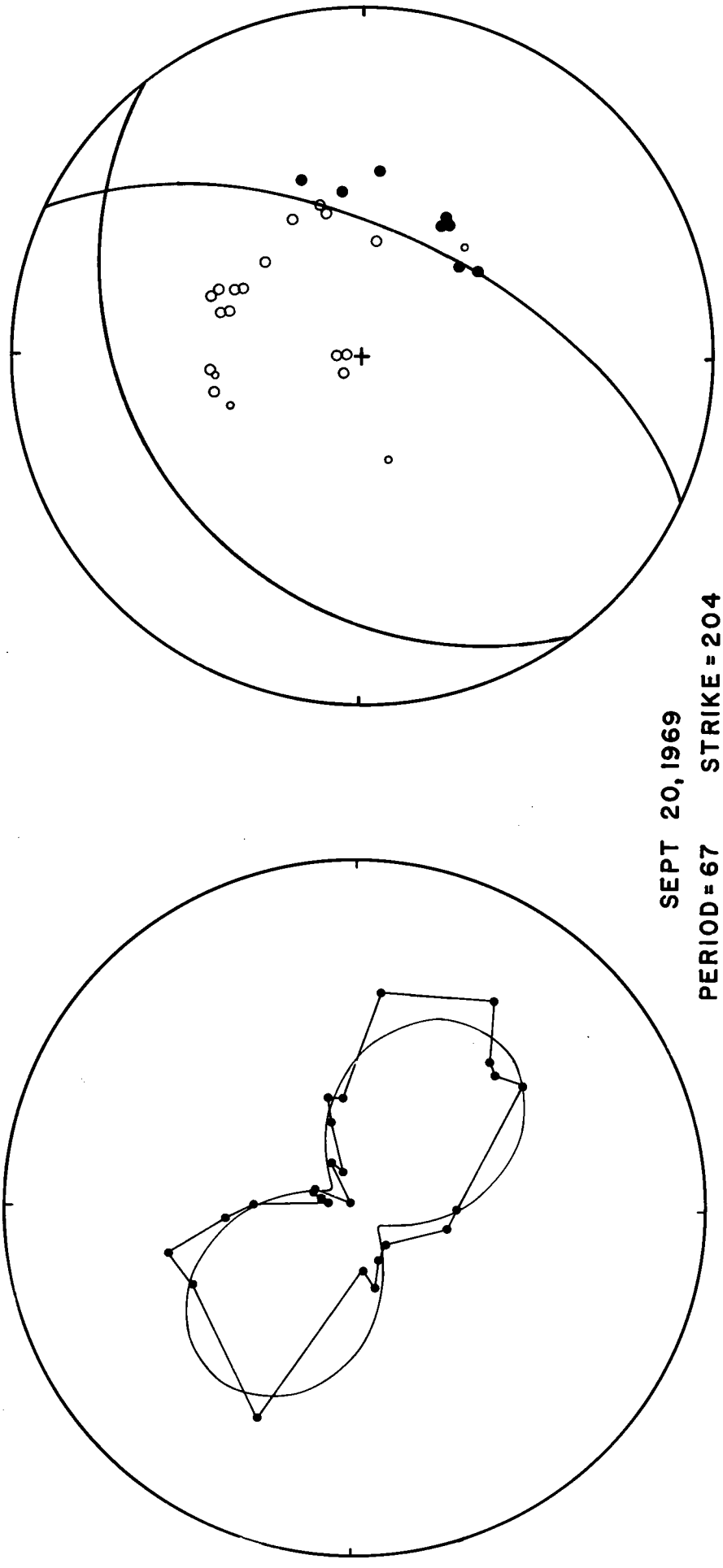

SEPT 20, 1969
PERIOD=67 STRIKE=204
Q=125 DIP=60
DEPTH=5 SLIP=-75

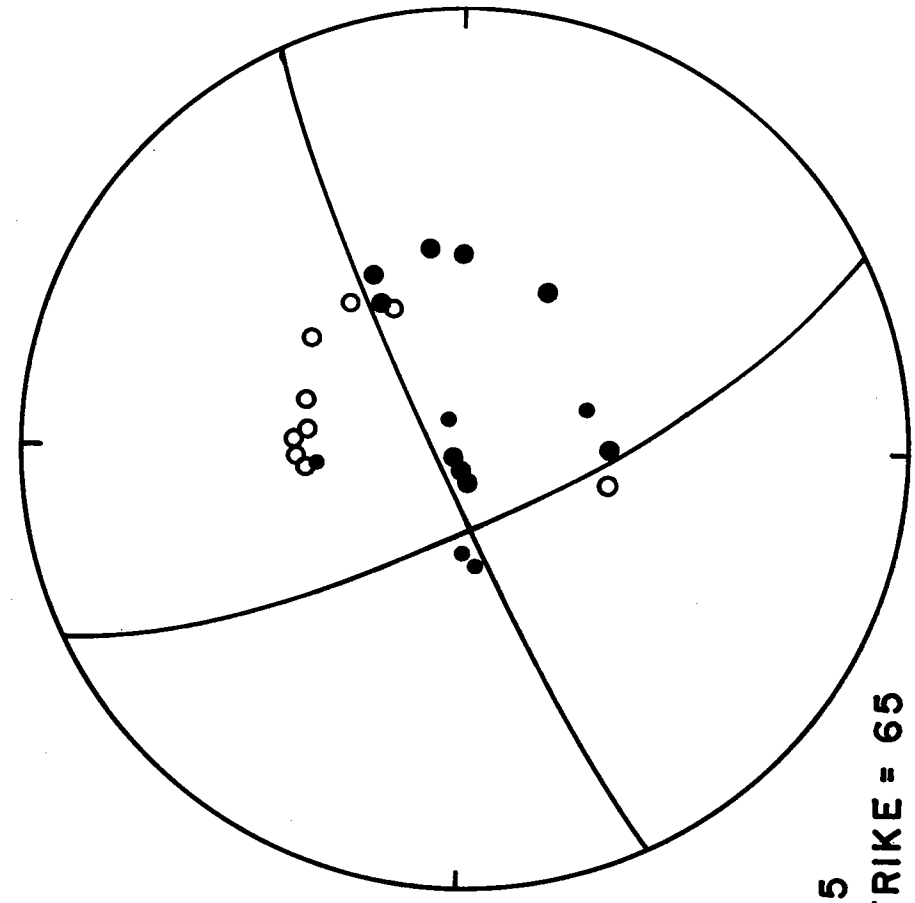

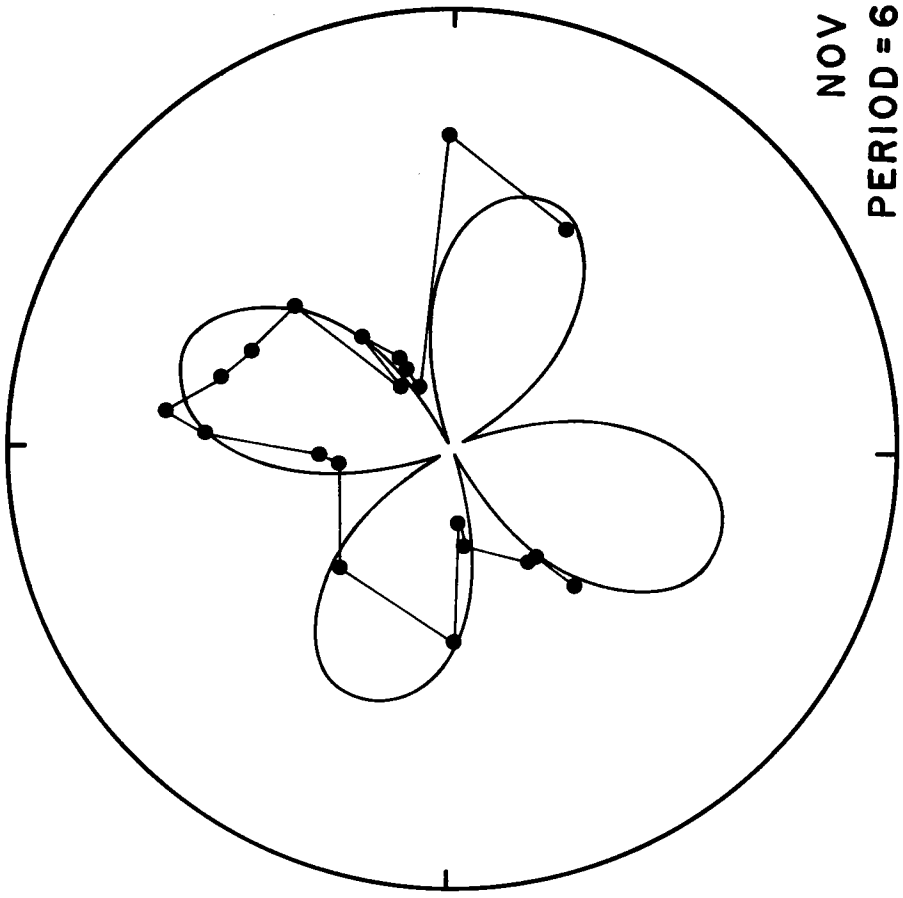

NOV 3, 1965
PERIOD=67 STRIKE = 65
Q = 125 DIP = 85
DEPTH = 5 SLIP = 165

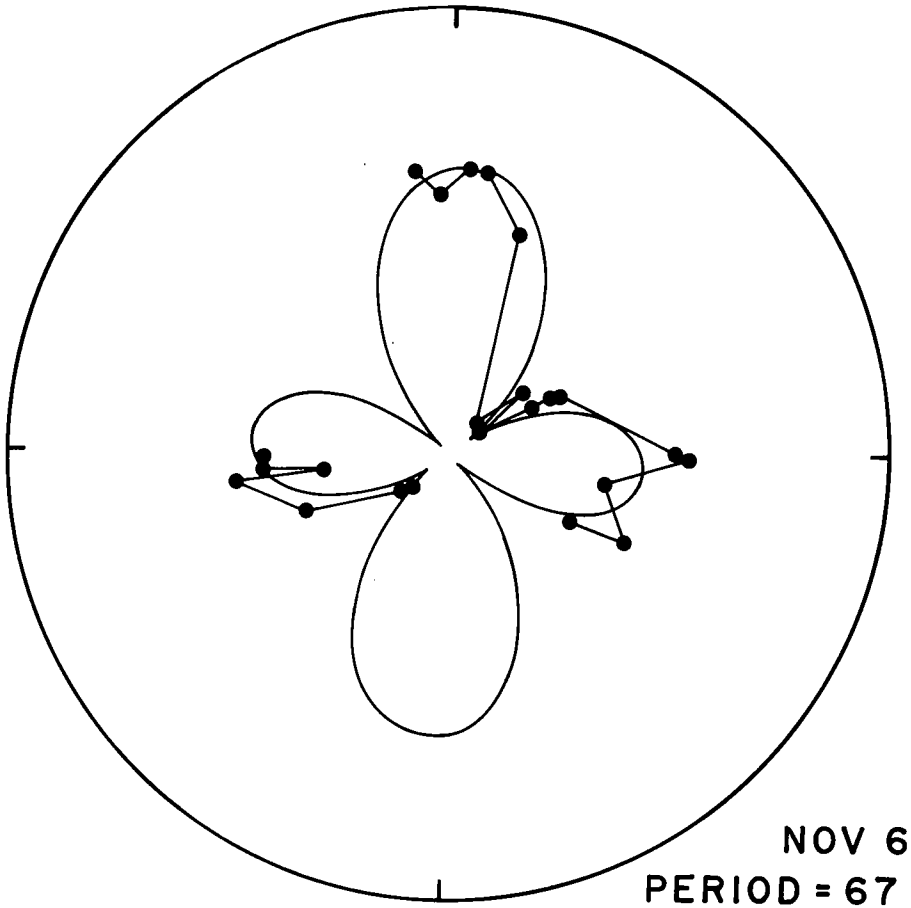

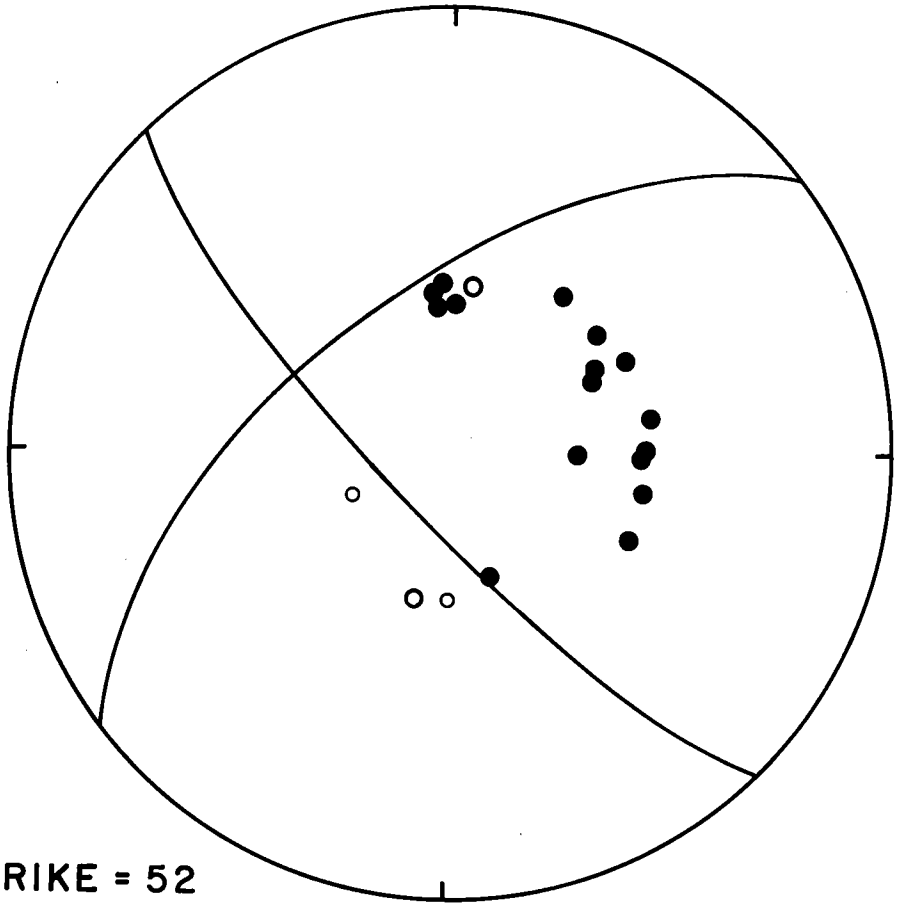

NOV 6, 1965

PERIOD = 67	STRIKE = 52
Q = 125	DIP = 60
DEPTH = 5	SLIP = 166

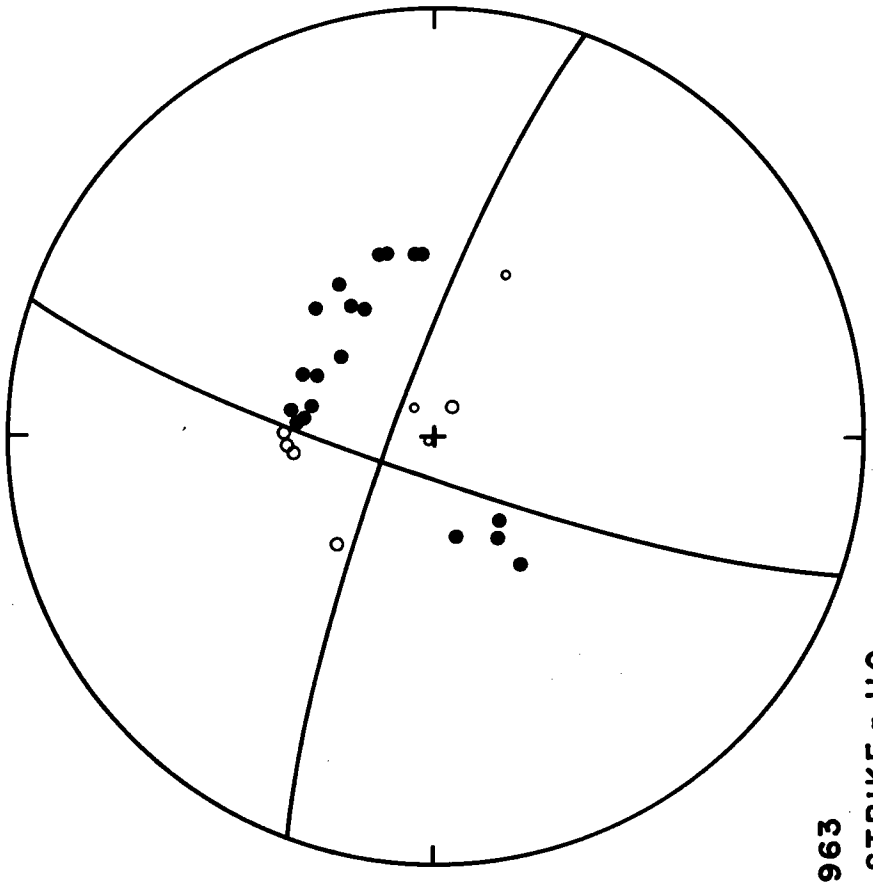

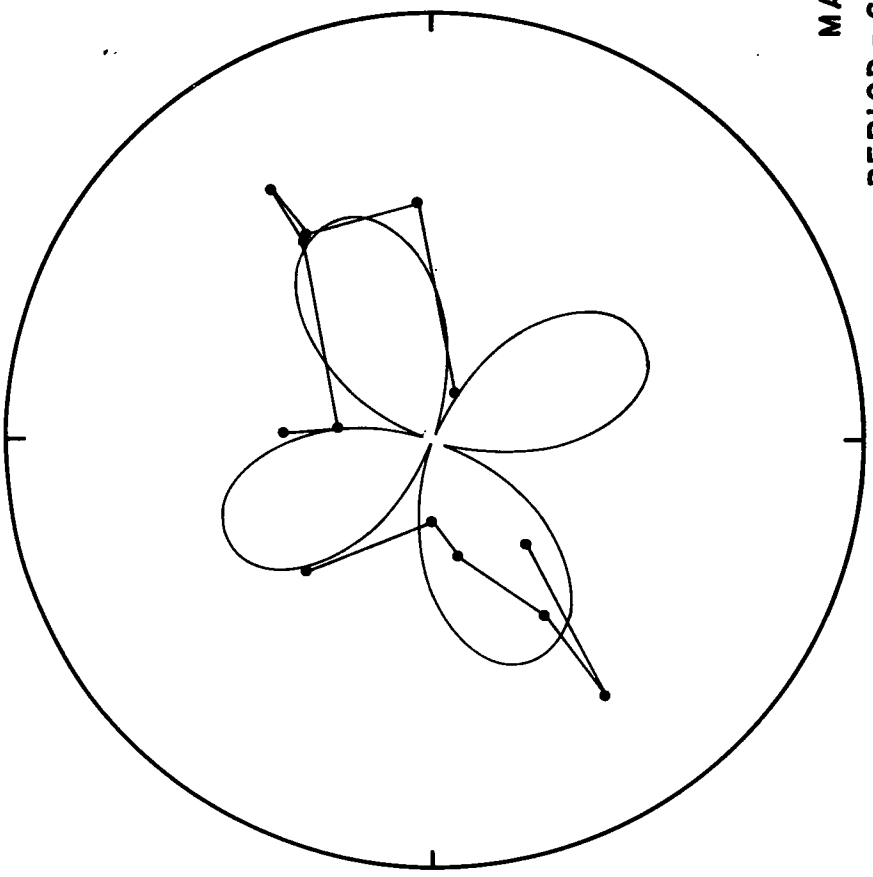

MARCH 7, 1963

PERIOD = 67 STRIKE = 110

Q = 125 DIP = 82

DEPTH = 5 SLIP = -8

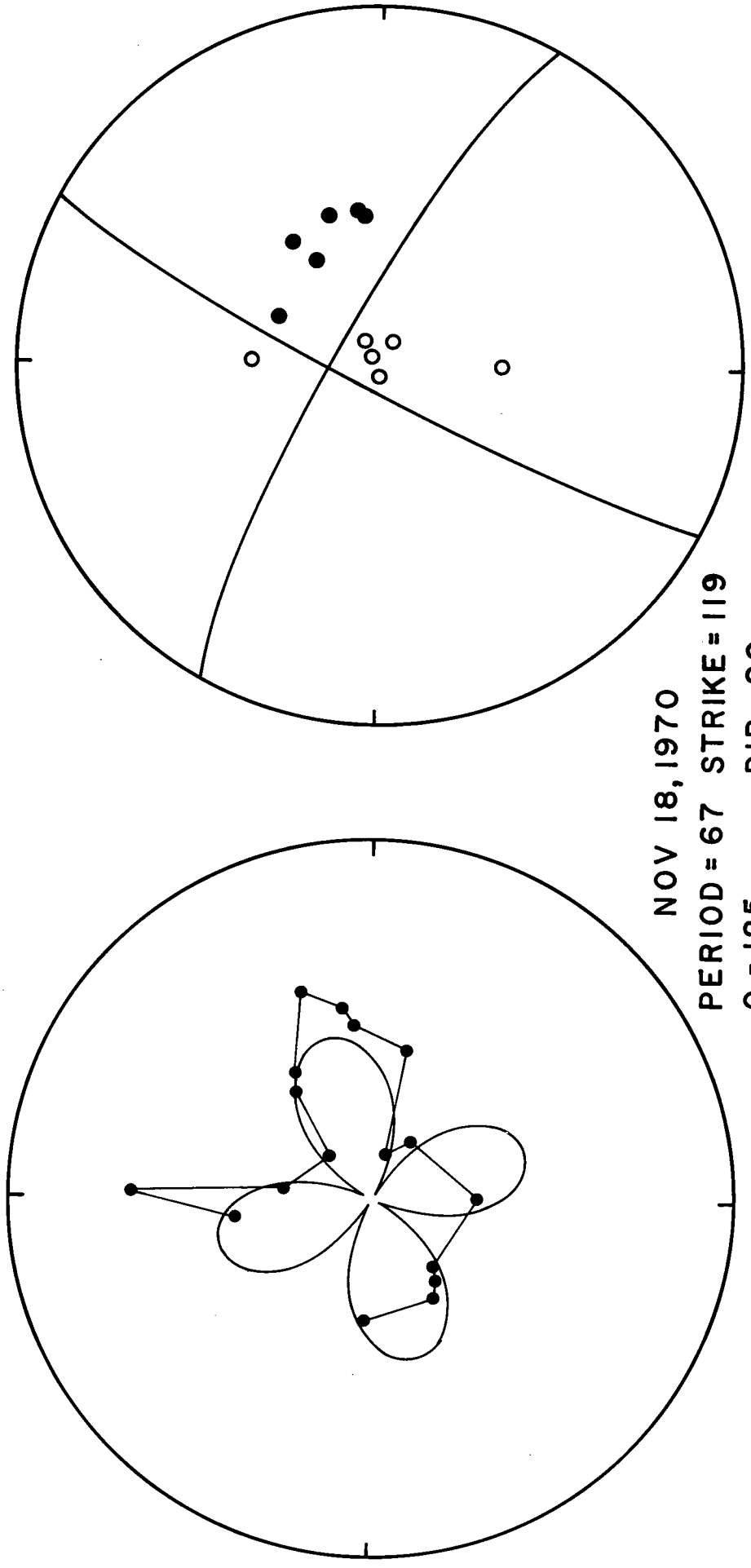

NOV 18, 1970
PERIOD = 67 STRIKE = 119
Q = 125 DIP = 80
DEPTH = 5 SLIP = -6

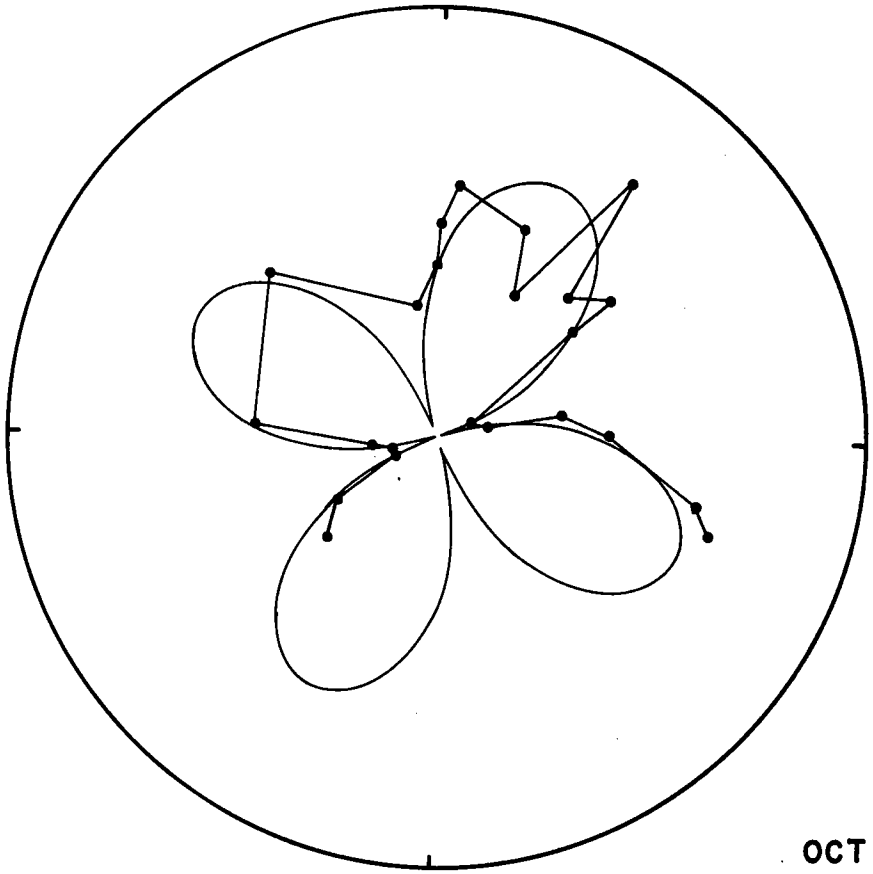

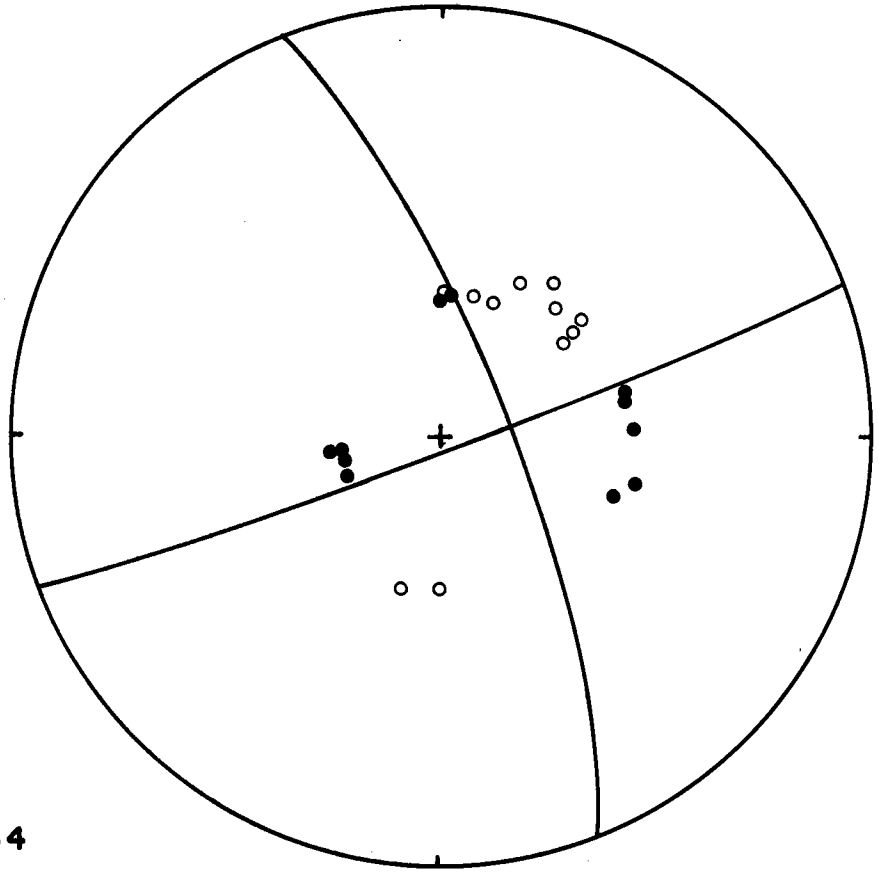

OCT 12, 1964

PERIOD = 67
Q = 125
DEPTH = 5

STRIKE = 249
DIP = 87
SLIP = 167

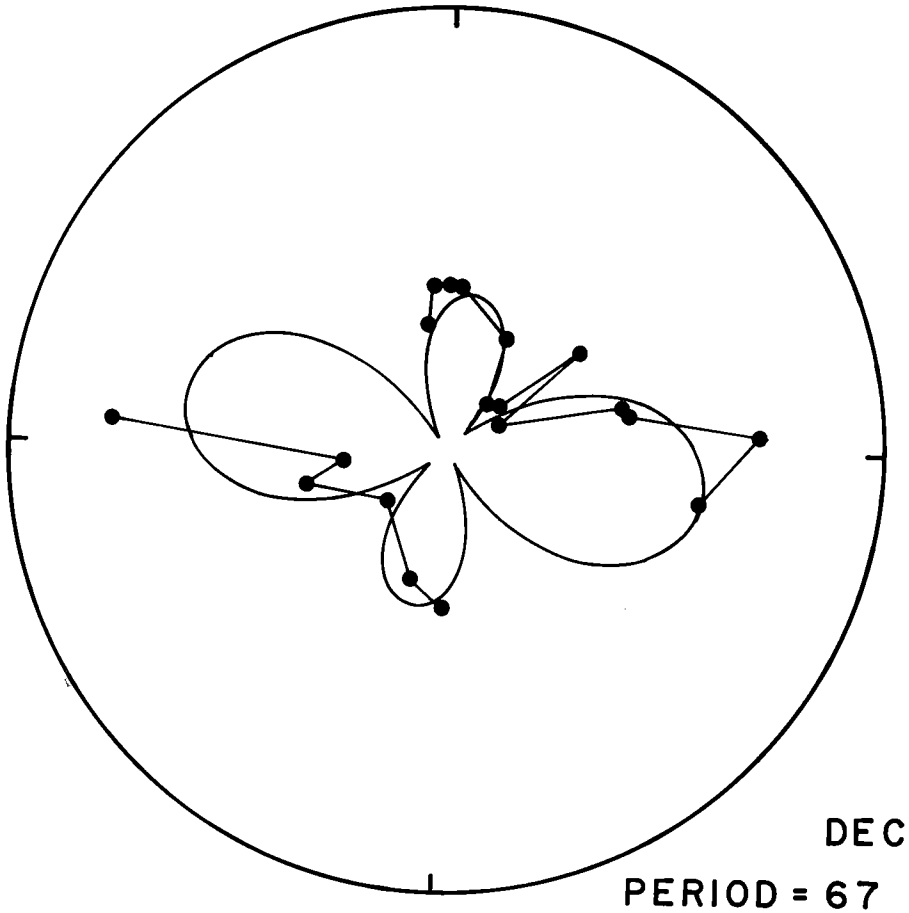

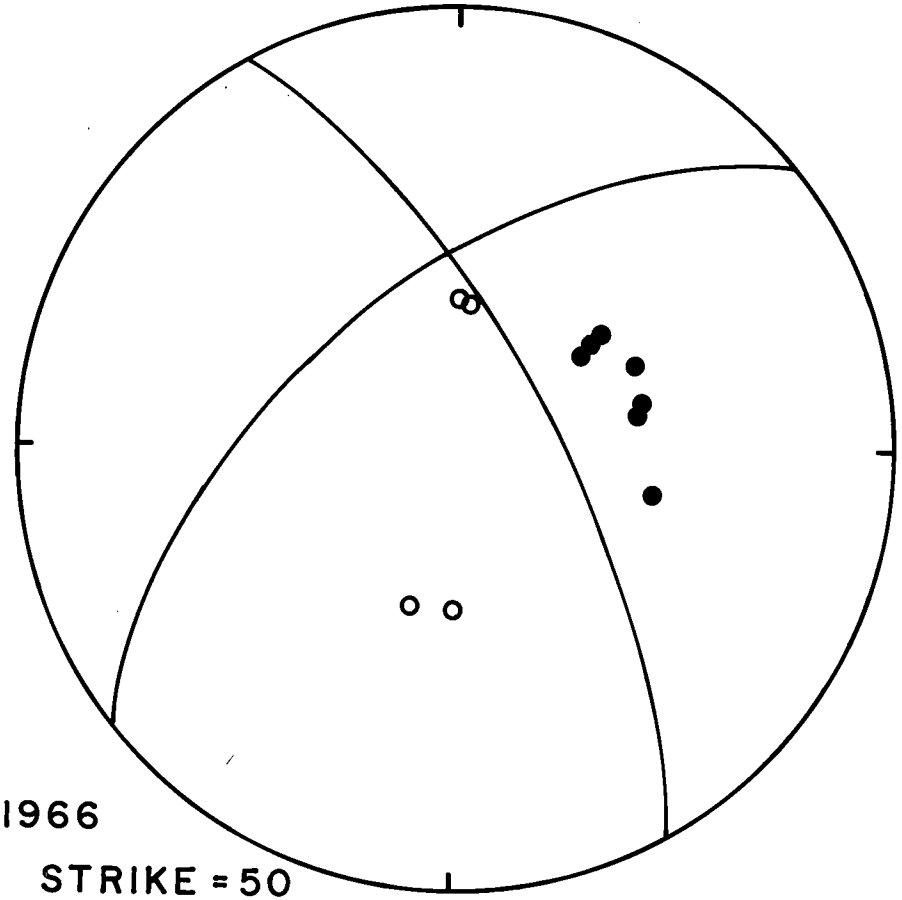

DEC 29, 1966

PERIOD = 67
Q = 125
DEPTH = 5

STRIKE = 50
DIP = 60
SLIP = -160

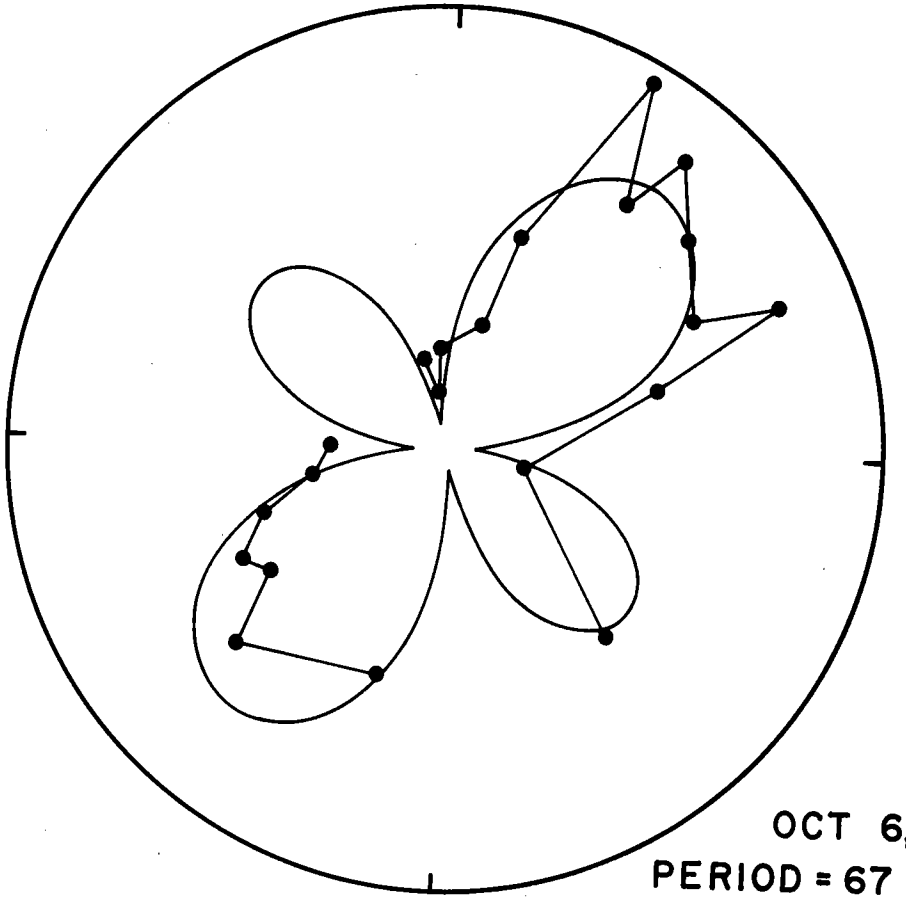

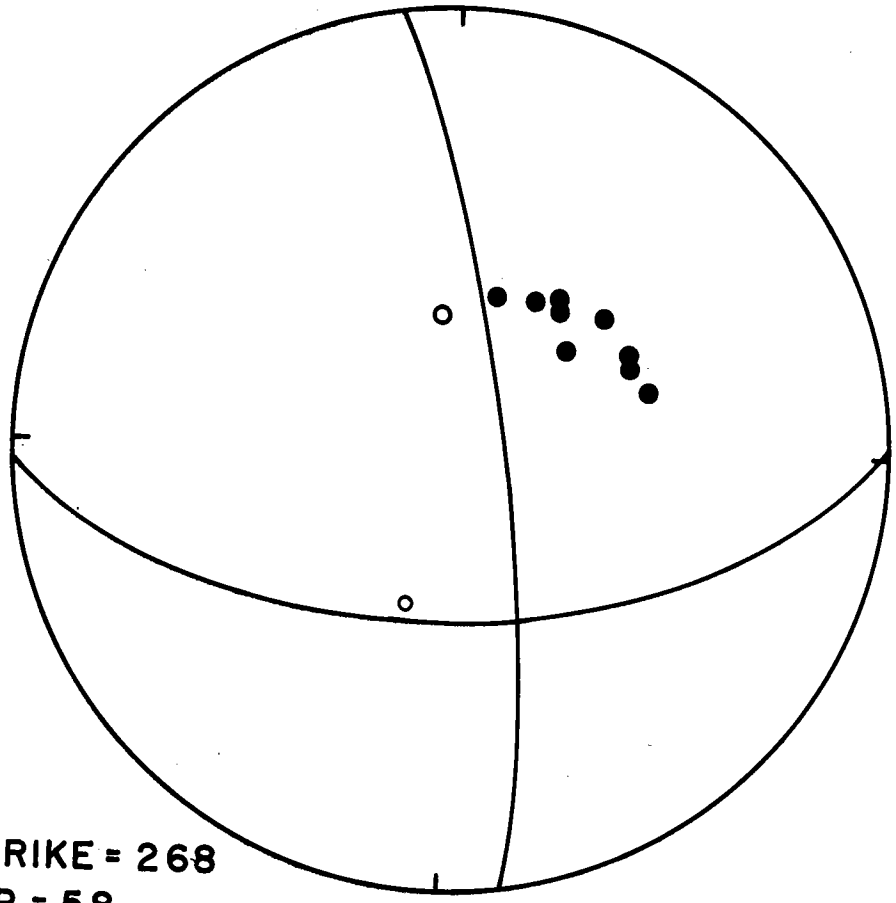

OCT 6, 1964

PERIOD = 67
Q = 125
DEPTH = 5

STRIKE = 268
DIP = 58
SLIP = -12

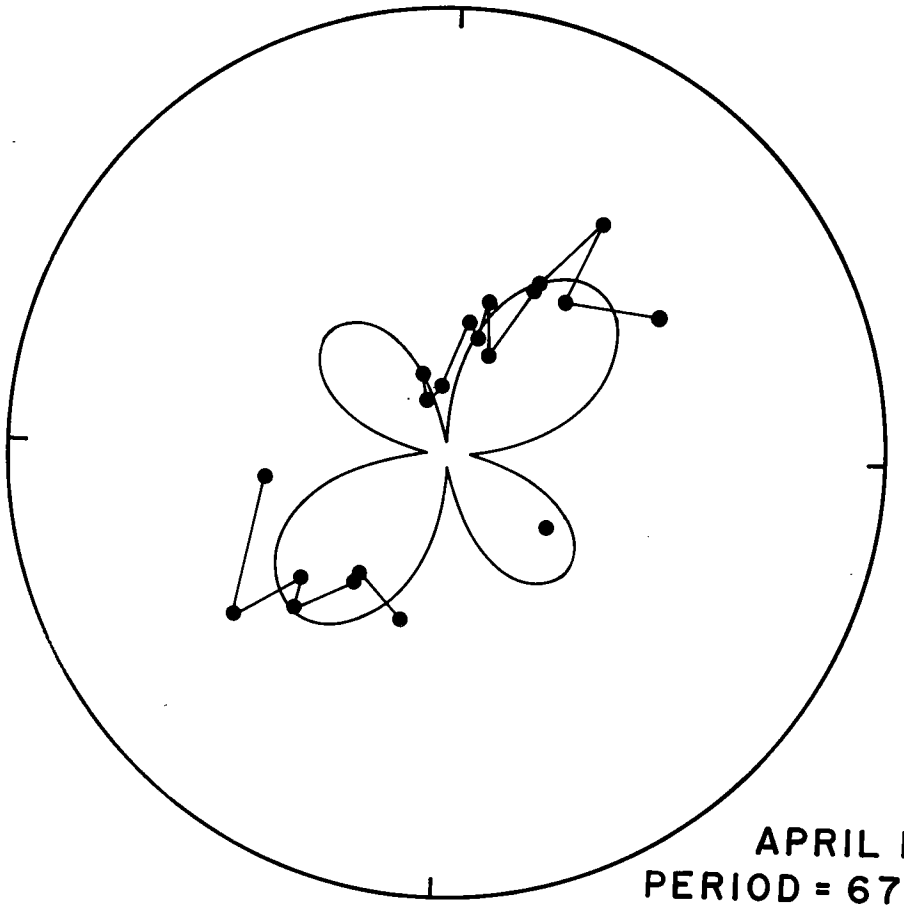

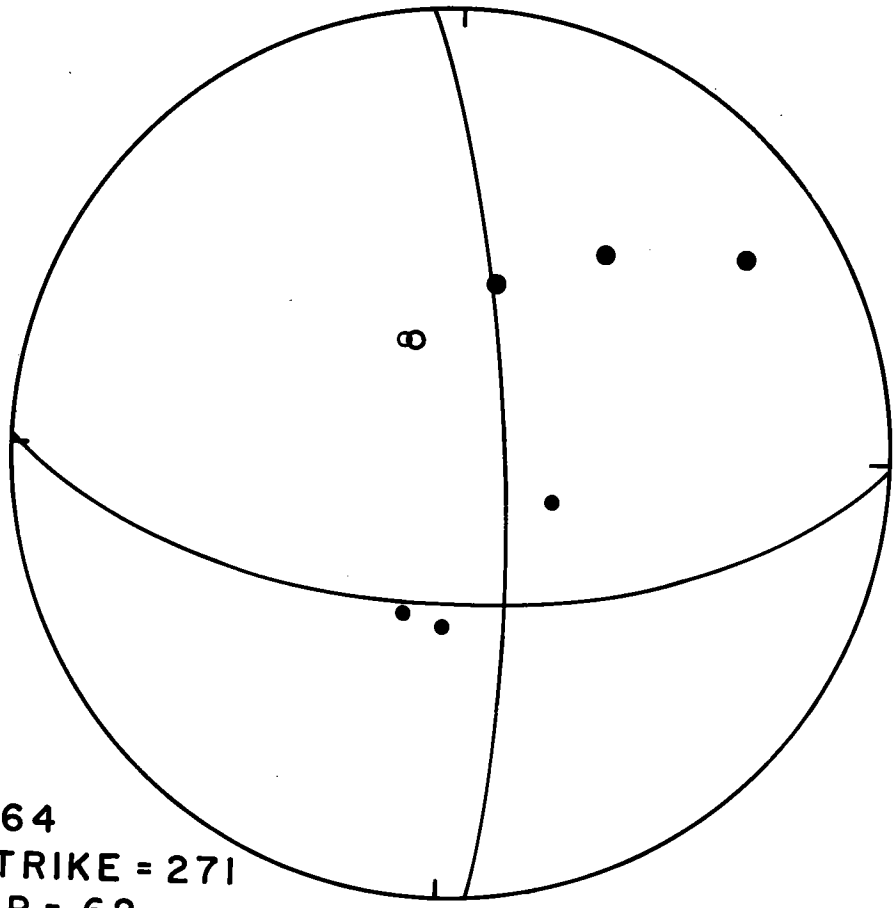

APRIL 19, 1964

PERIOD = 67
Q = 125
DEPTH = 5

STRIKE = 271
DIP = 62
SLIP = -11

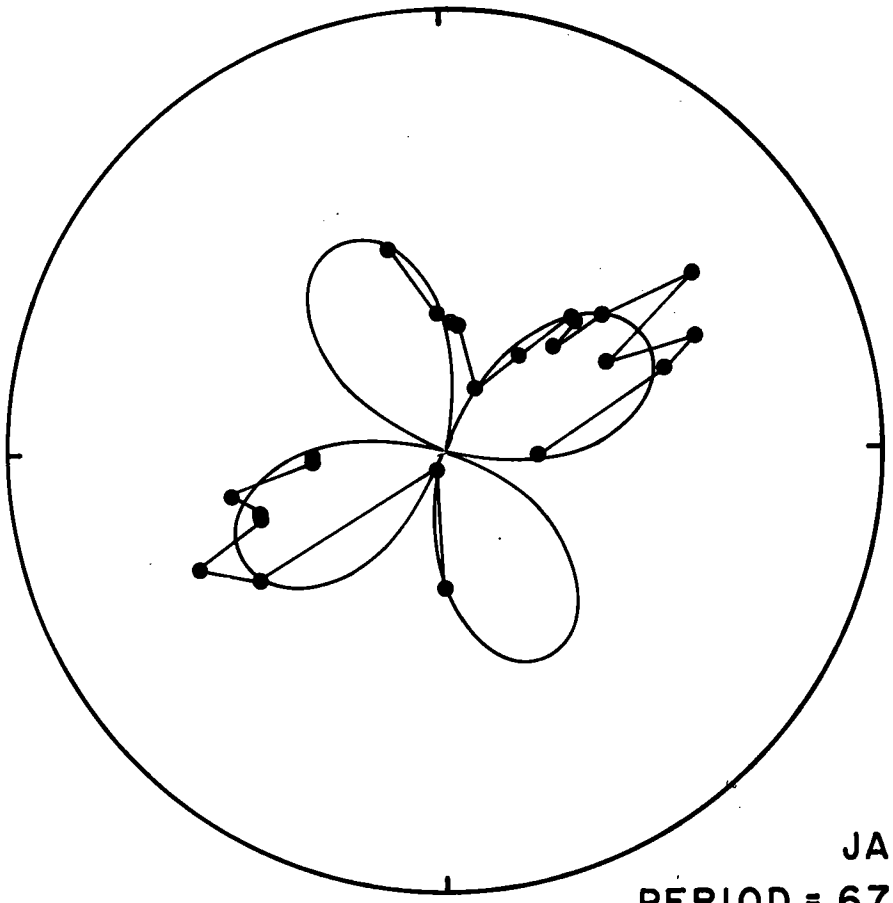

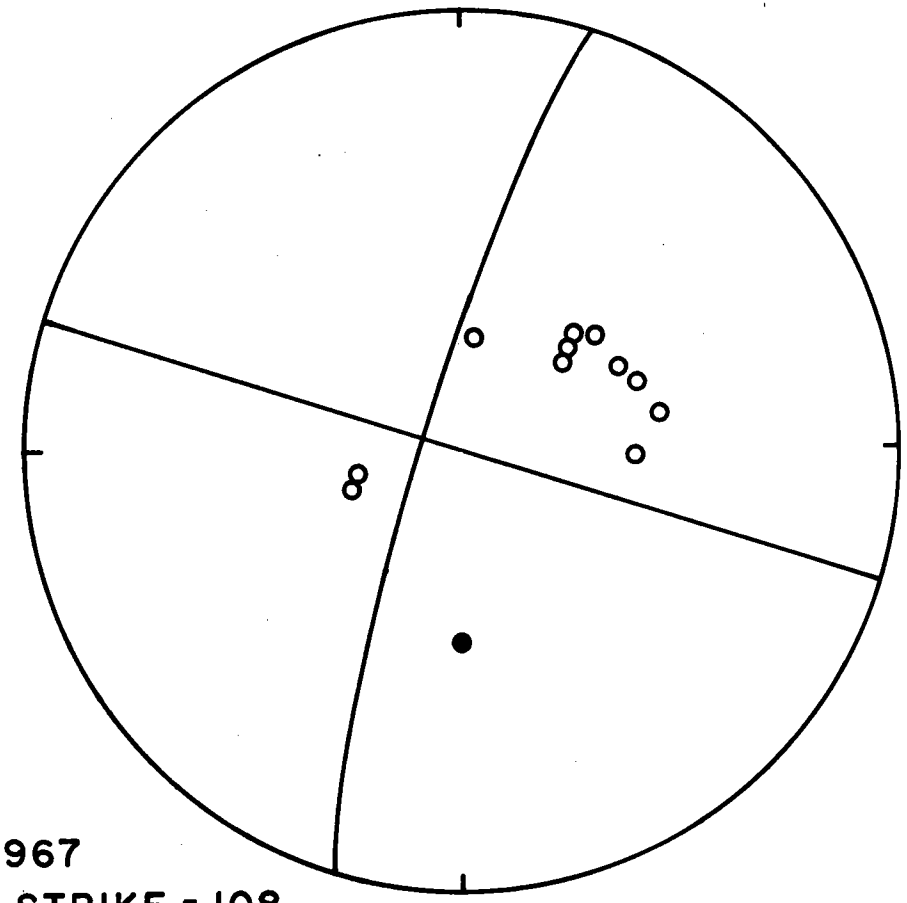

JAN 21, 1967

PERIOD = 67

Q = 125

DEPTH = 5

STRIKE = 108

DIP = 90

SLIP = 172

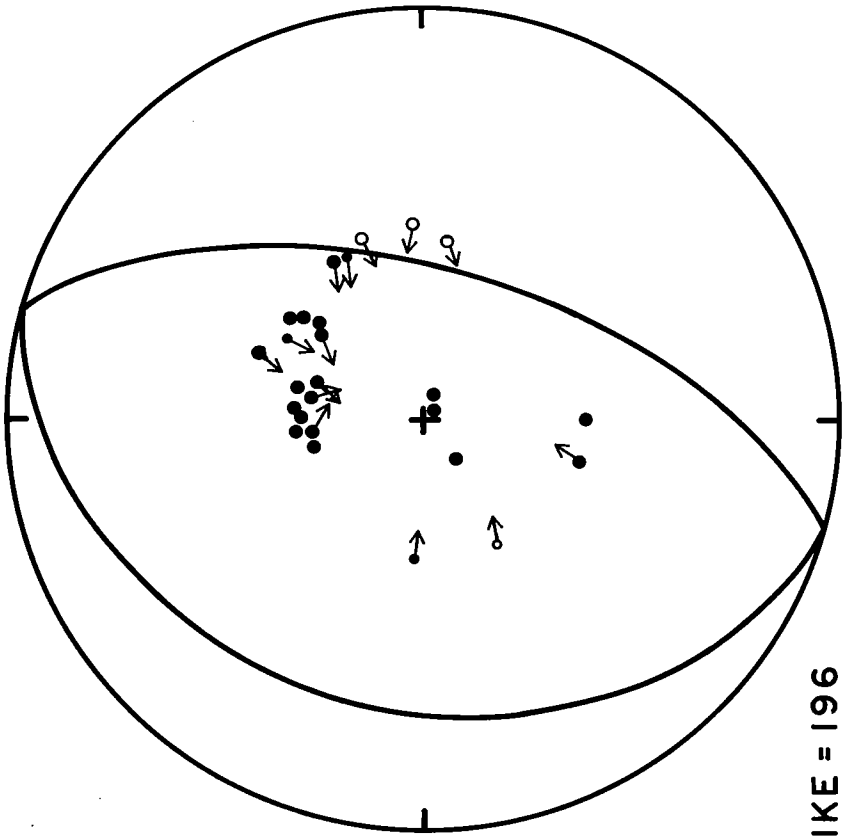

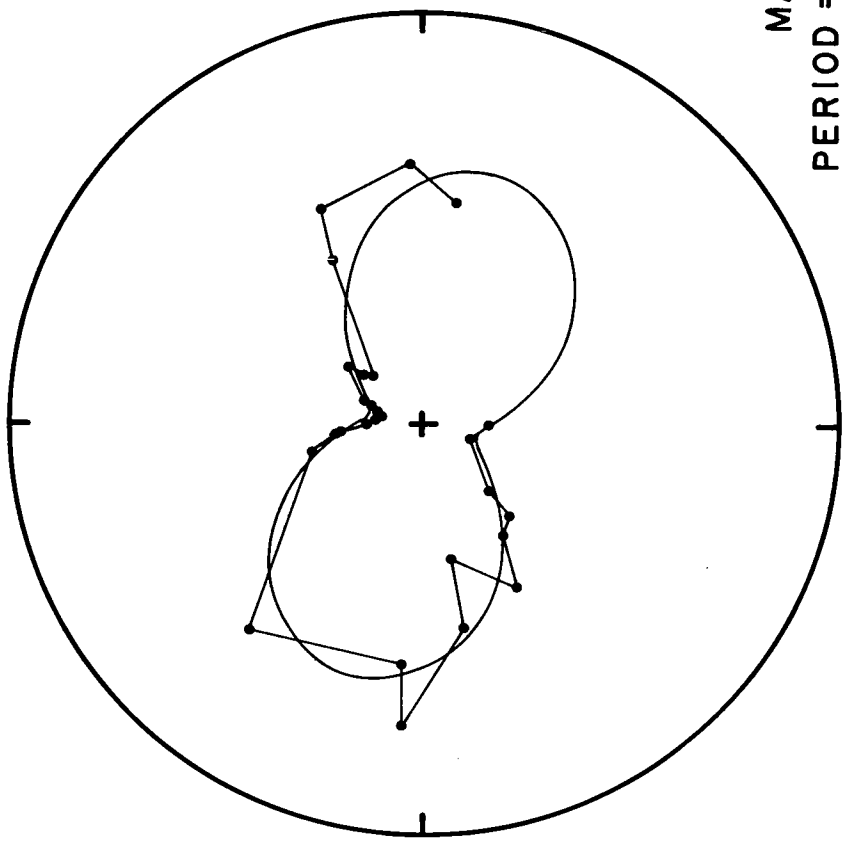

MAY 9, 1971
PERIOD = 67
Q = 125
DEPTH = 5
STRIKE = 196
DIP = 60
SLIP = 90

Appendix 3. Numerical surface wave refraction experiments.

An idealized model of the ridge-ocean basin system is illustrated in fig. A2. An earthquake source is located at the center of the figure, as indicated by the small circle. The diameter passing through the source represents the ridge axis. The local phase velocity at the ridge axis is V_1. The phase velocity increases linearly with distance from the ridge axis reaching a maximum of V_2 at distance w away from the axis. Outside this central zone, the phase velocity, V_2, is constant. Seismic stations are placed at uniform distance, d, away from the source, as indicated by the triangle. The angle between the ridge axis and the great circle path to the station is θ. The experiment consists of computing the difference between the travel time (total phase shift) of a wave following a great-circle path and a wave taking the least-time path. In the figure, the least time path is indicated by the curved line. The signal travels along this path reaching the station sooner than the predicted time for a straight-line path. The time difference corresponds to the error created by assuming great circle propagation.

The results of several experiments with different values of w and V_2 are shown in fig. A3. The curves give the time delay which would result if the waves traveled

a great circle path. In each experiment, V_1 was 4.0 km/sec and d was 4000 km. For curve 1, V_2 was 5% higher than V_1 and w was 200 km; curve 2, V_2 is 10% higher and w is 1000 km; curve 3, V_2 is 5% higher and w is 1000 km; curve 4, V_2 is 10% and w is 4000 km. When w is 200 km, the length of the great circle path within the central region is small except for azimuths very close to the ridge axis. Consequently, the time error is a significant fraction of the total time spent within the central zone (as seen by a great-circle path). The error is controlled by two factors: the velocity contrast and the width of the central zone compared to the length of the path.

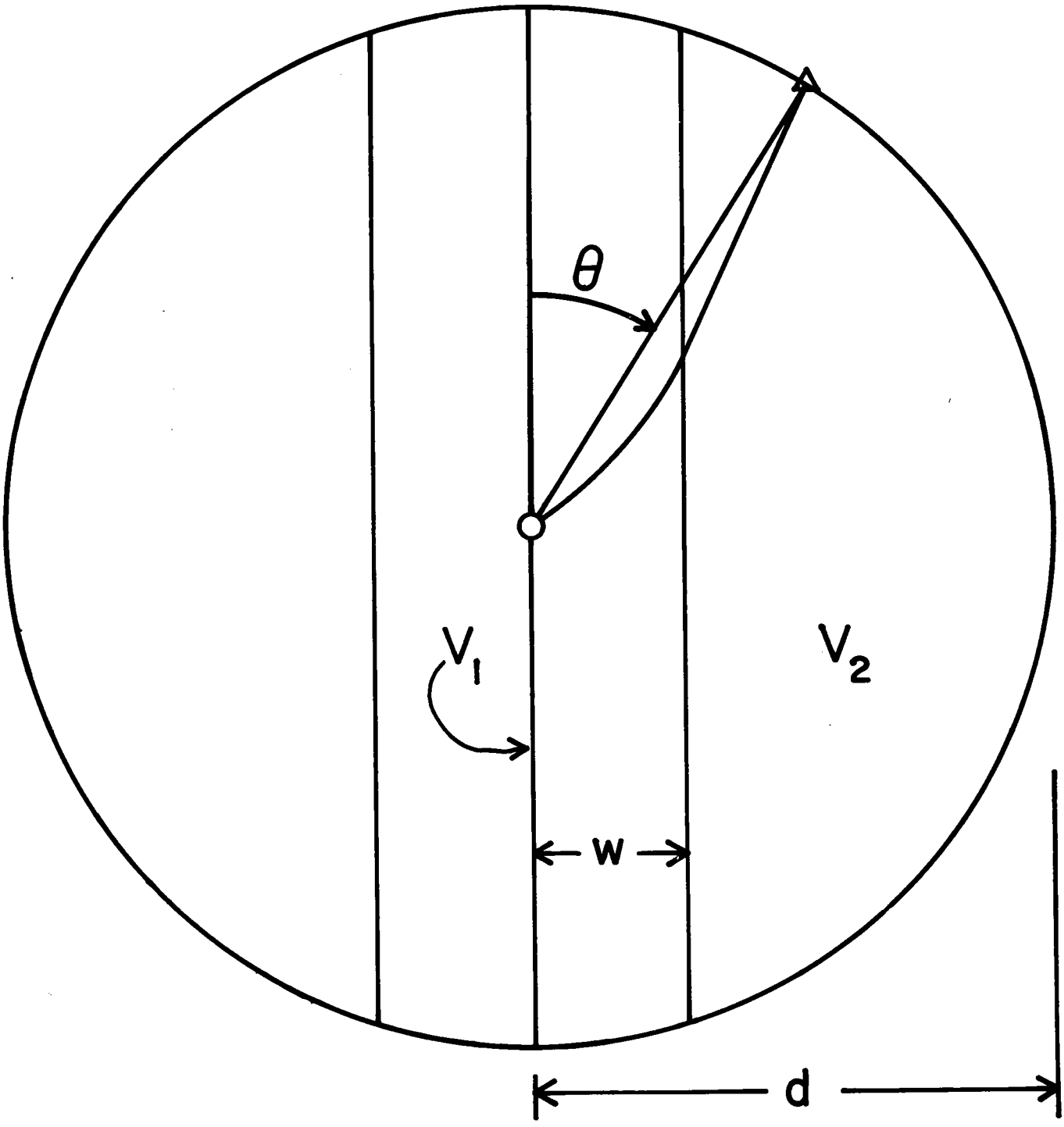
θ
V1
V2
w
d

Figure A3